NASA CR-132419

INVESTIGATION OF APPLICATION OF TWO-DEGREE-OF-FREEDOM DRY TUNED-GIMBAL GYROSCOPES TO STRAPDOWN NAVIGATION SYSTEMS

Final Report

APRIL 1974

Prepared under Contract No. NAS1-12175 by
TELEDYNE SYSTEMS COMPANY
Northridge, California

for

NATIONAL AERONAUTICS AND SPACE ADMINISTRATION

NASA CR-132419

INVESTIGATION OF APPLICATION OF TWO-DEGREE-OF-FREEDOM DRY TUNED-GIMBAL GYROSCOPES TO STRAPDOWN NAVIGATION SYSTEMS

Final Report

APRIL 1974

Prepared under Contract No. NAS1-12175 by
TELEDYNE SYSTEMS COMPANY
Northridge, California

for

NATIONAL AERONAUTICS AND SPACE ADMINISTRATION

ABSTRACT

This report describes the work accomplished during the investigation of the application of two-degree-of-freedom dry-tuned gimbal gyroscopes to strapdown navigation systems.

The initial phase of the study was concerned with the establishment of performance goals for such a system in the operating environment characteristic of VTOL aircraft. The fundamental performance goals which were established are:

(1) Cost: Less than $50,000 in quantities of 200.

(2) Reliability: Probability of failure less than 10^{-6} for a 30 minute flight.

(3) Accuracy: Navigation error less than 3 nautical miles per hour.

A "conventional" strapdown configuration, employing analog electronics in conjunction with digital attitude and navigation computation, was examined using various levels of redundancy and both orthogonal and non-orthogonal sensor orientations. It was concluded that the cost and reliability performance constraints which had been established could not be met simultaneously with such a system. This conclusion led to the examination of an alternative system configuration which utilizes an essentially new strapdown system concept. This system employs all-digital signal processing in conjunction with the newly-developed large scale integration (LSI) electronic packaging techniques and a new two-degree-of-freedom dry tuned-gimbal instrument which is capable of providing both angular rate and acceleration information. Such a system is capable of exceeding the established performance goals.

This page intentionally left blank.

TABLE OF CONTENTS

This page intentionally left blank.

LIST OF ILLUSTRATIONS

LIST OF ILLUSTRATIONS (Continued)

LIST OF ILLUSTRATIONS (Continued)

I. SUMMARY

This report describes the work accomplished during the investigation of the application of two-degree-of-freedom dry-tuned gimbal gyroscopes to strapdown navigation systems.

The initial phase of the study was concerned with the establishment of performance goals for such a system in the operating environment characteristic of VTOL aircraft. The fundamental performance goals which were established are:

(1) Cost: Less than $50,000 in quantities of 200.

(2) Reliability: Probability of failure less than 10^{-6} for a 30 minute flight.

(3) Accuracy: Navigation error less than 3 nautical miles per hour.

A "conventional" strapdown configuration, employing analog electronics in conjunction with digital attitude and navigation computation, was examined using various levels of redundancy and both orthogonal and non-orthogonal sensor orientations. It was concluded that the cost and reliability performance constraints which had been established could not be met simultaneously with such a system. This conclusion led to the examination of an alternative system configuration which utilizes an essentially new strapdown system concept. This system employs all-digital signal processing in conjunction with the newly-developed large scale integration (LSI) electronic packaging techniques and a new two-degree-of-freedom dry tuned-gimbal instrument which is capable of providing both angular rate and acceleration information. Such a system is capable of exceeding the established performance goals.

The conventional and all-digital configurations represent two extremes - a full spectrum of intermediate configurations exists which utilize the dry-tuned instrument under consideration and perform the desired system functions. These two extremes provide a useful basis for evaluation from which a meaningful extrapolation to intermediate configurations is possible.

An analysis and simulation of self-alignment techniques was conducted. Both optimal and sub-optimal alignment mechanizations were considered. It was concluded that alignment could be performed in the anticipated VTOL operational environment in less than 10 minutes.

The equations which must be solved in order to effect navigation and attitude solutions have been examined. Various mechanizations have been considered and traded off and a specific formulation has been selected.

A key element in any strapdown system is the conversion of sensor information into the digital form required for attitude and navigation computations. An extensive survey of analog-to-digital conversion techniques was conducted and an optimum mechanization for the VTOL application under consideration was selected.

An extensive computer simulation program has been written in order to evaluate various computational algorithms for attitude determination, navigation, and instrument compensation. This simulation includes detailed models of the inertial sensors and the A/D converter. Hardware tests have been performed in order to verify the mathematical models which are being employed.

The compensation requirements for the TDF tuned gimbal gyroscope have been extensively studied. A basic design for a conventional system is presented. This design may also be useful as the framework for compensation required using the all-digital approach.

II. INTRODUCTION

The objective of this study is to investigate the application of two-degree-of-freedom dry tuned-gimbal gyroscopes to strapdown inertial navigation systems.

Historically, the development of strapdown inertial systems has been retarded by two fundamental types of hardware limitation - the speed of the computer which must process the sensed inertial data in order to maintain a sufficiently accurate attitude reference and the dynamic range required of the gyroscopes which are utilized to provide this data. The development of modern high speed airborne digital computers has obviated the first limitation. Several types of gyros have been or are currently being developed which appear to possess a sufficiently large dynamic range to eliminate the second limitation.

One of the most promising types of gyroscope for strapdown navigation applications is the two-degree-of-freedom dry tuned-gimbal gyro. Such gyros are currently being manufactured in significant quantities, have been and are being tested under a variety of environmental conditions, and are being used in certain system applications, such as sounding-rocket type attitude control. To date, however, insufficient attention has been given to the merits of using such instruments in strapdown navigation system applications.

Strapdown navigators have application for a wide variety of requirements. In order to definitize the study, certain goals and restrictions have been applied for purposes of this study. These pertain primarily to performance-cost, reliability, and accuracy - and to operational environment - the study is limited to VTOL type applications. These considerations are described in Section III.

The primary advantages which are conventionally attributed to strapdown navigators when contrasted to their gimbaled counterparts are (1) higher reliability due to decreased component count; (2) simplified redundancy arising from the obviation of the necessity for gimbal structures and associated electronics and electromechanical devices; (3) simplified failure detection in redundant configurations;and (4) lower acquisition cost and cost of ownership. An additional important advantage, one which has not been generally recognized, is the possibility of utilizing all-digital processing, thus eliminating

the extensive analog electronics packages which typify both conventional strapdown and gimbaled mechanizations. The ability of the dry tuned gyro to capitalize on these advantages is of fundamental interest in this study. These considerations are discussed in detail in Section IV of this report.

Other important requirements of a strapdown navigator include the computation of attitude and navigation parameters, initial alignment, analog-to-digital and digital-to-analog data conversion, and compensation for both static and dynamic instrument errors. Various techniques for accomplishing these functions are analyzed and overall computational requirements are formulated in Section V.

In order to effectively trade-off the relative merits of the various mechanization and computational techniques being considered, extensive computer simulation has been employed. These simulations also provide, in conjunction with various analyses, the basis for evaluation of overall system accuracy. The veracity of the mathematical models used for the inertial instruments has been established by means of actual hardware tests. The simulation and testing is described in Section VI.

The final section of this report, Section VII, provides an analysis and interpretation of the results which have been obtained from the study, relates them to the goals of the study, and recommends areas of further study.

III. GOALS OF THE STUDY

The primary objective of this study is to investigate the application of two-degree-of-freedom dry tuned-gimbal gyroscopes to strapdown inertial navigation systems. The utlimate measure of such applicability is the performance of the system. The measure of system performance is, however, necessarily coupled to the tasks which the system is required to perform: performance which is acceptable or even outstanding in one application may be marginal or unacceptable in another. For this reason it is useful to specify an operating environment and a set of performance goals for the strapdown navigation systems which are to be considered in the study.

The operating environment which is used in this study is that characteristic of a commercial VTOL application. Such an environment imposes relatively severe conditions on the strapdown system in several respects: the high linear and angular vibration levels excite error modes in the inertial instruments which would be unimportant in a more benign environment; the vibratory and oscillatory vehicle motions provide a stringent test of the ability of the computational algorithms to track the motions of the vehicle; and the viability of the self-alignment operation is thoroughly tested by the presence of vibration, passenger-, baggage-, and fuel-loading, wind gust effects, and other similar disturbances as well as a limited time available for alignment. For purpose of the study, the following assumptions are made concerning the operational conditions:

(1) Linear and angular vibration amplitudes and frequencies are those typical of the CH-46 and similar large helicopters.

(2) Maximum angular rates are 4 rad/sec.

(3) Maximum flight duration is 2 hours, typical of short inter-city operations.

(4) Multi-stop, intra-city operation with 7 minute flight time, 3.5 minute ground time is a typical mission scenario.

(5) Alignment should be completed in 10 minutes or less.

Performance of the system is measured by three basic factors: reliability, cost, and accuracy. A strong correlation exists among these measures: increased reliability and/or accuracy is usually accompanied

by an increase in acquisition cost and cost-of-ownership. In order to retain a reasonable balance among the three basic performance parameters during the course of the study, the following performance goals have been established:

(1) Cost should be less than $50,000 in production quantities (200).

(2) Probability of failure for a 30 minute flight should be less than 10^{-6}.

(3) Navigational error should be less than 3 nautical miles per hour circular error probable (CEP).

Working within the constraints imposed by the operational and performance factors described above, a basic system configuration has evolved. Evaluation of this system includes the following factors:

(1) The weak links in the system have been defined from the standpoints of accuracy, reliability, and cost-of-ownership.

(2) Failure detection procedures and algorithms have been developed for both hard and soft failures.

(3) A set of equations capable of performing the requisite attitude, navigation, alignment, and compensation functions have been developed and the corresponding computer speed, memory, precision, and input/output requirements have been established.

(4) A comprehensive error analysis has been performed.

(5) The risk factors associated with the system development have been assessed.

IV. SYSTEM CONFIGURATIONS

All current strapdown navigators have two basic elements - an inertial sensor package and a digital processor. Several auxilliary elements are also required, including an analog-to-digital converter package which provides the essential interface between sensors and computer, power supplies for the inertial instrument pickoff excitation and gyro spin motors, servos for the inertial instrument caging loops, and display and external interface electronics.

Although all strapdown systems are comprised of the elements described above, there is a broad range of possible system configurations. Some of the variations which may be employed are:

(1) Instrument operating configuration: The two-degree-of-freedom dry tuned-gimbal instrument may be used as a conventional rate sensor or as a pendulous accelerometer. Also in development is a version of the instrument which provides both rate and acceleration simultaneously.

(2) Instrument orientation: The gyros and/or accelerometers may be oriented with their sensing axes mutually orthogonal or (particularily in redundant systems) non-orthogonal.

(3) Instrument caging and compensation: The caging loop and other sensor-related servo functions, as well as compensation for various instrument errors, may be performed in an analog "platform electronics" package; digitally, either in the central processor or in auxilliary processors; or a combination of digital and analog processing.

(4) Analog-to-digital conversion: Most conventional strapdown mechanizations employ separate reset integrator type voltage to frequency devices for digitization of each sensor signal. The contractor has recently developed and operated a versatile multiplexed analog-to-digital converter capable of converting all necessary information within a single unit. Other conversion mechanizations are also possible.

(5) Type and level of redundancy: Various types and levels of redundancy may be employed in order to achieve optimum reliability at minimum cost.

In this section these and other factors are examined and traded off in order to consider their effects on the various system performance parameters. Two basic system configurations - a conventional mechanization and an "all-digital" mechanization using the new dry-tuned spin-coupled accelerometer-gyro (SCAG) - are utilized as baseline systems from which the performance of intermediate variations in system configuration can readily be extrapolated.

System Organization

Two baseline types of strapdown navigation systems are utilized in the study. The first is a conventional design typical of most existing strapdown systems. A non-redundant form of such a system is indicated by the block diagram of Figure 1. The inertial sensor package consists of two or more two-degree-of-freedom dry tuned-gimbal gyros and three or more accelerometers. Alternatively, if the gyros are made pendulous, three gyros suffice to provide three axis rate and three axis acceleration information in a non-redundant configuration. Conventional spin motor and pickoff supplies and analog servo electronics packages are utilized. Also included is the requisite complement of analog-to-digital converters and an external interface and display package.

The second baseline system employs maximum utilization of digital processing by incorporating multiplexed A/D converters to assign virtually all non-mechanical functions to the digital processor. This all-digital baseline system also utilizes the spin-coupled gyro-accelerometer (SCAG) form of the dry tuned gimbal instrument. The SCAG is capable of providing two axes of angular information and two axes of acceleration information simultaneously. A block diagram of the all-digital SCAG system is shown in a triple-redundancy configuration in Figure 2.

The remainder of this section is devoted to a brief description of the all digital and SCAG concepts and their utility in a redundant strapdown navigation application. This system and its conventional counterpart described above, provide the basic framework for much of the discussion of the remainder of the report. Clearly, these two baseline systems represent but two of a multitude of possible system designs. They do, however, provide a firm basis for extrapolation of the performance obtainable by other system designs which are intermediate to these two.

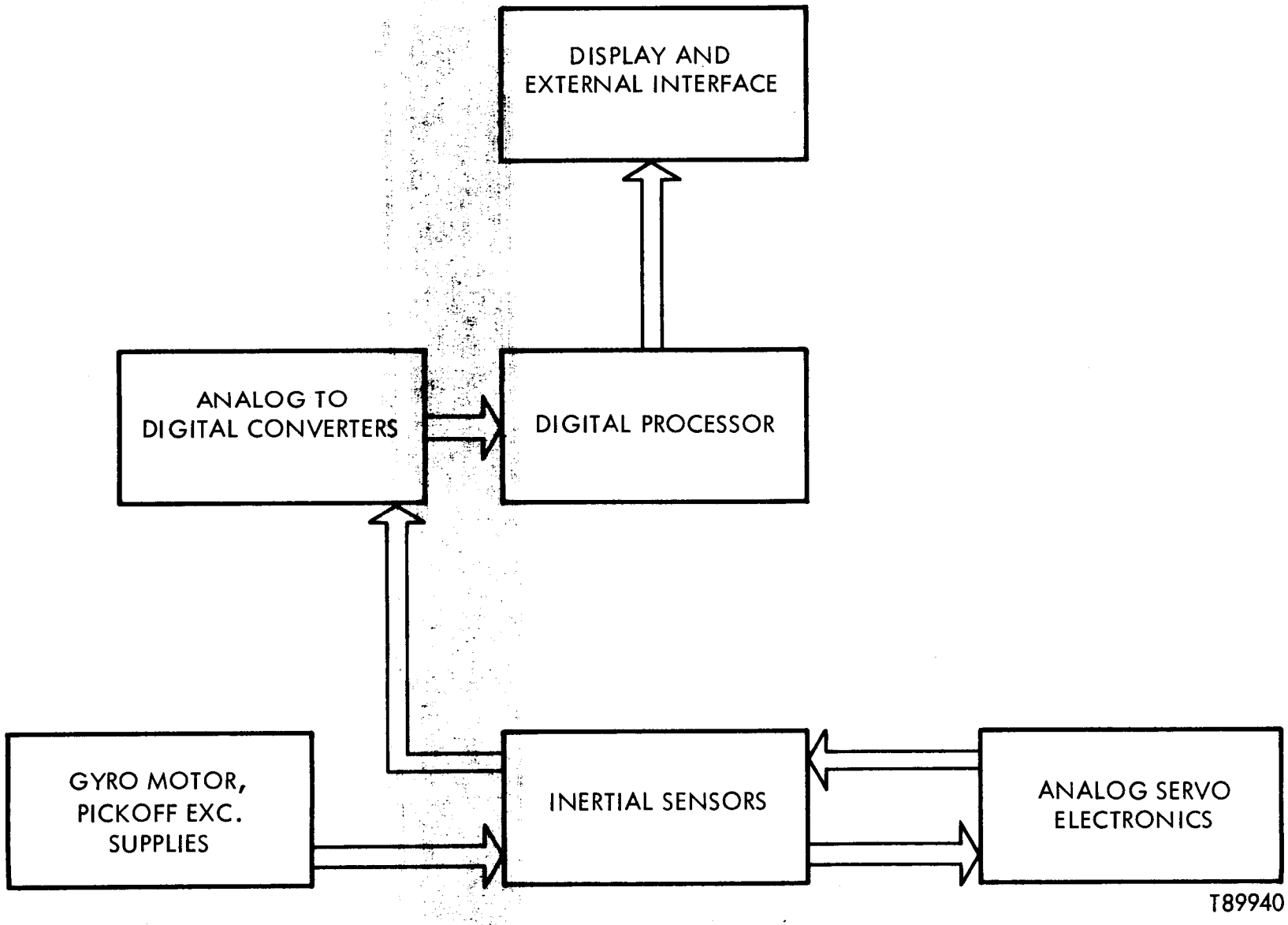

Figure 1. Non-Redundant Conventional Strapdown Mechanization Block Diagram

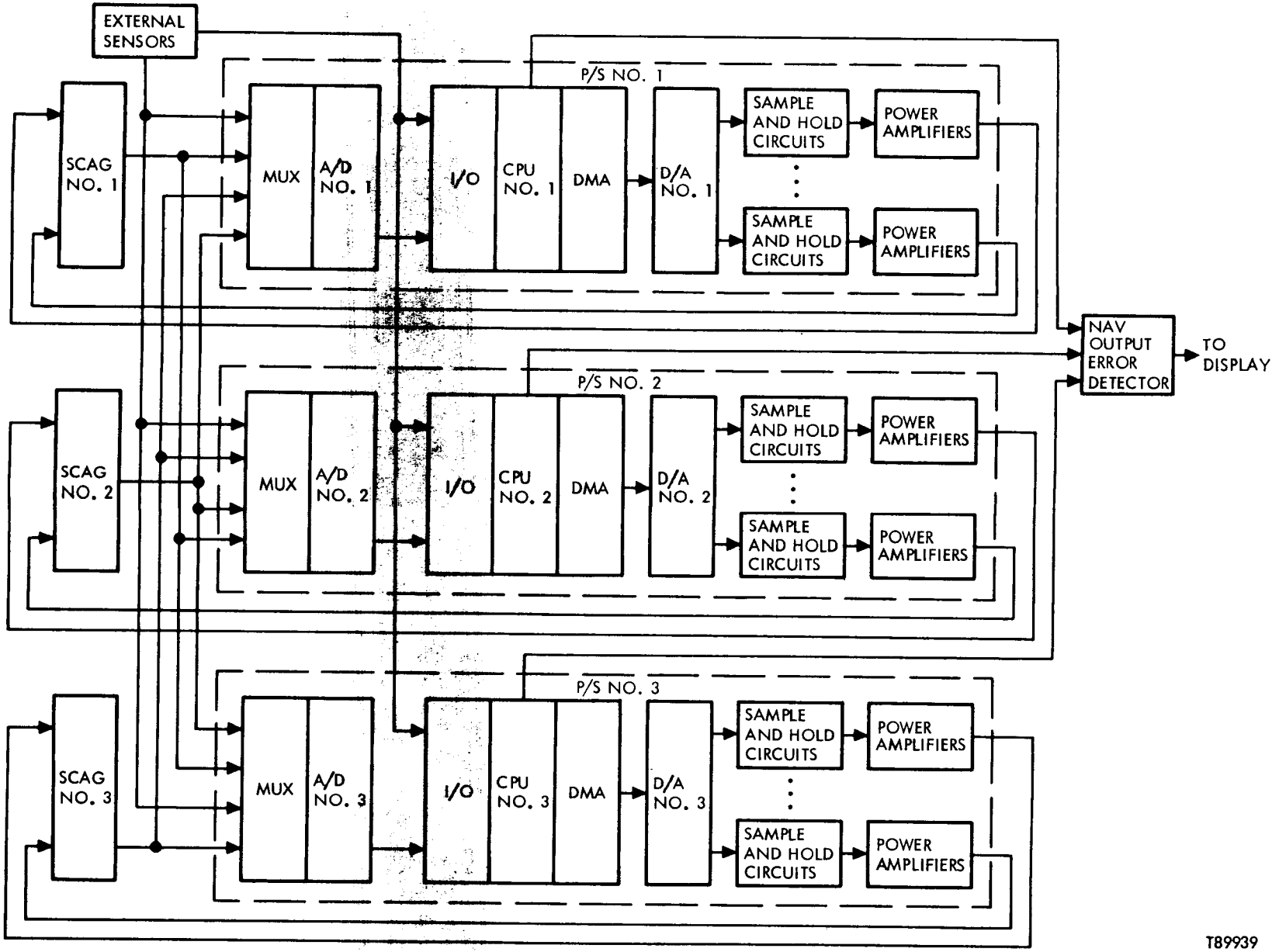

Figure 2. Triple Redundant All-Digital-SCAG Strapdown System Block Diagram

Redundant all-digital strapdown system. - The Redundant Digital Strapdown System design is based upon the following:

(1) The utilization of tuned inertial sensors, each of which supplies two axes of angular rate and two axes of linear acceleration information. This sensor, currently under study by Teledyne, is based upon a proprietary, but logical evolution of the current Teledyne Strapdown Gyro design. Two such sensors are required for a basic inertial system. Three such sensors provide sufficient redundancy information to provide a continuous self test for, and isolation of, a potential instrument failure. In the event of such a failure, the remaining two instruments continue to provide the required three axes of angular rate and linear accelerating sensing. Four sensors provide full Fail-Op/Fail-Op capability.

The almost total utilization of modern digital processing techniques and hardware for all of the non-mechanical operation of the inertial system, including the closing of the sensor control loops.

The application of the above two fundamental design concepts results directly in an extremely low redundant system failure rate (less than 10^{-6}/hr) at a production price of less than $50K per system. A correspondingly reliable conventional redundant system costs approximately $85K.

Spin-coupled accelerometer-gyro (SCAG). - In order to achieve the required inertial measurements at minimum cost it is obviously desirable to extract these measurements from the simplest combination of inertial instrument sensing mechanizations which provides the required accuracy and reliability. There exists a mechanization which, using a single tuned suspension rotor, provides both angular rate and linear acceleration sensing. This mechanization makes use of the Teledyne proprietary "spin-coupled" technique, currently under investigation and development. In the case of the Spin-Coupled Accelerometer-Gyro (SCAG), the instrument has the following characteristics:

(1) Separate two-axis angular rate and linear acceleration outputs.

(2) Angular rate output unaffected by mass unbalance, anisoelasticy, "fixed restraint", twice spin frequency angular input rectification, or any of the other usual error torque sources. This is an especially significant capability in that the need for gyro bias, mass unbalance, and temperature compensation is essentially eliminated.

(3) Simple construction, using fewer parts per sensor than for the current Teledyne Strapdown Gyro.

Teledyne is presently analyzing the SCAG concept in detail and formulating several candidate practical designs. Teledyne is also proving out the "spin-coupled" principle in a variation of the current gyro design. An in-house test and evaluation program for this gyro has been initiated.

General navigation system concepts employing SCAG sensors. - The basic non-redundant IMU requires only two SCAG sensors (with spin axes normally orthogonal to one another) for the entire instrument complement.

The SCAG sensors allow the optimum formulation of a redundant sensor system in that, with only a total of three SCAG sensors the following conditions are met:

(1) The three spin axes are normally oriented mutually orthogonal so that the condition of maximum angular sensitivity is met for error detection, as well as maximum navigation accuracy after a failure.

(2) Sufficient redundant information is available to provide specific error detection and isolation; the three SCAG sensors provide a total of six independent angular rate and six independent linear acceleration measurements. By continuously comparing the three axis angular rate and acceleration vectors as computed from each combination of three of the basic measurements for each (there is a total of 20 such combinations from each group of six measurements) quantity it is possible by a direct logical process to isolate a failure to a specific axis of a specific quantity (angular rate and/or linear acceleration) of a specific sensor.

(3) Detection and isolation of two failures (i.e., Fail-Op/ Fail-Op operation) is made possible by employing four sensors.

A system block diagram which illustrates the use of three SCAG sensors in such a redundant navigation system mechanization was shown in Figure 1. As shown there, the outputs from each SCAG are available to each of the triply redundant computer channels so that, in the event of a failure in any channel, the remaining channels are provided with sufficient information to continue system operation.

Utilization of digital processing techniques and hardware. - An analysis of the hardware content of present day inertial navigation systems and the associated costs shows that a significant fraction (on the order of 30%) of the system is made up of analog and computer interface electronics. The advent of newly available digital computer devices and high speed analog-to-digital and digital-to-analog- converters now makes practical:

(1) The replacement of essentially all of the analog electronics by equivalent digital computation elements.

(2) The modernization and expansion of the current computer interface electronics using a multiplexed input analog-to-digital converter to insert the required data into the digital processor and a multiplexed output digital-to-analog converter to drive all of the sensor torquers, spin motors, and pickoff excitation voltages. The former (computer input multiplexing) scheme is currently being employed successfully in the Teledyne SOFT Strapdown System. For the SCAG, the multiplexed input signals are the instrument pickoff angles (two per instrument), the instrument temperatures, and (optionally) the torquer currents; the output signals are as listed above.

The principal area of engineering design here is the determination of the specific software requirements for closing the instrument loops, including the usual instrument compensation. Further study is required to determine the specific computational speed and memory requirements for these functions, but preliminary estimates indicate that these requirements are comparable to the strapdown attitude computation requirements.

What is gained by all of this, of course, is that the presently cumbersome and necessarily specialized analog and digital interface circuitry can be replaced by a relatively modest increase to the much more versatile digital hardware that is already required for attitude and navigation computations.

Teledyne is currently studying, developing and producing advanced digital processors. One example of this work, the Teledyne TDY-52 series of processors, employs a new and unique design for programmable digital computers suitable for:

Dedicated Processors	Distributed Computer
Central Computer	Array Processors

The TDY-52 series computers consist of application-specified elements of central processing units (CPU), read only memories (ROM), and random access memories (RAM). The individual elements are extremely small and low powered. Thus it is more meaningful to consider the computer as an element or component of the overall strapdown inertial system rather than a separately designated subsystem.

The standard package for each computer exists in the form of (typically) a 2.5 inch diameter by 0.10 inch high hermetically sealed flat package. Non-standard form factors can be designed to take advantage of the space availability requirements. Contained within the package is the micro-programmed CPU, with some memory for program storage. Increased memory is obtained by adding memory packages. Each CPU and/or memory package weighs about 25 grams and dissipates from 0.5 to 7.0 watts of power. The performance of the TDY-52 models vary from typical micro-computer speeds of 10 μs for an ADD instruction to minicomputer speeds of 1 μs for an ADD instruction in 1976. The cost now is a little under $2,000. As the costs of the components are reduced, a projected cost of less than $500 in 1976 can be forseen for the higher performance models.

From a maintainability viewpoint, the computer may be considered disposable in that no calibration, adjustment, or repair is required. If a malfunction occurs, the package is merely replaced by a spare unit just as one handles any typical electronic component. The analytically predicted failure rate is 10^{-6} per hour.

The TDY-52 computer series combines advanced hybrid packaging technology used in conjunction with LSI semiconductor technology.

System Reliability Considerations

Let the system to be considered consist of n independent subsystems and assume that for the proper operation of the system each and every one of the n subsystems must be operating satisfactorily. The statement that the subsystems are independent implies that proper operation in question and thus its proper operation or its failure is not influenced by the proper operation or failure of any of the remaining subsystems. Let the probability that the r^{oth} subsystem operates satisfactorily be equal to R_{ro}. We note from the basic theory of probability that when dealing with a set of n independent events (n independent subsystems) each having a probability of occurrence (probability of operating satisfactorily) equal to $R_1, R_2, R_3, \ldots R_n$ then the proability, R_I that all the events will occur at the same time (probability that all the n subsystems operate satisfactorily) is equal to the product of the individual probabilities. Thus

$$R = R_1, R_2, R_3 \ldots\ldots R_{n-1}R_n \qquad (1)$$

Equation (1) states the reliability of a system comprised of n independent subsystems whose reliabilities are $R_1, R_2, R_3, \ldots R_n$. The reliability is defined as the probability of satisfactory operation under the operating conditions encountered for the intended period of time.

Reliability may be expressed in terms of failure rate and time as stated by

$$R_p = e^{-\lambda_p t} \qquad (2)$$

where λ_p is the chance failure rate (or, the reciprocal of λ_p is the mean time to failure) and t is the time of operation.

To illustrate the use of (1) and (2) in obtaining the probability of a system failure, consider a non-redundant strapdown navigation system comprised of the following:

Gyro Subsystem. - Assume this consists of 2 two-degree-of-freedom strapdown gyros each equipped with pickoff electronics and caging loops. The failure rate per gyro including that of pickoff electronic and caging loops is λ_G. The reliability per gyro is given by

$$R_G = e^{-\lambda_G t},$$

and the reliability of the gyro subsystem is

$$R_1 = R_G R_G = e^{-2\lambda_G t}, \tag{3}$$

Accelerometer Subsystem. - This consists of 3 single axis accelerometers each equipped with its restoring circuits. The failure rate per accelerometer including its electronics is λ_A. The reliability per accelerometer is

$$R_A = e^{-\lambda_A t},$$

and the reliability of the accelerometer subsystem is

$$R_2 = R_A R_A R_A = e^{-3\lambda_A t} \tag{4}$$

In a similar way we may define the reliabilities of

$$R_3 = R_P = e^{-\lambda_P t} \qquad \text{(Power Supply)} \tag{5}$$

$$R_4 = R_M = e^{-\lambda_M t} \qquad \text{(Multiplexer)} \tag{6}$$

$$R_5 = R_{A/D} = e^{-\lambda_{A/D} t} \qquad \text{(Analog/Digital Converter)} \tag{7}$$

$$R_6 = R_C = e^{-\lambda_C t} \qquad \text{(Computer)} \tag{8}$$

$$R_7 = R_D = e^{-\lambda_D t} \qquad \text{(Display Unit)} \tag{9}$$

Substituting (3) through (9) into (1) we obtain the expression for system reliability

$$R = \exp\left[(2\lambda_G + 3\lambda_A + \lambda_P + \lambda_M + \lambda_{A/D} + \lambda_C + \lambda_D)t\right] \tag{10}$$

For a short time of system operation, (10) can be approximated by

$$R = 1 - (2\lambda_G + 3\lambda_A + \lambda_P + \lambda_M + \lambda_{A/D} + \lambda_C + \lambda_D)t \tag{11}$$

Denoting by F the probability of system failures we have

$$F = 1 - R$$

and, substituting from (11), the probability that the system will fail in the time t is

$$F = (2\lambda_G + 3\lambda_A + \lambda_P + \lambda_M + \lambda_{A/D} + \lambda_C + \lambda_D)t \qquad (12)$$

From the component failure rate analysis we substitute the failure rates and obtain the mean time to system failure and the probability that the system will fail after 1/2 hour of operation.

Reliability of Gyro Redundant Subsystems

Two Gyro Subsystem (Non-redundant Configuration). - The spin axes of these gyros are normally orthogonal to each other and the torquer axes form an orthogonal triad. Two torquer axes are collinear. The reliability of the two gyro system is given by

$$R_2 = R_G^2 \cong 3^{-2\lambda_G t} = 1 - 2\lambda_G t \qquad (13)$$

where R_G is the reliability per gyro including its pickoff electronics and caging loops. It is assumed that a failure in one gyro axis produces an entire gyro failure. The probability of failure of a two gyro subsystem is

$$P_2 \cong 2\lambda_G t \qquad (14)$$

Three Gyro Subsystem (Single Redundant Configuration). -In one possible arrangement the spin axes of the three gyros form an orthogonal triad and thus there are two torquer axes along each axis of the triad as shown in Figure 3. Here H designates the gyro spin axes and the M_i designates the various torquer axes.

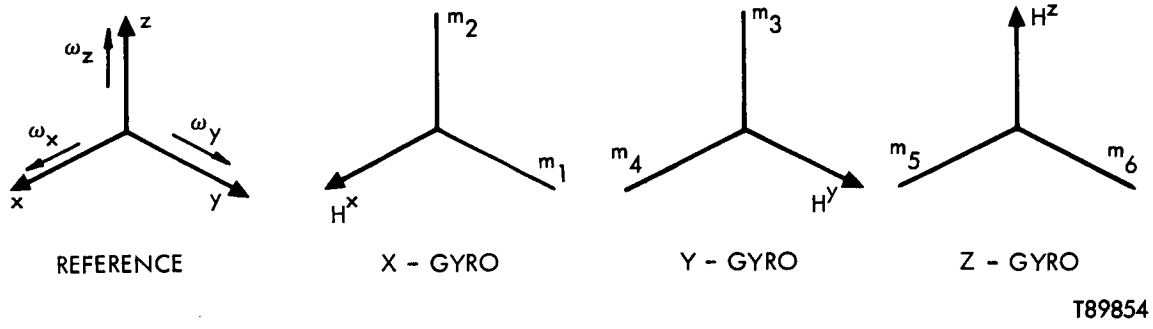

Figure 3. Orthogonal Orientation of the Gyros in the Three Gyro Subsystem

In a second possible arrangement of a three gyro subsystem the spin axes of the gyros form an orthogonal triad but the torquer axes are not orthogonal, as shown in Figure 4.

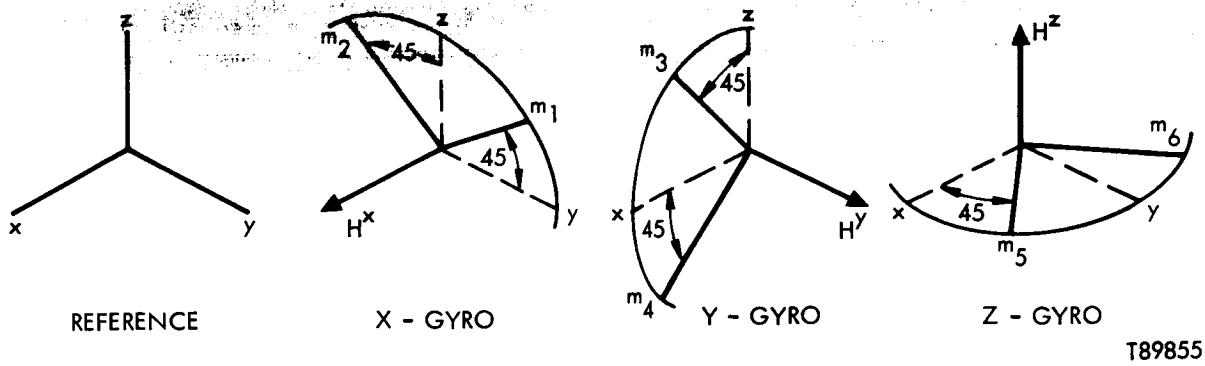

Figure 4. Non-orthogonal Orientation of the Gyros in the Three Gyro Subsystem

A three gyro subsystem of the orthogonal type operates in a Fail-Op mode, i.e. when one gyro fails the failed gyro can be detected and isolated. A three gyro subsystem of the non-orthogonal type also operates in a Fail-Op mode,but because of skewed torquer axes, single axis failures can be detected and a failed axis isolated so the system remains operational. The probability of a single axis failure without the failure of the entire gyro containing the failed axis is considered to be very small*, and thus the reliability of both the orthogonal and the non-orthogonal three gyro configurations will be assumed to have the same value. For completeness of analysis, however, failure detection equations will be derived and presented for both the orthogonal and the non-orthogonal configurations.

The reliability function for the three gyro subsystems will now be derived. The subsystem will operate satisfactorly if:

a) All the gyros operate satisfactorily
b) x-Gyro fails but y and z gyros operate satisfactorily
c) y-Gyro fails but x and z gyros operate satisfactorily
d) z-Gyro fails but x and y gyros operate satisfactorily

Assuming the reliability of each gyro to be the same and equal to R_G we have:

Probability that a) occurs is $R_G R_G R_G$

Probability that b) occurs is $(1 - R_G)R_G^2$

Probability that c) occurs is $(1 - R_G)R_G^2$

Probability that d) occurs is $(1 - R_G)R_G^2$

Events represented by cases a) through d) are mutually exclusive because if any two or more of these events occur simultaneously the subsystem will fail.

A basic theorem of probability states that the probability of occurrence of either one or any other mutually exclusive events is equal to the sum of the probabilities of the single events. Events are mutually exclusive if they can never occur at the same time. Thus the reliability of the gyro subsystem containing three two-degree-of-freedom gyros is

* This assumption is probably very well justified in case of catastrophic failures and has a lesser justification in the case of non-catastrophy.

$$R_3 = R_G^3 + 3\left(1 - R_G\right) R_G^2$$

$$= R_G^2 \left[R_G + 3 - 3R_G\right]$$

$$= R_G^2 \left(3 - 2\, R_G\right)$$

$$= e^{-2\lambda_G t}\left(3 - 2e^{-\lambda_G t}\right)$$

$$= 3\, e^{-2\lambda_G t} - 2e^{-3\lambda_G t} \qquad (15)$$

Expanding the exponentials

$$R_3 = 3\left[1 - \frac{2\lambda_G t}{1!} + \frac{(2\lambda_G t)^2}{2!} - \frac{(2\lambda_G t)^3}{3!} + \ldots\right]$$

$$-2\left[1 - \frac{3\lambda_G t}{1!} + \frac{(3\lambda_G t)^2}{2!} - \frac{(3\lambda_G t)^3}{3!} + \ldots\right]$$

$$= 3 - \frac{6\lambda_G t}{1} + \frac{12(\lambda_G t)^2}{2} - \frac{24(\lambda_G t)^3}{6} + \ldots$$

$$-2 + \frac{6\lambda_G t}{1} - \frac{18(\lambda_G t)^2}{2} + 2 \times 27 \frac{(\lambda_G t)^3}{6} - \ldots$$

$$= 1 - 3\,(\lambda_G t)^2 + \frac{1}{5}\,(\lambda_G t)^3 - \ldots \qquad (16)$$

Thus the probability of failure of a three gyro subsystem is

$$P_3 \cong 3\,(\lambda_G t)^2 - 5\,(\lambda_G t)^3 \qquad (17)$$

Four Gyro Subsystem. - Three possible (and there are more) gyro arrangements will be considered for the four gyro subsystem. In the first arrangement two orthogonal sets are used as shown in Figure 5.

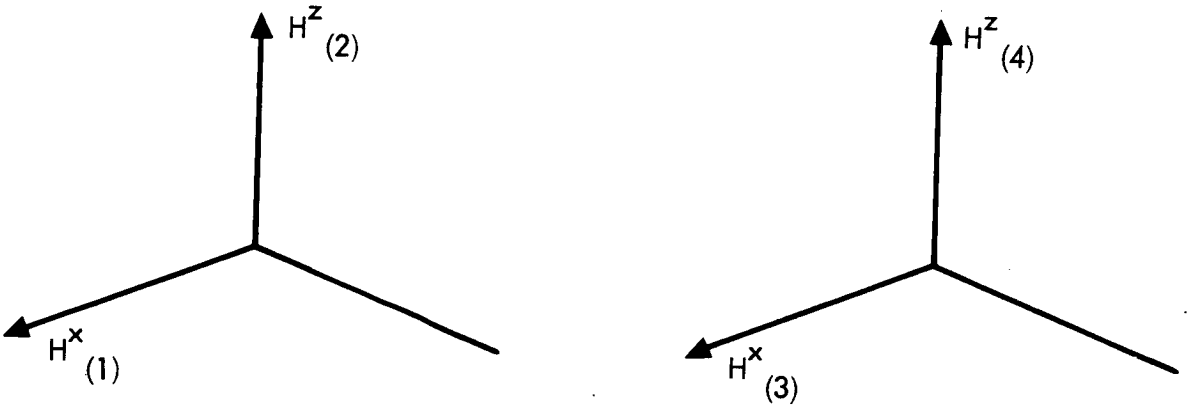

Figure 5. Four Orthogonal Gyros

The gyros whose spin axes have the same superscript notation measure the same input angular rate, i.e., the same rate is measured by the gyros whose spin axis are $H^x_{(1)}$ and $H^x_{(3)}$, and $H^x_{(2)}$ and $H^z_{(4)}$.

The arrangement shown in Figure 5 does not provide as high a reliability as that in which the four gyros are non-orthogonal. In a non-orthogonal configuration any two gyros can fail and the subsystem is still operational. In the orthogonal configuration, depicted in Figure 5, simultaneous failures of gyros whose spin axis are $H^x_{(1)}$ and $H^x_{(3)}$, and $H^z_{(2)}$ and $H^z_{(4)}$ cannot be tolerated, and therefore the reliability of this configuration is lower than that of a nonorthogonal 4 gyro subsystem described in the following paragraphs.

In one of the nonorthogonal configurations the spin axes of the gyros are normal to the surfaces of a regular tetrahedron. In the other configuration the spin axes of three gyros form an orthogonal triad and the sensing axes of these gyros are marked ① ② and ③ in Figure 6. The sensing axes of the fourth gyro ④ are along Ox and OA, i.e. one axis lies at 45^o with respect to y and z.

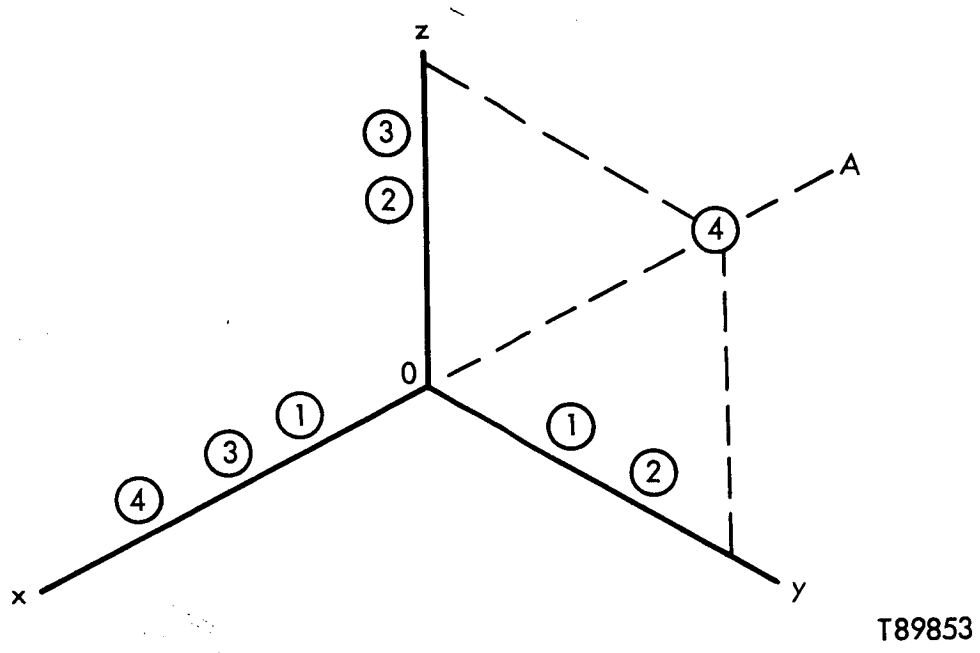

Figure 6. 4-Gyro Subsystem in Non-Orthogonal Configuration

The reliability of the two non-orthogonal 4 gyro configurations is the same because in each case any two gyros that are operational yield the total input rate information.

The reliability function for the four gyro subsystem will now be derived. **The subsystem will operate satisfactorily if:**

a) **All the gyros operate satisfactorily**
b) One gyro fails and the remaining gyros operate satisfactorily
c) Two gyros fail and the remaining gyros operate satisfactorily.

Probability that a) occurs is R_G^4

Probability that b) occurs is $4(1 - R_G) R_G^3$

Probability that c) occurs is $6(1 - R_G)^2 R_G^2$

The reliability of the gyro subsystem containing four non-orthogonal two degree of freedom gyros is thus

$$
\begin{aligned}
R_4 &= R_G^4 + 4\left(1 - R_G\right) R_G^3 + 6\left(1 - R_G\right)^2 R_G^2 \\
&= R_G^2 \left[R_G^2 + 4R_G - 4R_G^2 + 6 - 12R_G + 6R_G^2 \right] \\
&= R_G^2 \left[6 - 8R_G + 3R_G^2\right] \\
&= e^{-2\lambda_G t} \left[6 - 8\, e^{-\lambda_G t} + 3\, e^{-2\lambda_G t} \right] \\
&= 6\, e^{-2\lambda_G t} - 8\, e^{-3\lambda_G t} + 3\, e^{-4\lambda_G t}
\end{aligned} \tag{18}
$$

Expanding the exponentials

$$
R_4 = 1 - 4\,(\lambda_G t)^3 + 9\,(\lambda_G t)^4 \tag{19}
$$

Thus the probability of failure of a 4 gyro subsystem is

$$
P_4 \cong 4\,(\lambda_G t)^3 - 9\,(\lambda_G t)^4 \tag{20}
$$

Five Gyro Subsystem. -Assume five gyros whose sensing axes are non-orthogonal. This subsystem will operate satisfactorily if

a) All the gyros operate satsifactorily
b) One gyro fails and the remainder operate satisfactorily
c) Two gyros fail and the remainder operate satisfactorily
d) Three gyros fail and the remainder operate satisfactorily

Probability that a) occurs is R_G^5

Probability that b) occurs is ${}_5C_1 \left(1 - R_G\right) R_G^4$

Probability that c) occurs is ${}_5C_2 \left(1 - R_G\right)^2 R_G^3$

Probability that d) occurs is ${}_5C_3 \left(1 - R_G\right)^3 R_G^2$

The reliability of the gyro subsystem containing five non-orthogonal gyros is

$$R_5 = R_G^5 + 5(1 - R_G) R_G^4 + 10 (1 - R_G)^2 R_G^3 + 10 (1 - R_G)^3 R_G^2$$

$$= 10\, e^{-2\lambda_G t} - 20\, e^{-3\lambda_G t} + 15\, e^{-4\lambda_G t} - 4\, e^{-5\lambda_G t} \qquad (21)$$

Expanding

$$R_5 = 1 - 5 (\lambda_G t)^4 + 14 (\lambda_G t)^5 \qquad (22)$$

From Eqs (13, (16), (19) and (22) it is noted that for $(\lambda_G t) << 1$ the reliability of a gyro subsystem containing g gyros in which any two gyros will provide the desired information is given by the general equation

$$R_g = 1 - g (\lambda_G t)^{g-1} \qquad (23)$$

Reliability Of Accelerometer Redundant Subsystems

Assume that the minimum number of accelerometers for satisfactory operation of an accelerometer subsystem is equal to 3. Thus the reliability of a non-redundant accelerometer subsystem is

$$R_{A3} = R_A^3$$

$$= e^{-3\lambda_A t}$$

$$= 1 - 3\lambda_A t \qquad (24)$$

The reliability of an accelerometer subsystem containing four non-orthogonal accelerometers is

$$R_{A4} = R_A^4 + {}_4C_1 (1 - R_A) R_A^3$$

$$= R_A^4 + 4 (1 - R_A) R_A^3$$

$$= R_A^3 [R_A + 4 - 4R_A]$$

$$= R_A^3 (4 - 3R_A)$$

$$= e^{-3\lambda_A t} \left(4 - 3\, e^{-\lambda_A t}\right)$$

$$= 1 - 6 (\lambda_A t)^2 + 4 (\lambda_A t)^3 \tag{25}$$

Thus the probability of failure of a four accelerometer subsystem is

$$P_{4A} = 6 (\lambda_A t)^2 - 4 (\lambda_A t)^3 \tag{26}$$

Next establish the reliability of a five accelerometer subsystem

$$R_{A5} = R_A^5 + {}_5C_1 (1 - R_A) R_A^4 + {}_5C_2 (1 - R_A)^2 R_A^3$$

$$= R_A^5 + 5 (1 - R_A) R_A^4 + 10 (1 - 2R_A + R_A^2) R_A^3$$

$$= R_A^5 + 5 R_A^4 - 5 R_A^5 + 10 R_A^3 - 20 R_A^4 + 10 R_A^5$$

$$= 10 R_A^3 - 15 R_A^4 + 6 R_A^5$$

$$= 10\, e^{-3\lambda_A t} - 15\, e^{-4\lambda_A t} + 6\, e^{-\lambda_A t} \tag{27}$$

Expanding

$$R_{A5} = 1 - 10 (\lambda_A t)^3 + 30 (\lambda_A t)^4 \tag{28}$$

Finally establish the reliability of a six non-orthogonal accelerometer subsystem.

$$R_{A6} = R_A^6 + {}_6C_1 (1 - R_A) R_A^5 + {}_6C_2 (1 - R_A)^2 R_A^4$$

$$+ {}_6C_3 (1 - R_A)^3 R_A^3$$

$$= R_A^6 + 6 (1 - R_A) R_A^5 + 15 (1 - R_A)^2 R_A^4 + 20 (1 - R_A)^3 R_A^3$$

$$= R_A^6 + 6 R_A^5 - 6 R_A^6 + 15 (1 - 2 R_A + R_A^2) R_A^4$$

$$+ 20 (1 - 2 R_A + R_A^2) (1 - R_A) R_A^3$$

$$= R_A^6 + 6R_A^5 - 6R_A^6 + 15R_A^4 - 30R_A^5 + 15R_A^6$$

$$+ 20 (1 - R_A - 2 R_A + 2 R_A^2 + R_A^2 - R_A^3) R_A^3$$

$$= + 10 R_A^6 - 24 R_A^5 + 15 R_A^4$$

$$+ 20 R_A^3 - 20 R_A^4 - 40 R_A^4 + 40 R_A^5 + 20 R_A^5 - 20 R_A^6$$

$$= + 20 R_A^3 - 45 R_A^4 + 36 R_A^5 - 10 R_A^6$$

$$= 20 e^{-3\lambda_A t} - 45 e^{-4\lambda_A t} + 36 e^{-5\lambda_A t} - 10 e^{-6\lambda_A t} \qquad (29)$$

Expanding

$$R_{A6} = 1 - 15 (\lambda_A t)^4 + 898 (\lambda_A t)^5 \qquad (30)$$

Power Supply Redundancy

One may consider several ways of handling the improvement of reliability of power supplies feeding the various subsystems. One way is to provide individual power supplies to each component of a subsystem and adjust the failure rate of the component accordingly. Another way is to have a common power supply feeding the needs of the entire system and make this power supply redundant. In this case the standby redundancy concept appears to be quite applicable. It is felt that the latter method is more economical than the former and thus should be seriously considered in the process of configuring the system with maximum reliability and minimum cost objectives.

The equation for reliability of a two channel standby system is

$$R_P = e^{-\lambda_P t} (1 + \lambda_P t) \qquad (31)$$

Expanding

$$R_p = \left[1 - \frac{\lambda_P t}{1!} + \frac{\lambda_P t^2}{2!} - \frac{\lambda_P t^3}{3!} + \ldots\ldots\right][1 + \lambda t]$$

$$= 1 - \frac{1}{2}(\lambda_P t)^2 + \frac{1}{3}(\lambda_P t)^3 \qquad (32)$$

Reliabilities for the Proposed Configurations

The reliability goal of the strapdown inertial system design is set at a failure rate of 10^{-6} per half hour or less. Several sets of component elements were considered for the conventional strapdown configuration. The worst and best case failure rates are shown in Table 1 for each subsystem element. A buildup sequence of increased reliability is shown in Table 2. It is shown that the minimum required components of a nonredundant worst case system has a failure rate of 0.8×10^{-3} per half hour. The failure rate goal of 10^{-6} is not achieved until many subsystems are made redundant.

The all digital-SCAG strapdown system failure rates and costs are shown in Table 3. The failure rate F for a nonredundant system consisting of two channels is given by

$$F = 1 - R^2$$

where

$$R = e^{-\lambda t}$$

$$\lambda = 750 \times 10^{-6}$$

$$t = 1/2 \text{ hour}$$

$$\cong 1 - \left(1 - \frac{2\lambda t}{1!} + \frac{4\lambda^2 t^2}{2!}\right)$$

$$\cong 2\lambda t = 2(750 \times 10^{-6})(1/2) = 750 \times 10^{-6}$$

Clearly, the nonredundant system does not achieve the reliability requirement.

A voting redundant system is obtained by combining three channels in parallel. The probability of a system failure is computed by

$$F = 1 - (R^3 + 3(1-R)R^2)$$

$$= 1 - (3e^{-2\lambda t} - 2e^{-3\lambda t})$$

$$\cong 3\lambda^2 t^2 = 3\,(.75 \times 10^{-3})^2/4 = .42 \times 10^{-6}$$

Thus, a three channel system operating in parallel will have voting redundancy and provide an acceptable failure rate of $.42 \times 10^{-6}$ per half hour.

TABLE 1. SUBSYSTEM FAILURE RATES

Sub-System	Failure Rates Per 10^6 Hrs.	
	Best Case	Worst Case
Gyro and Caging Circuit	50	200
Accel. and Caging Circuit	50	200
A/D Converter	10	50
Power Supply	10	50
Computer	50	200
Display and Control	50	200
Multiplexer	10	50

TABLE 2. INS FAILURE PROBABILITY PER 0.5 HOURS FOR CONVENTIONAL MECHANIZATIONS

Sub-System	Best Case	Worst Case	Comments
Gyro and Caging Circuit (G) Accelerometer and Caging Circuit (A) A/D Converter (AID) Power Supply (P/S) Computer (CPU) Display and Control (D/C) Multiplexer (MUX) Gyro Accelerometer Accelerometer	$.19 \times 10^{-3}$	$.8 \times 10^{-3}$	Minimum Configuration
Accelerometer	1.15×10^{-4}	$.48 \times 10^{-3}$	Added Elements
MUX	1.1×10^{-4}	$.45 \times 10^{-3}$	
Gyro	$.6 \times 10^{-4}$	2.5×10^{-4}	
D/C	$.35 \times 10^{-4}$	1.5×10^{-4}	
A/D	$.3 \times 10^{-4}$	1.2×10^{-4}	
P/S	$.25 \times 10^{-4}$	1×10^{-4}	
CPU	$.56 \times 10^{-7}$	$.9 \times 10^{-6}$	
Accelerometer	$.2 \times 10^{-7}$	$.3 \times 10^{-6}$	
Gyro	10^{-8}	$.2 \times 10^{-7}$	

TABLE 3. REDUNDANT DIGITAL STRAPDOWN INERTIAL NAVIGATION SYSTEM FAILURE RATE

Sub System	Failure Rate Range Per 10^6 Hrs.
Inertial Sensor Unit	20 - 100
Power Supply	10 - 50
CPU	10 - 50
DMA	10 - 50
D/A and S&M	10 - 50
Power Amp	10 - 50
Digital MUX	10 - 50
Analog MUX	10 - 50
A/D	10 - 50
A/D Control	10 - 50
I/O	10 - 50
Memory	10 - 50
Display and Control	20 - 100
Total For Single Channel	150 - 750
Housing	.01 - .1
Total System (Three Channel)	.2 - 1.0

Cost

A preliminary cost tradeoff analysis was performed to determine the system configurations that will provide the required reliability factor and reasonable cost. A reliability failure rate of 10^{-6} per half hour was set as a goal. Thus, any system configuration that did not achieve this figure was eliminated from the cost analysis.

Two different strapdown inertial concepts were composed. The first was the conventional strapdown inertial system with associated analog platform electronics. The second was the advanced inertial sensor unit with digital processing. The costs and reliabilities of these basic implementations were then examined and compared.

Figure 7 shows the interrelationship of cost and reliability for the two system configurations. Worst-case and best-case curves for the conventional mechanization are derived from the costs listed in Table 4 together with the redundancy buildup sequence described in the preceding section (Table 2). The minimum redundancy configuration capable of achieving the desired failure rate of 10^{-6} per half hour consists of the following subsystem complement.

Gyro & Caging	3
Accelerometers & Caging	4
A/D	3
Power Supplies	2
CPU's	2
Display & Control	2
Multiplexer	1

The total worst-case for this system is estimated to be approximately \$85.5K. Lower failure rates, accompanied by higher costs, are achievable by adding additional redundant subsystems, as indicated in Figure 7.

The advanced digital strapdown system was placed in a triply redundant configuration. The total cost for a three channel system was estimated to be between \$38.5K to \$45.6K. The desired reliability goal is easily achieved with the advanced digital configuration. This is indicated in Figure 7.

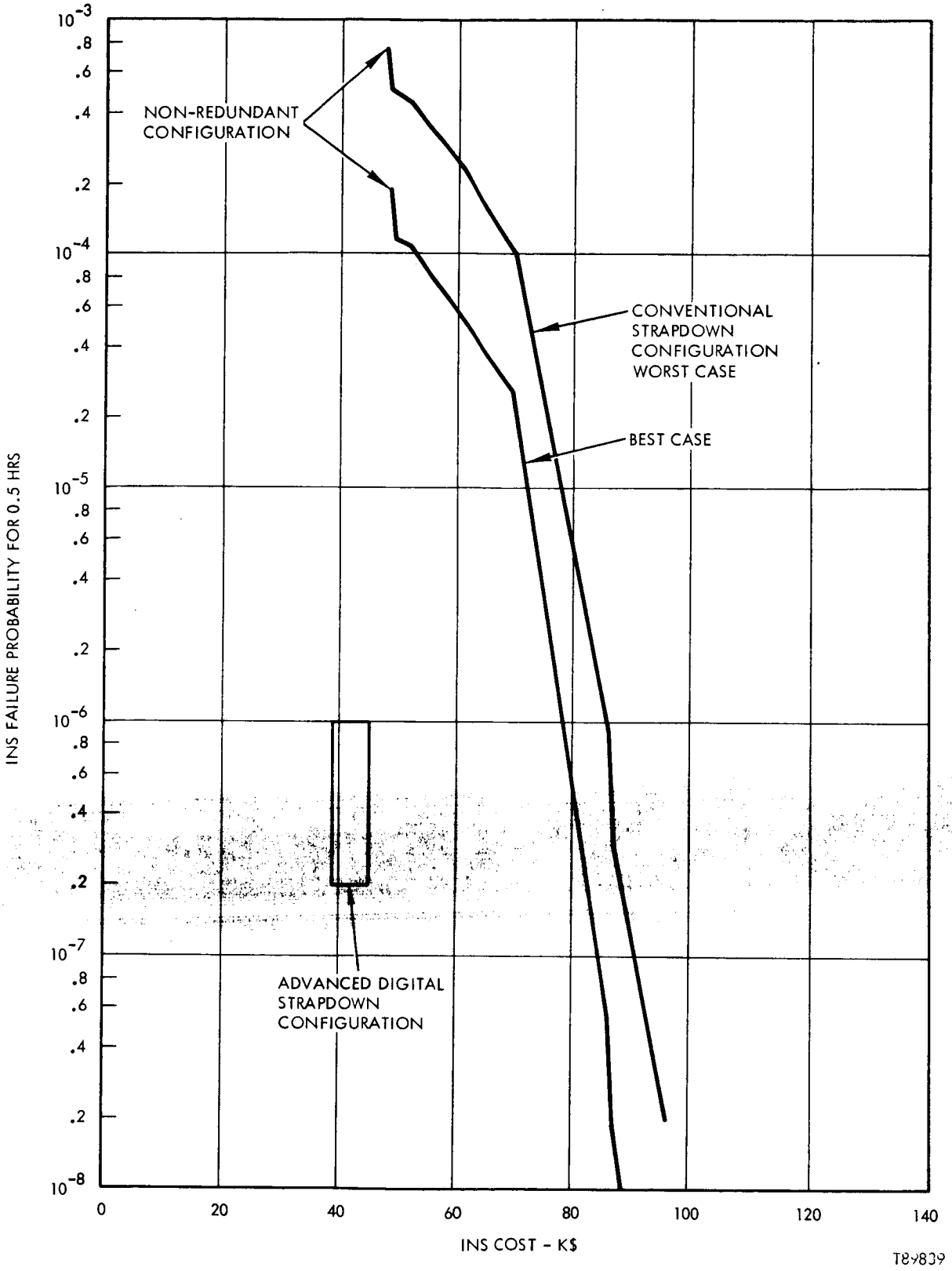

Figure 7. Strapdown Cost/Reliability Tradeoff

Having established the cost vs. reliability advantages of the all-digital and SCAG approaches by means of this rough preliminary analysis, a more detailed cost analysis was performed. This analysis considered four basic system configurations:

1) Conventional strapdown mechanization

2) SCAG sensors in conjunction with conventional electronics.

3) Conventional sensors in conjunction with the "All-Digital" mechanization of the servo and control functions.

4) SCAG sensors and "All-Digital" mechanization.

Tables 4 and 5 show the corresponding cost breakdowns for both Fail-Op and Fail-Op/Fail-Op configurations. It should be observed that the cost breakdowns are somewhat different for the more detailed analysis than those which appear in the midterm report. This reflects the evolution of the preliminary system design during the course of the study.

Component	Unit Cost $K	Conventional		Analog-SCAG		Digital-Gyro		Digital-SCAG	
Gyro	6.7	3	20.1			3	20.1		
Accel	1.2	5	6.0			5	6.0		
SCAG	4.5-5.0			3	13.5-15.0			3	13.5-15.0
Computer (TDY-43)	18.0	2	36.0	2	36.0				
CPU (TDY-52)	0.2-0.5					2	0.4-1.0	2	0.4-1.0
Memory (TDY-52)	0.2-0.5					2	0.4-1.0	2	0.4-1.0
Analog Electronics	2.1	2	4.2	2	4.2				
A/D	0.3-0.4	2	0.6-0.8	2	0.6-0.8	2	0.6-0.8	2	0.6-0.8
A/D & DMA Control	0.13	2	0.26	2	0.26	2	0.26	2	0.26
Digital MUX	0.07	2	0.14	2	0.14	2	0.14	2	0.14
D/A	0.08					2	0.16	2	0.16
Analog MUX & S/H	0.01					20-28	0.2-0.28	14-22	0.14-0.22
Power Amp	0.05					20-28	1.0-1.4	14-22	0.7-1.1
Interface	0.6	2	1.2	2	1.2	2	1.2	2	1.2
Power Supply	1.0-1.5	2	2.0-3.0	2	2.0-3.0	2	2.0-3.0	2	2.0-3.0
Display/Control (30%)	1.5	2	3.0	2	3.0	2	3.0	2	3.0
TOTALS			73.5-74.7		60.9-63.6		35.46-38.34		22.5-26.88

Table 4. Costs For Fail-Op System

Component	Unit Cost $K	Conventional		Analog-SCAG		Digital-Gyro		Digital-SCAG	
Gyro	6.7	4	26.8			4	26.8		
Accel	1.2	6	7.2			6	7.2		
SCAG	4.5-5.0			4	18.0-20.0			4	18.0-20.0
Computer (TDY-43)	18.0	3	54.0	3	54.0				
CPU (TDY-52)	0.2-0.5					3	0.6-1.5	3	0.6-1.5
Memory (TDY-52)	0.2-0.5					3	0.6-1.5	3	0.6-1.5
Analog Electronics	2.1	3	6.3	3	6.3	3	6.3		6.3
A/D	0.3-0.4	3	0.9-1.2	3	0.0-1.2	3	0.9-1.2	3	0.9-1.2
A/D & DMA Control	0.13	3	0.39	3	0.39	3	0.39	3	0.39
Digital MUX	0.07	3	0.21	3	0.21	3	0.21	3	0.21
D/A	0.08					3	0.24	3	0.24
Analog MUX & S/H	0.01					30-42	0.31-0.42	21-33	0.21-0.33
Power Amp	0.05					30-42	1.5-2.1	21-33	1.05-1.65
Interface	0.06	3	1.8	3	1.8	3	1.8	3	1.8
Power Supply	1.0-1.5	3	3.0-4.5	3	3.0-4.5	3	3.0-4.5	3	3.0-4.5
Display/Control (30%)	1.5	3	4.5	3	4.5	3	4.5	3	4.5
TOTALS		105.1-106.9		89.1-92.9		54.34-58.66		37.8-44.12	

Table 5. Costs For Fail-Op/Fail-Op System

Cost of Ownership

Acquisition cost is only one facet, albeit an important one, of the true cost of a system. It is equally as important in evaluating system cost to consider costs which will accrue after acquisition. The terms "cost of ownership" and "life cycle cost" are traditionally associated with such overall costs.

Cost of ownership analyses for new systems are somewhat subjective and hence are generally most useful when stated in comparative terms using an existing system (or class of systems) as a baseline. Since relatively abundant cost of ownership data is available for gimbaled dry gyro inertial navigators, this class of system is used as the baseline for the present analysis.

Life Cycle Cost Estimates. -Application of the analysis techniques described in the following sections has been made to both inertial navigation systems. The results of the analysis are provided in the following figures and clearly show the life cycle cost advantages of the strapped down dry gyro navigation system over an equivalent gimbaled system. Table 6 provides comparative total cost figures for various support and acquisition costs. Tables 7 and 8 provide a breakdown of the support costs by support elements and support sites. Tables 9 and 10 are depot support cost breakdowns by support elements and INS modules.

The life cycle cost difference between the strapped down dry gyro INS and the gimbaled dry gyro INS represents the cost penalty of the gimbaled system, due to the extra hardware which is required for the latter type. An additional cost penalty of the gimbaled system involves the unit level spares required due to the shipment of the entire unit to the depot for the repair of synchro, gimbal torquer, gimbal bearing and slip ring failures.

Life Cycle Cost Analysis Data. - Table 11 shows the assemblies that make up the systems that are compared in the analysis and Table 12 shows the comparative failure rates. The life cycle parameters that result from the previous figures are shown in Table 13.

The following assumptions are made for this analysis:

1. Both systems are state-of-the art
2. Both systems possess identical accuracy
3. Common design and components are used in both systems wherever applicable

Table 6. Life Cycle Cost Analysis

INERTIAL NAVIGATION SYSTEM

COST COMPARISON

	STRAPDOWN DRY GYRO	GIMBALED DRY GYRO
ACQUISITION COST FOR 100 SYSTEMS	$4,210,000.00	$6,260,000.00
LIFE CYCLE SUPPORT COST FOR 100 SYSTEMS	$2,473,747.00	$6,535,072.00
RATIO OF SUPPORT TO ACQUISITION COST	0.59	1.04
LIFE CYCLE SUPPORT COST PER REPAIR	$1,003.00	$2,034.00
DEPOT SUPPORT COST PER REPAIR	$558.00	$1,711.00
DEPOT LABOR/PARTS COST PER REPAIR	$462.00	$1,018.00
LIFE CYCLE SUPPORT COST PER OPERATING HOUR	$1.47	$3.89

T 789 73

Table 7.

STRAPDOWN INERTIAL NAVIGATION SYSTEM
LIFE CYCLE SUPPORT COST ANALYSIS

100 SYSTEMS	4 ORGANIZATIONAL SITES	4 INTERMEDIATE SITES	1 DEPOT SITE	TOTAL
SPARES	$ 0.	$ 270360.	$ 164661.	$ 435021.
SAFETY STOCK	0.	0.	31068.	31068.
NEW ITEM INTRODUCTION	0.	2564.	16305.	18869.
REPAIR PARTS	0.	0.	566548.	566548.
PACKING AND SHIPPING	0.	80.	3009.	3089.
AGE COST	0.	440000.	185000.	625000.
FACILITIES	0.	23840.	0.	23840.
LABOR COST	6920.	115600.	570746.	693266.
SPECIAL TRAINING	11100.	11100.	2846.	25046.
TECHNICAL DATA	4000.	16000.	32000.	52000.
TOTAL	$ 22020.	$ 879544.	$ 1572183.	$ 2473747.

T78974

Table 8.

GIMBALED INERTIAL NAVIGATION SYSTEM LIFE CYCLE SUPPORT COST ANALYSIS

100 SYSTEMS	4 ORGANIZATIONAL SITES	4 INTERMEDIATE SITES	1 DEPOT SITE	TOTAL
SPARES	$ 0.	$ 591112.	$ 1743965.	$ 2335077.
SAFETY STOCK	0.	0.	329138.	329139.
NEW ITEM INTRODUCTION	0.	3264.	16305.	19569.
REPAIR PARTS	0.	0.	1393575.	1393575.
PACKING AND SHIPPING	0.	164.	100657.	100821.
AGE COST	0.	440000.	185000.	625000.
FACILITIES	0.	23840.	0.	23840.
LABOR COST	10840.	180644.	1428140.	1619894.
SPECIAL TRAINING	11100.	11100.	3558.	25758.
TECHNICAL DATA	4000.	16000.	42400.	62400.
TOTAL	$ 25940.	$ 1266124.	$ 5498901.	$ 6535072.

T78975

Table 9.

DEPOT LEVEL SUPPORT COST ANALYSIS

STRAPDOWN SYSTEM

	GYRO MODULE	GYRO CAGE MODULE	GYRO A/D MODULE	ACCEL MODULE	ACCEL CAGE MODULE	ACCEL A/D MODULE	PITE ASSY MODULE	LOGIC ASSY MODULE	MEMORY ASSY MODULE	POWER SUPPLY MODULE	MAIN FRAME MODULE
SPARES	$103056.	$ 1246.	$ 4218.	$ 38867.	$ 658.	$ 2389.	$ 669.	$ 798.	$ 8108.	$ 4262.	$ 390.
SAFETY STOCK	19444.	235.	796.	7333.	124.	451.	126.	151.	1530.	804.	74.
NEW ITEM INTRODUCTION	1539.	342.	513.	3249.	342.	513.	171.	4104.	3993.	1539.	0.
REPAIR PARTS	300000.	806.	1736.	244447.	497.	1202.	865.	1445.	15119.	402.	29.
PACKING AND SHIPPING	2292.	60.	110.	103.	37.	76.	14.	15.	23.	170.	109.
AGE COST	70000.	7500.	7500.	55000.	7500.	7500.	7500.	7500.	7500.	7500.	0.
FACILITIES	0.	0.	0.	0.	0.	0.	0.	0.	0.	0.	0.
LABOR COST	266667.	3225.	6945.	273780.	1987.	4808.	1731.	2891.	4320.	3216.	1176.
SPECIAL TRAINING	285.	142.	142.	427.	142.	142.	142.	570.	427.	285.	142.
TECHNICAL DATA	4000.	2400.	2400.	4000.	2400.	2400.	2400.	4000.	4000.	4000.	1600.
TOTAL	$767282.	$ 15957.	$ 24361.	$627207.	$ 13688.	$ 19482.	$ 13619.	$ 21475.	$ 44960.	$ 22178.	$ 3520.

T78977

Table 10.

DEPOT LEVEL SUPPORT COST ANALYSIS

GIMBALED SYSTEM

	GYRO MODULE	GYRO CAGE MODULE	GYRO A/D MODULE	ACCEL MODULE	ACCEL CAGE MODULE	ACCEL A/D MODULE	BITE ASSY MODULE	LOGIC ASSY MODULE	MEMORY ASSY MODULE	POWER SUPPLY MODULE	MAIN FRAME/GIMBAL MODULE
SPARES	$ 542214.	$ 1246.	$ 4218.	$ 38867.	$ 658.	$ 2389.	$ 669.	$ 798.	$ 8108.	$ 4262.	$ *.
SAFETY STOCK	102305.	235.	796.	7333.	124.	451.	126.	151.	1530.	804.	*.
NEW ITEM INTRODUCTION	3249.	342.	513.	3249.	342.	513.	171.	4104.	3993.	1539.	0.
REPAIR PARTS	4532881.	806.	1736.	244447.	497.	1202.	865.	1445.	15119.	402.	174727.
PACKING AND SHIPPING	10388.	60.	110.	*.	37.	76.	14.	15.	23.	170.	*.
AGE COST	70000.	5455.	5455.	55000.	5455.	5455.	5455.	5455.	5455.	5450.	0.
FACILITIES	0.	0.	0.	0.	0.	0.	0.	0.	0.	0.	0.
LABOR COST	5288362.	3225.	6945.	273780.	1987.	4808.	1731.	2891.	4320.	3216.	262090.
SPECIAL TRAINING	285.	142.	142.	427.	142.	142.	142.	570.	427.	285.	142.
TECHNICAL DATA	4000.	2400.	2400.	4000.	2400.	2400.	2400.	4000.	4000.	4000.	1600.
TOTAL	$10553684.	$ 13911.	$ 22315.	$ 627207.	$ 11642.	$ 17436.	$ 11573.	$ 19429.	$ 42975.	$ 20128.	$438559.

	GIMBAL SERVO MODULE	SYNCHRO MODULE	GIMBAL TORQUER MODULE	*INERTIAL NAVIGATION SYSTEM
SPARES	$ 1603.	$ *.	*.	$ 1660860.
SAFETY STOCK	302.	*.	*.	313462.
NEW ITEM INTRODUCTION	0.	0.	0.	
REPAIR PARTS	1210.	119954.	137090.	
PACKING AND SHIPPING	90.	*.	*.	97770.
AGE COST	5455.	5455.	5455.	
FACILITIES	0.	0.	0.	
LABOR COST	9677.	228484.	182788.	
SPECIAL TRAINING	142.	285.	285.	
TECHNICAL DATA	2400.	3200.	3200.	
TOTAL	$ 20879.	$ 357378.	328818.	

T78978

INERTIAL NAVIGATION SYSTEMS

	ASSEMBLIES PER SYSTEM	
	STRAPDOWN	GIMBALED
GYRO	2	2
GYRO CAGE ASSY	4	4
GYRO A/D ASSY	3	3
ACCELEROMETER	3	3
ACCELEROMETER CAGE ASSY	3	3
ACCELEROMETER A/D ASSY	3	3
BITE ASSY	1	1
LOGIC ASSY	9	9
MEMORY ASSY	2	2
POWER SUPPLY ASSY	1	1
GIMBAL SERVO ASSY		4
SYNCHRO ASSY		4
GIMBAL TORQUER ASSY		4
MAIN FRAME	1	1
*GIMBAL SET		1

* INCLUDES BEARINGS AND SLIPRINGS

T78965

Table 11. Analysis Assemblies

FAILURE RATE COMPARISON

I.N.S	QTY PER SYSTEM	FAILURES PER 10^6 HOURS	
		STRAPDOWN	GIMBALED
GYROS	2	218	248
GYRO CAGE ASSYS	4	23.99	23.99
GYRO A/D, D/A ASSYS	3	51.67	51.67
ACCELEROMETERS	3	291.0	291.0
ACCEL CAGE ASSYS	3	14.78	14.78
ACCEL A/D ASSYS	3	35.77	35.77
B.I.T.E. ASSY	1	12.87	12.87
LOGIC ASSY	1	21.52	21.52
MEMORY ASSY	1	32.14	29.82
POWER SUPPLY	1	23.93	23.93
GIMBAL SERVOS	4	0	18.76
SYNCHROS	4	0	85.20
GIMBAL TORQUERS	4	0	85.20
MAIN FRAME & GIMBALS	1	8.75	13.12
TOTALS		734.42	955.63

T78966

Table 12.

Table 13. Life Cycle Parameters

INERTIAL NAVIGATION SYSTEM

LIFE CYCLE PARAMETERS

	STRAPDOWN	GIMBALED
SYSTEM FAILURES PER 10^6 OPERATING HOURS	734	956
SYSTEM REPAIRS PER 10^6 OPERATING HOURS	1,468	1,912
LIFE CYCLE OPERATING HOURS FOR 100 SYSTEMS	1,680,000	1,680,000
LIFE CYCLE REPAIRS FOR 100 SYSTEMS	2,466	3,212

T78971

The data sources for this analysis are:

1. Costs - estimated. These have secondary significance in the analysis provided all systems are treated alike.

2. Failure rates - Electronic parts from MIL Handbook 217A and electro-mechanical from FARADA.

3. Failure rates for the dry gyro - Martin-Marietta study under Contract RC1-1070000.

Life Cycle Cost Analysis Method. -The life cycle cost analysis presented here is based upon the following logical sequence of definitions, assumptions and computations:

a. The life cycle cost is defined as the sum of the:

   (1) Engineering Development and Design Costs

   (2) Investment (non-recurring) costs

   (3) "Equipment" Investment (recurring) cost

   (4) Support costs

Figure 8 shows in diagram form these life cycle cost categories.

b. The IMU Operational characteristics are as follows:

Life Cycle Period - Months	120
Total Number of Operational Systems	100
Number of Systems per Organizational Level (4)	25
Number of Systems per Direct Level (4)	25
Number of Systems per Depot Level	100
Operating Hours per Month per System	140

c. Maintenance actions are carried out at the organizational level, the direct level, and the depot level as shown in Figure 9. The support level cost elements are further divided as shown in Figure 10.

d. The IMU maintenance plan in terms of specific replacement and/or repair of the IMU subassemblies is shown in Tables 14 and 15 for the strapdown and gimbaled IMU's, respectively.

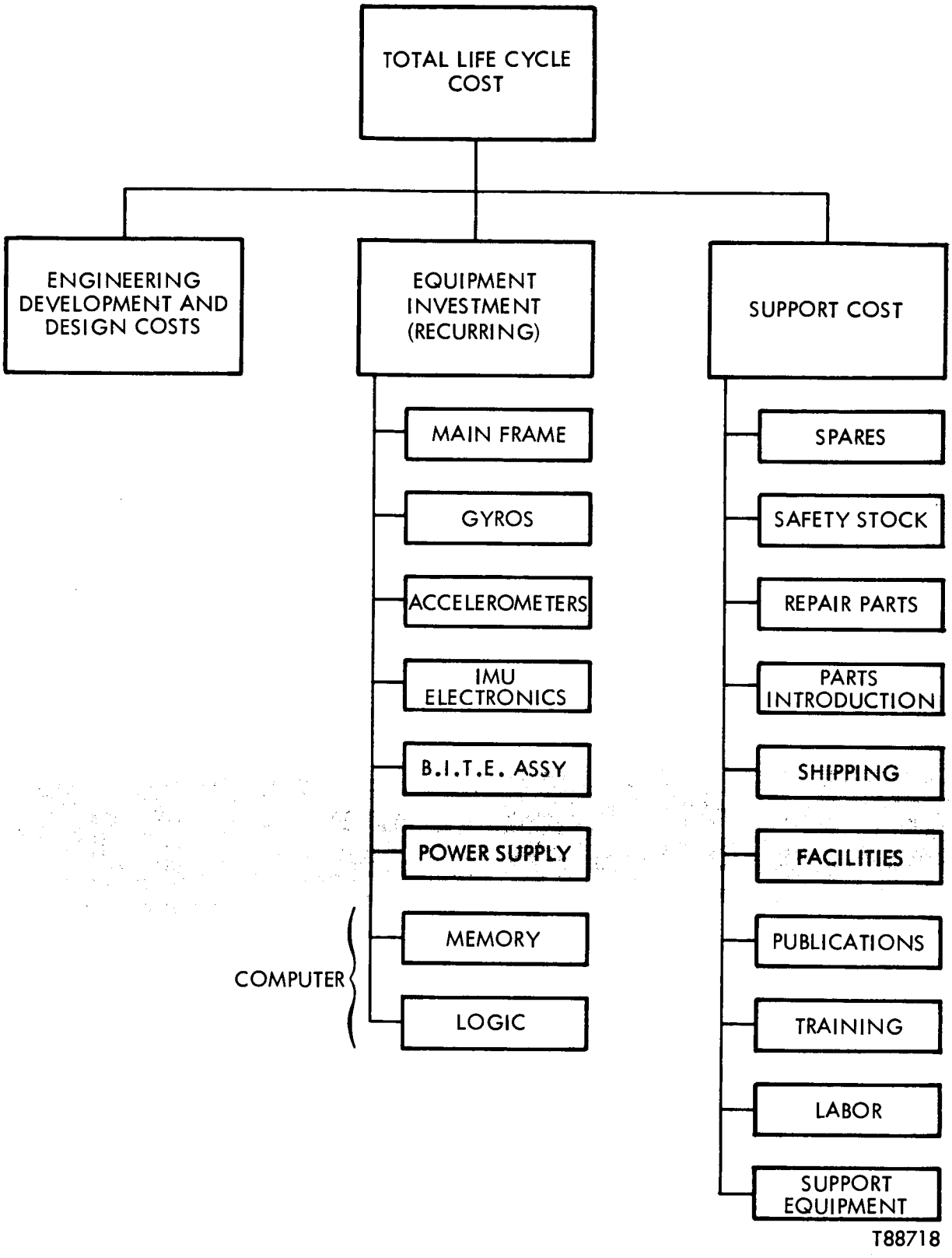

Figure 8. Life Cycle Cost Categories

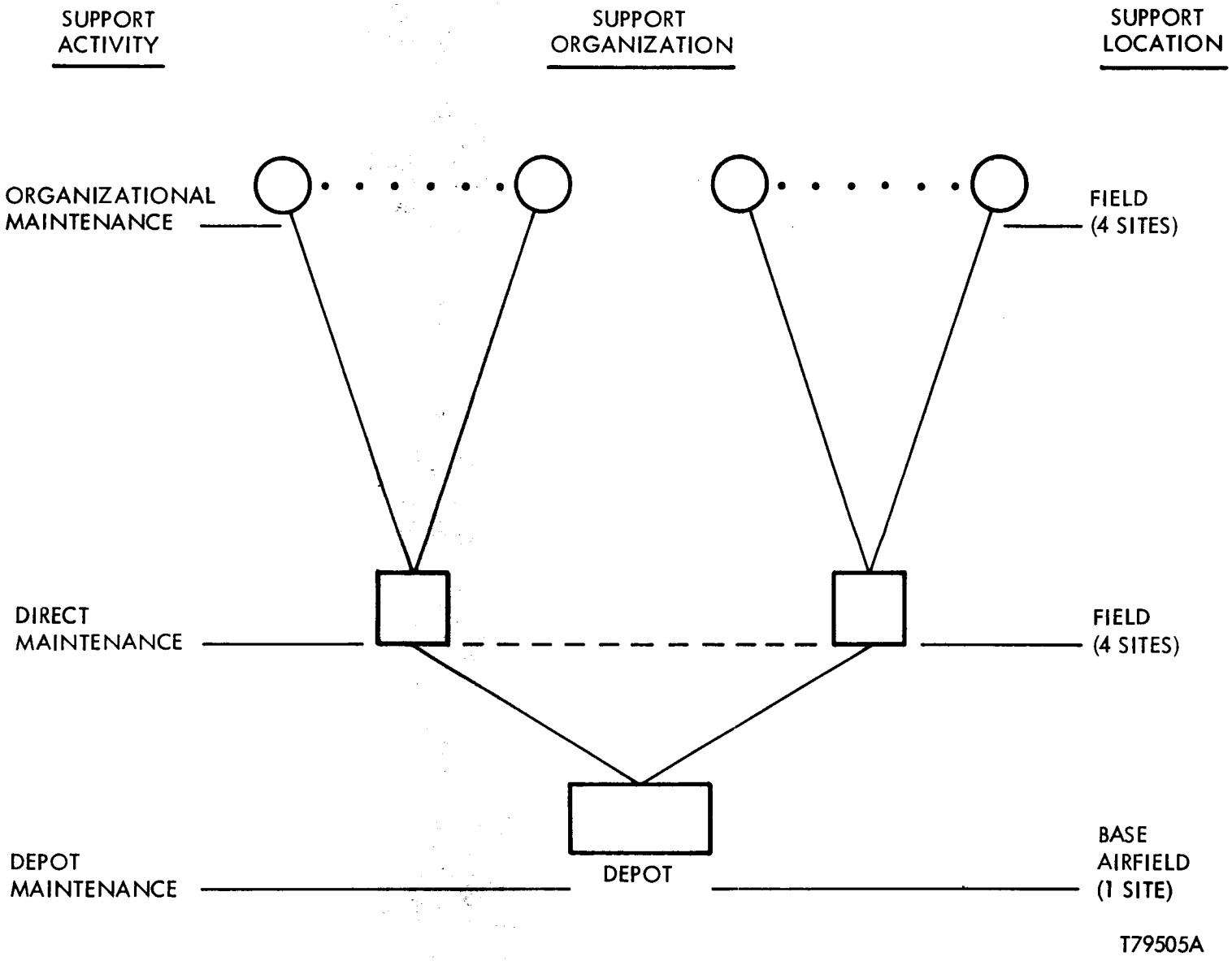

Figure 9. Support System Structure

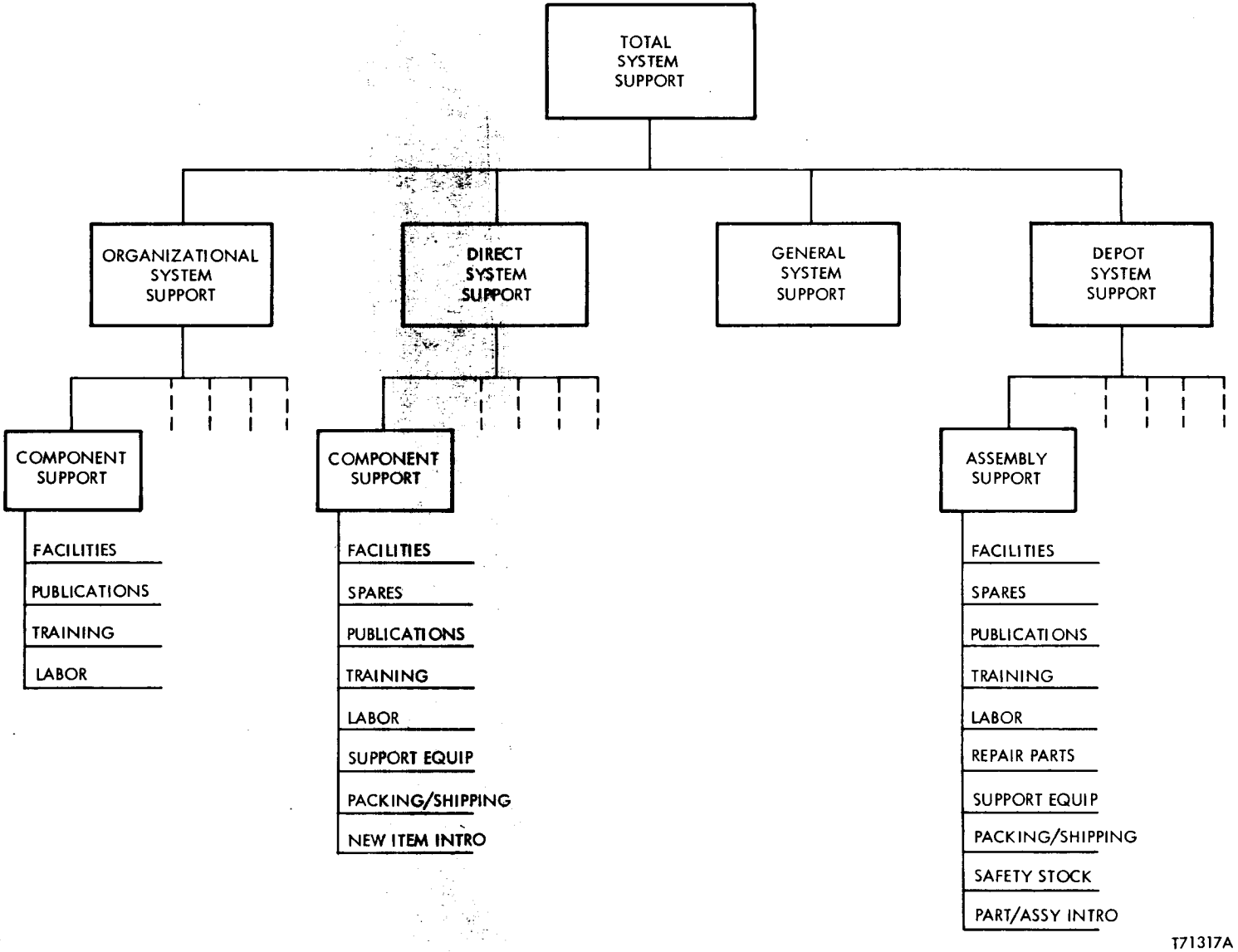

Figure 10. Support Level Cost Elements

Table 14. Strapdown IMU Maintenance Plan

Nomenclature	No. of Repairables	Organizational	Direct	Depot
Computer Set	1	RR		
Gyro	2		RR	RP
Gyro Cage Assembly	2		RR	RP
Accelerometer	3		RR	RP
Accel Cage Assembly	3		RR	RP
Main Frame	1			RP
A/D Assembly	1		RR	RP
Bite Assembly	1		RR	RP
Power Supply	1		RR	RP

RR = Remove and Replace

RP = Repair Item

Table 15. 4-Gimbal IMU Maintenance Concept

Nomenclature	No. of Repairables	Organizational	Direct	Depot
Computer Set	1	RR		
Gyro	2			RP
Gyro Cage Assembly	1		RR	RP
Accelerometer	3			RP
Accel Cage Assembly	3		RR	RP
Main Frame	1			RP
4-Gimbal Set	1			RP
A/D Assembly	1		RR	RP
Gimbal Servo Assembly	4		RR	RP
Resolver Assembly	4			RR
Torquer Assembly	4			RR
Bite Assembly	1		RR	RP
Power Supply	1		RR	RP

RR = Remove and Replace

RP = Repair Item

e. The failure rates for the subassemblies are as shown in Table 12.

f. The specific cost factors are as shown in Table 18, and the standard cost factors are shown in Table 17.

g. The support element cost calculations are as shown in Table 18.

Based upon the above definitions, assumptions, and computations, the life cycle costs for both the strapdown and the 4 gimbal IMU cases have been analyzed and summarized using a Teledyne computer program which has been specifically developed for computing these costs. The life cycle cost model used here has been compared with two U.S. Army computerized models, the Army Regulation (AR) No. 37-18 and the Computerized Cost Model for Electronic-Communications Equipment (ECOMP 11-4). Although there are some differences in the classification of certain categories of cost in terms of whether these are recurring investments or support costs, the same basic categories are integrated into each model. Some of the significant features of the life cycle computer model are as follows:

- Program written in FORTRAN IV
- Compatible with IBM 360 computers
- Input data provided on punched cards
- Analysis performed for each designated repair candidate
- Support cost breakdown provided for each site
- Total support cost provided for total number of systems

Table 16. Specific Cost Factors

Life Cycle in Months	120
Number of Support Sites	9
Number of Systems Per Organizational & Direct Support Sites	25
Number of Systems Per Depot Support Site	100
Item Cost	*
Item Weight	*
Items Per Next Higher Assembly	*
Training Cost Per Man-Week	750.00
Mean Time Between Maintenance	*
Man Hours Per Maintenance Action	*
New Assembly Introduced	*
New Parts Introduced	*
Parts Weight Per Maintenance Action	*
Parts Cost Per Maintenance Action	*
Special Support Equipment Cost**	*
Facilities Cost**	*
Technician Man-Weeks of Training**	*
Tech Data Pages**	*
Depot Special Support Equipment Cost	*
Depot Facilities Cost	*
Depot Technician Man-Weeks of Training	*
Depot Tech Data Pages	*

*As Required by Repair Candidate

**Organizational, Direct and Depot

Table 17. Standard Cost Factors

Depot Hourly Labor Rate	$ 10.00
Tech Data Cost Per Page	160.00
U.S. Transportation Rate per Pound	0.0376
Depot Repair Cycle in Months	2.0
Intermediate Repair Cycle in Months Depot	0.3
Depot Transportation Period (Months)	0.3
Introductory Inventory Cost per New Assembly	$233.09
Introductory Inventory Cost per New Part	171.01
Packing Labor Cost per Pound	0.1868
Packing Material Cost per Pound	0.0497
Packaged to Unpackaged Ratio	1.285/1.0

Table 18. Support Element Cost Calculations

SPARES		
UNIT SPARES	=	(demands/month/organization) (turnaround time) (unit price)
ASSEMBLY SPARES	=	(demands/month/organization) (turnaround time) (assy price)
REPAIR PARTS	=	(demands/month/organization) (life cycle) (ave cost parts/repair)
LABOR		
MAINT. LABOR	=	(demands/month/organization) (life cycle) (ave manhours/repair) (wage rate)
SUPPORT EQUIPMENT		
SPECIAL SUPPORT EQUIPMENT	=	(% apportioned/repair candidate) (acquisition cost)
TRAINING		
TRAINING	=	[(technicians/organization) + (replacement factor) (technician/organization)] (training duration) (ave cost per student week)
PUBLICATIONS		
PUBLICATIONS	=	$\frac{\text{(No. new pages) (cost per page)}}{\text{(No. organization)}}$
FACILITIES	=	(No. square feet) (cost per square foot)

Failure Detection and Isolation

Introduction. - In order to take advantage of the increased reliability afforded by redundant system components it is necessary that failures, when they occur, are detected and that the faulty component be isolated in order that its malfunction does not deleterously affect the performance of the system.

Two basic types of redundant system have been considered in the present study. The first is a Fail-Op system, ie., one in which a single failure of any component or subsystem can be detected, isolated and disregarded in succeeding operations - i.e., the system will operate properly in the presence of a single failure of any component or sub-system. The second level of redundancy considered is a Fail-Op/Fail-Op system, or one which will operate properly in the presence of failures in two functionally similar components or subsystems.

Fail-Op performance may be achieved in different ways. Figure 11 shows a fully triple redundant system configuration employing three complete inertial sensor units (i.e., two TDF gyros and three accelerometers) and three complete processing channels. Using simple voting it is possible to detect and isolate the failure of any one sensor unit, any one processing channel, or both and is, therefore, Fail-Op.

It is possible to achieve Fail-Op performance with fewer components than shown in Figure 11. If it is assumed that the strapdown system is but one element of a hybrid navigation/control system which is Fail-Op, it is likely that a Fail-Op central computer will be present which will have access to sufficient additional navigation information to perform "voting" and thus failure isolation, on any two strapdown computational channels. If this is the case only two such channels are required for Fail-Op redundancy. (Similarly, only three processing channels would be required in a Fail-Op/Fail-Op System.)

The second major area of component saving concerns the sensor packages in Figure 11. This has been alluded to previously in the discussion of system configurations (See Figure 2). Fail-Op performance may be achieved with 3 TDF gyros and 5 linear accelerometers (or 3 SCAG's). Fail-Op/Fail-Op performance is possible with 4 TDF gyros and 6 accelerometers (or with 4 SCAG's).

The remainder of this section describes some techniques for failure detection and isolation of gyro and electronics failures. Reference [18] describes additional failure detection and isolation techniques which, although primarily involving single degree of freedom gyroscopes, are equally applicable to linear accelerometers.

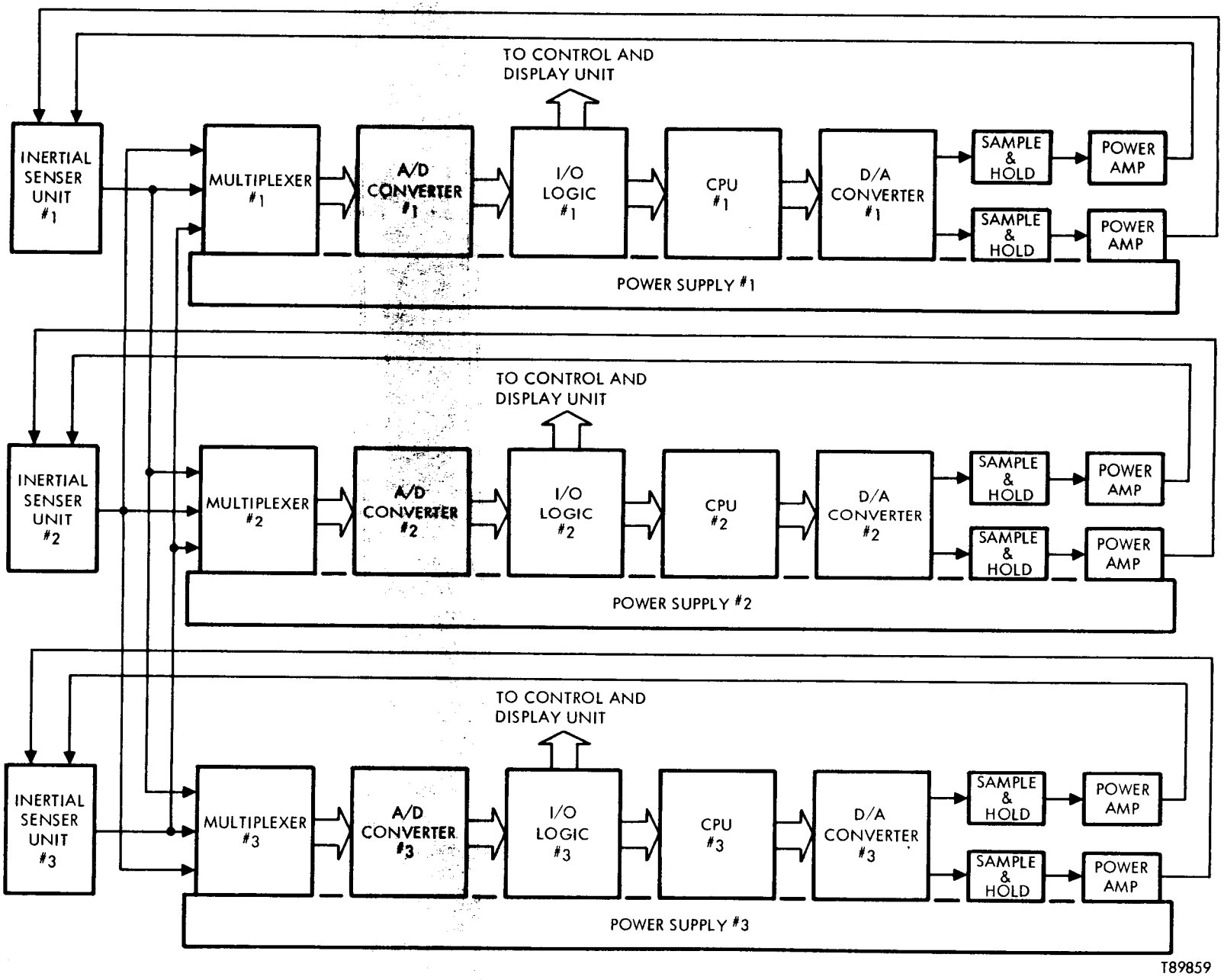

Figure 11. Block Diagram Redundant Digital Strapdown System

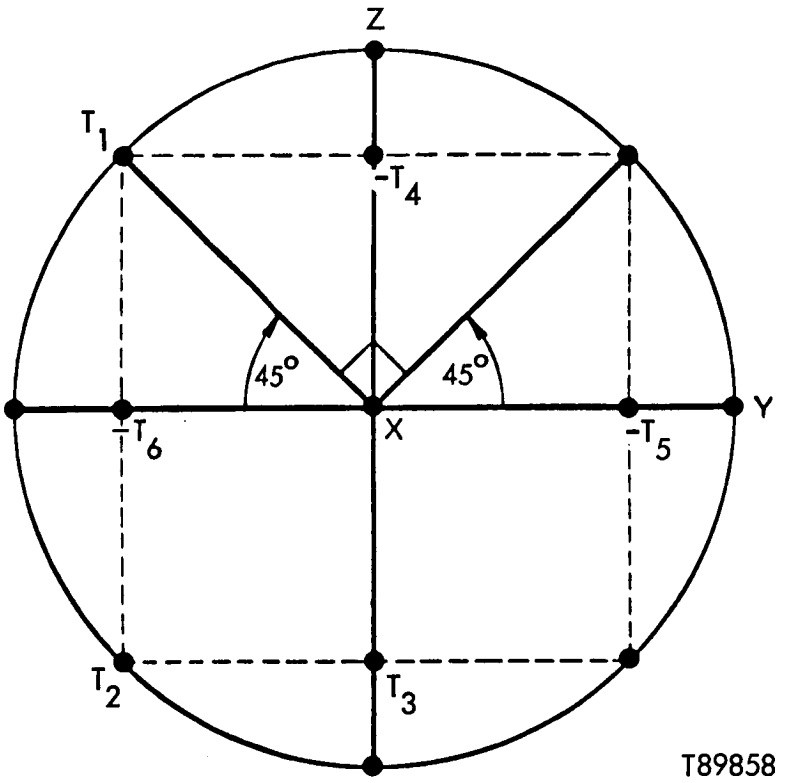

Figure 12. Unit Circle Diagram

Gyro Failure Detection. - One version of a redundant, three gyro system is described here which, by using relatively simple comparison and matching of the outputs, can isolate single axis as well as complete gyro failures or significant errors.

The configuration chosen consists of three two-degree-of-freedom gyros oriented such that the spin axes are mutually orthogonal and the torquer axes of each gyro are at a 45° angle to the spin axes of the other two gyros. Figure 12 depicts a unit circle which shows these relative orientations.

In Figure 12 X, Y, and Z represent the angular orientations of the three gyro spin vectors, T_1 and T_2 represent the angular orientations of the X gyro (spin vector along X) torquers, T_3 and T_4 represent the angular orientations of the Y gyro torquers, and T_5 and T_6 represent the angular orientation of the Z gyro torquers.

A general angular rate input, $\overline{\omega}$, can be assumed to be comprised of the vector sum of its three components ω_x, ω_y, and ω_z along the X, Y, and Z directions, respectively. With such an input, and assuming a pure gyroscopic precession torque response from each instrument,

$$T_1 = (\omega_z - \omega_y) H \cos 45^\circ \quad (1)$$

$$T_2 = -(\omega_z + \omega_y) H \cos 45^\circ \quad (2)$$

$$T_3 = (\omega_x - \omega_z) H \cos 45^\circ \quad (3)$$

$$T_4 = -(\omega_x + \omega_z) H \cos 45^\circ \quad (4)$$

$$T_5 = (\omega_y - \omega_x) H \cos 45^\circ \quad (5)$$

$$T_6 = -(\omega_y + \omega_x) H \cos 45^\circ \quad (6)$$

where H is the angular momentum of each gyro and T_i is the measured torque along the i torquer axis.

Assuming that the measurements T_1 through T_6, the gyro precession torques, are all continuously available there are six independent equations in the three desired quantities ω_x, ω_y, and ω_z. From these six equations we can obtain 20 combinations of three equations from which ω_x, ω_y, and ω_z can be extracted.

If one and only one of the measurements is in error then ten of these 20 combinations will yield the correct set of solutions while the remaining ten will result in non-coincident incorrect sets of solutions. This can be seen by observing that for the one incorrect measurement there are ten combinations of the remaining five measurements (taken two at a time to establish the total of three equations at a time required to determine the apparent solutions).

Since the solution of 20 sets of equations and the ensuing comparison of the results for the determination and isolation of a single incorrect input measurement may in general require a significant amount of computational hardware or computer capacity it is obviously desirable to make use of the symmetry we have chosen for the orientation of the gyro axes to simplify this process.

One approach to this problem is to take the following three sets of three equations for the determination of the corresponding three sets of solutions:

Table 19.

Set No.	Equations Used	Solutions For ω_x	Solutions For ω_y	Solutions For ω_z
1	(1), (2), (3)	$T_3' + \frac{T_1' - T_2'}{2}$	$-\frac{T_1' + T_2'}{2}$	$\frac{T_1' - T_2'}{2}$
2	(3), (4), (5)	$\frac{T_3' - T_4'}{2}$	$T_5' + \frac{T_3' - T_4'}{2}$	$-\frac{T_3' + T_4'}{2}$
3	(5), (6), (1)	$-\frac{T_5' + T_6'}{2}$	$\frac{T_5' - T_6'}{2}$	$T_1' + \frac{T_5' - T_6'}{2}$

where $T_1' = \frac{T_1}{H \cos 45^\circ}$, etc.

Now let us assume that we can examine for mutual equality among the three values of ω_x we have separately determined. Also assume we can do the same for the values of ω_y and ω_z. This comparison process can be shown schematically as in Figure 13.

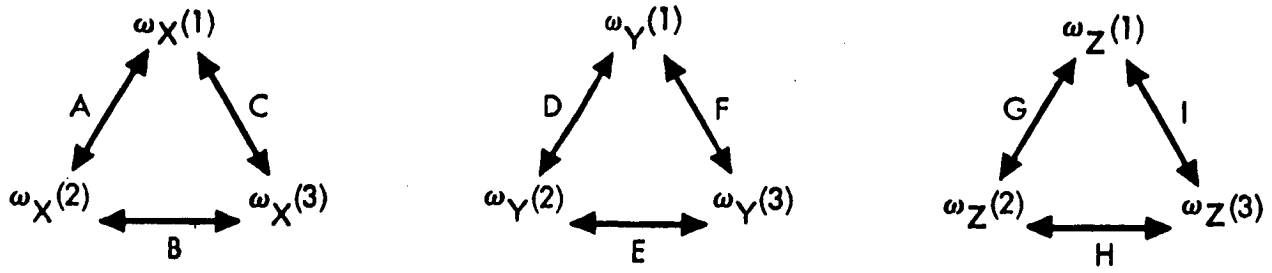

Figure 13. Rate Comparison Diagrams

In Figure 13 the symbol ω_x (1) represents the quantity ω_x as determined by the equation set number 1 of Table 6, and the letter A represents a comparison process between ω_x (1) and ω_x (2), etc. We can now create a table of the results of the comparison processes A through I for an error in any one of the measurements T_1 through T_6. Table 20 represents this matrix. The symbol 1 is used for comparison valid (equality), and the symbol 0 is used for comparison invalid (inequality due to a measurement error).

An inspection of Table 20 indicates the only six of the nine comparisons are necessary to isolate the single axis errors. For example the comparisons A, C, D, F, G, and H provide sufficient information to accomplish this. More than one such combination of six comparisons will produce equivalent results.

Table 20.

Error In	A	B	C	D	E	F	G	H	I
T_1	0	1	0	0	1	0	0	0	0
T_2	0	1	0	0	1	0	0	1	0
T_3	0	0	0	0	0	1	0	0	1
T_4	0	0	1	0	0	1	0	0	1
T_5	1	0	0	0	0	0	1	0	0
T_6	1	0	0	1	0	0	1	0	0

For a two-axis failure or measurable error for any one gyro only, the comparisons B, F, and G are required, as shown in Table 21. The two axis failure detection method which is suggested here is based on Table 21. In this

Table 21.

Gyro	Error In	B	F	G
1	T_1 and T_2	1	0	0
2	T_3 and T_4	0	1	0
3	T_5 and T_6	0	0	1

table it is noted that comparison B will isolate the errors in ω_x by comparing the torque measurements of gyros 2 and 3. In equation form

$$\delta_x = \omega_{x2} - \omega_{x3} \tag{7}$$

where from Table 19:

$$\omega_{x2} = \frac{T_3 - T_4}{K}$$

$$\omega_{x3} = -\frac{T_5 + T_6}{K}$$

$$K = 2H \cos 45^\circ = 2\sqrt{2}H$$

If no error exists, $\omega_{x2} = \omega_{x1}$ and δ_x becomes 0. This error detection can be accomplished quite easily in the CPU of each channel where the solutions for ω_{x2} and ω_{x3} have been computed. The solutions are then simply compared and if no error exists ($\delta_x = 0$) a logic "1" is generated. A logic "0" indicates an error in one of the two axes. Identical reasoning applies to the error detection in ω_y and ω_z. An analog of the suggested method of error detection and gyro selection is provided in Figure 14.

It is logically desirable to check first for single axis failures, then for two axis failures in order to minimize the required computations.

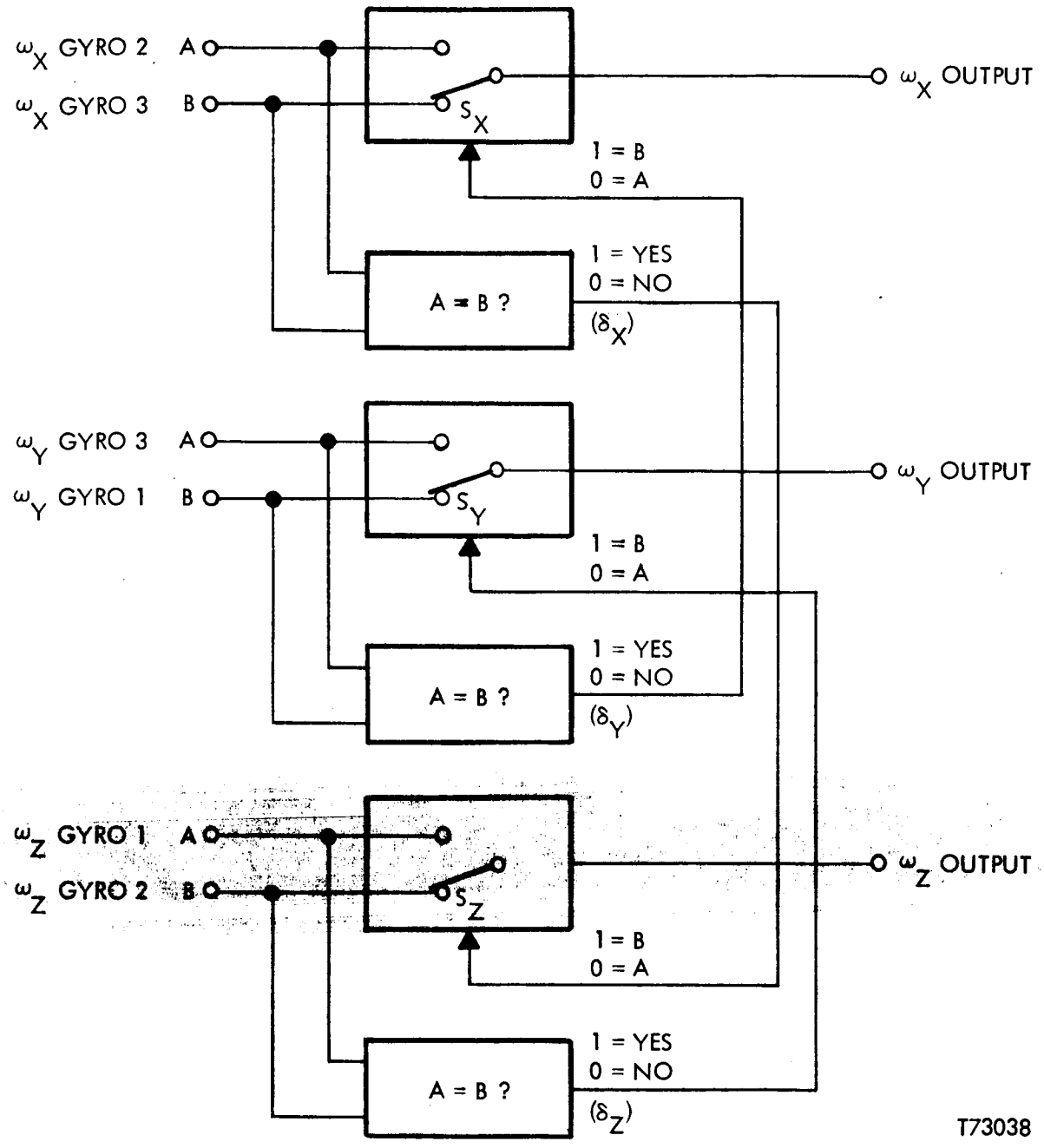

Figure 14. Error Detection Switching

Table 22 below illustrates the operation of this technique. Note that if either axis of a gyro fails, it is disconnected from the system by a logic "switch" (shown as S_x, S_y, or S_z in Figure 14).

Table 22.

Error In (Ref Table 1)	Error Detector State			Switch State			Gyro Used		
	δ_x	δ_y	δ_z	S_x	S_y	S_z	x	y	z
T_1 and/or T_2	1	0	0	0	0	1	3	1	2
T_3 and/or T_4	0	1	0	1	0	0	2	3	1
T_5 and/or T_6	0	0	1	0	1	0	3	3	1
No Error	1	1	1	1	1	1	2	1	1

This method would generally not be mechanized as circuitry (it can be if required), but would be part of the computer program. The switch would be in the hardware: a method of making switches redundant for any single failure of either a short or an open circuit is shown in Figure 15. A parallel arrangement of just two switches is immune to an open circuit, or failure to close, but is not immune to a short circuit in one or the other.

Electronics Failure Detection. - Detection of errors or failures in the small amount of electronics associated with each inertial sensor unit (e.g., buffer amplifiers, etc.) is automatically accomplished in the gyro failure detection technique described above.

In each digital channel of Figure 11 there are several blocks of electronics that could individually fail, resulting in the erroneous processing of otherwise valid gyro data. To circumvent this problem, several detection schemes have been included in these electronics.

In the Multiplexer and A/D converter, errors are detected when precision dual polarity self-test voltages are applied to multiplexer inputs and converted to digital words by the A/D converter. The converted outputs are then compared to pre-stored constants in the CPU. If an error exists, logic switching will remove the errant channel from operation leaving the

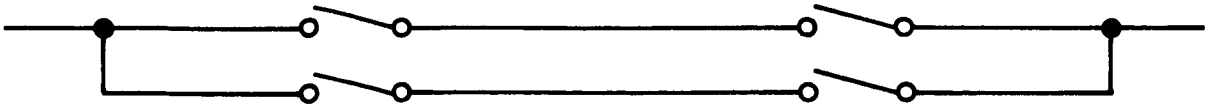

T89856

Figure 15. Redundant Switch

remaining two channels in full operation. Note that each channel is self-contained and that only two channels are required for complete system operation. This error detection occurs once every conversion and effectively self-tests the multiplexer, A/D converter, I/O Logic and the CPU.

Additionally the CPU contains a "built-in" self test routine that checks the operation of the CPU individually. Again, an error will cause shut-down of the entire channel. Further, note that failures in the Sample-and-Hold and Power Amplifier sections will appear as gyro errors and will be detected in the gyro failure detection scheme described previously.

Conclusions. -It is possible to detect single axis gyro errors in a three gyro redundant configuration as described in foregoing paragraphs. At least one configuration makes possible this detection and isolation process by the use of relatively simple equality comparisons that can be easily accommodated in each CPU. Electronic errors are detected by means of "built-in" self-test provisions. It is noteworthy that certain "soft" errors may not be sufficient to justify the shut-down of the errant component, particularly, if they are transient in nature. For this reason, the detection mechanism will have pre-set time and amplitude tolerances so that such errors will not trip the shut-down sequence.

Also, it is evident from the block diagram of Figure 11 that each individual channel outputs to the Control and Display unit the full compliment of position information. Thus the Control and Display unit must select which of the three output sets will be ultimately displayed as the correct position information.

V. SYSTEM REQUIREMENTS

This section describes the system mechanization requirements for the Strapdown Navigation System. Following a description of the notation which is employed the basic mechanization equations which are required for attitude and navigation computations are derived, followed by an alignment analysis and system error analysis. Next, the overall system computational requirements are discussed. Finally, a gyro compensation analysis is presented.

Notation

Coordinate Systems. -Several coordinate systems are of importance in inertial system analysis. These include:

Platform (p) Set. -This set is fixed to the instrument package (for a strapdown system it is fixed to the vehicle; for a gimbaled system it is fixed to the stable element). It is defined by the right-hand orthogonal set of unit vectors $\underline{x}$, $\underline{y}$, $\underline{z}$. These unit vectors coincide with the (ideally aligned) sensitive axes of the inertial instruments in conventional configurations in which a non-redundant orthogonal instrument complement is employed. The platform set is the coordinate system in which all inertial measurements are made.

Local Level True North (t) Set. - This set is defined by the right-hand orthogonal set of unit vectors $\underline{e}_t$, $\underline{n}_t$, $\underline{u}_t$ with $\underline{u}_t$ positive upward along the local geographic vertical, $\underline{n}_t$ normal to $\underline{u}_t$ and positive in the direction of true north, and $\underline{e}_t = \underline{n}_t \times \underline{u}_t$.

Reference (r) Set. - The reference, or computational, set is set to which attitude is referenced and in which navigation computations are performed. It is defined by the right hand orthogonal set of unit vectors $\underline{e}$, $\underline{n}$, $\underline{u}$. It is also locally level so that $\underline{u} = \underline{u}_t$. The unit vector $\underline{n}$ is normal to $\underline{u}$ and positive in the azimuth reference direction, and $\underline{e} = \underline{n} \times \underline{u}$. In true north mechanizations, the r and t sets coincide.

Vehicle (b) Set. - The vehicle, or body fixed, set is attached to the carrying vehicle. It is defined by the right hand orthogonal set of unit vectors $\underline{p}$, $\underline{q}$, $\underline{r}$ with $\underline{r}$ along the vehicle longitudinal (roll) axis, positive forward; $\underline{p}$ along the vehicle lateral (pitch) axis, positive starboard; and $\underline{q} = \underline{r} \times \underline{p}$ along the vehicle yaw axis, positive downward.

Earth Fixed (e) Set. - The earth fixed set is the set to which position is referenced. It is defined by the unit vectors $\underline{x}_e$, $\underline{y}_e$, $\underline{z}_e$ with $\underline{z}_e$ in the direction of the earth's spin vector; $\underline{x}_e$ in the equitorial plane and positive toward the Greenwich Meridian; and $\underline{y}_e = \underline{z}_e \times \underline{x}_e$.

Inertial (i) Set. - The inertial set is fixed in inertial space and forms the reference for inertial measurements. Since it is unnecessary to coordinatize any vectors in this set, the definition of specific axes is unimportant. It may be advantageous from a conceptual standpoint, however, to consider a right-hand orthogonal set of unit vectors $\underline{x}_i$, $\underline{y}_i$, $\underline{z}_i$ with $z_i = \underline{z}_e$; $\underline{y}_i$ normal to $\underline{z}_i$ and inertially fixed in some arbitrary direction; and $\underline{x}_i = \underline{y}_i \times \underline{z}_i$. With this choice, the i and e sets coincide once each (sidereal) day.

Certain additional coordinate frames will be useful in analyzing various system error effects. These will, in general, be nominally aligned with one of the above sets and differ from them only by small error angles. These will be designated by use of a prime (e.g. the r' set, defined by unit vectors $\underline{e}'$, $\underline{n}'$, $\underline{u}'$). Further discussion of these sets will be deferred until later sections.

Vectors. - All vectors are designated by lower case letters (exception: earth's spin vector $\underline{\Omega}$). Latin letters are used for linear variables, Greek letters for angular variables.

Uncoordinatized physical vectors are designated by an underscore. Coordinatized vectors are designated by the vector's symbol with a superscript designating the coordinate set in which it is resolved. Vector components are specified by subscripts designating the coordinate axes along which they lie. As an example, if $\underline{\xi}$ is any vector

$$\underline{\xi} = \xi_x \underline{x} + \xi_y \underline{y} + \xi_z \underline{z} \qquad \text{"p" set}$$

$$= \xi_e \underline{e} + \xi_n \underline{n} + \xi_u \underline{u} \qquad \text{"r" set}$$

$$= \xi_{et} \underline{e}_t + \xi_{nt} \underline{n}_t + \xi_{ut} \underline{u}_t \qquad \text{"t" set}$$

$$\xi^p = \begin{bmatrix} \xi_x \\ \xi_y \\ \xi_z \end{bmatrix}, \quad \xi^r = \begin{bmatrix} \xi_e \\ \xi_n \\ \xi_u \end{bmatrix} \quad \xi^t = \begin{bmatrix} \xi_{et} \\ \xi_{nt} \\ \xi_{ut} \end{bmatrix}$$

Non-physical vectors (i. e. column matrices) are also designated by lower case Latin letters. Components are designated by numerical subscript or by scalar representation as appropriate.

Matrices. -All matrices are designated by capital Latin or Greek letters (exception: column matrices - see above). Submatrices are designated by the same capital Latin or Greek letters with subscripts. Elements of matrices are designated by the corresponding lower case letters with subscripts. Matrix transposition is designated by a superscript T.

Additional Notation. -Computed, or estimated, quantities are designated by a "carrot" or "hat". Thus $\hat{x}$ is the computed value of the variable x.

Measured quantities are designated by a tilde. Thus $\tilde{y}$ is the measured value of the variable y.

Error quantities are designated by a prefix δ. Thus $\hat{\delta x} = \hat{x} - x$ and $\tilde{\delta y} = \tilde{y} - y$.

Mathematical expectation is designated by the operator E. Parentheses and brackets are omitted where it does not lead to confusion.

Continuous time arguments are represented by the letter t, discrete time arguments by k. Iteration period is designated by τ.

Differences are designated by a prefix Δ. Thus if x_1 and x_2 are two (compatibly dimensioned) variables, their difference may be designated by $\Delta x = x_2 - x_1$.

General Requirements. - Figure 16 depicts the fundamental relationships among the four coordinate sets which are of primary importance in strapdown inertial navigation. The inertial (i) set is the reference for the inertial sensor measurements of angular rate and acceleration. The earth set (e) is the reference for the specification of position. The earth set rotates at a constant vector angular rate $\underline{\Omega}$ relative to the inertial set.

The reference (r) set is the set in which the navigation computations are performed. The r set moves at a vector rate $\underline{\rho}$ with respect to the e set as the carrying vehicle moves over the surface of the earth. The relationship between the r and e sets specifies the position of the vehicle on the earth's surface (although not its altitude) as well as specifying the azimuth reference direction. This relationship is typically expressed in terms of Euler Angles (latitide (ϕ), longitude (λ), and "wander angle" (α)), by a direction cosine matrix C, or by a quaternion c.

The platform (p) set is the set in which the sensor measurements are performed. The p set moves at a vector rate $\underline{\zeta}$ with respect to the reference (r) set as the vehicle attitude and heading vary. The relationship between the p and r sets specifies the attitude of the vehicle with respect to the level plane and its heading with respect to the aximuth reference direction. This relationship is typically expressed in terms of Euler Angles (pitch (θ), roll (φ), and grid heading (ψ_G)), by a direction cosine matrix B, or by a quaternion b.

The angular rate $\underline{\omega}$ of the platform set with respect to the inertial set is the quantity sensed by the gyroscopes. The accelerometers similarly sense the inertially referenced linear acceleration of the platform set. The gyro measurements are used to maintain the attitude reference as specified by B, b, or (θ, φ, ψ_G). This reference provides the proper resolution of the accelerometer data for use in the computation of velocity in reference coordinates and of position, as specified by C, c, or (ϕ, λ, α).

Attitude Propagation - Direction Cosines.

Let $\underline{\xi}$ by any vector. The components of $\underline{\xi}$ in the platform coordinate set are related to the reference set components by

$$\begin{bmatrix} \xi_x \\ \xi_y \\ \xi_z \end{bmatrix} = B \begin{bmatrix} \xi_e \\ \xi_n \\ \xi_u \end{bmatrix} \qquad (1)$$

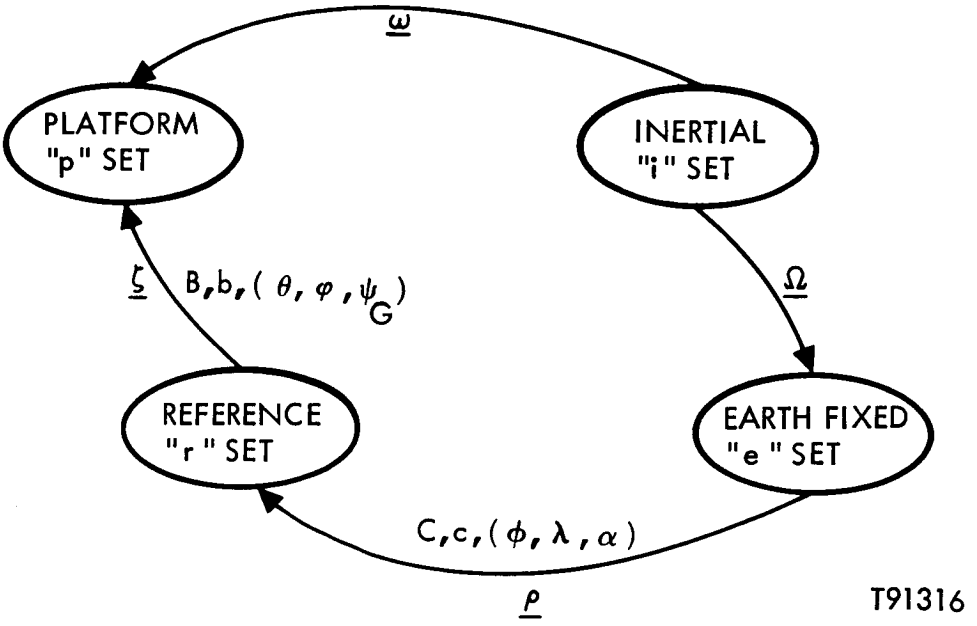

Figure 16. Relationship Among Coordinate Sets

where B is the direction cosine matrix relating the two coordinate systems. The matrix B will be termed the attitude direction cosine matrix, since it uniquely defines the attitude of the platform set and, hence, the vehicle attitude.

The propagation of the B matrix may be readily rounded by differentiating (1):

$$\begin{bmatrix} \dot{\xi}_x \\ \dot{\xi}_y \\ \dot{\xi}_z \end{bmatrix} = B \begin{bmatrix} \dot{\xi}_e \\ \dot{\xi}_n \\ \dot{\xi}_u \end{bmatrix} + \dot{B} \begin{bmatrix} \xi_e \\ \xi_n \\ \xi_u \end{bmatrix} \tag{2}$$

From classical vector calculus, however,

$$\left[\frac{d\underline{\xi}}{dt}\right]_r = \left[\frac{d\underline{\xi}}{dt}\right]_p + \underline{\zeta} \times \underline{\xi} \tag{3}$$

where $\underline{\zeta}$ is the vector angular rate of the x, y, z axes with respect to the e, n, u axes and where the operators $\left[\frac{d}{dt}\right]_r$ and $\left[\frac{d}{dt}\right]_p$ indicate differentiation with

respect to the r and p coordinate sets, respectively. Rewriting (3) in vector-matrix form in platform coordinates

$$B\begin{bmatrix}\dot{\xi}_e\\ \dot{\xi}_n\\ \dot{\xi}_u\end{bmatrix} = \begin{bmatrix}\dot{\xi}_x\\ \dot{\xi}_y\\ \dot{\xi}_z\end{bmatrix} + \begin{bmatrix}0 & -\zeta_z & \zeta_y\\ \zeta_z & 0 & -\zeta_x\\ -\zeta_y & \zeta_x & 0\end{bmatrix}\begin{bmatrix}\xi_x\\ \xi_y\\ \xi_z\end{bmatrix}$$

$$= \begin{bmatrix}\dot{\xi}_x\\ \dot{\xi}_y\\ \dot{\xi}_z\end{bmatrix} - Z\begin{bmatrix}\xi_x\\ \xi_y\\ \xi_z\end{bmatrix} \qquad (4)$$

where Z is the attitude rate matrix

$$Z = \begin{bmatrix}0 & \zeta_z & -\zeta_y\\ -\zeta_z & 0 & \zeta_x\\ \zeta_y & -\zeta_x & 0\end{bmatrix} \qquad (5)$$

Now, substituting (2) into (4)

$$B\begin{bmatrix}\dot{\xi}_e\\ \dot{\xi}_n\\ \dot{\xi}_u\end{bmatrix} = B\begin{bmatrix}\dot{\xi}_e\\ \dot{\xi}_n\\ \dot{\xi}_u\end{bmatrix} + \dot{B}\begin{bmatrix}\xi_e\\ \xi_n\\ \xi_u\end{bmatrix} - Z\begin{bmatrix}\xi_x\\ \xi_y\\ \xi_z\end{bmatrix} \qquad (6)$$

or, using (1) and simplifying,

$$(\dot{B} - ZB)\begin{bmatrix}\xi_e\\ \xi_n\\ \xi_u\end{bmatrix} = \begin{bmatrix}0\\ 0\\ 0\end{bmatrix} \qquad (7)$$

Finally, since $\underline{\xi}$ was arbitrary, the equality (7) implies that

$$\dot{B} = ZB \qquad (8)$$

Equation (8) is the fundamental matrix-matrix attitude differential equation which must be solved by the computer in a direction cosine mechanization of a strap-down navigation. The initial condition for the solution of (8) is determined by the system alignment as described in a later section.

Attitude Propagation - Euler Angles. - Attitude and grid heading may be specified by the Euler Angles

ψ_G = grid heading angle

θ = pitch angle

φ = roll angle

These angles are shown in Figure 17. (It is assumed that $\underline{x} = \underline{p}$, $\underline{y} = \underline{r}$, $\underline{z} = -\underline{q}$, i. e., that the platform and vehicle sets are coincident). If $\underline{\xi}$ is any vector, it is seen that

$$\begin{bmatrix} \xi_{x'} \\ \xi_{y'} \\ \xi_u \end{bmatrix} = \begin{bmatrix} \cos\psi_G & \sin\psi_G & 0 \\ -\sin\psi_G & \cos\psi_G & 0 \\ 0 & 0 & 1 \end{bmatrix} \begin{bmatrix} \xi_e \\ \xi_n \\ \xi_u \end{bmatrix} \tag{9}$$

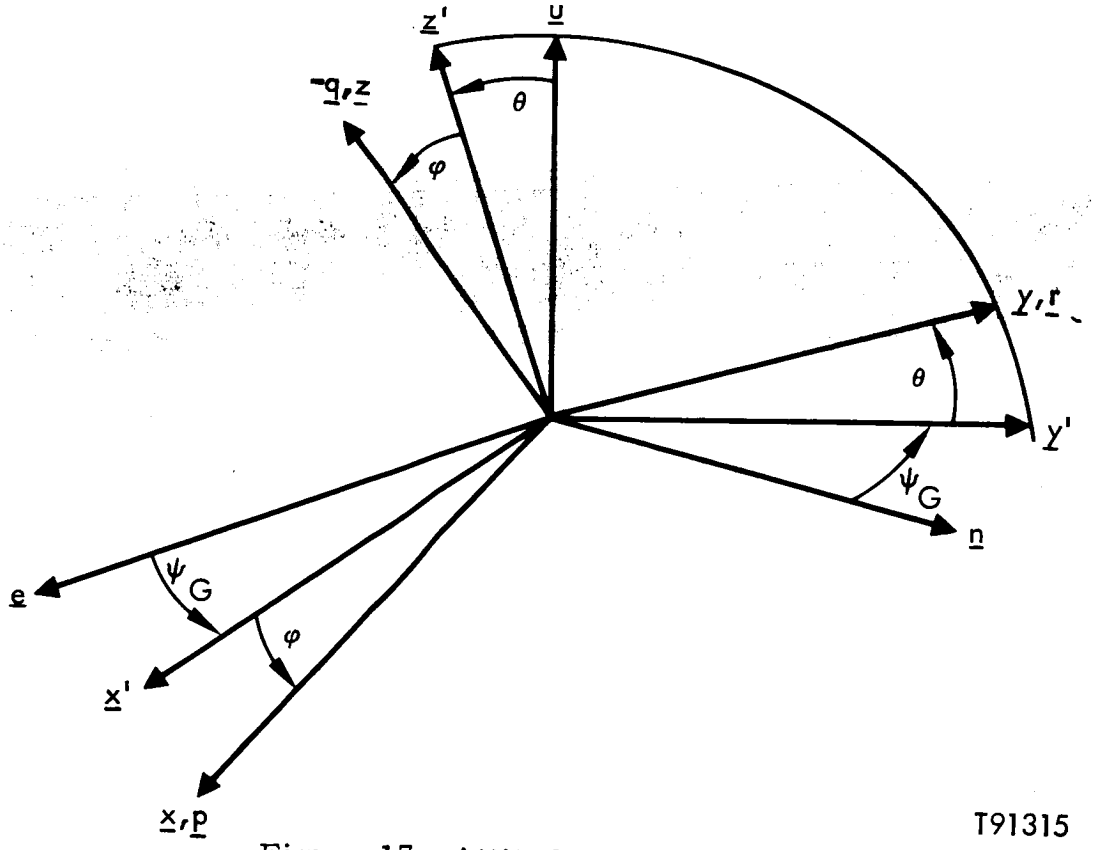

T91315

Figure 17. Attitude Euler Angles

$$\begin{bmatrix} \xi_x'' \\ \xi_y'' \\ \xi_z'' \end{bmatrix} = \begin{bmatrix} 1 & 0 & 0 \\ 0 & \cos\theta & \sin\theta \\ 0 & -\sin\theta & \cos\theta \end{bmatrix} \begin{bmatrix} \xi_{x'} \\ \xi_{y'} \\ \xi_u \end{bmatrix} \tag{10}$$

$$\begin{bmatrix} \xi_x \\ \xi_y \\ \xi_z \end{bmatrix} = \begin{bmatrix} \cos\varphi & 0 & -\sin\varphi \\ 0 & 1 & 0 \\ \sin\varphi & 0 & \cos\varphi \end{bmatrix} \begin{bmatrix} \xi_x'' \\ \xi_y'' \\ \xi_z'' \end{bmatrix} \tag{11}$$

$$= \begin{bmatrix} \cos\varphi & 0 & -\sin\varphi \\ 0 & 1 & 0 \\ \sin\varphi & 0 & \cos\varphi \end{bmatrix} \begin{bmatrix} 1 & 0 & 0 \\ 0 & \cos\theta & \sin\theta \\ 0 & -\sin\theta & \cos\theta \end{bmatrix}$$

$$\begin{bmatrix} \cos\psi_G & \sin\psi_G & 0 \\ -\sin\psi_G & \cos\psi_G & 0 \\ 0 & 0 & 1 \end{bmatrix} \begin{bmatrix} \xi_e \\ \xi_n \\ \xi_u \end{bmatrix}$$

or, upon multiplying,

$$\begin{bmatrix} \xi_x \\ \xi_y \\ \xi_z \end{bmatrix} = \begin{bmatrix} \cos\varphi\cos\psi_G & \cos\varphi\sin\psi_G & -\sin\varphi\cos\theta \\ -\sin\varphi\sin\theta\sin\psi_G & +\sin\varphi\sin\theta\cos\psi_G & \\ -\cos\theta\sin\psi_G & \cos\theta\cos\psi_G & \sin\theta \\ \sin\varphi\cos\psi_G & \sin\varphi\sin\psi & \cos\varphi\cos\theta \\ +\cos\varphi\sin\theta\sin\psi_G & -\cos\varphi\sin\theta\cos\psi_G & \end{bmatrix} \begin{bmatrix} \xi_e \\ \xi_n \\ \xi_u \end{bmatrix} \tag{12}$$

The matrix in (12) is seen from (1) to be the attitude direction cosine matrix B expressed in terms of the attitude Euler angles.

The attitude rate vector $\underline{\zeta}$ may be expressed in terms of the rates of change of the attitude Euler angles as

$$\underline{\zeta} = \dot{\psi}_G \underline{u} + \dot{\theta}\underline{x}' + \dot{\varphi}\underline{y}'' \tag{13}$$

Using (9) through (11) this is

$$\begin{bmatrix} \zeta_x \\ \zeta_y \\ \zeta_z \end{bmatrix} = \begin{bmatrix} \cos\varphi & 0 & -\sin\varphi \\ 0 & 1 & 0 \\ \sin\varphi & 0 & \cos\varphi \end{bmatrix} \begin{bmatrix} 1 & 0 & 0 \\ 0 & \cos\theta & \sin\theta \\ 0 & -\sin\theta & \cos\theta \end{bmatrix} \begin{bmatrix} 0 \\ 0 \\ \dot{\psi}_G \end{bmatrix} + \begin{bmatrix} \cos\varphi & 0 & -\sin\varphi \\ 0 & 1 & 0 \\ \sin\varphi & 0 & \cos\varphi \end{bmatrix} \begin{bmatrix} \dot{\theta} \\ 0 \\ 0 \end{bmatrix} + \begin{bmatrix} 0 \\ \dot{\varphi} \\ 0 \end{bmatrix} \tag{14}$$

or, in component form,

$$\begin{aligned} \zeta_x &= -\dot{\psi}_G \sin\varphi\cos\theta + \dot{\theta}\cos\varphi \\ \zeta_y &= \dot{\psi}_G \sin\theta + \dot{\varphi} \\ \zeta_z &= \dot{\psi}_G \cos\varphi\cos\theta + \dot{\theta}\sin\varphi \end{aligned} \tag{15}$$

from which it is seen that

$$\begin{aligned} \dot{\psi}_G &= (-\zeta_x \sin\varphi + \zeta_z \cos\varphi)\sec\theta \\ \dot{\theta} &= (\zeta_x \cos\varphi + \zeta_z \sin\varphi) \\ \dot{\varphi} &= \zeta_y - \dot{\psi}_G \sin\theta \\ &= \zeta_y - (\zeta_x \sin\varphi + \zeta_z \cos\varphi)\tan\theta \end{aligned} \tag{16}$$

Equations (14-16) are the fundamental attitude differential equations which must be solved by the computer in an Euler angle mechanization of a strapdown navigator. The initial conditions for (16) are provided by the system alignment.

Attitude Propagation - Quaternions. - Let $\underline{\xi}$ be any vector. The components of $\underline{\xi}$ in the platform coordinate set are related to the reference set components by

$$\underline{\xi}^p = b^* \underline{\xi}^r b \tag{17}$$

where b is the quaternion relating the two coordinate systems. The quaternion b will be termed the attitude quaternion, since it uniquely defines the attitude of the platform set and vehicle set.

Differentiating (17) with respect to time

$$\dot{\underline{\xi}}^p = \dot{b}^* \underline{\xi}^r b + b^* \dot{\underline{\xi}}^r b + b^* \underline{\xi}^r \dot{b} \tag{18}$$

Using (4) and observing that $B\dot{\underline{\xi}}^r = b^* \dot{\underline{\xi}}^r b$,

$$b^* \dot{\underline{\xi}}^r b = \dot{\underline{\xi}}^p + \underline{\zeta}^p \times \underline{\xi}^p$$

or (19)

$$b^* \dot{\underline{\xi}}^r b = \dot{\xi}^p + \zeta^p \underline{\xi}^p$$

where $\zeta^p = 0 + \underline{\zeta}^p$

= attitude rate quaternion

Substituting (18) into (19)

$$b^* \dot{\underline{\xi}}^r b = \dot{b}^* \underline{\xi}^r b + b^* \dot{\underline{\xi}}^r b + b^* \underline{\xi}^r \dot{b} - \zeta^p \underline{\xi}^p \tag{20}$$

Simplifying and substituting $\underline{\xi}^r = b\underline{\xi}^p b^*$

$$\begin{aligned} \underline{0} &= \dot{b}^* \underline{\xi}^r b + b^* \underline{\xi}^r \dot{b} - \zeta^p \underline{\xi}^p \\ &= \dot{b}^* b \underline{\xi}^p + \underline{\xi}^p b^* \dot{b} - \zeta^p \underline{\xi}^p \end{aligned} \tag{21}$$

Next consider the identity

$$b^* b = 1 + \underline{0} \tag{22}$$

Differentiating with respect to time

$$\dot{b}^* b + b^* \dot{b} = 0 + \underline{0} \tag{23}$$

Carrying out the indicated quaternion multiplication with $b = b_0 + \underline{b}$

$$\dot{b}*b = (\dot{b}_0 b_0 + \dot{\underline{b}} \cdot \underline{b}) + (\dot{b}_0 \underline{b} - b_0 \dot{\underline{b}} - \dot{\underline{b}} \times \underline{b})$$

$$\triangleq \beta_0 + \underline{\beta} \tag{24}$$

$$b*\dot{b} = \beta_0 - \underline{\beta}$$

so that (23) implies

$$\beta_0 = \dot{b}_o b_o + \dot{\underline{b}} \cdot \underline{b}$$

$$\equiv 0 \tag{25}$$

Substituting (25) into (21) and solving for the vector part

$$\underline{0} = \underline{\beta} \times \underline{\xi} - \underline{\xi} \times \underline{\beta} - \underline{\zeta} \times \underline{\xi} \tag{26}$$

or

$$2\underline{\beta} \times \underline{\xi} = \underline{\zeta} \times \underline{\xi} \tag{27}$$

Then since $\underline{\xi}$ was arbitrary, (27) implies that

$$\underline{\beta} = 1/2\ \underline{\zeta} \tag{28}$$

Equations (25) and (28) may be rewritten, using (24), as

$$b*\dot{b} = 1/2\ (0 + \underline{\zeta}) \tag{29}$$

and with $\zeta \triangleq 0 + \underline{\zeta}$

$$\dot{b} = 1/2 b\zeta^{p} \tag{30}$$

which is the fundamental attitude differential equation which must be solved by the computer in a quaternion mechanization of a strapdown navigator. The initial condition for (30) is determined by the system alignment.

Position Equations - Direction Cosines. - Let $\underline{\xi}$ be any vector. The components of $\underline{\xi}$ in reference coordinates are related to the earth-fixed components by

$$\begin{bmatrix} \xi_e \\ \xi_n \\ \xi_u \end{bmatrix} = C \begin{bmatrix} \xi_{xe} \\ \xi_{ye} \\ \xi_{ze} \end{bmatrix} \tag{31}$$

where C is the direction cosine matrix relating the two coordinate systems. The matrix C will be referred to as the position direction cosine matrix since it uniquely specifies the vehicle's position over the surface of the earth as well as the azimuth reference direction.

The propagation of the C matrix may be found in exactly the same way that the B matrix was derived. Differentiating (31)

$$\begin{bmatrix} \dot{\xi}_e \\ \dot{\xi}_n \\ \dot{\xi}_u \end{bmatrix} = C \begin{bmatrix} \dot{\xi}_{xe} \\ \dot{\xi}_{ye} \\ \dot{\xi}_{ze} \end{bmatrix} + \dot{C} \begin{bmatrix} \xi_{xe} \\ \xi_{ye} \\ \xi_{ze} \end{bmatrix} \tag{32}$$

From classical vector calculus, however,

$$\left[\frac{d\underline{\xi}}{dt}\right]_e = \left[\frac{d\underline{\xi}}{dr}\right]_r + \underline{\rho} \times \underline{\xi} \tag{33}$$

where $\underline{\rho}$ is the vector angular rate of the reference axes with respect to the earth and where $\left[\frac{d}{dt}\right]_e$ and $\left[\frac{d}{dt}\right]_r$ indicate differentiation with respect to the e and r sets, respectively. Rewriting (33) into vector-matrix form in reference coordinates.

$$C \begin{bmatrix} \dot{\xi}_{xe} \\ \dot{\xi}_{ye} \\ \dot{\xi}_{ze} \end{bmatrix} = \begin{bmatrix} \dot{\xi}_e \\ \dot{\xi}_n \\ \dot{\xi}_u \end{bmatrix} + \begin{bmatrix} 0 & -\rho_u & \rho_n \\ \rho_u & 0 & -\rho_e \\ -\rho_n & \rho_e & 0 \end{bmatrix} \begin{bmatrix} \xi_e \\ \xi_n \\ \xi_u \end{bmatrix} = \begin{bmatrix} \dot{\xi}_e \\ \dot{\xi}_n \\ \dot{\xi}_u \end{bmatrix} - P \begin{bmatrix} \xi_e \\ \xi_n \\ \xi_u \end{bmatrix} \tag{34}$$

where P is the position rate matrix

$$P = \begin{bmatrix} 0 & \rho_u & -\rho_n \\ -\rho_u & 0 & \rho_e \\ \rho_n & -\rho_e & 0 \end{bmatrix} \tag{35}$$

Substituting (32) into (34)

$$C \begin{bmatrix} \dot{\xi}_{xe} \\ \dot{\xi}_{ye} \\ \dot{\xi}_{ze} \end{bmatrix} = C \begin{bmatrix} \dot{\xi}_{xe} \\ \dot{\xi}_{ye} \\ \dot{\xi}_{ze} \end{bmatrix} + \dot{C} \begin{bmatrix} \xi_{xe} \\ \xi_{ye} \\ \xi_{ze} \end{bmatrix} - P \begin{bmatrix} \xi_e \\ \xi_n \\ \xi_u \end{bmatrix} \tag{36}$$

and, using (31) and simplifying,

$$(\dot{C} - PC) \begin{bmatrix} \xi_e \\ \xi_n \\ \xi_u \end{bmatrix} = \begin{bmatrix} 0 \\ 0 \\ 0 \end{bmatrix} \tag{37}$$

Then, since $\underline{\xi}$ was arbitrary, (37) implies that

$$\dot{C} = PC \tag{38}$$

Equation (38) is the fundamental matrix-matrix position differential equation which must be solved by the computer in a direction cosine position mechanization. The initial condition for (38) is determined by the system's known initial position and the (arbitrary) choice of azimuth reference direction, as described in a later section.

Position Equations - Euler Angles. - Position and azimuth reference direction ("grid north") may be specified by the Euler angles

λ = east longitude of vehicle's present position

ϕ = geodetic latitude of vehicle's present position

α = angle between azimuth reference direction and true north.

These angles are shown in Figure 18.

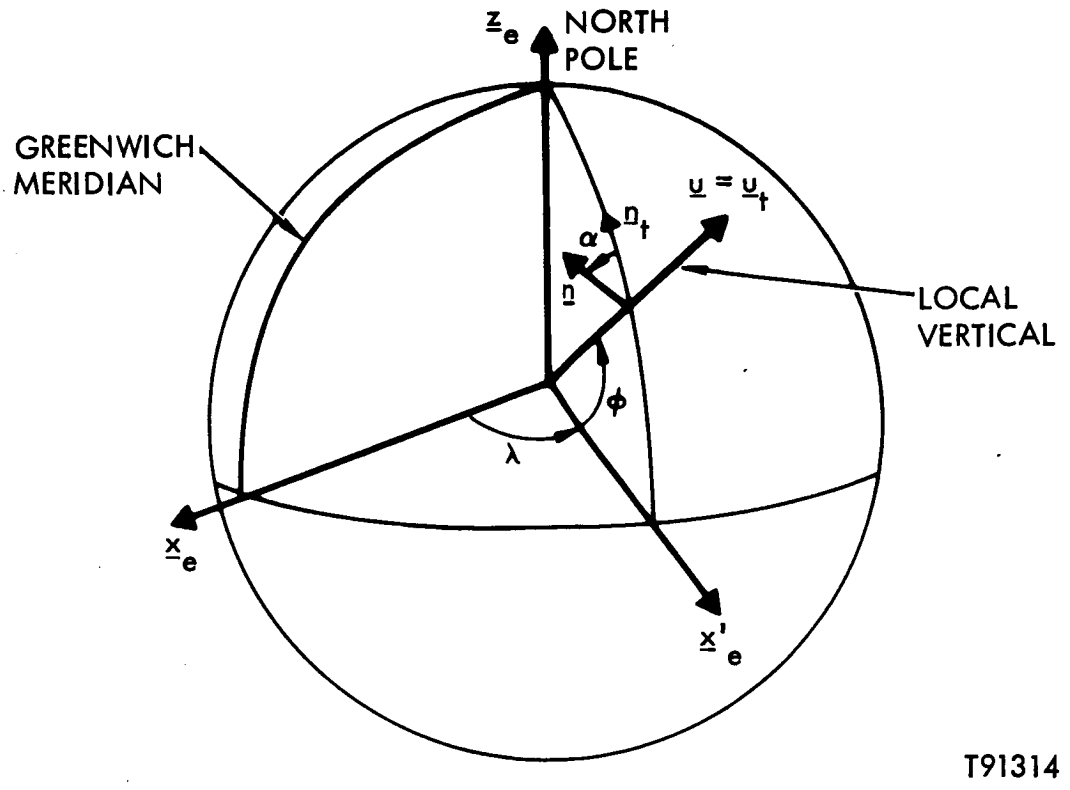

Figure 18. Position Euler Angles

It is seen from Figure 3 that the reference set may be obtained from the earth-fixed set by a positive rotation λ about z_e followed by a positive rotation $(90^\circ - \phi)$ about the rotated y_e ($\underline{y}'e$) axis and finally through the angle $(90^\circ + \alpha)$ about the $\underline{u}$ axis. Thus if $\underline{\xi}$ is any vector

$$\begin{bmatrix} \xi_e \\ \xi_n \\ \xi_u \end{bmatrix} = \begin{bmatrix} -\sin\alpha & \cos\alpha & 0 \\ -\cos\alpha & -\sin\alpha & 0 \\ 0 & 0 & 1 \end{bmatrix} \begin{bmatrix} \sin\phi & 0 & -\cos\phi \\ 0 & 1 & 0 \\ \cos\phi & 0 & \sin\phi \end{bmatrix} \begin{bmatrix} \cos\lambda & \sin\lambda & 0 \\ -\sin\lambda & \cos\lambda & 0 \\ 0 & 0 & 1 \end{bmatrix} \begin{bmatrix} \xi_{xe} \\ \xi_{ye} \\ \xi_{ze} \end{bmatrix}$$

$$= \begin{bmatrix} -\sin\alpha\sin\phi\cos\lambda - \cos\alpha\sin\lambda & -\sin\alpha\sin\phi\sin\lambda + \cos\alpha\cos\lambda & \sin\alpha\cos\phi \\ -\cos\alpha\sin\phi\cos\lambda + \sin\alpha\sin\lambda & -\cos\alpha\sin\phi\sin\lambda - \sin\alpha\cos\lambda & \cos\alpha\cos\phi \\ \cos\phi\cos\lambda & \cos\phi\sin\lambda & \sin\phi \end{bmatrix} \begin{bmatrix} \xi_{xe} \\ \xi_{ye} \\ \xi_{ze} \end{bmatrix} \qquad (39)$$

The matrix in (39) is seen from (31) to be the position direction cosine matrix C expressed in terms of the position Euler angles.

The position rate vector $\underline{\rho}$ may be expressed in terms of the rates of change of the position Euler angles as

$$\underline{\rho} = \dot{\underline{\alpha}} - \dot{\phi}\underline{y}'_e + \dot{\lambda}\underline{z}_e$$

$$= \begin{bmatrix} 0 \\ 0 \\ \dot{\lambda} \end{bmatrix} + \begin{bmatrix} -\sin\alpha & \cos\alpha & 0 \\ -\cos\alpha & -\sin\alpha & 0 \\ 0 & 0 & 1 \end{bmatrix} \begin{bmatrix} 0 \\ -\dot{\phi} \\ 0 \end{bmatrix} + \begin{bmatrix} \cos\alpha & \sin\alpha & 0 \\ -\sin\alpha & \cos\alpha & 0 \\ 0 & 0 & 1 \end{bmatrix}$$

$$\begin{bmatrix} \sin\phi & 0 & -\cos\phi \\ 0 & 1 & 0 \\ \cos\phi & 0 & \sin\phi \end{bmatrix} \begin{bmatrix} 0 \\ 0 \\ \dot{\lambda} \end{bmatrix} = \begin{bmatrix} -\dot{\phi}\cos\alpha + \dot{\lambda}\cos\phi\sin\alpha \\ \dot{\phi}\sin\alpha + \dot{\lambda}\cos\phi\cos\alpha \\ \dot{\alpha} + \dot{\lambda}\sin\phi \end{bmatrix} \tag{40}$$

from which it is found that

$$\begin{aligned} \dot{\lambda} &= (\rho_e \sin\alpha + \rho_n \cos\alpha)\sec\phi \\ \dot{\phi} &= (-\rho_e \cos\alpha + \rho_n \sin\alpha) \\ \dot{\alpha} &= \rho_u - \dot{\lambda}\sin\phi \\ &= \rho_u - (\rho_e \sin\alpha + \rho_n \cos\alpha)\tan\phi \end{aligned} \tag{41}$$

Equations (41) are the general form of the position differential equations which must be solved by the computer in an Euler angle mechanization. The initial conditions for (41) are provided by knowledge of the vehicle's initial position and by the choice of an initial value for the angle α.

Position Equations - Quaternions. - Let $\underline{\xi}$ be any vector. The components of $\underline{\xi}$ in the reference coordinate set are related to the earth-fixed coordinates by

$$\underline{\xi}^r = c^* \underline{\xi}^e c \tag{42}$$

where c is the "position" quaternion relating the two coordinate systems. Differentiating (42) with respect to time

$$\dot{\underline{\xi}}^r = \dot{c}^* \underline{\xi}^e c + c^* \dot{\underline{\xi}}^e c + c^* \underline{\xi}^{e\cdot} c \tag{43}$$

Using (4) and observing that $C\underline{\xi}^e = c^*\underline{\xi}^e c$ it is seen that

$$c^*\dot{\underline{\xi}}^e c = \dot{\underline{\xi}}^r + \rho^r \underline{\xi}^r \tag{44}$$

where $\rho^r = 0 + \underline{\rho}^r$ is the position rate quaternion. Substituting (13) into (14) and using the identity $\underline{\xi}^e = c\underline{\xi}^r c^*$

$$\begin{aligned} \underline{0} &= \dot{c}^*\underline{\xi}^e c + c^*\underline{\xi}^e \dot{c} - \rho^r \underline{\xi}^r \\ &= \dot{c}^* c\underline{\xi}^r + \underline{\xi}^r c^*\dot{c} - \rho^r \underline{\xi}^r \end{aligned} \tag{45}$$

Letting $c = c_0 + \underline{c}$ and carrying out the indicated quaternion multiplications

$$\begin{aligned} \dot{c}^*c &= (\dot{c}_0 c_0 + \dot{\underline{c}} \cdot \underline{c}) + (\dot{c}_0 \underline{c} - c_0 \dot{\underline{c}} - \dot{\underline{c}} \times \underline{c}) \\ &\triangleq \gamma_0 + \underline{\gamma} \end{aligned} \tag{46}$$

$$c^*\dot{c} = \gamma_0 - \underline{\gamma}$$

so that, by analogy with (25),

$$\begin{aligned} \gamma_0 &= \dot{c}_0 c_0 + \dot{\underline{c}} \cdot \underline{c} \\ &\equiv 0 \end{aligned} \tag{47}$$

Substituting (47) into (45) and solving for the vector part

$$\underline{0} = \underline{\gamma} \times \underline{\xi} - \underline{\xi} \times \underline{\gamma} - \underline{\rho} \times \underline{\xi} \tag{48}$$

or

$$2\,\underline{\gamma} \times \underline{\xi} = \underline{\rho} \times \underline{\xi} \tag{49}$$

which, since $\underline{\xi}$ was arbitrary, implies that

$$\underline{\gamma} = 1/2\ \underline{\rho} \tag{50}$$

Rewriting (47) and (49), using (46),

$$c^*\dot{c} = 1/2\ (0 + \underline{\rho}) \tag{51}$$

and, premultiplying by c,

$$\dot{c} = 1/2\ c\rho^r \tag{52}$$

where $\rho = 0 + \underline{\rho}$.

Equation (52) is the fundamental position differential equation which must be solved if the position equations are mechanized in quaternions. The initial condition for (52) is determined by the initial position of the vehicle and the choice of an initial value for the azimuth reference direction.

Position Rate Equations. - Regardless of the type of the position representation which is employed (i. e., quaternions, direction cosines, or Euler angles), the computation of position requires knowledge of the position rate vector $\underline{\rho}$. Two components of this vector may be computed from the level components of vehicle velocity, as described below. The third component depends upon the choice of aximuth reference. This is described in a later section.

Let $\underline{r}$ be the radius vector from the center of the earth to the vehicle's present position. Assuming the shape of the earth to be an oblate spheroid

$$\underline{r} = (\nu + h)\,\underline{u} - (e^2 \nu \sin\phi)\cdot\underline{z}_e \tag{53}$$

where $\nu = a\,[1-e^2\sin^2\phi]^{-1/2}$

$\simeq a\,(1 + f\sin^2\phi + \ldots\ldots)$

= Radius of curvature of the spheroid normal to the meridian

$e = \sqrt{2f - f^2}$

= Eccentricity of the spheroid (0.082 for the International Spheroid)

f = Flattening (ellipticity) of the spheroid (1/297.00) for the International Spheroid)

a = Equitorial radius of the earth (20, 926, 488 feet for the International Spheroid)

h = Altitude above the spheroid

Rewriting (53)

$$\begin{bmatrix} r_e \\ r_n \\ r_u \end{bmatrix} = \begin{bmatrix} 0 \\ 0 \\ \nu+h \end{bmatrix} - C \begin{bmatrix} 0 \\ 0 \\ e^2 \nu \sin\phi \end{bmatrix} \tag{54}$$

Neglecting powers of f greater than the first and observing that $\sin\phi = c_{33}$

$$\begin{bmatrix} r_e \\ r_n \\ r_u \end{bmatrix} = \begin{bmatrix} -2afc_{13}c_{33} \\ -2afc_{23}c_{33} \\ a(1-fc_{33}^2)+h \end{bmatrix} \tag{55}$$

Differentiating with respect to time

$$\begin{bmatrix} \dot{r}_e \\ \dot{r}_n \\ \dot{r}_u \end{bmatrix} = \begin{bmatrix} -2af(c_{13}\dot{c}_{33} + \dot{c}_{13}c_{33}) \\ -2af(c_{23}\dot{c}_{33} + \dot{c}_{23}c_{33}) \\ -2afc_{33}\dot{c}_{33} + \dot{h} \end{bmatrix} \tag{56}$$

while using (4) with $\underline{\xi}$ replaced by $\underline{r}$

$$C\begin{bmatrix} \dot{r}_{xe} \\ \dot{r}_{ye} \\ \dot{r}_{ze} \end{bmatrix} = \begin{bmatrix} \dot{r}_e \\ \dot{r}_n \\ \dot{r}_u \end{bmatrix} - P\begin{bmatrix} r_e \\ r_n \\ r_u \end{bmatrix}$$

$$= \begin{bmatrix} \dot{r}_e - \rho_u r_n + \rho_n r_u \\ \dot{r}_n - \rho_e r_u + \rho_u r_e \\ \dot{r}_u - \rho_n r_e + \rho_e r_n \end{bmatrix} \tag{57}$$

and since, by definition,

$$\underline{v} = \left[\frac{d\underline{r}}{dt}\right]_e \tag{58}$$

= velocity of the vehicle relative to the earth

the reference system velocity components are given by

$$\begin{bmatrix} v_e \\ v_n \\ v_u \end{bmatrix} = C\begin{bmatrix} \dot{r}_{xe} \\ \dot{r}_{ye} \\ \dot{r}_{ze} \end{bmatrix}$$

$$= \begin{bmatrix} -2afc_{13}\dot{c}_{33} + a\rho_n(1 + fc_{33}^2 + \frac{h}{a}) \\ -2afc_{23}\dot{c}_{33} - a\rho_e(1 + fc_{33}^2 + \frac{h}{a}) \\ \dot{h} \end{bmatrix} \tag{59}$$

which may be solved for ρ_e and ρ_n as

$$\rho_e = \frac{-v_n - 2afc_{23}\dot{c}_{33}}{a\left(1 + fc_{33}^2 + \frac{h}{a}\right)}$$

$$\simeq -\frac{v_n}{a}\left(1 - \frac{h}{a} - fc_{33}^2\right) - 2fc_{23}\dot{c}_{33} \qquad (60)$$

$$\rho_n \simeq \frac{v_e}{a}\left(1 - \frac{h}{a} - fc_{33}^2\right) + 2fc_{23}\dot{c}_{33}$$

as well as providing

$$\dot{h} = v_u \qquad (61)$$

The derivation of (60) and (61) has been performed in direction cosine notation. Clearly (61) is independent of the choice of position representation, while (60) may be transformed into quaternion notation as

$$\rho_e \simeq -\frac{v_n}{a}\left[1 - \frac{h}{a} - f(c_0^2 - c_1^2 - c_2^2 + c_3^2)^2\right] - 4f\,(c_2c_3 + c_1c_0)(c_0\dot{c}_0 - c_1\dot{c}_1 - c_2\dot{c}_2 + c_3\dot{c}_3)$$

$$\rho_n = \frac{v_e}{a}\left[1 - \frac{h}{a} - f\,(c_0^2 - c_1^2 - c_2^2 + c_3^2)^2\right] + 4f\,(c_1c_3 - c_0c_2)(c_0\dot{c}_0 - c_1\dot{c}_1 - c_2\dot{c}_2 + c_3\dot{c}_3) \qquad (62)$$

or, using (39), into Euler angle notation

$$\rho_e \simeq -\frac{v_n}{a}\left(1 - \frac{h}{a} - f\sin^2\phi + 2f\cos^2\phi\cos^2\alpha\right) - \left(2f\cos^2\phi\sin\alpha\cos\right)\frac{v_e}{a}$$

$$\rho_n \simeq \frac{v_e}{a}\left(1 - \frac{h}{a} - f\sin^2\phi + 2f\cos^2\phi\sin^2\alpha\right) + \left(2f\cos^2\phi\sin\alpha\cos\alpha\right)\frac{v_n}{a} \qquad (63)$$

The third rate component ρ_u is dependent upon the choice of azimuth reference direction as described in a later section.

Velocity Equations.

Let

$\underline{a}$ = vector whose components are sensed by the accelerometers

$\underline{\Omega}$ = vector inertial angular velocity of the earth

g_m = mass attraction vector of the earth

Then

$$\left[\frac{d\underline{r}}{dt}\right]_i = \underline{v} + \underline{\Omega} \times \underline{r} \tag{64}$$

= time derivative of $\underline{r}$ relative to an inertially fixed frame

$$\left[\frac{d^2\underline{r}}{dt^2}\right]_i = \left[\frac{d\underline{v}}{dt}\right]_r + (2\underline{\Omega} + \underline{\rho}) \times \underline{v} + \underline{\Omega} \times (\underline{\Omega} \times \underline{r}) \tag{65}$$

and using

$$\underline{a} = \left[\frac{d^2\underline{r}}{dt^2}\right]_i - \underline{g}_m \tag{66}$$

it is found that

$$\begin{aligned}\left[\frac{d\underline{v}}{dt}\right]_r &= \underline{a} - (2\underline{\Omega} \times \underline{\rho}) \times \underline{v} - \underline{\Omega} \times (\underline{\Omega} \times \underline{r}) + g_m \\ &= \underline{a} - (2\underline{\Omega} \times \underline{\rho}) \times \underline{v} - g\end{aligned} \tag{67}$$

where

$$\underline{g} = -g_m + \underline{\Omega} \times (\underline{\Omega} \times \underline{r}) \tag{68}$$

= Earth's gravity vector

$$g \simeq g_o \left(1 - 2\frac{h}{a} + \epsilon \sin^2 \phi\right) \tag{69}$$

g_0 = sea level gravity

= 32.172 ft/sec^2

ϵ = 0.00529

In vector-matrix form

$$\begin{bmatrix}\dot{v}_e \\ \dot{v}_n \\ \dot{v}_u\end{bmatrix} = \begin{bmatrix}a_e \\ a_n \\ a_u\end{bmatrix} + (2\Omega + P)\begin{bmatrix}v_e \\ v_n \\ v_u\end{bmatrix} - \begin{bmatrix}0 \\ 0 \\ g\end{bmatrix} \tag{70}$$

where Q is the earth rate matrix

$$Q \triangleq \begin{bmatrix} 0 & \Omega_u & -\Omega_n \\ -\Omega_u & 0 & \Omega_e \\ +\Omega_n & -\Omega_e & 0 \end{bmatrix} \tag{71}$$

Attitude Rate Equations. - From Figure 16 and the accompanying discussion it is clear that

$$\underline{\omega} = \underline{\Omega} + \underline{\rho} + \underline{\zeta} \tag{72}$$

i.e., the total inertial angular rate of the sensor package, as measured by the gyros, is the vector sum of the earth's inertial angular rate $\underline{\Omega}$, the rate $\underline{\rho}$ of the vehicle over the earth's surface, and the vehicle's attitude and heading rate $\underline{\zeta}$.

The vector $\underline{\zeta}$ is required for solution of the attitude equations. Since $\underline{\omega}$ is measured, $\underline{\Omega}$ is constant and known, and $\underline{\rho}$ may be computed from vehicle velocity, $\underline{\zeta}$ may be solved for (to within the accuracy imposed by measurement and computational errors) by

$$\underline{\zeta} = \underline{\omega} = \underline{\Omega} - \underline{\rho} \tag{73}$$

or

$$\begin{bmatrix} \zeta_x \\ \zeta_y \\ \zeta_z \end{bmatrix} = \begin{bmatrix} \omega_x \\ \omega_y \\ \omega_z \end{bmatrix} - B \begin{bmatrix} \rho_e + \Omega c_{13} \\ \rho_n + \Omega c_{23} \\ \rho_u + \Omega c_{33} \end{bmatrix} \tag{74DC}$$

$$= \begin{bmatrix} \omega_x \\ \omega_y \\ \omega_z \end{bmatrix} - b^* \left(\underline{\rho}^r + c^* \underline{\Omega}^e c\right) b \tag{74Q}$$

Acceleration Resolution. - The primary use of attitude information in performing the navigation function, as opposed to the flight control function, is the resolution of measured acceleration components into computational coordinates. This resolution is straight-forward if the attitude computations are mechanized in direction cosines. From (1) it is seen that

$$\begin{bmatrix} a_x \\ a_y \\ a_z \end{bmatrix} = B \begin{bmatrix} a_e \\ a_n \\ a_u \end{bmatrix} \tag{75}$$

so that

$$\begin{bmatrix} a_e \\ a_n \\ a_u \end{bmatrix} = B^{-1} \begin{bmatrix} a_x \\ a_y \\ a_z \end{bmatrix} = B^T \begin{bmatrix} a_x \\ a_y \\ a_z \end{bmatrix} \tag{76}$$

where the latter equality follows from the orthonormality of direction cosine matrices.

If an Euler angle mechanization is used, the direction cosine matrix may be constructed directly from the Euler angles, or their sines and cosines, by using (12). Having this determined the B matrix, the relation (75) may be used to perform the resolution.

The resolution of acceleration in the case in which attitude is maintained as a quaternion is less obvious. From (17)

$$\underline{a}^p = b^* \underline{a}^r b \tag{77}$$

Premultiplying by b and postmultiplying by b*

$$\begin{aligned} \underline{a}^r &= b\underline{a}^p b^* \\ &= (b_0 + \underline{b})\, \underline{a}^p (b_0 - \underline{b}) \\ &= (b_0 + \underline{b}) [-\underline{a}^p \cdot (-\underline{b}) + b_0 \underline{a}^p - (\underline{a}^p \times \underline{b})] \\ &= [(b_0)\, (\underline{a}^p \cdot \underline{b}) - \underline{b} \cdot (b_0 \underline{a}^p - \underline{a}^p \times \underline{b})] \\ &\quad + [b_0\, (b_0 \underline{a}^p - \underline{a}^p \times \underline{b}) + (\underline{a}^p \cdot \underline{b})\, \underline{b} + \underline{b} \times (b_0 \underline{a}^p - \underline{a}^p \times \underline{b})] \end{aligned} \tag{78}$$

Using the vector identities

$$\underline{\alpha} \cdot (\underline{\beta} \times \underline{\alpha}) = 0 \tag{79}$$

$$(\underline{\alpha} \cdot \underline{\beta})\, \underline{\alpha} = \underline{\alpha}^2 \beta + \underline{\alpha} \times (\underline{\alpha} \times \underline{\beta}) \tag{80}$$

equation (78) may be rewritten as

$$\begin{aligned}\underline{a}^r &= 0 + (b_0^2 + \underline{b}^2)\,\underline{a}^p + 2\underline{b} \times (\underline{b} \times \underline{a}^p) + 2b_0\,(\underline{b} \times \underline{a}^p) \\ &= \underline{a}^p + 2\underline{b} \times (\underline{b} \times \underline{a}^p) + 2b_0\,(\underline{b} \times \underline{a}^p)\end{aligned} \tag{81}$$

where the latter equality follows from the quaternion identity

$$b_0^2 + b_1^2 + b_2^2 + b_3^2 = 1 \tag{82}$$

rewriting (81) in component form

$$\begin{aligned}a_e &= a_x + 2\left[(b_1b_2a_y + b_1b_3a_z - (b_2^2 + b_3^2)a_x\right] + 2b_0\left[b_2a_z - b_3a_y\right] \\ &= a_x(1 - 2b_2^2 - 2b_3^2) + a_y(2b_1b_2 - 2b_0b_3) + a_z(2b_1b_3 + 2b_0b_2) \\ &= (b_0^2 + b_1^2 - b_2^2 - b_3^2)\,a_x + 2(b_1b_2 - b_0b_3)\,a_y + 2(b_1b_3 + b_0b_2)\,a_z\end{aligned} \tag{83}$$

$$a_n = 2(b_1b_2 + b_0b_3)\,a_x + (b_0^2 - b_1^2 + b_2^2 - b_3^2)\,a_y + 2(b_2b_3 - b_0b_1)a_z \tag{84}$$

$$a_u = 2(b_1b_3 - b_0b_2)a_x + 2(b_2b_3 + b_0b_1)a_y + (b_o^2 - b_1^2 - b_2^2 + b_3^2)a_z \tag{85}$$

Equations (83) through (85) are the equations which are required for acceleration resolution in a quaternion attitude mechanization. These equations may be compared to (75) to obtain the relation between direction cosines and the quaternion elements:

$$B^T = \begin{bmatrix} (b_0^2+b_1^2-b_2^2-b_3^2) & 2(b_1b_2 - b_0b_3) & 2(b_1b_3 + b_0b_2) \\ 2(b_1b_2+b_0b_3) & (b_0^2-b_1^2+b_2^2-b_3^2) & 2(b_2b_3 - b_0b_1) \\ 2(b_1b_3-b_0b_2) & 2(b_2b_3+b_0b_1) & (b_0^2-b_1^2-b_2^2+b_3^2) \end{bmatrix} \tag{86}$$

It should be noted that is is not necessary to mechanize the vertical velocity-position equations in an inertial navigator. The vertical channel is inherently unstable and thus must be damped using external (e.g., barometric) information if it is mechanized. Such a mechanization is discussed further in a later section. If the vertical channel is not mechanized it is not necessary to compute (85) in a quaternion mechanization or to compute the third row of the matrix B in a Euler angle mechanization.

It is usually desirable to perform the attitude equations at a higher rate than the navigation computations since the latter vary at a much slower rate. In such cases the acceleration (or delta velocity) components may simply be accumulated between navigation updates, i. e.,

$$\underline{\Delta v}^{r} = \tau \sum_{i=1}^{m} B\,(t + i\tau)\,\underline{a}^{p}\,(t + i\tau) \tag{87}$$

where m is the number of attitude updates per navigation update.

In cases where the ratio m is large, it has been suggested [1] that the accumulation be performed in body coordinates according to

$$\underline{\Delta v}^{b}\,(t + \tau) = \tau \underline{a}^{b}\,(t) + \tau \begin{bmatrix} 0 & \omega_z & -\omega_y \\ -\omega_z & 0 & \omega_x \\ \omega_y & -\omega_x & 0 \end{bmatrix} \underline{\Delta v}^{b}\,(t) \tag{88}$$

which is accurate to within small angle approximations in $\tau\underline{\omega}$. Since $\underline{\Delta v}$ is then always available in current body coordinates at time $t + i\tau$, the resolution need only be performed once per navigation update cycle.

$$\underline{\Delta v}^{r}\,(t + m\tau) = B\,(t + m\tau)\,\underline{\Delta v}^{b}\,(t + m\tau) \tag{89}$$

The additional operations in (88) are more than outweighed by the computational savings attributed to the need for only a single resolution (89) instead of (87) if m is large.

Vertical Channel. - It is well known that the "Schuler Tuning" implicit in (60) assures that the level axis position and velocity errors resulting from accelerometer bias errors remain bounded. This effect does not carry over to the vertical channel, however: if the value of g in (70) is computed from (69), the attitude error resulting from accelerometer bias increases hyperbolically with time. If g is assumed constant, altitude and altitude rate are computed open-loop and thus increase with the square of time. In either case, the performance is unacceptable for most applications. For example, in one hour, a 10^{-4} g bias would integrate into an altitude error of

$$\delta h = (10^{-4} g)\,(32.2 \text{ ft/sec}^2/g)\,(1/2)\,(3600 \text{ sec})^2 \tag{90}$$

$$= 20,866 \text{ feet}$$

The instability of the vertical channel requires that it be damped by some external source of altitude or altitude rate information if it is to be mechanized. Typically, a barometric altimeter is employed. In such a case the short-term vertical loop performance is determined by the inertial instruments while the long term accuracy is bounded by the altimeter accuracy. Typical mechanization equations are

$$\begin{aligned} \dot{v}_u &= a_u - k_v (h - h_b) \\ \dot{h} &= v_u - k (h - h_b) \end{aligned} \tag{91}$$

Specification of Azimuth Reference. - The attitude and position equations presented in the preceding sections possess one degree of freedom, the azimuth reference direction. The choice of this reference, i.e., the specification of the "wander" angle $\alpha(t)$, can significantly affect the system design and operation.

Perhaps the most obvious choice for the angle α is

$$\alpha(t) \equiv 0 \tag{92}$$

so that the azimuth reference is true north. In this case the position equations become particularly simple. Specifically, the Euler angle equations (41) become

$$\begin{aligned} \dot{\lambda} &= \rho_n \sec\phi \\ \dot{\phi} &= -\rho_e \\ \dot{\alpha} &= 0 \end{aligned} \tag{93}$$

(The latter equation obviously does not need to be computed in this case.) The direction cosine position mechanization is also simplified - the C matrix in (39) reduces to

$$C = \begin{bmatrix} -\sin\lambda & \cos\lambda & 0 \\ -\sin\phi\cos\lambda & -\sin\phi\sin\lambda & \cos\phi \\ \cos\phi\cos\lambda & \cos\phi\sin\lambda & \sin\phi \end{bmatrix} \tag{94}$$

and only the first (or second) column of (95) must be computed in order to specify position. The resulting differential equation is

$$\begin{bmatrix} \dot{c}_{11} \\ \dot{c}_{21} \\ \dot{c}_{31} \end{bmatrix} = P \begin{bmatrix} c_{11} \\ c_{21} \\ c_{31} \end{bmatrix} \tag{95}$$

Thus the original matrix-matrix equation has been reduced to a vector-matrix equation.

The major difficulty encountered in a "true North" mechanization results when the vehicle approaches the earth's geographic poles. From (93) it is seen that the longitude rate $\dot{\lambda}$ increases without bound as the latitude ϕ approaches $\pm 90^{\circ}$. In such case the computer cannot "keep up" and the position reference is lost. An analogous situation occurs in a direction cosine or quaternion mechanization, since from (41), the rate component ρ_u is

$$\begin{aligned} \rho_u &= \rho_n \tan\phi \\ &= \dot{\lambda} \sin\phi \end{aligned} \tag{96}$$

and also becomes arbitrarily large as $\phi \rightarrow 90^{\circ}$.

The most common alternative to a true north mechanization, the "wander azimuth" mechanization, obviates the pole problem. In this case α is specified by requiring that

$$\rho_u \equiv 0 \tag{97}$$

so that, from (41)

$$\dot{\alpha} = -(\rho_e \sin\alpha + \rho_n \cos\alpha) \tan\phi \tag{98}$$

In this case all three components of $\underline{\rho}$ are always finite and the C matrix or c quaternion may be computed without difficulty.

Many other reasonable approaches have been devised and mechanized. There appears to be no substatial benefit in their use for the present application, however, thus they will not be considered further.

Approximations. - The basic accuracy requirement for the present application is 3 nautical miles per hour. This relatively large allowable error permits certain simplifications to be made in the equations which have been derived in the preceding sections.

Consider the position angular rate equations (63). If the vehicle velocity $|\underline{v}|$ is assumed to be limited by

$$|\underline{v}| \leq 200 \text{ ft/sec} \tag{99}$$

and the altitude h limited by

$$h \leq 20,000 \text{ feet} \tag{100}$$

the terms

$$\begin{aligned} &(1 - \frac{h}{a} - f\sin^2\phi + 2f\cos^2\phi\cos^2\alpha) \\ &(1 - \frac{h}{a} - f\sin^2\phi + 2f\cos^2\phi\sin^2\alpha) \end{aligned} \tag{101}$$

are limited to values between $(1 - \frac{h}{a} - f)$ and $(1 - \frac{h}{a} + 2f)$. Thus if the terms in f are neglected in (101) the maximum error in ρ_e or ρ_n will be

$$\begin{aligned} \delta\rho &= (\frac{2\theta 0 \text{ ft/sec}}{a})\ (2f) \\ &\simeq .014^\circ/\text{hr} \end{aligned} \tag{102}$$

which will produce a maximum position error (see error analysis section) of about 0.18 n. mi.

If the term $\frac{h}{a}$ in (101) is neglected, the maximum error in ρ_e is

$$\begin{aligned} \delta\rho &= (\frac{200}{a})\ (\frac{h}{a}) \\ &\simeq .002^\circ/\text{hr} \end{aligned} \tag{103}$$

which produces a maximum position error of about 0.03 n. mi. at 20,000 ft. altitude, and zero error at sea level.

Finally consider the cross-coupling terms of (63), i.e.,

$$\begin{aligned} &(2f\cos^2\phi\sin\alpha\cos\alpha)\ \frac{v_e}{a} \\ &(2f\cos^2\phi\sin\alpha\cos\alpha)\ \frac{v_n}{a} \end{aligned} \tag{104}$$

The maximum value of these terms is f so that the maximum error in ρ_e

$$\begin{aligned} \delta\rho &= (\frac{200}{a})\ (f) \\ &\simeq .007^\circ/\text{hr} \end{aligned} \tag{105}$$

which causes a maximum position error of about 0.09 n. mi.

All of the above errors are very small compared to the 3 n. mi./hr requirement. Thus (60), (62), or (63) may be approximated by

$$\rho_e \simeq -\frac{v_n}{a}$$
$$\rho_n \simeq \frac{v_e}{a} \tag{106}$$

Finally consider the terms proportional to v_u in (70). The errors resulting from neglecting these terms are

$$\delta\dot{v}_e = -(2\Omega_n + \rho_n)\, v_u$$
$$\delta\dot{v}_n = \rho_e v_u \tag{107}$$

Assuming that altitude changes occur during periods which are short compared to the Schuler period (about 84 minutes) these errors may be considered to be impulsive and hence to cause errors

$$\delta v_e = -2\,(\Omega_n + \rho_n)\Delta h$$
$$\delta v_n = \rho_e \Delta h \tag{108}$$

where Δh is the altitude change. For assumed worst case conditions of $(2\Omega_n + \rho_n) = 32^\circ/\text{hr}$ and $\Delta h = 10000$ ft. The maximum error is

$$(\delta\rho)_{max} = \frac{(\delta v_e)_{max}}{a}$$
$$= \frac{(32^\circ/\text{hr})\,(10^4\,\text{ft})}{(2.1 \times 10^7)\,\text{ft}} \tag{109}$$
$$= .015^\circ/\text{hr}$$

which produces a maximum position error of about 0.2 n. mi.

Attitude Extraction. - If the attitude equations are mechanized in Euler angles, pitch (θ) and roll (φ) information is available directly, while true heading (ψ_T) is found from

$$\psi_T = \psi_G + \alpha \tag{110}$$

where α is the "wander angle" used in the position equations. If direction cosines or quaternions are used in the representation of attitude, however, the attitude and heading angles are somewhat more difficult to obtain. (These angles are not required by the inertial navigator but are usually desired for display and flight control purposes.)

The angles θ, φ, and ψ_G may be obtained from inverse trigonometric operations on the direction cosine elements. (The direction cosines are available even in a quaternion mechanization since they are needed for resolution of the acceleration measurements into reference coordinates). From (12) it is seen that

$$\begin{aligned} \theta &= \sin^{-1}(b_{23}) \\ \varphi &= \tan^{-1}\left(\frac{-b_{13}}{+b_{23}}\right) \\ \psi_G &= \tan^{-1}\left(\frac{-b_{21}}{+b_{22}}\right) \end{aligned} \tag{111}$$

True heading (ψ_T) may then be obtained from (111) and knowledge of the angle α. (For a true north mechanization $\alpha \equiv 0$ and $\psi_T = \psi_G$).

Position Extraction. - If the Euler Angle representation is chosen for position the latitude angle (ϕ), longitude angle (λ) and wander angle (α) are available. If quaternions or direction cosines are used to represent position these angles must be extracted from the direction cosine or quaternion elements. From (39) it is seen that

$$\begin{aligned} \phi &= \sin^{-1}(c_{33}) \\ \lambda &= \tan^{-1}\left(\frac{+c_{32}}{+c_{31}}\right) \\ \alpha &= \tan^{-1}\left(\frac{+c_{13}}{+c_{23}}\right) \end{aligned} \tag{112}$$

If direction cosines are used these elements are available directly. If quaternion are used there may be found from

$$\begin{aligned} c_{33} &= c_0^2 - c_1^2 - c_2^2 + c_3^2 \\ c_{13} &= 2(c_1c_3 - c_0c_2) \\ c_{31} &= 2(c_1c_3 + c_0c_2) \end{aligned} \tag{113}$$

$$c_{23} = 2\,(c_2c_3 + c_0c_1)$$

$$c_{32} = 2\,(c_2c_3 - c_0c_1) \qquad (113)$$

Integration Algorithms. - The preceding equations include three sets of differential equations which must be solved in the navigation computer; the altitude equations, the velocity equations, and the position equations. Since these equations are to be solved digitally they cannot be solved exactly and the choice of approximations which are to be utilized, i. e., the integration algorithms, become key design parameters. This is particularly true of the attitude equations, whose parameters are rapidly changing compared to the navigation parameters: $|\underline{\zeta}|$ may be of the order of 250^{o}/sec while $|\underline{\rho} + \underline{\Omega}|$ is at most 17^{o}/hr.

A number of algorithms for the critical attitude integration have been proposed and investigated [1, 2, 3, 4, 5] for both quaternion and direction cosine representations of attitude. The analyses and conclusions of this literature have been investigated and extended during the course of the present study. The computer simulation described in a later section has been used to test the veracity of the analytic conclusions.

Two basic types of algorithm have been selected as representatives of the general class: an exponential expansion or "Transition Matrix" approach and a Runge-Kutta numerical integration approach. The former is a one-pass technique in which the order of approximation is governed by the number of terms which are included. The latter is essentially iterative in nature with the order determined by the number of iterations.

Both techniques are designed to approximate the Taylor Series expansion of the quaternion (or direction cosine matrix) given by

$$b\,(t + \tau) = b(t) + \tau\dot{b}(t) + 1/2\tau^{2}\ddot{b}(t) + 1/6\tau^{3}\dddot{b}(t) + \ldots$$

where t is the time of the preceding iteration and τ is the iteration interval. The value of the exponent of τ in the truncated expansion is the order of the algorithm.

The exponential expansion technique considers the analytic solution of the quaternion (or direction cosine) differential equation. In matrix form this equation is of the form

$$\begin{aligned}\dot{b}(t) &= M\,(\underline{\zeta}^{p}(t))\,b(t) \\ &= [M\,(\omega^{p}(t)) - M\,(\underline{\rho}^{p}(t) + \underline{\Omega}^{p}(t))]\,b(t)\end{aligned} \qquad (114)$$

where

$$M(\xi) = 1/2 \begin{bmatrix} 0 & -\xi_1 & -\xi_2 & -\xi_3 \\ \xi_1 & 0 & \xi_3 & -\xi_2 \\ \xi_2 & -\xi_3 & 0 & \xi_1 \\ \xi_3 & \xi_2 & -\xi_1 & 0 \end{bmatrix}$$

Neglecting for the moment the (small) term in $(\underline{\rho} + \underline{\Omega})$, the solution is

$$b(t+\tau) = \left[\exp \int_t^{t+\tau} M(\underline{\omega}^p(\xi))\, d\xi \right] b(t)$$

$$= \left[I + \int_t^{t+\tau} M(\underline{\omega}^p(\xi))d\xi + 1/2 \left[\int_t^{t+\tau} M(\underline{\omega}^p(\xi))d\xi \right]^2 + \ldots \right] b(t) \qquad (116)$$

$$= \left[I + \tau M + 1/2\tau^2(M^2 + M^0) + 1/6\tau^3(M^3 + MM + 2MM + M) + \ldots \right] b(t)$$

The accumulated x-axis rate output of the A/D converter over the k conversions between t and t+τ is

$$\Delta\theta_x(t,\ t+\tau) = \sum_{i=1}^{k} \omega_x\left(t + \frac{i\tau}{k}\right)$$

$$\simeq \int_t^{t+\tau} \omega_x(\xi)\, d\xi$$

$$= \int_t^{t+\tau} \left[\omega_x(t) + (\tau - \xi)\,\omega_x(t) + 1/2\,(\tau - \xi)^2 \omega_x(t) + \ldots \right] d\xi$$

$$= \tau\omega_x(t) + 1/2\tau^2\omega_x(t) + 1/2\tau^3\omega_x(t) + \ldots$$

with similar expressions for y and z axes. The terms in M and its derivatives in (116) are then expressed, to within the desired order of τ, in terms of $\Delta\theta_x$, $\Delta\theta_y$, and $\Delta\theta_z$ to obtain the solution. For third and higher order algorithms it is

necessary to utilize previous values of $\underline{\Delta\theta}$ (i.e., $\underline{\Delta\theta}$ (t - τ, t), etc). A rigorous derivation of the exponential expansion approximations for orders through the third and for both quaternions and direction cosines is presented in reference [2] and, hence, will not be repeated here.

The Runge-Kutta technique is a standard method in numerical analysis. It consists essentially of obtaining an nth-order approximation by combining the results of a sequence of n first order approximations. Again neglecting the term in ($\underline{\rho} + \underline{\Omega}$) in (114), the algorithm computes sequentially

$$\Delta b_i = \tau M(\omega(t))\, b(t)$$

$$\Delta b_i = \tau M(\omega(t + \alpha_i \tau))\left[b(t) + \beta_i \Delta b_{i-1}\right] \quad i = 2, 3, \ldots, n \tag{118}$$

where α_i and β_i are constants less than unity and n is the order of the algorithm. The quaternion (or direction cosine matrix) is then updated according to

$$b(t + \tau) = b(t) + \sum_{i=1}^{n} \gamma_i \Delta b_i \tag{119}$$

where the γ_i are constants satisfying the equality

$$\sum_{i=1}^{n} \gamma_i = 1 \tag{120}$$

The values of ω are obtained from the A/D converter outputs. For third and higher-order algorithms it is necessary to sample the accumulated A/D outputs at intervals less than τ in order to maintain the required order of accuracy. This process has been termed rate extraction ((8)) and is described in a later section of this report.

The selection of the type and order of integration algorithm to be used primarily involves consideration of accuracy and of computer time and memory utilization. For higher order integrations the iterative nature of the Runge-Kutta approach tends to minimize the memory utilization. For lower order integrations this factor is less important and the exponential expansion technique appears preferable. The "break point" appears to be at third order, where there is no clear-cut advantage for either approach. With this in mind, the choice of algorithm type may be made by next considering accuracy.

Table 23 shows the errors attributed to the integration algorithm for various orders and for both quaternion and direction cosine representations for constant-rate slewing over one computer iteration interval τ, with $\underline{\Delta\theta}(\tau) = \underline{\omega}\tau$. The three types of errors shown are those commonly used in algorithm performance evaluation:

a) Drift errors represent the departure of the computer attitude from the true attitude and, hence, are the primary error of concern.

b) Length or scale errors represent the departure of the quaternion or direction cosine matrix from normality: The sum of the squares of the quaternion elements should equal unity, as should the sums of the squares of the elements of each now and column of the direction cosine matrix. The primary effect of such errors is to mis-scale the resolved acceleration measurements. The effects of such errors can be minimized, however, by re-normalizing the quaternion or matrix periodically.

c) Skew or non-orthogonality errors represent the departure of the rows (or columns) or the direction cosine matrix from mutual orthogonality. These errors may be minimized by periodic re-orthogonalization [3]. No equivalent errors are present in a quaternion mechanization.

The peak angular rates expected in the current application are of the order of 4 rad/sec. Thus, assuming computer iteration rates of 25 to 100 Hz, the maximum drift error per iteration for a second order direction cosine mechanization is between

$$\frac{\left[\left(4\ \frac{\text{rad}}{\text{sec}}\right)\left(\frac{1}{25}\text{sec}\right)\right]^3}{6} = 6.83 \times 10^{-4}\ \text{rad}$$

$$= 141\ \widehat{\text{sec}} \qquad (121)$$

and

$$\frac{\left[(4)\left(\frac{1}{100}\right)\right]^3}{6} = 1.07 \times 10^{-5}\ \text{rad}$$

$$= 2.2\ \widehat{\text{sec}} \qquad (122)$$

since the total computational error for the entire mission should be kept below 2 $\widehat{\text{sec}}$ it is clear that a second order scheme is unacceptable for the attitude computations in the present application.

Algorithm Order	Drift Errors		Skew Errors		Scale Errors	
	D. C.	Quat.	D. C.	Quat.	D. C.	Quat.
1	$\frac{-\Delta\theta_o}{3}\ i$	$\frac{-\Delta\theta_o^2}{12}$	$-\Delta_j\theta_k$	0	$1/2\ (\Delta\theta_j^2 + \Delta\theta_k^2)$	$1/4\Delta\theta_o^2$
2	$\frac{\Delta\theta_o^2}{6}\ i$	$\frac{\Delta\theta_o^2}{24}\ i$	$-\Delta\theta_o^2\ \Delta\theta_j\Delta\theta_k$	0	$\frac{\Delta\theta_o^2}{8}\ (\Delta\theta_j^2 + \Delta\theta_k^2)$	$1/64\Delta\theta_o^4$
3	$\frac{\Delta\theta_o^4}{30}\ i$	$\frac{\Delta\theta_o^4}{480}\ i$	$\frac{\Delta\theta_o^2}{12}\ \Delta\theta_j\Delta\theta_k$	0	$\frac{-\Delta\theta_o^2}{24}\ (\Delta\theta_j^2 + \Delta\theta_k^3)$	$-1/192\Delta\theta_o^4$
4	$\frac{-\Delta\theta_o^4}{120}$	$\frac{-\Delta\theta_o^4}{1920}\ i$	$\frac{\Delta\theta_o^4}{72}\ \Delta\theta_j\Delta\theta_k$	0	$\frac{-\Delta\theta_o^4}{144}\ (\Delta\theta_j^2 + \Delta\theta_k^3)$	$-1/4608\Delta\theta_o^4$

Table 23. Per Iteration Algorithm Truncation Errors

Similar calculations for a third order integration yield the following drift errors per iteration.

$$\frac{\left[(4)\ (\frac{1}{25})\right]^5}{30} = 3.50 \times 10^{-6} \text{ rad}$$
$$= .72 \widehat{\text{sec}} \tag{123}$$

$$\frac{\left[(4)\ (\frac{1}{100})\right]^5}{30} = 3.41 \times 10^{-9} \text{ rad}$$
$$= 7.04 \times 10^{-4} \widehat{\text{sec}} \tag{124}$$

Thus a third order integration at 100 Hz, together with a direction cosine representation, appears to be adequate from a maximum rate standpoint. Next consider the drift rate resulting from a sustained rate of 20^o/sec:

$$\delta\omega = \frac{1}{\tau}\Delta\theta$$
$$= \frac{1}{.01}\ \frac{\left[(\frac{20}{57.3})\ (0.1)\right]^5}{30} \tag{125}$$
$$= 1.73 \times 10^{-12} \text{ rad/sec}$$
$$= 3.6 \times 10^{-7o}/\text{hr}$$

which is clearly negligible compared to the sensor drift rates. Thus it appears that this scheme is satisfactory for the present application.

Next consider a quaternion representation with a fourth order algorithm and 30 Hz iteration rate. The maximum per iteration error is

$$\Delta\theta_{max} = \frac{\left[(4)\ (\frac{1}{30})\right]^5}{1920}$$
$$= 2.19 \times 10^{-8} \text{ rad} \tag{126}$$
$$= 4.53 \times 10^{-3} \widehat{\text{sec}}$$

which is satisfactory. For a sustained 20^{o}/sec rate the algorithm drift rate is

$$\delta\omega = \frac{1}{\tau}\,\Delta\theta$$

$$= \frac{1}{\left(\frac{1}{30}\right)} \frac{\left[\left(\frac{20}{57.3}\right)\left(\frac{1}{30}\right)\right]^{5}}{1920}$$

$$= 3.33 \times 10^{-12} \text{ rad/sec} \qquad (127)$$

$$= 6.87 \times 10^{-7o}/\text{hr}$$

which is also satisfactory. Thus the use of the more accurate quaternion representation and the increase of the integration algorithm order from 3 to 4 allows a threefold reduction in computer iteration frequency for equivalent accuracy.

In summary, then, the range of acceptable algorithms is fairly broad: within the range of reasonable computation frequencies, say less than 100 Hz, it is possible to utilize either quaternions or direction cosines and algorithm orders as low as three. Considering all major tradeoff factors (accuracy, computer time, and computer memory), however, the fourth order, Runge-Kutta, quaternion mechanization appears to be an optimum choice.

Returning now to the original quaternion differential equation (114)

$$\dot{b}(t) = M\left(\underline{\xi}^{p}(t)\right) b(t)$$

$$= M\left(\underline{\omega}^{p}(t) - \left(\underline{\rho}^{p}(t) + \underline{\Omega}^{p}(t)\right)\right) b(t) \qquad (128)$$

$$= M\left(\underline{\omega}^{p}(t)\right) b(t) - M\left(\underline{\rho}^{p}(t) + \underline{\Omega}^{p}(t)\right) b(t)$$

$$= M\left(\underline{\omega}^{p}(t)\right) b(t) - M^{+}\left(\underline{\rho}^{r}(t) + \underline{\Omega}^{r}(t)\right) b(t)$$

where

$$M^{+}\left(\underline{\xi}\right) = 1/2 \begin{bmatrix} 0 & -\xi_1 & -\xi_2 & -\xi_3 \\ \xi_1 & 0 & -\xi_3 & \xi_2 \\ \xi_2 & \xi_3 & 0 & -\xi_1 \\ \xi_3 & -\xi_2 & \xi_1 & 0 \end{bmatrix} \qquad (129)$$

Computing successive time derivatives of b(t)

$$\dot{b} = [M - M^+]\, b$$

$$\ddot{b} = (\dot{M} - \dot{M}^+]\, b + [M - M^+]^2 b \tag{130}$$

$$= (\dot{M} + M^2)\, b - (MM^+ + M^+M)\, b + (M^{+2} - \dot{M}^+)\, b$$

The term $1/2\tau^2 b$ thus includes, in addition to the term $(\dot{M} + M^2)b$ (corresponding to the terms examined in previous paragraphs), terms of the order $|\underline{\omega}^\rho||\underline{\rho}^r + \underline{\Omega}^r|$, $|\underline{\rho}^r + \underline{\Omega}^r|^2$, and $|\dot{\underline{\rho}}^r + \dot{\underline{\Omega}}^r|$. The maximum value of $|\underline{\omega}|$ is assumed to be 4 rad/sec. The maximum value of $|\underline{\rho}|$ is $|\underline{v}_{max}|/a$, where $\underline{v}_{max}$ is the maximum vehicle velocity. Assuming $|\underline{v}_{max}| = 200$ ft/sec, $|\underline{\rho}|_{max} = 2^o/hr$. The earth rate term is of constant magnitude $|\underline{\Omega}| \simeq 15^o/hr$. The value of $|\dot{\underline{\rho}}^r + \dot{\underline{\Omega}}^r|$ is reasonably assumed to be smaller than $|\underline{\rho}^r + \underline{\Omega}^r|$. Considering, then, the largest term

$$(|\underline{\omega}^\rho||\underline{\rho}^r + \underline{\Omega}^r|)_{max} \simeq (4\ \frac{rad}{sec})\ (17^o/hr)$$

$$= (4\ rad/sec)\ (8.25 \times 10^{-5}\ \frac{rad}{sec}) \tag{131}$$

$$= 3.3 \times 10^{-4}\ rad/sec^2$$

it is seen that omission of the final two terms in (129) will result in a maximum error of the order

$$(1/2)\ (\tau^2)\ (3.3 \times 10^{-4})\ rad \tag{132}$$

which for a 30 Hz computational frequency is about 2×10^{-7} rad. Hence the integration of (128) may be accomplished using a higher order (e.g., 4th order Runge-Kutta) algorithm for the first term and a simply, first order integration for the second term. The recommended algorithm is as follows

$$\begin{aligned}
\Delta b_0 &= -\tau M^+ (\underline{\rho}^r(t) + \underline{\Omega}^r(t))\, b(t) \\
b_1 &= b(t) \\
\Delta b_1 &= \tau M\, (\underline{\tilde{\omega}}^\rho(t))\, b_1 \\
b_2 &= b(t) + 1/2\, \Delta b_0 + 1/2 \Delta b_1 \\
\Delta b_2 &= \tau M\, (\underline{\tilde{\omega}}^\rho\, (t + 1/2\tau))\, b_2 \\
b_3 &= b(t) + 1/2 \Delta b_0 + 1/2 \Delta b_2
\end{aligned} \tag{133}$$

$$
\begin{aligned}
\Delta b_3 &= \tau M\left(\tilde{\omega}^{\rho}\left(t + 1/2\tau\right)\right) b_3 \\
b_4 &= b(t) + \Delta b_0 + \Delta b_3 \\
\Delta b_4 &= \tau M\left(\tilde{\omega}\left(t + \tau\right)\right) b_4 \\
b(t + \tau) &= b(t) + \Delta b_0 + 1/6\left[\Delta b_1 + 2\Delta b_2 + 2\Delta b_3 + \Delta b_4\right]
\end{aligned}
\tag{133}
$$

Turning now to the navigation computations, the basic differential equation for a direction cosine mechanization is, from (38)

$$
\dot{C} = PC \tag{134}
$$

The elements of P are the components of the position rate vector $\underline{\rho}^{r}$. As described previously, $\left|\underline{\rho}^{r}\right|_{max} \leq 2^{o}/hr$. The maximum angular acceleration may be estimated by assuming a high speed 180^{o} turn. Assuming a velocity of 100 ft/sec and a 10 second turn time, the rate of change of $\underline{\rho}$ is of the order

$$
\begin{aligned}
\left|\dot{\underline{\rho}}^{r}\right| &\simeq \left[\left(\frac{+100}{a}\right) - \left(\frac{-100}{a}\right)\right]/10 \text{ sec} \\
&\simeq (2^{o}/hr)/10 \text{ sec} \\
&= .2^{o}/hr/sec \\
&= 10^{-6} \text{ rad/sec}^{2}
\end{aligned}
\tag{135}
$$

From Table it is seen that, for a constant rate $|\underline{\rho}| = 2^{o}/hr$, the algorithm drift per iteration for a first order integration is of the order of

$$
\frac{\left[\left(10^{-5}\ \frac{rad}{sec}\right)\left(\frac{1}{10}\right)\right]^{3}}{3} = 3.3 \times 10^{-19} \text{ rad} \tag{136}
$$

for a 10 Hz iteration rate. The corresponding drift rate is 3.3×10^{-18} rad/sec or about $10^{-12^{o}}/hr$. Considering the second derivative term in the Taylor Series expansion for C, it is seen that the $\underline{\rho}$ term computed above would cause per iteration errors of the order

$$
\left(\frac{1}{2}\right)\left(10^{-6}\ \frac{rad}{sec}\right)\left(\frac{1}{10}\ sec\right)^{2} = 5 \times 10^{-9} \text{ rad} \tag{137}
$$

which corresponds to about 0.1 feet on the earth's surface. Since accelerations of this magnitude are of limited duration for the missions under consideration, it appears that a first order position integration at 10 Hz is acceptable for the present applications.

Rate Extraction. - The 3rd and 4th order Runge-Kutta algorithms require three rates for each iteration; $\underline{\omega}(t)$, $\underline{\omega}(t + 1/2\tau)$, and $\underline{\omega}(t + \tau)$, where t is the time of the preceeding iteration and τ is the iteration interval. The A/D convertor output, after accumulation over τ, is

$$\begin{aligned}\Delta\theta(t, t + \tau) &= \tau \sum_{i=1}^{\tau/\delta} \omega(t + i\delta) \\ &\simeq \int_{t}^{t+\tau} \omega(\xi)d\xi\end{aligned} \tag{138}$$

where δ is the time between successive A/D conversions. The approximation of the requisite rates can be readily accomplished by sampling the A/D output accumulation twice per iteration (at $t + 1/2\tau$ and $t + \tau$) and assuming that $\underline{\omega}$ is linear over the interval $(t, t + \tau)$. This process is termed (second order) rate extraction [5].

The term rate extraction is somewhat misleading since it implies that differentiation is performed. This is not the case. Although angular rates appear in the attitude differential equations (8), (16), and (30), the corresponding difference equations used to solve them digitally involve the rate $\underline{\omega}$ only in conjunction with the factor τ. As is described below, it is possible to express terms involving $\omega_i \tau$ (i = x, y, z) directly in terms of the accumulated A/D outputs.

Let the sum of the A/D conversions for the ith axis from t to $t + 1/2\tau$ be designated by $\Delta\theta_{i1}$ and the sum from t to $t + \tau$ be designated by $\Delta\theta_{i2}$. Let ω_i be the actual rate sensed by the gyro and approximate $\omega_i(t)$ as linear in time over $(t, t + \tau)$, i.e.,

$$\omega_i(t + \xi) = \alpha + \beta\xi \tag{139}$$

then

$$\begin{aligned}\Delta\theta_i(t, t + \xi) &= \int_{t}^{t+\xi} \omega_i(t + \beta)d\beta \\ &= \alpha\xi + 1/2\beta\xi^2\end{aligned} \tag{140}$$

where it is assumed that $\Delta\theta_i(t)$ is reset to zero. Then

$$\Delta\theta_{i1} = \alpha\frac{\tau}{2} + 1/2\,\beta\left(\frac{\tau}{2}\right)^2$$
$$\Delta\theta_{i2} = \alpha\xi + 1/2\beta\xi^2 \tag{141}$$

which may be solved for α and β as

$$\alpha = \frac{1}{\tau}\left(4\Delta\theta_{i1} - \Delta\theta_{i2}\right)$$
$$\beta = \frac{1}{\tau 2}\left(4\Delta\theta_{i2} - 8\Delta\theta_{i1}\right) \tag{142}$$

so that

$$\tau\omega_i(t) = 4\Delta\theta_{i1} - \Delta\theta_{i2}$$
$$\tau\omega_i(t + 1/2\tau) = \Delta\theta_{i2} \tag{143}$$
$$\tau\omega_i(t + \tau) = 3\Delta\theta_{i2} - 4\Delta\theta_{i1}$$

An alternate formulation results if the accumulation of A/D outputs is reset at $t + \tau/2$. In this case

$$\tau\omega_i(t) = 3\Delta\theta_{i1} - \Delta\theta_{i2}$$
$$\tau\omega(t + 1/2\tau) = \Delta\theta_{i1} + \Delta\theta_{i2} \tag{144}$$
$$\tau\omega(t + \tau) = 3\Delta\theta_{i2} - \Delta\theta_{i1}$$

Equation Mechanization. - The preceding sections have presented the mechanization requirements for the inertial navigator and various tradeoffs which are involved in selecting a specific mechanization. In this section a mechanization is selected which is suitable and near-optimal for the VTOL application under consideration.

The attitude representation which is selected is the quaternion representation. An Euler angle representation is clearly inferior for use in conjunction with whole number digital comuputer due to the large number of trigonometric computations which must be made. The major disadvantage with the quaternion representation is the necessity of computing most or all of the direction cosine

matrix in order to resolve the accelerometer measurements. A careful analysis has shown, [6], however, that the quaternion mechanization is less demanding on the computer for higher order integration schemes as well as being inherently more accuarate. It appears, therefore, that the quaternion representation of attitude, together with the recommended fourth-order Runge-Kutta integration scheme, provides an optimum tradeoff between accuracy and computational burden.

The nature of the missions under consideration, i.e., short range VTOL missions, assures that the vehicle will not travel near the geographic poles. This is the overwhelming factor determining the optimum position representation: since a true-north mechanization may therefore be used, the Euler angle and direction cosine computations become particularly simple. As described in a preceeding section. (there is not a corresponding simplification in the quaternion computations.) The Euler angle representation is selected as it is somewhat less demanding on the computer than is the direction cosine approach.

A first order integration at 10 Hz will be used for both position and velocity integrations.

The approximations which have been previously discussed may be used in order to reduce the computational load. The resultant saving does not appear substantial, however, and for this reason, the full equations will be incorporated - a conservative approach.

The mechanization equations are summarized below. A block diagram of the Navigation and Attitude Computations is shown in Figure 19.

Attitude Equations (30 Hz).

$$
\begin{aligned}
\Delta b_0 &= -\tau M^t \left(\underline{\rho}^r(t) + \underline{\Omega}^r(t)\right) \\
\Delta b_1 &= \tau M \left(\tilde{\underline{\omega}}^p(t)\right) b(t) \\
\Delta b_2 &= \tau M \left(\tilde{\underline{\omega}}^p(t)\right) \left[b(t) + 1/2\Delta b_0 + 1/2\Delta b_1\right] \\
\Delta b_3 &= \tau M \left(\tilde{\underline{\omega}}^p(t)\right) \left[b(t) + 1/2\Delta b_0 + 1/2\Delta b_2\right] \\
\Delta b_4 &= \tau M \left(\tilde{\underline{\omega}}^p(t)\right) \left[b(t) \pm \Delta b_0 + \Delta b_3\right] \\
b(t+\tau) &= b(t) + \Delta b_0 + 1/6\left[\Delta b_1 + 2\Delta b_2 + 2\Delta b_3 + \Delta b_4\right]
\end{aligned}
\tag{145}
$$

Acceleration Resolution (30 Hz).

$$
\begin{aligned}
\hat{a}_e &= (b_0^2 + b_1^2 - b_2^2 - b_3^2)\,\tilde{a}_x + 2(b_1b_2 - b_0b_3)\tilde{a}_y + 2(b_1b_3 + b_0b_2)\,\tilde{a}_z \\
\hat{a}_n &= 2(b_1b_2 + b_0b_3)\,\tilde{a}_x + (b_0^2 - b_1^2 + b_2^2 - b_3^2)\,\tilde{a}_y + 2(b_2b_3 - b_0b_1)\,\tilde{a}_z \\
\hat{a}_u &= 2(b_1b_3 - b_0b_2)\,\tilde{a}_x + (b_2b_3 + b_0b_1)\,\tilde{a}_y + (b_0^2 - b_1^2 - b_2^2 + b_3^2)\,\tilde{a}_z
\end{aligned}
\tag{146}
$$

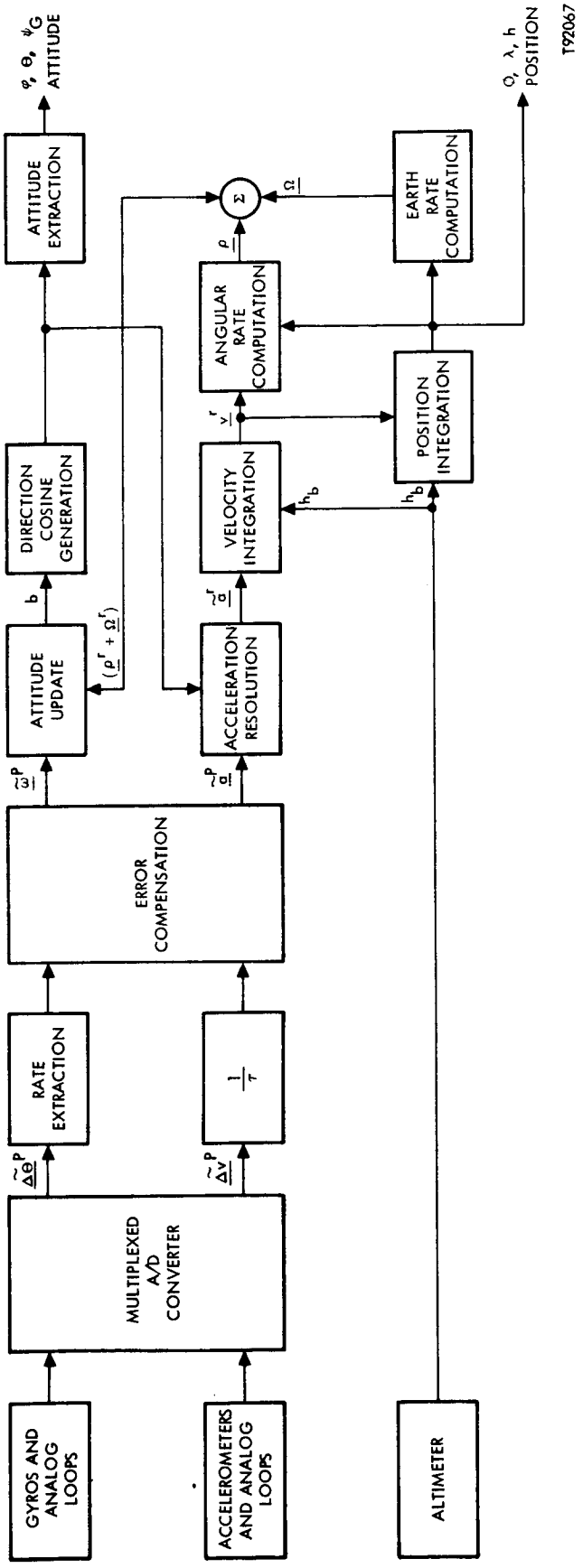

Figure 19. Computational Block Diagram

Velocity Integration (10 Hz)

$$v_e(t+3\tau) = v_e(t) + 3\tau\left[\hat{a}_e + 2(\Omega_u + \rho_u)v_n - 2(\Omega_n + \rho_n)v_u\right]$$

$$v_n(t+3\tau) = v_n(t) + 3\tau\left[\hat{a}_n + 2\rho_e v_u - 2(\Omega_u + \rho_u)v_n\right] \quad (147)$$

$$v_u(t+3\tau) = v_u(t) + 3\tau\left[\hat{a}_u - g_0 - k_v(h - h_b)\right]$$

Position Rate (10 Hz)

$$\rho_e = -\frac{v_n}{a}\left(1 - \frac{h}{a} - f\sin^2\phi + 2f\cos^2\phi\right)$$

$$\rho_n = \frac{v_e}{a}\left(1 - \frac{h}{a} - f\sin^2\phi\right) \quad (148)$$

$$\rho_u = \rho_n \tan\phi$$

Position Equations (10 Hz)

$$\phi(t+3\tau) = \phi(t) + 3\tau\rho_e$$

$$\lambda(t+3\tau) = \lambda(t) + 3\tau(\rho_n \sec\phi) \quad (149)$$

$$h(t+3\tau) = h(t) + 3\tau\left[v_u - k_p(h - h_b)\right]$$

Earth Rate (10 Hz)

$$\Omega_n = \Omega\cos\phi$$

$$\Omega_u = \Omega\sin\phi \quad (150)$$

Attitude & Heading Extraction (As Required)

$$\theta = \sin^{-1}(b_{23})$$

$$\varphi = \tan^{-1}\left(\frac{-b_{13}}{b_{33}}\right) \quad (151)$$

$$\psi_T = \tan^{-1}\left(\frac{-b_{21}}{b_{22}}\right)$$

Alignment Error Propagation. -The quaternion*b which relates the platform components of a vector v to the reference set components via the relation

$$\underline{v}^p = b^* \underline{v}^r b \tag{1}$$

propagates according to

$$\dot{b} = \frac{1}{2} b \underline{\zeta}^p \tag{2}$$

where ζ is the vector angular rate of the platform set with respect to the reference set and where the indicated multiplications are quaternion products.

The computed value $\hat{b}$ of the attitude quaternion similarly propagates according to

$$\dot{\hat{b}} = \frac{1}{2} \hat{b} \hat{\underline{\zeta}}^p \tag{3}$$

and differs from b due to errors in the initial value of $\hat{b}$ and to errors in the computed rate vector $\hat{\underline{\zeta}}$.

The inertial angular rate of the platform set, i. e. the vector whose components are measured by the gyros, is designated by $\underline{\omega}$. Assuming stationary alignment, the inertial rate of the reference set is simply earth rate $\underline{\Omega}$. Thus

$$\underline{\zeta} = \underline{\omega} - \underline{\Omega} \tag{4}$$

and (2) may be rewritten as

$$\dot{b} = \frac{1}{2} b (\underline{\omega}^p - \underline{\Omega}^p) \tag{5}$$

$$= \frac{1}{2} b (\underline{\omega}^p - b^* \underline{\Omega}^r b)$$

$$= \frac{1}{2} b \underline{\omega}^p - \frac{1}{2} \underline{\Omega}^r b$$

* This derivation will be made using quaternion notation. The results would be identical if direction cosine or Euler Angle notation were employed.

The latter form is convenient since the components of $\underline{\Omega}$ in reference coordinates depend only upon latitude and the initial wander angle, which is arbitrary and usually chosen to be zero, while the components of $\underline{\omega}$ in the platform set correspond (to within error quantities) to the components measured by the gyros.

The computed value of $\underline{\xi}$ is

$$\hat{\underline{\xi}} = \tilde{\underline{\omega}} - \hat{\underline{\Omega}} - \underline{\xi} \tag{6}$$

where $\tilde{\underline{\omega}}$ is the gyro measured rate vector, $\hat{\underline{\Omega}}$ is the computed earth rate vector, and $\underline{\xi}$ is the alignment correction vector, i. e. the correction which is used to effect alignment. Substituting (6) into (3) yields

$$\dot{\hat{b}} = \frac{1}{2}\hat{b}\,(\tilde{\underline{\omega}}^p - \hat{\underline{\Omega}}^p - \underline{\xi}^p) \tag{7}$$

$$= \frac{1}{2}\hat{b}\,\tilde{\underline{\omega}}^p - \frac{1}{2}(\hat{\underline{\Omega}}^r + \underline{\xi}^r)\,\hat{b}$$

as the propagation equation for computed attitude.

Let $\underline{v}$ be an arbitrary vector and consider the transformation

$$\underline{v}^{r'} = \hat{b}\,\underline{v}^p\,\hat{b}^* \tag{8}$$

$$= \hat{b}\,b^*\,\underline{v}^r\,b\,\hat{b}^*$$

In the absence of errors in $\hat{b}$ (i. e. no alignment error), $\hat{b} = b$ and $\underline{v}^{r'}$ and $\underline{v}^r$ are equal. In general, however, $\underline{v}^{r'}$ will differ from $\underline{v}^r$ by the error rotation $\delta b \triangleq b\,\hat{b}^*$. Assuming that this rotation is sufficiently small that small angle approximations are valid, δb may be expressed as

$$\delta b \triangleq b\,\hat{b}^* \tag{9}$$

$$\simeq [1, \frac{1}{2}\varphi_e, \frac{1}{2}\varphi_n, \frac{1}{2}\varphi_u]^T$$

$$\simeq 1 + \frac{1}{2}\underline{\varphi}^r$$

$$= 1 - \frac{1}{2}\underline{\varphi}^{r'}$$

where $\underline{\varphi}^{r'} = [\varphi_e', \varphi_n', \varphi_u']^T$ is the vector of misalignment angles about the misaligned reference system axes, i. e. the vector which is to be nulled in order to effect alignment and $\underline{\varphi}^r \simeq -\underline{\varphi}^{r'}$ is the corresponding vector in reference coordinates.

The propagation of the error quaternion δb is found by differentiating (9) with respect to time and substituting (5) and (7):

$$\dot{\delta b} = 0 - \frac{1}{2}\underline{\dot{\varphi}}^{r'} \tag{10}$$

$$= \dot{b}\hat{b}^* + b\hat{\dot{b}}^*$$

$$= \frac{1}{2}[b\underline{\omega}^p - \underline{\Omega}^r b]\hat{b}^* + \frac{1}{2}b[\hat{b}\underline{\tilde{\omega}}^p - (\underline{\hat{\Omega}}^r + \underline{\xi}^r)\hat{b}]^*$$

$$= \frac{1}{2}[b\underline{\omega}^p - \underline{\Omega}^r b]\hat{b}^* + \frac{1}{2}b[-\underline{\tilde{\omega}}^p\hat{b}^* - \hat{b}^*(-\underline{\hat{\Omega}}^r\underline{\xi}^r)]$$

$$= \frac{1}{2}b(\underline{\omega}^p - \underline{\tilde{\omega}}^p)\hat{b}^* - \frac{1}{2}(\underline{\Omega}^r b\hat{b}^* - b\hat{b}^*\underline{\hat{\Omega}}^r) + \frac{1}{2}b\hat{b}^*\underline{\xi}^r$$

$$= -\frac{1}{2}b\,\delta\underline{\tilde{\omega}}^p\hat{b}^* - \frac{1}{2}(\underline{\Omega}^r\delta b - \delta b\underline{\hat{\Omega}}^r) + \frac{1}{2}\delta b\underline{\xi}^r$$

where $\delta\underline{\omega}^p \triangleq \underline{\tilde{\omega}}^p - \underline{\tilde{\omega}}^p$ is the vector of gyro measurement errors. Carrying out the indicated quaternion multiplications yields

$$b\,\delta\underline{\tilde{\omega}}^p\hat{b}^* = \delta\underline{\tilde{\omega}}^r\,\delta b \tag{11}$$

$$= \frac{1}{2}\delta\underline{\tilde{\omega}}^r \cdot \underline{\varphi}^{r'} + \delta\underline{\tilde{\omega}}^r - \frac{1}{2}\delta\underline{\tilde{\omega}}^r \times \underline{\varphi}^{r'}$$

$$\underline{\Omega}^r\delta b = \frac{1}{2}\underline{\Omega}^r \cdot \underline{\varphi}^{r'} + \underline{\Omega}^r - \frac{1}{2}\underline{\Omega}^r \times \underline{\varphi}^{r'} \tag{12}$$

$$\delta b\,\underline{\hat{\Omega}}^r = \frac{1}{2}\underline{\varphi}^{r'} \cdot \underline{\Omega}^r + \underline{\hat{\Omega}}^r - \frac{1}{2}\underline{\varphi}^{r'} \times \underline{\Omega}^r \tag{13}$$

$$= \frac{1}{2}\underline{\Omega}^r \cdot \underline{\varphi}^{r'} + \underline{\hat{\Omega}}^r + \frac{1}{2}\underline{\Omega}^r \times \underline{\varphi}^{r'}$$

$$\delta b\,\xi^r = \frac{1}{2}\underline{\xi}^r \cdot \varphi^{r'} + \underline{\xi}^r - \frac{1}{2}\underline{\xi}^r \times \varphi^{r'} \tag{14}$$

Collecting terms and solving for the vector part of (10) yields

$$\underline{\phi}^{r\,\prime} = \delta\underline{\tilde{\omega}}^{r} + \frac{1}{2}\,\delta\underline{\tilde{\omega}}^{r} \times \underline{\varphi}^{r\,\prime} - (\underline{\hat{\Omega}}^{r} - \underline{\Omega}^{r}) - \underline{\Omega}^{r} \times \underline{\varphi}^{r\,\prime} - \underline{\xi}^{r} - \frac{1}{2}\,\underline{\xi}^{r} \times \underline{\varphi}^{r\,\prime} \qquad (15)$$

$$\simeq \delta\underline{\tilde{\omega}}^{r} - \delta\underline{\hat{\Omega}}^{r} - \underline{\xi}^{r} - (\underline{\Omega}^{r} + \frac{1}{2}\,\underline{\xi}^{r}) \times \underline{\varphi}^{r\,\prime}$$

where the approximation results from neglecting the second order term $\frac{1}{2}\,\delta\underline{\tilde{\omega}}^{r} \times \underline{\varphi}^{r\,\prime}$.

Equation (15) is a very general equation for the propagation of attitude errors in a stationary inertial navigation system, either strapdown or gimbaled. Assuming that no alignment control is used ($\underline{\xi}^{r} = 0$) and, for simplicity, that the gyros are drift free ($\delta\underline{\tilde{\omega}}^{r} = 0$) and latitude is known exactly ($\delta\underline{\hat{\Omega}}^{r} = 0$), the response of the misalignment vector $\underline{\varphi}$ to its initial condition may be readily found using Laplace transform techniques. Equation (15) yields

$$s\underline{\varphi}^{r\,\prime}(s) = \underline{\varphi}^{r\,\prime}(0) - \begin{bmatrix} 0 & -\Omega_u & \Omega_u \\ \Omega_u & 0 & 0 \\ -\Omega_u & 0 & 0 \end{bmatrix} \underline{\varphi}^{r\,\prime}(s) \qquad (16)$$

Solving for $\underline{\varphi}^{r\,\prime}(s)$

$$\underline{\varphi}^{r\,\prime}(s) = \left\{ sI + \begin{bmatrix} 0 & -\Omega_u & \Omega_u \\ \Omega_u & 0 & 0 \\ -\Omega_u & 0 & 0 \end{bmatrix} \right\}^{-1} \underline{\varphi}^{r\,\prime}(0) \qquad (17)$$

$$= \begin{bmatrix} \frac{s}{s^2+\Omega^2} & \frac{\Omega_u}{s^2+\Omega^2} & \frac{-\Omega_n}{s^2+\Omega^2} \\ \frac{-\Omega_u}{s^2+\Omega^2} & \frac{s^2+\Omega_n^2}{s(s^2+\Omega^2)} & \frac{\Omega_n\,\Omega_u}{s(s^2+\Omega^2)} \\ \frac{\Omega_n}{s^2+\Omega^2} & \frac{-\Omega_n\,\Omega_u}{s(s^2+\Omega^2)} & \frac{s^2+\Omega_u^2}{s(s^2+\Omega^2)} \end{bmatrix} \underline{\varphi}^{r\,\prime}(0)$$

where $\Omega = |\underline{\Omega}|$. Then since $\Omega_n = \Omega\cos\phi$ and $\Omega_u = \Omega\sin\phi$, the time response is found to be

$$\underline{\varphi}^{r'}(t) = \mathcal{L}^{-1}\,\underline{\varphi}^{r'}(s) \tag{18}$$

$$= \begin{bmatrix} (\cos\Omega t) & (\sin\Omega t\,\sin\phi) & (-\sin\Omega t\,\cos\phi) \\ (-\sin\Omega t\,\sin\phi) & (\cos\Omega t + \cos^2\phi\,(1-\cos\Omega t)) & (\sin\phi\cos\phi\,(1-\cos\Omega t)) \\ (\sin\Omega t\,\cos\phi) & (-\sin\phi\cos\phi\,(1-\cos\Omega t)) & (\cos\Omega t + \sin^2\phi\,(1-\cos\Omega t)) \end{bmatrix} \underline{\varphi}^{r'}(0)$$

thus the alignment errors are seen to be oscillatory.

For ideal alignment, i.e. $\underline{\varphi}^{r'}(t) = 0$, it is necessary that either (1) the initial condition $\underline{\varphi}^{r'}(0)$ be zero or (2) that the correction vector $\underline{\xi}^{r}$ be chosen in such a way that the error vector is driven to zero, i.e. the oscillations are damped. The former case is termed "one shot" alignment and is discussed in the following section. The latter case is discussed in succeeding sections.

One-Shot Alignment. -Suppose that the vehicle attitude is known to within a few degrees, so that small angle approximations may be used. If the measured acceleration components $\tilde{\underline{a}}^{p}$ are resolved through the corresponding attitude quaternion $\hat{b}$, the resulting computed components of acceleration are

$$\hat{\underline{a}}^{r'} = \hat{b}\,\tilde{\underline{a}}^{p}\,\hat{b}^{*} \tag{19}$$

$$= \hat{b}\,b^{*}\,\underline{a}^{r}\,b\,\hat{b}^{*} + \hat{b}\,\delta\tilde{\underline{a}}^{p}\,\hat{b}^{*}$$

$$= \delta b^{*}\,\underline{a}^{r}\,\delta b + \hat{b}\,\tilde{\delta\underline{a}}^{p}\,\hat{b}^{*}$$

Assume for the moment that the measurements are perfect ($\tilde{\delta\underline{a}} = 0$). Then, in the absence of vehicle accelerations, the vector $\hat{\underline{a}}^{r}$ is simply

$$\underline{a}^{r} = [0,\ 0,\ g]^{T} \tag{20}$$

and since

$$\delta b \simeq \left[1, -\frac{1}{2}\varphi_{e}', -\frac{1}{2}\varphi_{n}', -\frac{1}{2}\varphi_{u}'\right]^{T} \tag{21}$$

the computed acceleration vector $\underline{\hat{a}}^{r'}$ in (19) is

$$\underline{\hat{a}}^{r'} \simeq \begin{bmatrix} -g\varphi_{n}' \\ g\varphi_{e}' \\ g \end{bmatrix} \tag{22}$$

If the measured angular rate components $\delta\underline{\tilde{\omega}}^{p}$ are similarly resolved through the quaternion $\hat{b}$,

$$\underline{\hat{\omega}}^{r'} = \hat{b}\,\underline{\omega}^{p}\,\hat{b}^{*} \tag{23}$$

$$= \delta b^{*}\,\underline{\omega}^{r}\,\delta b + \hat{b}\,\delta\underline{\tilde{\omega}}^{p}\,\hat{b}^{*}$$

and, in the absence of measurement errors and vehicle angular rates, the vector $\underline{\omega}^{r}$ is

$$\underline{\omega}^{r} = [0, \Omega\cos\phi, \Omega\sin\phi]^{T} \tag{24}$$

$$= [0, \Omega_{n}, \Omega_{u}]^{T}$$

so that

$$\underline{\hat{\omega}}^{r'} \simeq \begin{bmatrix} -\Omega_{u}\,\varphi_{n}' + \Omega_{n}\,\varphi_{u}' \\ \Omega_{n} + \Omega_{u}\,\varphi_{e}' \\ \Omega_{u} - \Omega_{n}\,\varphi_{e}' \end{bmatrix} \tag{25}$$

Since g and Ω are accurately known and ϕ is generally known to within a few seconds of arc (i.e. vehicle position during alignment is known to within a few hundred feet), (22) and (25) may be solved for the misalignment angles

$$\hat{\varphi}_e' = \frac{1}{g}\hat{a}_n' \tag{26}$$

$$\hat{\varphi}_n' = \frac{1}{g}\hat{a}_e'$$

$$\hat{\varphi}_u' = \frac{1}{\Omega_n}\hat{\omega}_e' - \frac{\Omega_u}{\Omega_n g}\hat{a}_n'$$

$$= \frac{1}{\Omega_u}\hat{\omega}_e' - \frac{\tan\phi}{g}\hat{a}_n'$$

These estimated angles may be used to correct the computed quaternion. Since

$$\delta b = b\hat{b}^* \tag{27}$$

and the estimated error quaternion is, from (21) and (26),

$$\hat{\delta b} = \left[1, -\frac{1}{2}\hat{\varphi}_e', -\frac{1}{2}\hat{\theta}_n', -\frac{1}{2}\hat{\theta}_u'\right]^T \tag{28}$$

the corrected quaternion is

$$\hat{b}_{corr} = \hat{\delta b}\hat{b}^* \tag{29}$$

In the error-free case described above,

$$\hat{b}_{corr} = b$$

and the correction (i.e. alignment) is perfect.

Consider next the effects of instrument errors and disturbance motions on the estimated misalignment angles (26). Letting $\underline{a}_d$ and $\underline{\omega}_d$ represent the disturbance acceleration and angular rate vectors, respectively, (20) and (24) are replaced by

$$\underline{a}^r = [a_{de}, a_{dn}, g + a_{du}]^T \tag{30}$$

$$\underline{\omega}^r = [\omega_{de}, \Omega_n + \omega_{dn}, \Omega_u + \omega_{du}]^T \tag{31}$$

Substituting (30) and (31) into (19) and (23) and resolving the instrument errors $\underline{\tilde{a}}^P$ and $\underline{\tilde{\omega}}^P$ along the misaligned axes, it is found that

$$\underline{a}^{r\,\prime} = \begin{bmatrix} -g\varphi_n' + \delta\tilde{a}_e' + a_{de}' \\ g\varphi_e' + \delta\tilde{a}_n' + a_{dn}' \\ g + \delta\tilde{a}_u' + a_{dn}' \end{bmatrix} \tag{32}$$

$$\underline{\omega}^{r\,\prime} = \begin{bmatrix} -\Omega_u\varphi_n' + \Omega_n\varphi_u' + \delta\tilde{\omega}_e' + \omega_{de}' \\ \Omega_n + \Omega_u\varphi_e' + \delta\tilde{\omega}_n' + \omega_{dn}' \\ \Omega_u - \Omega_n\varphi_e' + \delta\tilde{\omega}_u' + \omega_{du}' \end{bmatrix} \tag{33}$$

so that the estimated misalignment angles are, from (26),

$$\hat{\varphi}_e' = \frac{1}{g}\hat{a}_n' \tag{34}$$

$$= \varphi_e' - \frac{\delta\tilde{a}_n'}{g} - \frac{a_{dn}'}{g}$$

$$\hat{\varphi}_n' = \varphi_n' + \frac{\delta\tilde{a}_e'}{g} + \frac{a_{de}'}{g}$$

$$\hat{\varphi}_u' = \varphi_u' + \frac{\delta\tilde{\omega}_e'}{\Omega_n} + \frac{\omega_{de}'}{\Omega_n} - \tan\phi\left(\frac{\delta\tilde{a}_n'}{g} + \frac{a_{dn}'}{g}\right)$$

The errors in estimated level misalignment angles $\hat{\varphi}_e'$ and $\hat{\varphi}_n'$ due to accelerometer errors, using typical values of 10^{-4}g for $\delta\tilde{a}_e'$ and $\delta\tilde{a}_n'$, are seen to be of the order of 10^{-4} radians (20 sec). The azimuth error $(\hat{\varphi}_u' - \varphi_u')$ due to the east component of gyro drift, using a typical error of

10^{-2} °/hr, is of the order of one milliradian at 45° latitude ($\Omega_n = 10°/hr$). (The effect of the accelerometer error $\delta\tilde{a}_n'$ on azimuth error is roughly an order of magnitude smaller.)

The effects of disturbance motions on the accuracy of one-shot alignment are more serious. Ten milli-g's of lateral acceleration is seen to result in more than half a degree of level misalignment, while even 10^{-3} degrees per second disturbance rate about the east axis will result in an azimuth misalignment of approximately 20 degrees.

The most obvious solution to the disturbance motion problem is to average the estimated misalignment angles over some suitable time period in order to reduce the disturbance effects, i.e.

$$\hat{\varphi}_e = \frac{1}{T}\int_o^T \left(\frac{1}{g}\hat{a}_n'\right) dt \qquad (35)$$

$$\hat{\varphi}_n = \frac{1}{T}\int_o^T \left(-\frac{1}{g}\hat{a}_e'\right) dt$$

$$\hat{\varphi}_u = \frac{1}{T}\int_o^T \left(\frac{\hat{\omega}_e'}{\Omega_n} - \tan\phi\,\frac{\hat{a}_n'}{g}\right) dt$$

For sufficiently large T, the effects of disturbance motions on the estimated angles becomes negligible. These estimates, however, represent <u>average</u> misalignments and thus may be in error by as much as the peak angular deviation of the instrument platform orientation from this average. Such errors are generally of sufficient magnitude to render the one-shot alignment scheme unacceptable, except perhaps for a preliminary "coarse" alignment, which may be useful to reduce errors to a sufficient level for application of alternative "fine" alignment techniques.

<u>Continuous Alignment</u>. -As described in the preceding section, discrete, or "one-shot", alignment is generally unsuitable for alignment of a system which is subject to even moderate disturbance motions during the alignment period. For this reason, a continuous alignment technique is more commonly employed. This technique, or, more accurately, class of techniques, utilizes continuous tracking of the vehicle motions by the attitude computation

process (i.e. the attitude quaternion or direction cosine matrix is updated as in post-alignment modes) in conjunction with a corrective signal which is used to damp the oscillations caused by the initial misalignment. The analytic machinery required for the discussion of this technique has been established by the inclusion of the corrective vector $\underline{\xi}$ in the derivation of the alignment error propagation.

Classical self-alignment of inertial platforms utilizes the outputs of the accelerometers as error signals which, when appropriately weighted and filtered, are used to null the misalignment angles of the platform. In strapdown systems, the east component of gyro-measured angular rate may also be considered for use as an alignment error signal (note that in conventional gimbaled systems such rate information is not available). In either case the filters are of the "fixed gain" type and traditionally separated into two modes: In "leveling" mode the azimuth loop corrections are rendered inoperative and the filter gains are selected in order to effect rapid alignment about the level axes; in "gyrocompass" mode the azimuth loop is closed and the filter gains adjusted to provide satisfactory alignment about the vertical axis.

Modern estimation theory techniques may also be applied to the alignment problem. Such methods generally provide substantial reduction in the time required to effect alignment. Their usefulness is limited primarily by the requirement for accurate statistical modeling of the error sources affecting alignment (instrument errors and disturbance motions) and by the substantial increase in computational requirements which is imposed by their implementation.

In the following section a simplified, intuitive, description of inertial self-alignment is presented which is applicable to each of the schemes which will be described in succeeding sections. Next, several fixed-gain alignment mechanizations are described and their relative merits compared. Finally, a Kalman filter mechanization is described.

Simplified Description of Strapdown Inertial System Self-Alignment. -This section presents a brief intuitive description of the self-alignment process in an inertial navigator. The presentation follows traditional lines, with separate modes for leveling and for azimuth alignment (gyrocompassing). Only the more important error sources and cross-channel coupling terms are considered in order to eliminate any possible confusion which would result from their inclusion.

Leveling. -Equation (15) may be rewritten in component form as

$$\dot{\varphi}_e' = \delta\tilde{\omega}_e - \delta\hat{\Omega}_e - \xi_e - \Omega_n\varphi_u' + \Omega_u\varphi_n' - \frac{1}{2}\xi_n\varphi_u' + \frac{1}{2}\xi_u\varphi_n' \tag{36}$$

$$\simeq \delta\tilde{\omega}_e - \xi_e - \Omega_n\varphi_u'$$

$$\dot{\varphi}_n' \simeq \delta\tilde{\omega}_n - \xi_n$$

$$\dot{\varphi}_u' \simeq \delta\tilde{\omega}_u - \xi_u$$

Here it has been assumed that φ_e' and φ_n' have been "coarse aligned" to sufficient accuracy (e. g. by means of a one shot alignment) that the cross coupling terms involving these quantities are negligibly small. Also neglected are the terms in $\underline{\xi} \times \underline{\varphi}$, which are of the order of $|\underline{\varphi}|^2$ and, hence, of only minor importance in the analysis which follows.

Equation (36) demonstrates that, on a short-term basis at least, the uncontrolled (i. e. $\underline{\xi} = 0$) inertial system drifts about the three reference axes at rates corresponding to the components of the gyro drift rate vector which lie along the reference axes plus an additional small drift about the east axis which results from misresolving the computed earth rate due to azimuth misalignments.

As has been described previously, the computed level components of acceleration are direct measures of level misalignment. Neglecting disturbance accelerations,

$$\hat{a}_e' \simeq -g\varphi_n' + \tilde{\delta a}_e \tag{37}$$

$$\hat{a}_n' \simeq g\varphi_e' + \tilde{\delta a}_n$$

thus if these values are used as error signals, i. e. if the correction rates are selected as

$$\xi_e = k_e\hat{a}_n' \tag{38}$$

$$\xi_n = -k_n\hat{a}_e'$$

the level axis propagation equations become

$$\dot{\varphi}_e' = \delta\tilde{\omega}_e - k_e \hat{a}_n' - \Omega_u \varphi_u' \tag{39}$$

$$= \delta\tilde{\omega}_e + k_e (g\varphi_e' + \delta\hat{a}_n) - \Omega_u \varphi_u'$$

$$\dot{\varphi}_n' = \delta\tilde{\omega}_n + k_n (-g\varphi_n' + \delta\tilde{a}_n)$$

Figure 20 shows an error block diagram of (39).

The computational error equations (4) are directly analogous to the situation which exists in a gimbaled platform which is nominally level and north-pointing. Any misalignment of the stable element about the north (east) axis causes the east (north) accelerometer to sense a component of gravity. This signal may then be used to slew the platform until the measured acceleration component is zero at which time, to within the accuracy limitations imposed by system error sources, the platform is level, i.e. φ_e' and φ_n' are zero.

It is seen from the error block diagrams that the steady state errors for the simple leveling scheme described above are

$$\varphi_e'(\text{s.s.}) = -\frac{\delta\tilde{a}_n}{g} + \frac{\delta\tilde{\omega}_e}{gk_e} - \frac{\Omega_n \varphi_u'}{gk_e} \tag{40}$$

$$\varphi_n'(\text{s.s.}) = \frac{\delta\tilde{a}_e}{g} + \frac{\delta\tilde{\omega}_n}{gk_n}$$

and, for typical values of k_e and k_n,

$$\varphi_e'(\text{s.s.}) \simeq -\frac{\delta\tilde{a}_n}{g} \tag{41}$$

$$\varphi_n'(\text{s.s}) \simeq \frac{\delta\tilde{a}_e}{g}$$

Thus the accuracy of leveling is determined primarily by the accelerometer errors $\delta\tilde{a}_n$ and $\delta\tilde{a}_e$.

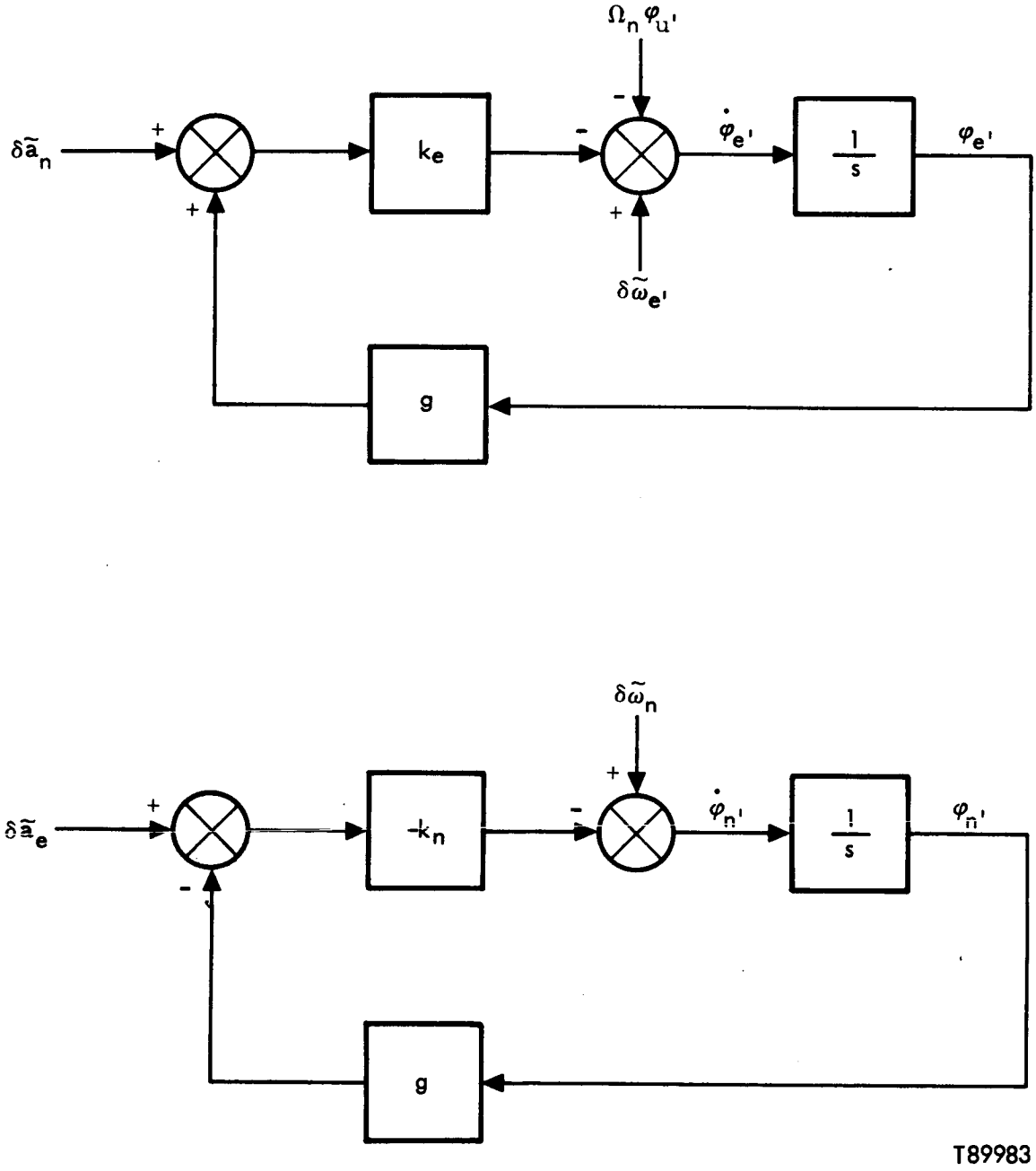

Figure 20. Level Loop Error Block Diagrams

Gyrocompassing. -Azimuth alignment, or gyrocompassing, is accomplished by nulling the term in $\Omega_n \varphi_u'$ which appears in (39). Again using the analog of a gimbaled system, it is seen that any misalignment φ_u' about the azimuth axis will cause the platform to drift off level about the east axis. If the measured north acceleration is used as an azimuth error signal as well as a level error signal, i. e. if

$$\xi_u = - k_u \hat{a}_n' \tag{42}$$

the error diagram of Figure 21 results. (The north axis tilt is essentially decoupled from the east-azimuth loop and is hence omitted from the diagram.)

Again examining steady-state errors, it is seen that

$$\delta\tilde{\omega}_e - \Omega_n \varphi_u'(ss) + k_e (\delta\tilde{a}_n + g\varphi_e'(ss)) = 0 \tag{43}$$

$$\delta\tilde{\omega}_u + k_u (g\varphi_e'(ss) + \delta\tilde{a}_n) = 0$$

from which

$$\varphi_e'(s.s.) = - \frac{\delta\tilde{a}_n}{g} - \frac{\delta\tilde{\omega}_u}{gk_u} \tag{44}$$

$$\varphi_u'(s.s.) = \frac{\delta\tilde{\omega}_e}{\Omega_n} - \frac{k_e}{\Omega_n} (\delta\tilde{a}_n + g\varphi_e'(s.s.))$$

$$= \frac{\delta\tilde{\omega}_e}{\Omega_n} + \frac{k_e}{k_u} \frac{\delta\tilde{\omega}_u}{\Omega_n}$$

which, for typical values of k_e and k_u are approximately

$$\varphi_e'(s.s.) \simeq - \frac{\delta\tilde{a}_n}{g} \tag{45}$$

$$\varphi_u'(s.s.) \simeq \frac{\delta\tilde{\omega}_e}{\Omega_n}$$

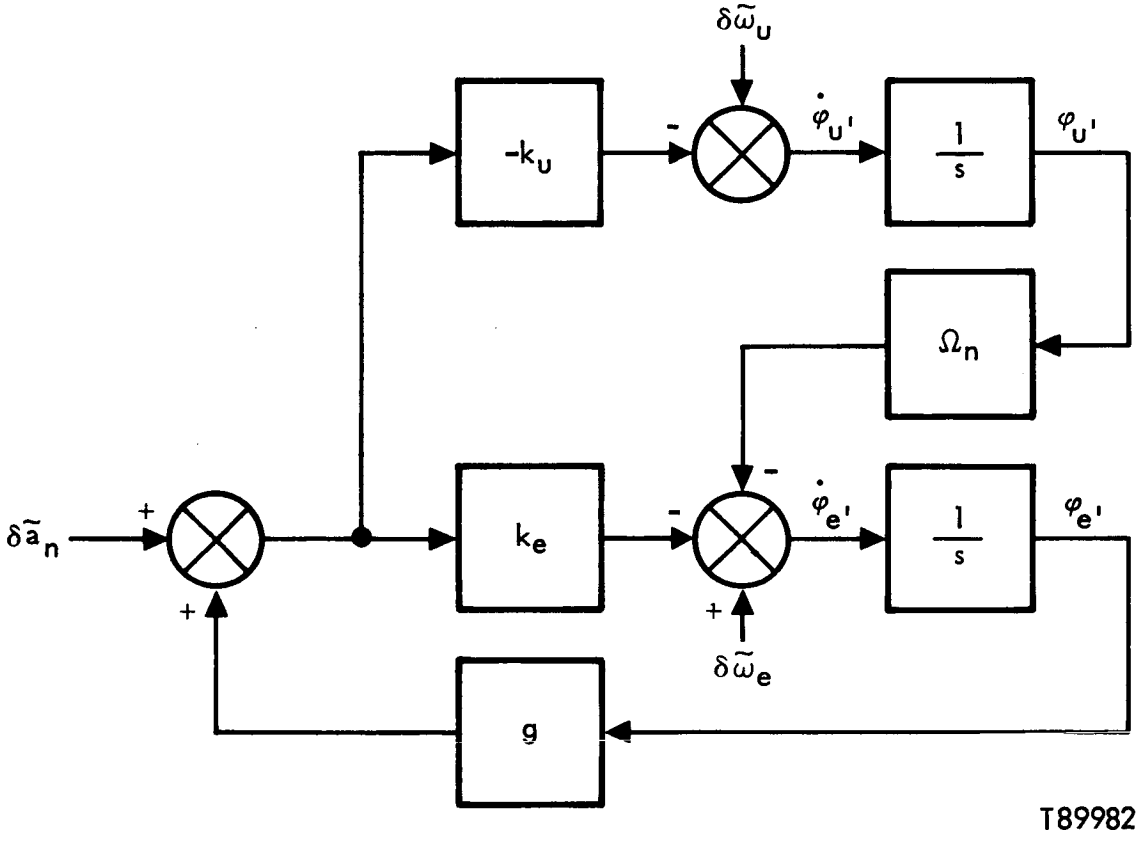

Figure 21. Simple Gyrocompassing Loop Error Block Diagram

Thus the east axis leveling error is due essentially to the north component of acceleration error, while the gyrocompassing error is due primarily to the east component of gyro drift.

In any practical mechanization, the presence of disturbance motions necessitates the incorporation of filtering in addition to that provided by the simple loops described above. Such filtering is described in succeeding the sections which follow.

Fixed Gain Alignment. -The signals which are used for the one-shot alignment scheme described previously, i. e.

$$\hat{\phi}_e' = -\frac{1}{g}\hat{a}_n' \tag{46}$$

$$\hat{\phi}_n' = \frac{1}{g}\hat{a}_e'$$

$$\hat{\phi}_u' = \frac{1}{\Omega_u}\hat{\omega}_e' - \frac{\tan\phi}{g}\hat{a}_n'$$

are also appropriate for use in continuous alignment. In the simplest form of such alignment, the vector $\underline{\xi}$ is chosen to be

$$\underline{\xi} = K\,\hat{\underline{\phi}}^{r'} \tag{47}$$

$$= K \begin{bmatrix} 0 & -\frac{1}{g} & 0 \\ \frac{1}{g} & 0 & 0 \\ 0 & -\frac{\tan\phi}{g} & \frac{1}{\Omega_u} \end{bmatrix} \begin{bmatrix} \hat{a}_n' \\ \hat{a}_e' \\ \hat{\omega}_e' \end{bmatrix}$$

where K is an appropriate 3 x 3 weighting matrix. The relations (34) repeated here for clarity,

$$\hat{\varphi}_e' = \varphi_e' - \frac{\delta\tilde{a}_n'}{g} - \frac{a_{dn}'}{g} \tag{48}$$

$$\hat{\varphi}_n' = \varphi_n' + \frac{\delta\tilde{a}_e'}{g} + \frac{a_{de}'}{g}$$

$$\hat{\varphi}_u' = \varphi_u' + \frac{\delta\tilde{\omega}_e'}{\Omega_n} + \frac{\omega_{de}'}{\Omega_n} - \frac{\tan\phi}{g}\,\tilde{\delta a}_n' - \frac{\tan\phi}{g}\,a_{dn}'$$

The attitude error propagation equation (15) becomes

$$\dot{\underline{\varphi}}^{r\,\prime} = \delta\tilde{\underline{\omega}}^r - \delta\hat{\underline{\Omega}}^r - \underline{\xi}^r - \underline{\Omega}^r \times \underline{\varphi}^{r\,\prime} - \frac{1}{2}\underline{\xi}^r \times \underline{\varphi}^{r\,\prime} \tag{49}$$

$$\simeq \delta\tilde{\underline{\omega}}^r - \delta\hat{\underline{\Omega}}^r - \underline{\Omega}^r \times \underline{\varphi}^{r\,\prime} - K\,\hat{\underline{\varphi}}^{r\,\prime} - \frac{1}{2}\underline{\xi}^r \times \underline{\varphi}^{r\,\prime}$$

$$\simeq (\delta\tilde{\underline{\omega}}^r - \delta\hat{\underline{\Omega}}^r) - \underline{\Omega}^r \times \underline{\varphi}^{r\,\prime} - K\,\hat{\underline{\varphi}}^{r\,\prime}$$

where the final approximation results from neglecting the term in $\underline{\xi} \times \underline{\varphi}$, which is seen from (48) to consist only of higher order error terms. Rewriting (49) in vector matrix form and using (48)

$$\begin{bmatrix} \dot{\varphi}_e' \\ \dot{\varphi}_n' \\ \dot{\varphi}_u' \end{bmatrix} = \begin{bmatrix} \delta\tilde{\omega}_e - \delta\hat{\Omega}_e \\ \delta\tilde{\omega}_n - \delta\hat{\Omega}_u \\ \delta\tilde{\omega}_u - \delta\hat{\Omega}_u \end{bmatrix} - K \begin{bmatrix} \hat{\varphi}_e' \\ \hat{\varphi}_n' \\ \hat{\varphi}_u' \end{bmatrix} - \begin{bmatrix} 0 & -\Omega_u & \Omega_n \\ \Omega_u & 0 & 0 \\ -\Omega_n & 0 & 0 \end{bmatrix} \begin{bmatrix} \varphi_e' \\ \varphi_n' \\ \varphi_u' \end{bmatrix} \tag{50}$$

$$= \begin{bmatrix} \delta\tilde{\omega}_e - \delta\hat{\Omega}_e \\ \delta\tilde{\omega}_n - \delta\hat{\Omega}_n \\ \delta\tilde{\omega}_u - \delta\hat{\Omega}_u \end{bmatrix} - K' \begin{bmatrix} \varphi_e \\ \varphi_n \\ \varphi_u \end{bmatrix} - K \begin{bmatrix} -\frac{1}{g}(\delta\tilde{a}_n' + a_{dn}') \\ \frac{1}{g}(\delta\tilde{a}_e' + a_{de}') \\ \frac{1}{\Omega_n}(\delta\tilde{\omega}_e' + \omega_{de}') - \frac{\tan\phi}{g}(\delta\tilde{a}_n' + a_{dn}') \end{bmatrix}$$

where

$$K' = K + \begin{bmatrix} 0 & -\Omega_u & \Omega_n \\ \Omega_u & 0 & 0 \\ -\Omega_n & 0 & 0 \end{bmatrix} \tag{51}$$

The simplest form of alignment from the standpoint of analysis results from selecting

$$K = \begin{bmatrix} k_{le} & \Omega_u & 0 \\ -\Omega_u & k_{ln} & 0 \\ \Omega_n & 0 & k_{lu} \end{bmatrix} \tag{52}$$

so that

$$K' = \text{diag}\,[k_{le}, k_{ln}, k_{lu}] \tag{53}$$

and (50) decouples into three first-order scalar equations

$$\dot{\varphi}_e' = -k_{le}\varphi_e' + (\delta\tilde{\omega}_e' - \delta\hat{\Omega}_e') + \frac{k_{le}}{g}(\delta\tilde{a}_n' + a_{dn}') - \frac{\Omega_u}{g}(\delta\tilde{a}_e' + a_{de}') \tag{54}$$

$$\dot{\varphi}_n' = -k_{ln}\varphi_n' + (\delta\tilde{\omega}_n' - \delta\hat{\Omega}_n') - \frac{k_{ln}}{g}(\delta\tilde{a}_e' + a_{de}') - \frac{\Omega_u}{g}(\delta\tilde{a}_n' + a_{dn}')$$

$$\dot{\varphi}_u' = -k_{lu}\varphi_u' + (\delta\tilde{\omega}_u' - \delta\hat{\Omega}_u') - \frac{k_{lu}}{\Omega_n}(\delta\tilde{\omega}_e' + \omega_{de}') + \frac{k_{lu}\tan\phi + \Omega_u}{g}(\delta\tilde{a}_n' + a_{dn}')$$

The primary limitation to this scheme is the time required to filter the errors of disturbance motions. Laplace transforming the equation for φ_u' and neglecting all error terms but ω_{de}' yields

$$\varphi_u'(s) = \frac{1}{(s+k_{1u})}\left[\varphi_u'(0) + \frac{k_{1u}}{\Omega_n}\omega_{de}'(s)\right] \tag{55}$$

The gain k_{in} determines the rate of decay of the initial azimuth error $\varphi_u'(0)$, i.e. it is the inverse of the loop time constant. The peak amplitude of φ_u' in response to a sinusoidal disturbance rate $\omega_{de}' = \omega \sin \beta t$ is

$$\left|\varphi_u'\right|_{max} = \left|\frac{k_{1u}}{j\beta + k_{1n}}\right| \frac{\omega}{\Omega_n} \tag{56}$$

$$= \left|\frac{1}{\frac{j\beta}{k_{1n}} + 1}\right| \frac{\omega}{\Omega_n}$$

As an example of the susceptibility of this scheme to distrubance motions, consider the following case:

Disturbance Amplitude $\omega = .01^\circ/\text{sec}$

Distrubance Frequency $\beta = .1$ rad/sec

Allowable Azimuth Error $\left|\varphi_u'\right|_{max} = 1$ m. r.

Latitude $\phi = 45^\circ$

Solving (56) for $\tau = \frac{1}{k_{1u}}$, it is found that a time constant of approximately 10 hours would be required. For higher disturbance amplitudes or lower disturbance frequencies the required time constant is even larger. Thus it is clear that this scheme is unsatisfactory for the application under consideration without additional filtering.

A classical alignment, corresponding to the simplified technique described in the preceding section, results from choosing

$$K = \begin{bmatrix} k_{2e} & \Omega_u & 0 \\ -\Omega_u & k_{2n} & 0 \\ -k_{2u}+\Omega_n & 0 & 0 \end{bmatrix} \tag{57}$$

so that

$$K' = \begin{bmatrix} k_{2e} & 0 & \Omega_n \\ 0 & k_{2n} & 0 \\ k_{2u} & 0 & 0 \end{bmatrix} \tag{58}$$

In this case the rate-derived error signal $\hat{\varphi}_u'$ is not used. The error propagation equation decouples into one second order loop involving φ_e' and φ_u' and one first order equation involving only φ_n':

(59)

$$\begin{bmatrix} \dot{\varphi}_e' \\ \dot{\varphi}_u' \end{bmatrix} = \begin{bmatrix} -k_{2e} & -\Omega_n \\ -k_{2u} & 0 \end{bmatrix} \begin{bmatrix} \varphi_e' \\ \varphi_n' \end{bmatrix} + \begin{bmatrix} (\delta\tilde{\omega}_e' - \delta\hat{\Omega}_e') + \frac{k_{2e}}{g}(\delta\tilde{a}_n' + a_{dn}') - \frac{\Omega_u}{g}(\delta\tilde{a}_e' + a_{de}') \\ (\delta\tilde{\omega}_u' - \delta\hat{\Omega}_u' + \frac{(k_{2u}+\Omega_n)}{g}(\delta\tilde{a}_n' + a_{dn}') \end{bmatrix}$$

$$\dot{\varphi}_n' = -k_{2n}\varphi_n' + (\delta\tilde{\omega}_n' - \delta\hat{\Omega}_n') - \frac{k_{2n}}{g}(\delta\tilde{a}_e' + a_{de}') - \frac{\Omega_u}{g}(\delta\tilde{a}_n' + a_{dn}')$$

These first equation corresponds directly to the error block diagram of Figure 21 except that more (small) error terms are present. It is seen from (59) that the azimuth error φ_u' does not depend upon angular rate disturbances in this mechanization. The applicability of this technique is limited, however, by the presence of north-axis acceleration disturbances. Although these effects are generally not as severe as those due to rate disturbances, they still preclude the use of this technique for rapid alignment in a helicopter environment.

The level axis misalignments φ_e' and φ_n' are also affected by acceleration disturbances, both using this classical alignment and the previously described scheme. Although the level axis effects are not as severe as the azimuth effects, it is desirable to reduce them as well.

The most obvious solution to the sensitivity of alignment to disturbance motions is to introduce additional filtering. This is readily accomplished: One such mechanization is shown in Figure 22. It is seen by comparison

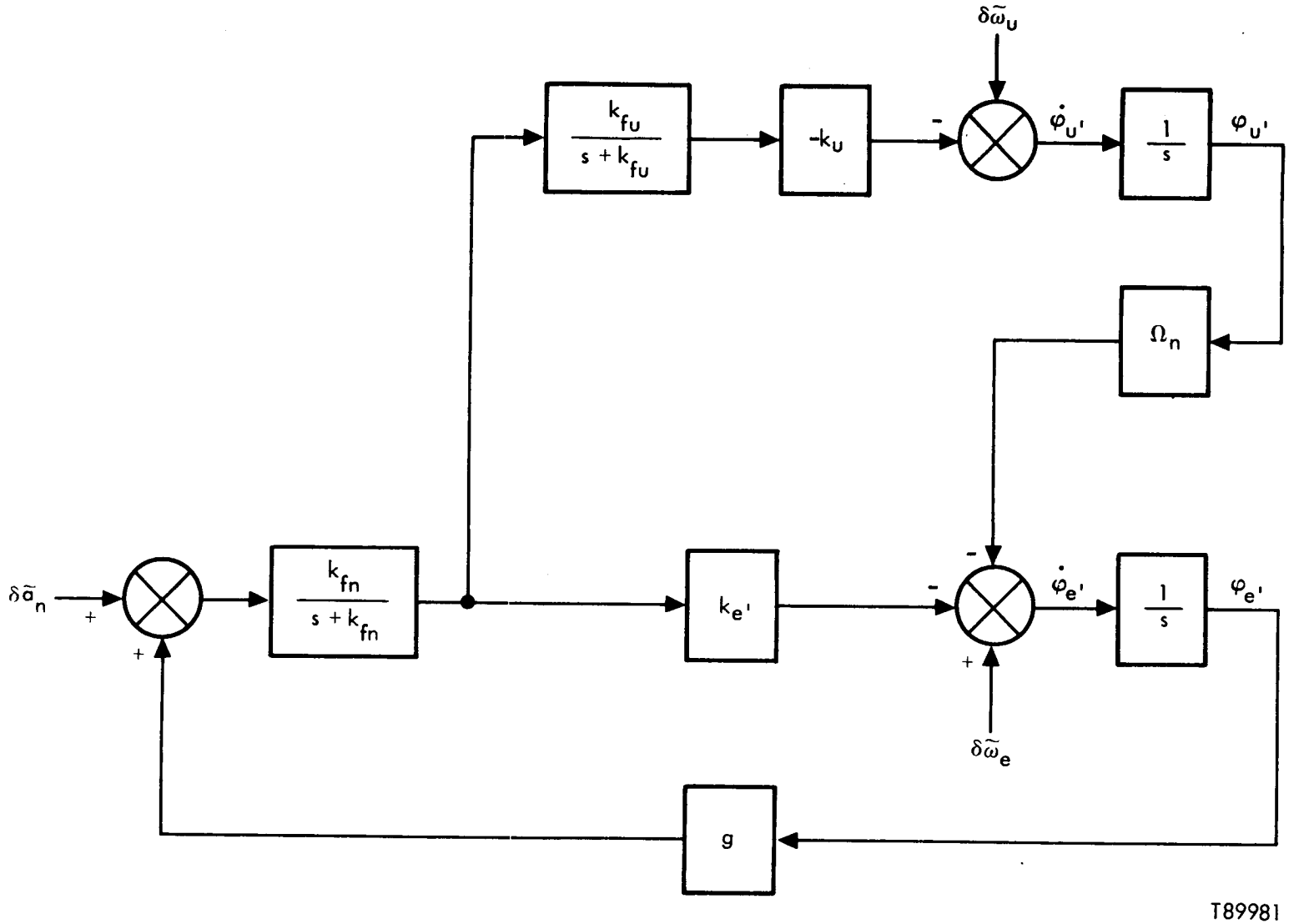

Figure 22. Fourth Order Gyrocompassing Loop Error Block Diagram

with Figures 20 and 21 that the basic alignment loops are unchanged except for the presence of three simple first-order digital filters. These filters are arranged in such a way that the error signal provided by the north accelerometer passes through two levels of filtering before use as an azimuth correction signal. (This is desirable since the azimuth error exhibits the most sensitivity to disturbances.)

Denoting the filter outputs by f_e, f_n, and f_u, the following equations describe the filters and correction signals

$$\dot{f}_e = -k_{fe} f_e - k_{fe} g \hat{\varphi}_n' \tag{60}$$

$$\dot{f}_n = -k_{fn} f_n + k_{fn} g \hat{\varphi}_e'$$

$$\dot{f}_u = -k_{fu} f_u + k_{fu} f_n$$

$$\underline{\xi} = K \begin{bmatrix} \varphi_e' \\ \varphi_n' \\ \varphi_u' \\ f_e' \\ f_n \\ f_u \end{bmatrix} \tag{61}$$

where K is an appropriate 3 x 6 weighting matrix. Combining (49) and (60), the following vector differential equation is obtained after some manipulation:

$$\begin{bmatrix} \dot{\varphi}_e' \\ \dot{\varphi}_n' \\ \dot{\varphi}_u' \\ \dot{f}_e \\ \dot{f}_n \\ \dot{f}_u \end{bmatrix} = \begin{bmatrix} \delta\tilde{\omega}_e' - \delta\hat{\Omega}_e' \\ \delta\tilde{\omega}_n' - \delta\hat{\Omega}_n' \\ \delta\tilde{\omega}_u' - \delta\hat{\Omega}_u' \\ k_{fe}(\tilde{\delta a}_e' + a_{de}') \\ k_{fn}(\tilde{\delta a}_n' + a_{dn}' \\ 0 \end{bmatrix} - \left\{ K + \begin{bmatrix} 0 & -\Omega_u & \Omega_n & k_{fe} & 0 & 0 \\ \Omega_u & 0 & 0 & 0 & k_{fn} & 0 \\ -\Omega_n & 0 & 0 & 0 & 0 & k_{fu} \end{bmatrix} \right\} \begin{bmatrix} \varphi_e' \\ \varphi_n' \\ \varphi_u' \\ f_e \\ f_n \\ f_u \end{bmatrix} \tag{62}$$

In order to correspond to Figure 22, K must be of the form

$$K = \begin{bmatrix} 0 & \Omega_u & 0 & 0 & k_e & 0 \\ -\Omega_u & 0 & 0 & -k_n & 0 & 0 \\ \Omega_n & 0 & 0 & 0 & 0 & -k_u \end{bmatrix} \tag{63}$$

In this case (62) decouples into a fourth-order loop involving φ_e' and φ_u' and a second order φ_n' loop, namely

$$\begin{bmatrix} \dot{\varphi}_e' \\ \dot{\varphi}_u' \\ \dot{f}_n' \\ \dot{f}_u' \end{bmatrix} = \begin{bmatrix} 0 & -\Omega_n & -k_e & 0 \\ 0 & 0 & 0 & +k_u \\ gk_{fn} & 0 & -k_{fn} & 0 \\ 0 & 0 & k_{fu} & -k_{fu} \end{bmatrix} \begin{bmatrix} \varphi_e' \\ \varphi_u' \\ f_n' \\ f_u' \end{bmatrix} + \begin{bmatrix} \delta\tilde{\omega}_e - \delta\hat{\Omega}_e' \\ \delta\tilde{\omega}_u - \delta\hat{\Omega}_u' \\ k_{fn}(\tilde{\delta a}_n' + a_{dn}') \\ 0 \end{bmatrix} \tag{64}$$

$$\begin{bmatrix} \dot{\varphi}_n' \\ \dot{f}_e' \end{bmatrix} = \begin{bmatrix} 0 & +k_n \\ gk_{fe} & -k_{fe} \end{bmatrix} \begin{bmatrix} \varphi_n' \\ f_e' \end{bmatrix} + \begin{bmatrix} \delta\tilde{\omega}_n' - \delta\hat{\Omega}_n' \\ k_{fe}(\tilde{\delta a}_e' + a_{de}') \end{bmatrix}$$

The Laplace transform solution of the first equation is

$$\begin{bmatrix} \varphi_e'(s) \\ \varphi_u'(s) \\ f_n'(s) \\ f_u(s) \end{bmatrix} = \begin{bmatrix} s & \Omega_n & k_e & 0 \\ 0 & s & 0 & -k_u \\ -gk_{fn} & 0 & (s+k_{fn}) & 0 \\ 0 & 0 & -k_{fu} & (s+k_{fu}) \end{bmatrix}^{-1} \left\{ \begin{bmatrix} \varphi_e'(0) \\ \varphi_u'(0) \\ f_n(0) \\ f_u(0) \end{bmatrix} + \begin{bmatrix} \delta\tilde{\omega}_e'(s) - \delta\hat{\Omega}_e'(s) \\ \delta\tilde{\omega}_u'(s) - \delta\hat{\Omega}_u'(s) \\ k_{fn}(\tilde{\delta a}_n(s) + a_{dn}(s)) \\ 0 \end{bmatrix} \right\} \tag{65}$$

The characteristic equation is

$$CE = s[s(s+k_{fn})(s+k_{fu})] - gk_{fn}[-k_{fu}k_u\Omega_n - s(s+k_{fu})k_e] \tag{66}$$

$$= s^4 + (k_{fn}+k_{fe})s^3 + (k_{fn}k_{fe}+gk_{fn}k_e)s^2 + gk_ek_{fu}k_{fn}s + gk_{fn}k_{fu}k_u\Omega_n$$

and the indicated matrix inverse is

$$M^{-1} = \frac{1}{CE}\begin{bmatrix} s(s+k_{fn})(s+k_{fu}) & -\Omega_n(s+k_{fn})(s+k_{fu}) & -s(s+k_{fu})k_e & -k_u\Omega_n(s+k_{fn}) \\ & & -\Omega_n k_u k_{fu} & \\ gk_uk_{fn}k_{fu} & s(s+k_{fn})(s+k_{fu}) & sk_uk_{fu} & sk_u(s+k_{fn}) \\ & +gk_ek_{fn}(s+k_{fu}) & & +gk_ek_uk_{fn} \\ +gk_{fn}s(s+k_{fu}) & -gk_{fn}\Omega_n(s+k_{fu}) & s^2(s+k_{fu}) & -k_u\Omega_n gk_{fn} \\ +gk_{fn}k_{fu}s & -g\Omega_n k_{fn}k_{fu} & s^2k_{fu} & s^2(s+k_{fn}) \\ & & & +gk_{fu}k_e s \end{bmatrix} \tag{67}$$

Applying the final value theorem, it is seen that the steady-state errors resulting from the bias instrument errors

$$\delta\widetilde{\omega}_e'(s) = \frac{\delta\omega_e'}{s} \tag{68}$$

$$\delta\widetilde{\omega}_u'(s) = \frac{\delta\omega_u'}{s}$$

$$\delta\widetilde{a}_n'(s) = \frac{\delta a_n'}{s}$$

are

$$\varphi_e'(s.s.) = -\frac{\delta\omega_u'}{gk_u} - \frac{\delta\widetilde{a}_n'}{g} \tag{69}$$

$$\varphi_u'(s.s.) = \frac{\delta\omega_e'}{\Omega_n} + \frac{k_e}{k_u}\frac{\delta\omega_u'}{\Omega_n}$$

which is in agreement with the steady-state errors of (44).

Experience has shown that a desirable transient response to initial errors results from choosing the constants k_{fn}, k_{fu}, k_e, and k_u so that the characteristic equation (66) is of the form

$$CE = [s^2 + 2\sigma s + (\sigma^2 + \omega^2)]^2 \tag{70}$$

$$= (s + \sigma + j\omega)^2 (s + \sigma - j\omega)^2$$

$$= s^4 + 4\sigma s^3 + (6\sigma^2 + 2\omega^2)s^2 + (4\sigma^3 + 4\sigma\omega^2)\, s + (\sigma^4 + 2\omega^2\sigma^2 + \omega^4)$$

$$= s^4 + 4\sigma s^3 + (8\sigma^2)\, s^2 + 8\sigma^3 s + 4\sigma^4$$

Equating terms in (66) and (70) it is found that

$$k_{fn} = k_{fu} = 2\sigma \tag{71}$$

$$k_e = \frac{\sigma^2 + \omega^2}{g\delta} = \frac{2\sigma^2}{g\sigma} = \frac{2\sigma}{g}$$

$$k_u = \frac{\sigma^4 + 2\omega^2\sigma^2 + \omega^4}{4g\Omega_n\sigma^2} = \frac{4\sigma^4}{4g\Omega_n\sigma^2} = \frac{1}{g\Omega_n\tau}$$

The response of φ_u' to disturbance accelerations is seen from (65) and (67) to be

$$\varphi_u'(s) = \frac{sk_u k_{fu}}{CE} k_{fn} a_{dn}'(s) \tag{72}$$

It is convenient for purposes of further analysis to assume $\omega = 0$, i. e. four equal system poles. This assumption has only minor effect on the accuracy of the results which follow. Under this assumption

$$\varphi_u'(s) = \frac{(s)\left(\frac{\sigma^2}{4g\Omega_n}\right)(4\sigma^2)}{(s+\sigma)^4} a_{dn}'(s) \tag{73}$$

$$= \frac{1}{\Omega_n} \frac{\sigma^4 s}{(s+\sigma)^4} \frac{a_{dn}'(s)}{g}$$

$$= \frac{1}{\Omega_n} \frac{s}{(\tau s+1)^4} \frac{a_{dn}'(s)}{g}$$

where $\tau = \frac{1}{\sigma}$ is the loop time constant. For a sinusoidal disturbance acceleration of the form $a_{dn}'(t) = a_{dn}' \sin \beta t$, the peak azimuth error is found from

$$\left|\varphi_u'\right|_{max} = \left|\frac{j\beta/\Omega_n}{(j\beta\tau+1)^4}\right| \frac{a_{dn}'}{g} \tag{74}$$

A useful asymptotic plot showing the relationships among τ, $|\varphi_u'|_{max}$, a_{dn}', and β is shown in Figure 23. Here the abscissa is the disturbance frequency β in rad/sec, the ordinate is the disturbance amplitude in g's normalized by the allowable maximum azimuth misalignment $|\varphi_u'|_{max}$ in milliradians, and the various curves represent the loop time constant required to achieve this misalignment value. The dashed line indicates the use of this plot for the case

Allowable $|\varphi_u'|_{max}$ = 1 m.r.

Disturbance Amplitude a_{dn}' = 10^{-4} g's

Disturbance Frequency β = 10^{-1} rad/sec

Latitude ϕ = 45^{o}

which shows that a loop time constant of approximately 30 seconds is required to filter the disturbance. Satisfactory reduction of initial errors in a fourth-order loop such as this requires approximately 7 time constants, so that a total gyrocompassing time of about 3 1/2 minutes would be required for this disturbance level.

The second equation in (64) describes the propagation of φ_n', the north axis level error. This error is much less sensitive to disturbance accelerations than is the azimuth error. For this reason, the time constant for this level loop is typically chosen to be of the order of 10 seconds. Since this is a second order loop, approximately 4 time constants are required to errect satisfactory alignment.

If a large east axis level error is present at the start of alignment, undesirable transients are intorduced into the gyrocompassing loop (62). For this reason the correction signal ξ_u is typically zeroed (by setting k_u to zero) and the level axis gain k_e increased in order to level align about the east axis prior to gyrocompassing. In this mode the response of φ_e' is essentially the same as the φ_n' response described above.

Kalman Filter Alignment. - The Kalman filter mechanization of inertial self-alignment is relatively straight-forward. The only major complication is in appropriate statistical modeling of the system error sources, specifically the instrument errors and the disturbance motions. The mechanization used in the alignment simulation is described in Section VI. The notation is identical with that utilized in the preceding sections.

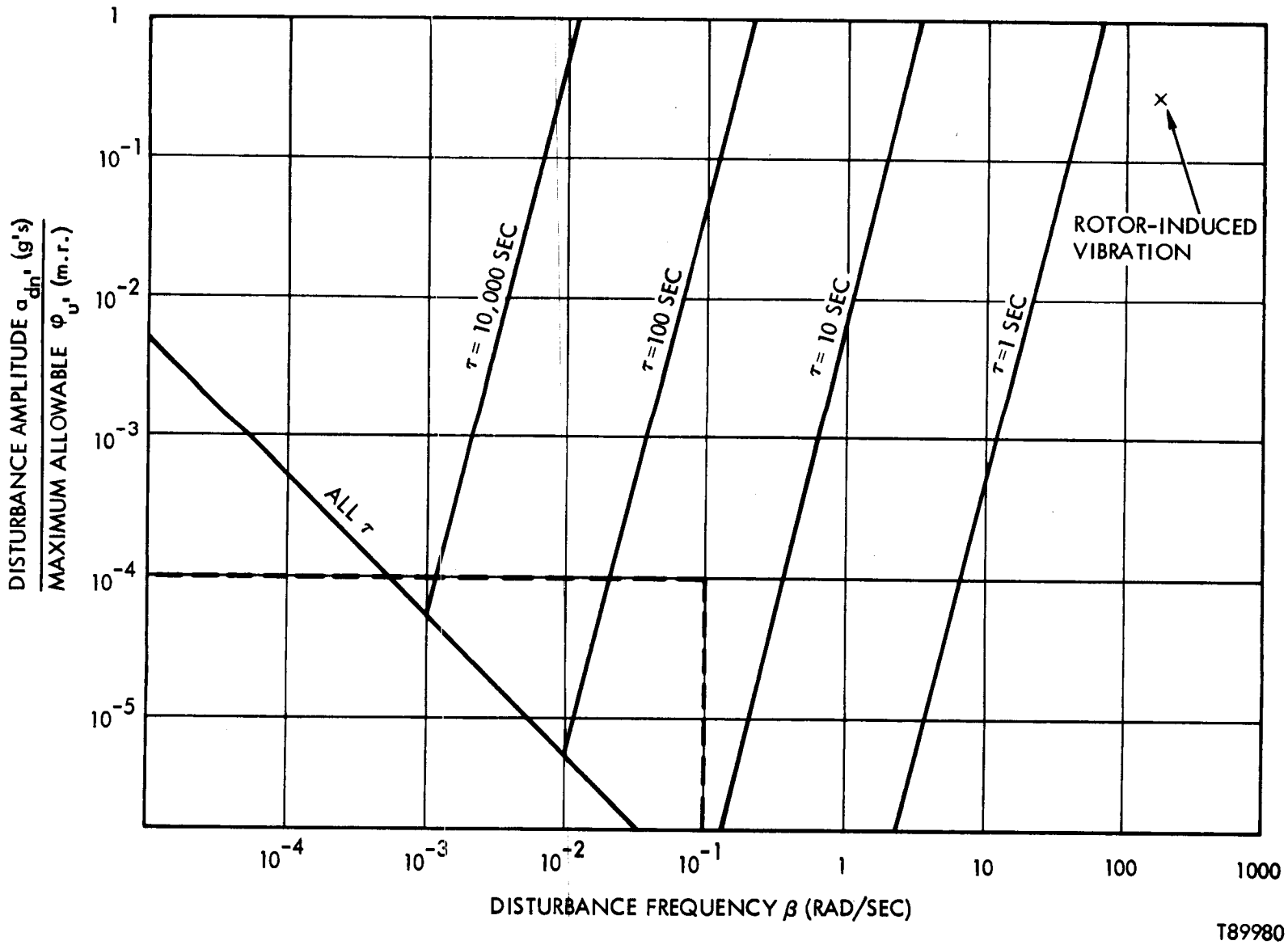

Figure 23. Required Gyrocompassing Loop Time Constants for Fourth Order Fixed Gain Filtering

Error Analysis

Introduction. -The error sources which contribute to navigation and attitude errors are of three general types: instrument or sensor errors, computational errors, and errors arising from approximations used in the mechanization equations. As described previously, the "full" set of mechanization equations are to be mechanized so that approximation errors are negligible in the present application. Computational errors are to a large extent under the control of the programmer. Care must be taken to assure that the resolution, precision, etc., used for each computation is compatible with the overall system accuracy requirements. Sensor errors are less easily controlled and consequently are the major contributors to system error.

In this section both the sensor and computation errors are analyzed in order to estimate the navigation and attitude accuracy of the strapdown navigator. A conventional "Schuler loop" technique is employed in order to obtain a simple and reasonably complete understanding of the essential error behavior without the complicating effects of cross-channel coupling. Experience has shown this technique to be valid for mission times of a few hours or less, particularly for low velocity and moderate accuracy applications such as the one being considered here.

At least two other error analysis techniques are appropriate for estimating the accuracy of navigation and attitude information for a strapdown navigator. The first is, in actuality, an extension of the Schuler loop analysis technique which is employed in this section. This method involves solving a complete set of error differential equations, including cross-coupling terms, on a digital computer in conjunction with a mission profile generator which provides the mission-dependent parameters needed for the solution. This type of analysis is quite useful in applications involving high velocities and/or long mission times since the cross-coupling effects are important to such cases. The primary disadvantage in this technique is that the essential understanding of the system error behavior is easily lost in the complexity of the program, i.e., even though the results are somewhat more accurate for any specific set of mission conditions, it is difficult to extrapolate to more general conditions from the outputs of the simulation. For this reason the Schuler loop "hand" analysis has been chosen for the present analysis.

The second alternative technique involves direct simulation of the system (as opposed to the linearized error equations). Using this method it is possible to evaluate computational errors, non-linear effects, algorithm truncation errors, etc. directly by comparing the error-corrupted effects with a "truth model" generated by a parallel simulation channel. The major problem with this technique

is that it is very inefficient - it may require many hours of computer time to simulate even a few minutes of real time operation. Such a program has been written during the course of the present study and is described in a later section. Due to the time limitations described above, however, this program has been used primarily as a verification tool for the analytical studies which have been conducted.

The error analysis in this section is performed for a non-redundant instrument configuration. This is somewhat pessimistic since a redundant system provides angular rate and acceleration information which is inherently more accurate than a non-redundant system (assuming all instruments are operating).

Derivation of the Schuler Loop Model. - The attitude error propagation of the strapdown system has been derived for a stationary system in the alignment section (Equation (15)). The corresponding error propagation for a moving vehicle is obtained by replacing the earth rate vector $\underline{\Omega}$ by the sum of earth rate and position rate, i. e., by $\underline{\Omega} + \underline{\rho}$, and deleting the alignment control vector $\underline{\xi}$. The resulting propagation equation is readily found to be

$$\dot{\underline{\varphi}}^{r'} \simeq \delta\tilde{\underline{\omega}}^{r} - \delta\hat{\underline{\Omega}}^{r} - \delta\underline{\rho}^{r} - (\underline{\Omega}^{r} + \underline{\rho}^{r}) \times \underline{\varphi}^{r'} \tag{1}$$

where

$$\underline{\delta\rho} \triangleq \hat{\underline{\rho}} - \underline{\rho} \tag{2}$$

Observing that

$$\delta\underline{\rho}^{r'} = \delta b^{*}\delta\underline{\rho}^{r}\delta b$$

$$= \begin{bmatrix} \delta\rho_e & - & \rho_u\varphi_n' & + & \rho_n\varphi_u' \\ \delta\rho_n & - & \rho_e\varphi_u' & + & \rho_u\varphi_e' \\ \delta\rho_u & - & \rho_n\varphi_e' & + & \rho_e\varphi_n' \end{bmatrix} \tag{3}$$

$$= \delta\underline{\rho}^{r} + \underline{\rho}^{r} \times \underline{\varphi}^{r'}$$

(1) may be rewritten as

$$\dot{\underline{\varphi}}^{r'} \simeq \delta\tilde{\underline{\omega}}^{r} - \delta\hat{\underline{\Omega}}^{r} - \delta\underline{\rho}^{r'} - \underline{\Omega}^{r} \times \underline{\varphi}^{r'} \tag{4}$$

The earth rate cross-coupling given by the last term in (4) may reasonably be neglected except for terms involving φ_u' since the leveling errors φ_e' and φ_n' are quite small. In this case

$$\begin{aligned}
\dot{\varphi}_e' &\simeq \delta\tilde{\omega}_e - \delta\hat{\Omega}_e - \delta\rho_e' - \Omega_n\varphi_u' \\
\dot{\varphi}_n' &\simeq \delta\tilde{\omega}_n - \delta\hat{\Omega}_n - \delta\rho_n' \\
\dot{\varphi}_u' &\simeq \delta\tilde{\omega}_u - \delta\hat{\Omega}_u - \delta\rho_u'
\end{aligned} \tag{5}$$

Consider next the error in computation of level axis velocity components. The true rate of change of velocity is given by

$$\dot{\underline{v}} = \underline{a} + (2\underline{\Omega} + \underline{\rho}) \times \underline{v} - \underline{g} \tag{6}$$

while the computed vector is

$$\hat{\dot{\underline{v}}} = \tilde{\underline{a}} + (2\hat{\underline{\Omega}} + \hat{\underline{\rho}}) \times \hat{\underline{v}} - \hat{\underline{g}} \tag{7}$$

so that the error is

$$\begin{aligned}
\delta\hat{\dot{\underline{v}}} &= \hat{\dot{\underline{v}}} - \dot{\underline{v}} \\
&= (\hat{\underline{a}} - \underline{a}) - (\hat{\underline{g}} - \underline{g}) + [(2\hat{\underline{\Omega}} + \hat{\underline{\rho}}) \times \hat{\underline{v}} - (2\underline{\Omega} + \underline{\rho}) \times \underline{v}] \\
&\simeq \hat{\underline{a}} - \underline{a}
\end{aligned} \tag{8}$$

where the approximation arises from neglecting gravity errors and errors in the computation of the small acceleration correction terms involving corolis and centrupital accelerations. Using (19) this becomes

$$\begin{aligned}
\delta\hat{\dot{\underline{v}}}^{r'} &= \hat{\underline{a}}^{r'} - \underline{a}^{r'} \\
&= \delta b^* \underline{a}^r \delta b + \hat{b}\delta\tilde{\underline{a}}^p\hat{b}^* - \underline{a}^r
\end{aligned} \tag{9}$$

and the level error components are

$$\begin{bmatrix} \delta\hat{\dot{v}}_e' \\ \delta\hat{\dot{v}}_n' \end{bmatrix} = \begin{bmatrix} -g\varphi_n' \\ g\varphi_e' \end{bmatrix} + \begin{bmatrix} \delta\tilde{a}_e' \\ \delta\tilde{a}_n' \end{bmatrix}$$

$$\begin{bmatrix} -g\varphi_n' + \delta\tilde{a}_e \\ g\varphi_e' + \delta\tilde{a}_n \end{bmatrix} \tag{10}$$

The position rate errors $\delta\rho_e'$ and $\delta\rho_n'$ are directly related to the level velocity errors. Neglecting the second order effects of altitude and ellipticity

$$\delta\rho_e' \simeq -\frac{\delta v_n'}{a}$$

$$\delta\rho_n' \simeq \frac{\delta v_e'}{a} \tag{11}$$

Finally, consider the errors in computing position. It is convenient for error analysis purposes to consider east and north position errors rather than latitude and longitude errors. Thus

$$\begin{aligned} \delta\hat{p}_e &= \hat{p}_e - \dot{p}_e \\ &= a\cos\phi\,(\hat{\dot{\lambda}} - \dot{\lambda}) \\ &= \hat{v}_e - v_e \\ &= \delta\hat{v}_e \\ &\simeq \delta\hat{v}_e' + v_n\varphi_u' \\ \delta\hat{p}_n &= a\,(\hat{\dot{\phi}} - \dot{\phi}) \\ &= \delta\hat{v}_n \\ &\simeq \delta\hat{v}_n' - v_e\varphi_u' \end{aligned} \tag{12}$$

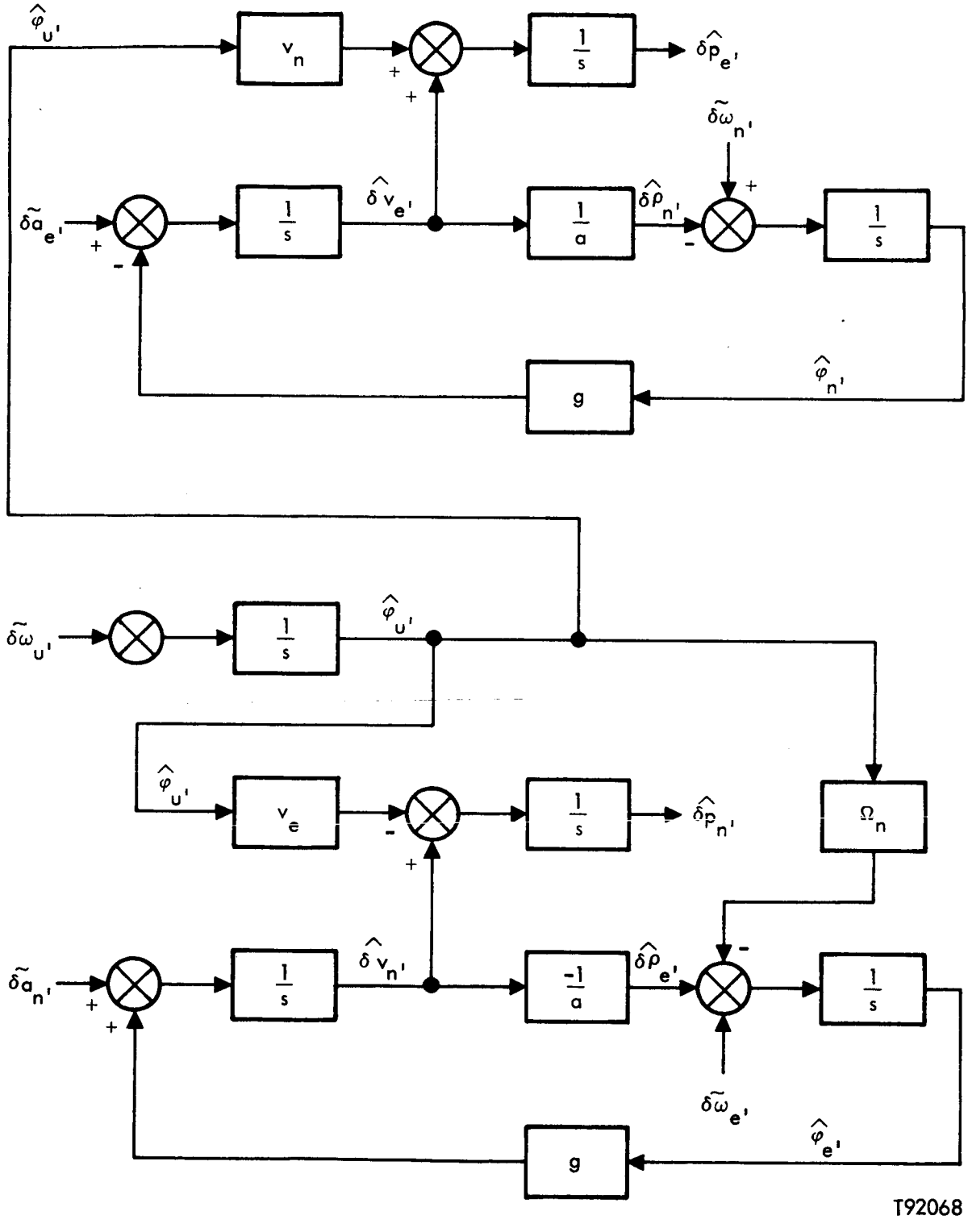

Figure 24. Schuler Loop Block Diagram

Error Propagation. - The differential equation describing error propagation in the east gyro -- north accelerometer loop is

$$\begin{bmatrix} \dot{\hat{\delta p}}_n \\ \dot{\hat{\delta v}}_n' \\ \dot{\hat{\varphi}}_e' \\ \dot{\hat{\varphi}}_u' \end{bmatrix} = \begin{bmatrix} 0 & 1 & 0 & -v_e \\ 0 & 0 & g & 0 \\ 0 & -\frac{1}{a} & 0 & -\Omega_n \\ 0 & 0 & 0 & 0 \end{bmatrix} \begin{bmatrix} \hat{\delta p}_n \\ \hat{\delta v}_n' \\ \hat{\varphi}_e' \\ \hat{\varphi}_u' \end{bmatrix} + \begin{bmatrix} 0 \\ \delta\tilde{a}_n \\ \delta\tilde{\omega}_e \\ \delta\tilde{\omega}_u \end{bmatrix} \tag{13}$$

The solution, assuming constant v_e and Ω_n, is given by

$$\begin{bmatrix} \hat{\delta p}_n \\ \hat{\delta v}_n' \\ \hat{\varphi}_e' \\ \hat{\varphi}_u' \end{bmatrix} = e^{At} \left\{ \begin{bmatrix} \hat{\delta p}_n(0) \\ \hat{\delta v}_n'(0) \\ \hat{\varphi}_e'(0) \\ \hat{\varphi}_u'(0) \end{bmatrix} + \int_0^t e^{-A\tau} \begin{bmatrix} 0 \\ \delta\tilde{a}_n(\tau) \\ \delta\tilde{\omega}_e(\tau) \\ \delta\tilde{\omega}_u(\tau) \end{bmatrix} d\tau \right\} \tag{14}$$

where e^{At} is readily found, using Laplace transform techniques, to be

$$e^{At} = \begin{bmatrix} 1 & \frac{1}{\beta}\sin\beta t & a(1-\cos\beta t) & -v_e t - a\Omega_n\left(t-\frac{1}{\beta}\sin\beta t\right) \\ 0 & \cos\beta t & \sqrt{ag}\,\sin\beta t & -a\Omega_n(1-\cos\beta t) \\ 0 & -\frac{1}{\sqrt{ag}}\sin\beta t & \cos\beta t & -\frac{\Omega_n}{\beta}\sin\beta t \\ 0 & 0 & 0 & 1 \end{bmatrix} \tag{15}$$

where $\beta = \sqrt{g/a}$ is the Schuler frequency.

The response of the loop to initial condition errors may be found directly by subsituting (15) into (14). The response to bias type instrument errors is found by performing the indicated integration in (14):

$$e^{At}\int_0^t e^{-A\tau}\begin{bmatrix}0\\ \delta\tilde{a}_n\\ \delta\tilde{\omega}_e\\ \delta\tilde{\omega}_u\end{bmatrix}d\tau = e^{At}\int_0^t e^{-A\tau}d\tau\begin{bmatrix}0\\ \delta\tilde{a}_n\\ \delta\tilde{\omega}_e\\ \delta\tilde{\omega}_u\end{bmatrix}$$

$$= \begin{bmatrix} t & \frac{1}{\beta^2}(1-\cos\beta t) & a(t-\frac{1}{\beta}\sin\beta t) & -\frac{1}{2}(v_e + a\Omega_n)t^2 + \frac{a\Omega_n}{\beta^2}(1-\cos\beta t)\\ 0 & \frac{1}{\beta}\sin\beta t & a(1-\cos\beta t) & a\Omega_n(t-\frac{1}{\beta}\sin\beta t)\\ 0 & -\frac{1}{g}(1-\cos\beta t) & \frac{1}{\beta}\sin\beta t & -\frac{\Omega_n}{\beta^2}(1-\cos\beta t)\\ 0 & 0 & 0 & t \end{bmatrix}\begin{bmatrix}0\\ \delta\tilde{a}_n\\ \delta\tilde{\omega}_e\\ \delta\tilde{\omega}_u\end{bmatrix} \quad (16)$$

Finally, consider the effects of instrument noise-type errors. Assuming that these are independent zero-mean white gaussian processes with

$$E\delta\tilde{a}_n(t)\,\delta\tilde{a}_n(\tau) = q_{an}\delta(t-\tau)$$

$$E\delta\tilde{\omega}_e(t)\,\delta\tilde{\omega}_e(\tau) = q_{\omega e}\delta(t-\tau) \quad (17)$$

$$E\delta\tilde{\omega}_n(t)\,\delta\tilde{\omega}_e(\tau) = q_{\omega u}\delta(t-\tau)$$

where $\delta(t-\tau)$ is the Dirac delta function, the covariance of the resulting errors is found from

$$\text{cov}\begin{bmatrix}\delta\hat{p}_n\\ \delta\hat{v}_n'\\ \hat{\varphi}_e'\\ \hat{\varphi}_u'\end{bmatrix} = E\int_0^t\int_0^t e^{A\tau}\begin{bmatrix}0\\ \delta\tilde{a}_n(\tau)\\ \delta\tilde{\omega}_e(\tau)\\ \delta\tilde{\omega}_n(\tau)\end{bmatrix}\begin{bmatrix}0\\ \delta\tilde{a}_n(\xi)\\ \delta\tilde{\omega}_e(\xi)\\ \delta\tilde{\omega}_u(\xi)\end{bmatrix}^T e^{A^T\xi}d\xi d\tau$$

$$= \int_0^t e^{A\tau}\,\text{diag}\,[0,\ q_{an},\ q_{\omega e},\ q_{\omega u}]\,e^{A^T\tau}d\tau \quad (18)$$

which may be integrated to obtain

$$E[\delta\hat{p}_n(t)]^2 = q_{an}\left[\frac{1}{\beta^2}\left(\frac{1}{2}t - \frac{1}{4\beta}\sin 2\beta t\right)\right]$$

$$+ q_{\omega e}\left[a^2\left(\frac{3}{2}t - \frac{2}{\beta}\sin\beta t + \frac{1}{4\beta}\sin 2\beta t\right)\right]$$

$$+ q_{\omega u}\left[(v_e + a\Omega_n)^2\frac{t^3}{3} - \frac{2a\Omega_n(v_e + a\Omega_n)}{\beta^2}(\sin\beta t - \beta t\cos\beta t) + \frac{a^2\Omega_n^2}{\beta^2}\left(\frac{1}{2}t - \frac{1}{4\beta}\sin 2\beta t\right)\right]$$

$$E[\delta\hat{v}_n'(t)]^2 = q_{an}\left[\frac{1}{2}t + \frac{1}{4\beta}\sin 2\beta t\right]$$

$$+ q_{\omega e}\left[ag\left(\frac{1}{2}t - \frac{1}{4\beta}\sin 2\beta t\right)\right] \qquad (20)$$

$$+ q_{\omega u}\left[a^2\Omega_n^2\left(\frac{3}{2}t - \frac{2}{\beta}\sin\beta t + \frac{1}{4\beta}\sin 2\beta t\right)\right]$$

$$E[\hat{\varphi}_e'(t)]^2 = q_{an}\left[\frac{1}{ag}\left(\frac{1}{2}t - \frac{1}{4\beta}\sin 2\beta t\right)\right]$$

$$+ q_{\omega e}\left[\frac{1}{2}t + \frac{1}{4\beta}\sin 2\beta t\right]$$

$$+ q_{\omega u}\left[\frac{\Omega_n^2}{\beta^2}\left(\frac{1}{2}t - \frac{1}{4\beta}\sin 2\beta t\right)\right]$$

$$E[\hat{\varphi}_u'(t)]^2 = q_{\omega u}t$$

The error propagation for the north gyro-east accelerometer loop may be obtained almost by inspection from the results obtained above. The response to initial conditions is

$$\begin{bmatrix} \hat{\delta p}_e \\ \hat{\delta v}_e' \\ \hat{\varphi}_n' \end{bmatrix} = \begin{bmatrix} 1 & \frac{1}{\beta}\sin\beta t & -a\,(1-\cos\beta t) & v_n t \\ 0 & \cos\beta t & -\sqrt{ag}\sin\beta t & 0 \\ 0 & \frac{1}{\sqrt{ag}}\sin\beta t & \cos\beta t & 0 \end{bmatrix} \begin{bmatrix} \hat{\delta p}_e\,(0) \\ \hat{\delta v}_e'\,(0) \\ \hat{\varphi}_n'\,(0) \\ \hat{\varphi}_u'\,(0) \end{bmatrix} \tag{21}$$

The response to bias sensor errors is

$$\begin{bmatrix} \hat{\delta p}_e \\ \hat{\delta v}_e' \\ \hat{\varphi}_n' \end{bmatrix} = \begin{bmatrix} \frac{1}{\beta^2}(1-\cos\beta t) & -a(t-\frac{1}{\beta}\sin\beta t) & \frac{1}{2}v_n t^2 \\ \frac{1}{\beta}\sin\beta t & -a\,(1-\cos\beta t) & 0 \\ \frac{1}{g}(1-\cos\beta t) & \frac{1}{\beta}\sin\beta t & 0 \end{bmatrix} \begin{bmatrix} \widetilde{\delta a}_e \\ \widetilde{\delta\omega}_n \\ \widetilde{\delta\omega}_n \end{bmatrix} \tag{22}$$

Finally, the response to noise-type errors is

$$\begin{aligned} E\,[\hat{\delta p}_e(t)]^2 &= q_{ae}\left[\frac{1}{\beta^2}\left(\frac{1}{2}t - \frac{1}{4\beta}\sin 2\beta t\right)\right] \\ &\quad + q_{\omega n}\left[a^2\left(\frac{3}{2}t - \frac{2}{\beta}\sin\beta t + \frac{1}{4\beta}\sin 2\beta t\right)\right] \\ &\quad + q_{\omega u}\left[v_n^2\,\frac{t^3}{3}\right] \\ E\,[\hat{\delta v}_e'(t)]^2 &= q_{ae}\left[\frac{1}{2}t + \frac{1}{4\beta}\sin 2\beta t\right] \\ &\quad + q_{\omega n}\left[ag\left(\frac{1}{2}t - \frac{1}{4\beta}\sin 2\beta t\right)\right] \\ E\,[\hat{\varphi}_n'(t)]^2 &= q_{ae}\left[\frac{1}{ag}\left(\frac{1}{2}t - \frac{1}{4\beta}\sin 2\beta t\right)\right] \\ &\quad + q_{\omega n}\left[\frac{1}{2}t + \frac{1}{4\beta}\sin 2\beta t\right] \end{aligned} \tag{23}$$

Sensor Errors. - The propagation of errors which has been derived above is sufficient to evaluate the effects of all important types of sensor errors and initial alignment errors. The effects of initial condition errors, bias errors, and noise-type errors may be evaluated directly using the equations which have been developed. Other types of errors may be treated similarily by assuming nominal mission conditions.

Gyro scale factor uncertainty errors are proportional to the total inertial angular rate components in platform coordinates. As discussed previously,

$$\begin{bmatrix} \omega_x \\ \omega_y \\ \omega_z \end{bmatrix} = \begin{bmatrix} \zeta_x \\ \zeta_y \\ \zeta_z \end{bmatrix} + \begin{bmatrix} \Omega_x \\ \Omega_y \\ \Omega_z \end{bmatrix} + \begin{bmatrix} \rho_x \\ \rho_y \\ \rho_z \end{bmatrix}$$

For "straight and level" flight the body rate vector $\underline{\zeta}$ is zero, while the components of $\underline{\Omega} + \underline{\rho}$ are approximately constant. Thus if γ_{xsf} is the sacle factor of the x-gyro and A/D converter is, the resulting error is equivalent to an x-gyro bias of

$$\delta\omega_x = \gamma_{xsf} (\Omega_x + \rho_x)$$

with similar results for the y and z axes. Since, in the present application, pitch and roll motions are limited in magnitude, the effects of scale factor errors on ζ_x and ζ_y average approximately to zero. Azimuth motion is unlimited, however, and can result in significant scale factor errors. Assuming that the turns are made in times short compared to the Schuler period, these errors may be approximated by step function azimuth alignment errors of magnitude

$$\varphi_z = \gamma_{zsf} \Delta\psi$$

where $\Delta\psi$ is the total change in heading angle. Such errors propagate in the same manner as an initial azimuth error. Thus if t* is the time of the heading change, and $\underline{y} = \underline{n}$ (0^o heading) after the turn, the resultant n' - velocity error is, using (15)

$$\delta v_n'(t) = -a\Omega_n (1 - \cos\beta(t-t^*))$$

Gyro mass unbalance and quadrature errors result in gyro drifts during periods of vehicle acceleration. Assuming the acceleration periods are short compared to the Schuler period, these errors can be treated as step function level and azimuth misalignment errors. For example, the "tilt" offset resulting from a brief velocity change of Δv_x for a gyro with mass unbalance coefficient m_x is

$$\varphi_x = M_x \Delta v_x$$

which would propagate in the same manner as an initial leveling error. Similarily, a quadrature coefficient q_x would result in a step tilt of

$$\varphi_x = \Omega_x \Delta v_y$$

Gyro anisoelastic (g^2-sensitive- errors may be treated in a manner similar to g-sensitive errors except that they result from simultaneous accelerations along the gyro spin and input axes. Thus, again assuming brief acceleration periods, an x gyro anisoelasticity coefficient of A_x would result in a step tilt error of

$$\varphi_x = A_x \Delta v_x \Delta v_y$$

which, or course, propagates in the same manner as an initial level error.

Gyro non-orthogonality or instrument alignment errors behave in the same manner as scale factor errors except that they are proportional to the orthogonal components of $\underline{\omega}$ rather than the direct component. Thus an x-gyro non-orthorogality coefficient of γ_{xno} (assuming $\underline{\zeta} = 0$ as before) results in an error which is equivalent to a bias error of

$$\delta\omega_x = \gamma_{xno} \left[(\Omega_x + \rho_x)^2 + (\Omega_y + \rho_y)^2 \right]^{1/2}$$

Accelerometer errors may be treated in much the same manner as gyro errors. The primary difference is that g-sensitive errors result in step velocity errors rather than step tilt errors. Such step velocity errors propagate in the same manner as initial velocity errors.

Digital Computation Errors - There are three basic types of quantization errors which affect the accuracy of the computations. The first is quantization of the inputs to the computation. The second is the quantization of coefficients used in the computation. The third type is quantization of the result of the computation. Each of the three types of error affects the accuracy of the system in different ways [7, 8].

Problems associated with coefficient rounding can frequently be eliminated or ameliorated by careful scaling. In cases where this is not possible, selective double precision computations may be used to remove the problem.

Quantization of the results of a computation is generally most critical in cases for which the result is used for succeeding computations of the same parameter. An example is the computation of attitude where the computed

quaternion for one iteration is used in the update computations for the next iteration. Again, this type of quantization error may be minimized by using full or partial double precision computations in critical areas. Such errors have been extensively evaluated during the present study by means of computer simulation. This simulation is described in a later section.

While the effects of coefficient and result quantization errors can generally be kept small by appropriate programming this is not generally the case for input errors. The most serious of these errors are the result of quantization in the A/D conversion process.

Assume that the conversion is k bits (i.e., k-1 plus sign). One LSB is then $s_{max} 2^{-k+1}$, where s_{max} is the maximum signal to be converted. The maximum quantization error per conversion is 1/2 LSB, or $s_{max} 2^{-k}$. In order to examine the effects of such errors, assume that the angular rate conversions in the normal operating range of the A/D converter are scaled for a maximum rate of 8^{o}/sec and that a 14 bit conversion is used. Then the error per iteration is uniformly distributed with variance

$$\sigma_d^2 = \frac{(s_{max} 2^{-k})^2}{3}$$

$$= \frac{(8^{o}/\text{sec})^2 (2^{-14})^2}{3} = 2.42 \times 10^{-11} \left(\frac{\text{rad}}{\text{sec}}\right)^2$$

Since typically several LSB's of noise are present on the gyro output the quantization error will be random from conversion to conversion, i.e., it will appear as a zero mean white noise sequence. The "equivalent" white noise process (continuous rather than discrete) has variance

$$\sigma_c^2 = \sigma_d^2 \tau$$

where τ is the conversion iteration time for the signal. The conversion rate is typically 8 KHz so that τ is 125 μsec and

$$\sigma_c^2 = (2.42 \times 10^{-11}) (1.25 \times 10^{-4}) = 3.03 \times 10^{-15}$$

which is equivalent to a random drift rate of

$$\delta\omega_{random} = \sqrt{\sigma_c^2}$$

$$= .011^{o}/\text{hr}$$

It has been shows previously that such random errors propagate with the square root of time and result in errors which are negligibly small compared with bias type errors of similar magnitude.

Mission Profile. - In order to examine the relative importance of the individual error sources it is useful to select a typical mission profile in order to evaluate the specific error propagation. To this end the following assumptions are made:

1) The system aligns on the ground with the longitudinal axis pointing in an easterly direction.

2) The vehicle takes off and accelerates in 60 seconds to 200 ft/sec velocity.

3) Heading during acceleration is 0^{o}.

4) Vehicle cruises at 200ft/sec and 0^{o} heading for 2 hour flight with level attitude.

5) Geographic latitude is 45^{o}

These conditions are appropriate for the application under consideration and are particularly useful from the standpoint of analysis since

1) Initial alignment errors are effectively decorrelated from instrument biases.

2) Accelerations are brief so that the g-sensitive approximations described previously may be utilized.

3) Accelerations occur near the beginning of the mission and may thus be treated as initial condition errors.

4) Earth rate is isolated to the y and z axes and position rate to the x axis during flight.

Table 24 shows the position errors resulting from each of the major system error sources for the chosen mission conditions for mission times of 1 and 2 hours. All bias and scale factor errors include both sensor and A/D converter errors since it is assumed that the corresponding parameters are calibrated on the system level rather than individually. It is apparent from Table 24 that the system accuracy, expressed in terms of the circular error probable (CEP) is 1.0 to 1.5 nautical miles per hour and thus well in excess of the required 3 miles per hour.

Table 24. Error Analysis Summary

Error Source	Error Magnitude	t = 1 hr $\delta p_{e'}$	t = 1 hr $\delta p_{n'}$	t = 2 hr $\delta p_{e'}$	t = 2 hr $\delta p_{n'}$
X-Gyro Bias Stability	$.01^{o}$/hr	--	4460	--	6930
X-Gyro Random Drift	$.005^{o}$/hr	--	43	--	51
X-Gyro A/D Quantization	14 Bits	--	85	--	101
X-Gyro SF Uncertainty	100 ppm	--	89	--	139
X-Gyro SF Non-Linearity	70 ppm	--	63	--	97
X-Gyro Non-Orthogonality	20 $\widehat{sec}$	--	631	--	977
X-Gyro Mass Unbalance	$.1^{o}$/hr/g	--	63	--	118
X-Gyro Quadrature	$.1^{o}$/hr/g	--	neg	--	neg
X-Gyro Anisoelasticity	$.05^{o}$/hr/g^2	--	neg	--	neg
Y-Gyro Bias Stability	$.01^{o}$/hr	4460	--	6930	--
Y-Gyro Random Drift	$.005^{o}$/hr	43	--	51	--
Y-Gyro A/D Quantization	14 Bits	85	--	101	--
Y-Gyro SF Uncertainty	100 ppm	446	--	693	--
Y-Gyro SF Non-Linearity	70 ppm	312	--	485	--
Y-Gyro Non-Orthogonality	20 $\widehat{sec}$	455	--	707	--
Y-Gyro Mass Unbalance	$.1^{o}$/hr/g	neg	--	neg	--
Y-Gyro Quadrature	$.1^{o}$/hr/g	neg	--	neg	--
Y-Gyro Anisoelasticity	$.05^{o}$/hr/g^2	neg	--	neg	--
Z-Gyro Bias Stability	$.02^{o}$/hr	126	560	503	2440
Z-Gyro Random Drift	$.005^{o}$/hr	neg	neg	neg	neg
Z-Gyro A/D Quantization	14 Bits	neg	neg	neg	neg
Z-Gyro SF Uncertainty	100 ppm	neg	28	25	122
Z-Gyro SF Non-Linearity	70 ppm	neg	20	18	85
Z-Gyro Non-Orthogonality	20 $\widehat{sec}$	neg	29	26	124
Z-Gyro Mass Unbalance	$.1^{o}$/hr/g	neg	neg	neg	neg
Z-Gyro Quadrature	$.1^{o}$/hr/g	neg	13	neg	21
Z-Gyro Anisoelasticity	$.05^{o}$/hr/g^2	neg	neg	neg	neg

Table 24. Error Analysis Summary (Continued)

Error Source	Error Magnitude	t = 1 hr $\delta p_{e'}$	t = 1 hr $\delta p_{n'}$	t = 2 hr $\delta p_{e'}$	t = 2 hr $\delta p_{n'}$
X Accel Bias Stability	10^{-4} g	2630	--	3930	--
X Accel A/D Quantization	14 Bits	19	--	neg	--
X Accel SF Uncertainty	100 ppm	16	--	8	--
X Accel SF Non-Linearity	70 ppm	11	--	6	--
X Accel Non-Orthogonality	20 $\widehat{sec}$	neg	--	neg	--
X Accel Cross-Coupling	$5\mu g/g^2$	neg	--	neg	--
Y Accel Bias Stability	10^{-4} g	--	2630	--	3930
Y Accel A/D Quantization	14 Bits	--	neg	--	neg
Y Accel SF Uncertainty	100 ppm	--	neg	--	neg
Y Accel SF Non-Linearity	70 ppm	--	neg	--	neg
Y Accel Non-Orthogonality	20 $\widehat{sec}$	--	16	--	8
Y Accel Cross-Coupling	$5\mu g/g^2$	--	neg	--	neg
Initial X-Axis Level Error	20 $\widehat{sec}$	--	2630	--	3930
Initial Y-Axis Level Error	20 $\widehat{sec}$	2630	--	3930	--
Initial Z-Axis Misalignment	1 mr	720	4460	1440	6930
Initial East Position Error	1000 ft	1000	--	1000	--
Initial North Position Error	1000 ft	--	1000	--	1000
RSS Totals		5981	7440	9140	11620
CEP		7860 ft = 1.3 nmi		12150 ft = 2.0 nmi	

Computational Requirements

A preliminary analysis of computational requirements for the strapdown navigator has been performed. Table 25 summarizes the memory requirements for the basic inertial navigation mechanization equations. The memory requirements shown are based upon a direction cosine attitude representation. The corresponding quaternion representation requires approximately the same number of total words.

Table 26 shows the corresponding timing analysis for both quaternion and direction cosine implementations of the attitude equations. It is clear from this analysis that use of the quaternion representation provides a significant advantage in terms of computer timing requirements, but that neither representation is overly demanding on computer time for the 30 Hz iteration rate.

These estimates are somewhat optimistic in that single precision operations have been assumed for the attitude update equations. The use of selective double precision operations in these computations will increase both memory and time requirements by a small amount.

The memory and timing requirements of Tables 25 and 26 are independent of the type and level of redundancy which is employed. Other areas resulting in substantial computer loading are affected by such considerations, however. These are sensor error compensation, failure detection and isolation, and the data processing associated with combining the redundant sensor data into the basic angular rate and acceleration required for the attitude and navigation equations.

The sensor error compensation corrects for the important "static" and dynamic sensor and converter errors. The static error compensation includes corrections for sensor biases, scale factor variations, non-orthogonality errors, direct and quadrature gyro mass unbalance errors, etc., and for temperature sensitive variations in these parameters. The dynamic error compensation corrects for all important (predictable) sensor errors which occur under dynamic operating conditions. For a non-redundant system these computations require approximately 400 words of memory and roughly 400 μsec of time per computer iteration. For a full fail-op/fail-op redundant system the number of sensors doubles and hence the sensor error compensation computer requirements also increase by approximately a factor of two (although some memory saving may result from "looping" repetitive computations).

The computer requirements associated with failure detection and isolation and with the processing of multiple signals varies widely with the level and type of redundancy which is employed, with the sensor orientations which are used, and with the degree of sophistication which is used in the computations.

Table 25. Computer Storage Requirements for Solution of Strapdown Inertial Navigation Mechanization Equations

Routines	Iteration Rate	Permanent Words	Dedicated Scratch
Data Inputs and Rate Extraction	60 Hz	79	40
Update Accelerometer Terms	30 Hz	25	3
Align Computations	30 Hz	190	45
Gyro Rate Computations	30 Hz	54	9
Initialize (B)	30 Hz	55	12
Extrapolate (B)	30 Hz	164	9 (Shared)
Initialize (C)	10 Hz	62	18
Extrapolate (C)	10 Hz	40	18 (Shared)
Update Vehicle Velocity	10 Hz	54	12
Position Rates	10 Hz	38	6
Gravity Compensation	10 Hz	11	3
10 Hz Divider	10 Hz	5	1
Present Position Equations	10 Hz	34	3
Attitude and Heading	10 Hz	35	4
Interrupt Service	N. A.	8	2

Table 25. Computer Storage Requirements for Solution of Strapdown Inertial Navigation Mechanization Equations (Continued)

Routines	Iteration Rate	Permanent Words	Dedicated Scratch
Executive and Miscellaneous	N. A.	60	5
Power on Initialization	N. A.	75	15
Floated Arc. $\tan^{-1}$	Async	31	-
Tan^{-1}	"	63	-
Sine-Cosine	"	27	-
Sin^{-1}	"	23	-
ABS/X	"	7	-
Float	"	21	-
Constants	"	110	-
Total Words		1271	205

Table 26. Timing Analysis for Solution of Strapdown Inertial Navigation Mechanization Equations

Computer Instructions

Attitude Mechanization	Add/ Sub	Load/ Store	Multi- ply	Trans- fer	Shift	Total Time (μsec)
Direction Cosine						
Number	93	155	78	29	36	
Time (μsec)	248	413	468	77	96	1302
Quaternion						
Number	63	105	66	29	18	
Time (μsec)	168	280	396	77	48	969

It is estimated that a minimum of 1000 words of memory would be required for fail-op/fail-op redundancy. The number could easily double if more sophisticated processing techniques are employed. Timing requirements appear to be comparable to the requirements for the inertial computations.

In summary, it appears that

1) The TDY-43 speed is more than adequate for the computations which are required for a fail-op/fail op strapdown inertial navigation.

2) A non-redundant system will require between 2000 and 2500 words of memory. A 4K memory is thus more than adequate for such a system.

3) It appears that a 4K memory is marginal for redundant applications if the failure detection/isolation and signal processing algorithms are kept as simple as possible. For more sophisticated (and hence more accurate) techniques additional memory will be required.

Study of Analog to Digital Conversion Techniques

Introduction. -Early in the development of the two-degree-of-freedom dry tuned-gimbal gyro the need for an accurate torquing method that would produce a digital representation of the angular rates was recognized. Investigation showed that neither pulse torquing nor a voltage-to-frequency conversion would be as accurate as a well implemented analog-to-digital technique. Therefore, it was decided to analog torque the gyros, as this gives the best accuracy, and to use a multiplexed A/D converter. The purpose of this portion of the study is to examine the various A/D conversion techniques in common usage today, establish which technique is most appropriate for the present Strapdown System Application and to analyze this technique for its contribution to the overall system error budget.

There are many problems that are common to any type of A/D converter regardless of what technique is utilized. These problems relate not only to operation, circuitry and performance, but also to such propositions as to whether or not a sample/hold circuit is needed at the input, or buffering at the output, to power supply and reference supply requirements, to amplifier characteristics, to trade-offs, to the form of input and output signals, bipolar operation, etc. This study will concentrate on operation and performance, hence most of these latter problems will not be discussed in great detail.

In the course of this investigation, the field of candidate A/D converter techniques was rapidly narrowed to two very popular and widely used types that are quite adaptable for system work. These two types are the successive-approximation A/D converter and the integration or simple ramp-comparison A/D converter.

The technique which appears the most adaptable to the subject system application, utilizes a Main A/D converter that is a high-speed, linear successive-approximation type. In general the performance of a successive-approximation A/D converter is a compromise between static accuracy and conversion speed. The higher the conversion speed is set, the lower will be the accuracy that can be obtained from the converter. As mechanized by Teledyne, this converter utilizes various peripheral techniques to enhance the accuracy of the main A/D converter while preserving its inherent speed. These techniques are detailed in the following study.

Summary of Various A/D Converter Techniques. -A wide variety of A/D converter techniques is known today, however the most popular conversion techniques in actual use can be catagorized into the following types:

1. Parallel-feedback direct A/D converter.
2. Serial-feedback direct A/D converter.
3. Indirect A/D converter
4. Voltage to incremental digital converter.
5. Logarithmic A/D converter.

After some initial investigation, it was quickly determined that of the whole spectrum of candidate techniques, only two showed any promise for the subject application. These are the successive-approximation A/D converter and the integration or simple ramp-comparision A/D converter. The others were eliminated based on inaccuracy, conversion speed, circuit complexity etc. The successive-approximation technique falls under the category of parallel-feedback direct A/D conversion while the integration technique is an indirect A/D converter method. The comparison of these two converter techniques is the subject of the following paragraphs.

Integration (Simple Ramp-Comparison) A/D Converter. -The ramp-comparison technique is the fundamental principle of all indirect converters. This family of converters is quite popular. Its members perform the indirect conversion by first converting to a function of time, then converting from the time function to a digital number using a counter.

This study will consider a particular type of ramp-comparison converter that has been frequently used in inertial navigation systems. The converter is basically a dual ramp Reset Integrator type, whereby an analog integrator is utilized to generate a ramp output which is proportional to the dc current input. A threshold detector generates a reset pulse when the ramp exceeds a preset threshold. This is accomplished by switching into the integrator input an analog current which is opposite in polarity and of magnitude relative to the input signal such as to cause the output of the integrator to reverse direction and drop below the threshold point of the detector by a fixed increment. The threshold detector and reset pulse maintains the ramp amplitude below the threshold with a series of reset pulses. The rate at which the ramp continues to exceed the threshold, in the presence of the reset pulses, is indicative of the average dc current injected at the input. Hence, the pulse rate is proportional to the input dc current.

The basic Reset Integrator is illustrated in Figure 25. The output of the Reset Integrator is ternary in nature. That is, pulses are generated at the plus or minus outputs (but not simultaneously) depending on the polarity of the input current. The current at the input is transformed into a voltage by utllizing shunt resistors which also scale the input quantity to the dynamic voltage range of the A/D converter input. A typical range for the converter is $\pm$ 10 volts dc. The input voltage is integrated with the operational amplifier

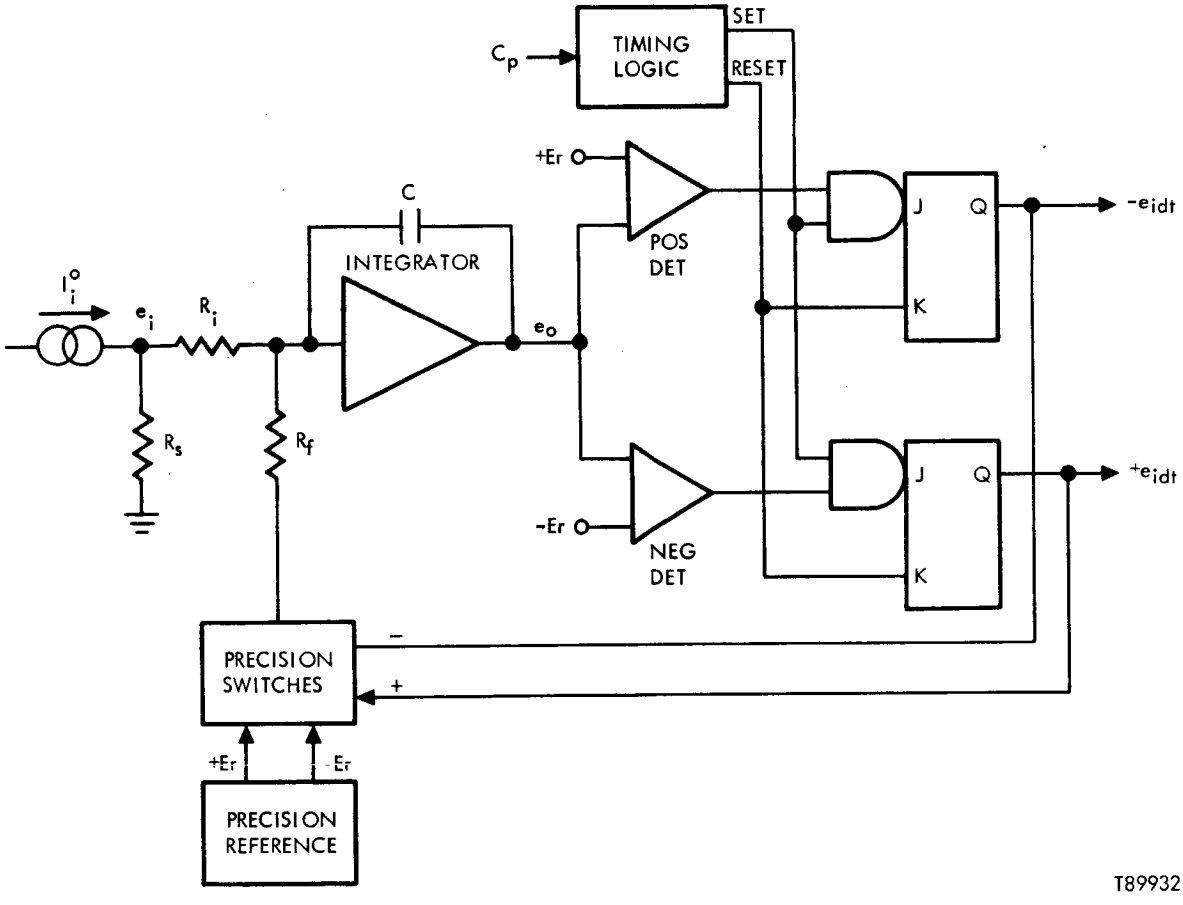

Figure 25. Block Diagram of Reset Integrator

integrator, where the output voltage is equal to the integral of the input voltage (assuming the precision feedback switches are "off"). The output expressed mathematically is:

$$e_o = \frac{1}{R_i C}\int e_i \, dt \tag{1}$$

The output voltage is applied simultaneously to two differential comparator level detectors which determine when the output exceeds the voltage threshold. A separate detector is used for each input polarity. When the output of the integrator exceeds a threshold, the output of the detector enables its corresponding flip flop to be set. The timing logic causes the flip flop to be set at the appropriate bit time which is in synchronism with the computer clock since the basic timing signal for the A/D converter, Cp, is derived from the computer clock. The timing logic also generates a reset pulse for the flip flop, providing precise timing for the reset pulse width. The output of the flip flop is high for one pulse width period, as controlled by the set-reset pulse separation. It generates an output, $e_i dt$, to the computer and a precise pulse width signal, t_1, to the feedback switch. A diagram illustrating the basic timing for the A/D converter is shown in Figure 26.

The feedback switch enables a reference voltage, E_r, to be applied to the integrator summing junction through the reset feedback resistor, R_f. The polarity of the reference voltage applied to the amplifier is a function of the threshold detector whose threshold was exceeded. The net reset voltage is integrated, thereby driving the output voltage below the threshold. The reset pulse, which is a precise increment, can be defined as

$$\Delta e_o = \int_o^{t_1} \frac{E_r \, dt}{R_f C}$$

$$\Delta e_o = \frac{E_r t_1}{R_f C} \tag{2}$$

In actual operation, at any given time t, the integrator output, as reset by the feedback pulses, has a value corresponding to

$$e_o = \int_o^t \frac{e_i \, dt}{R_i C} - N\Delta e_o \tag{3}$$

where N is the accumulation, or number, of pulses out of the Reset Integrator.

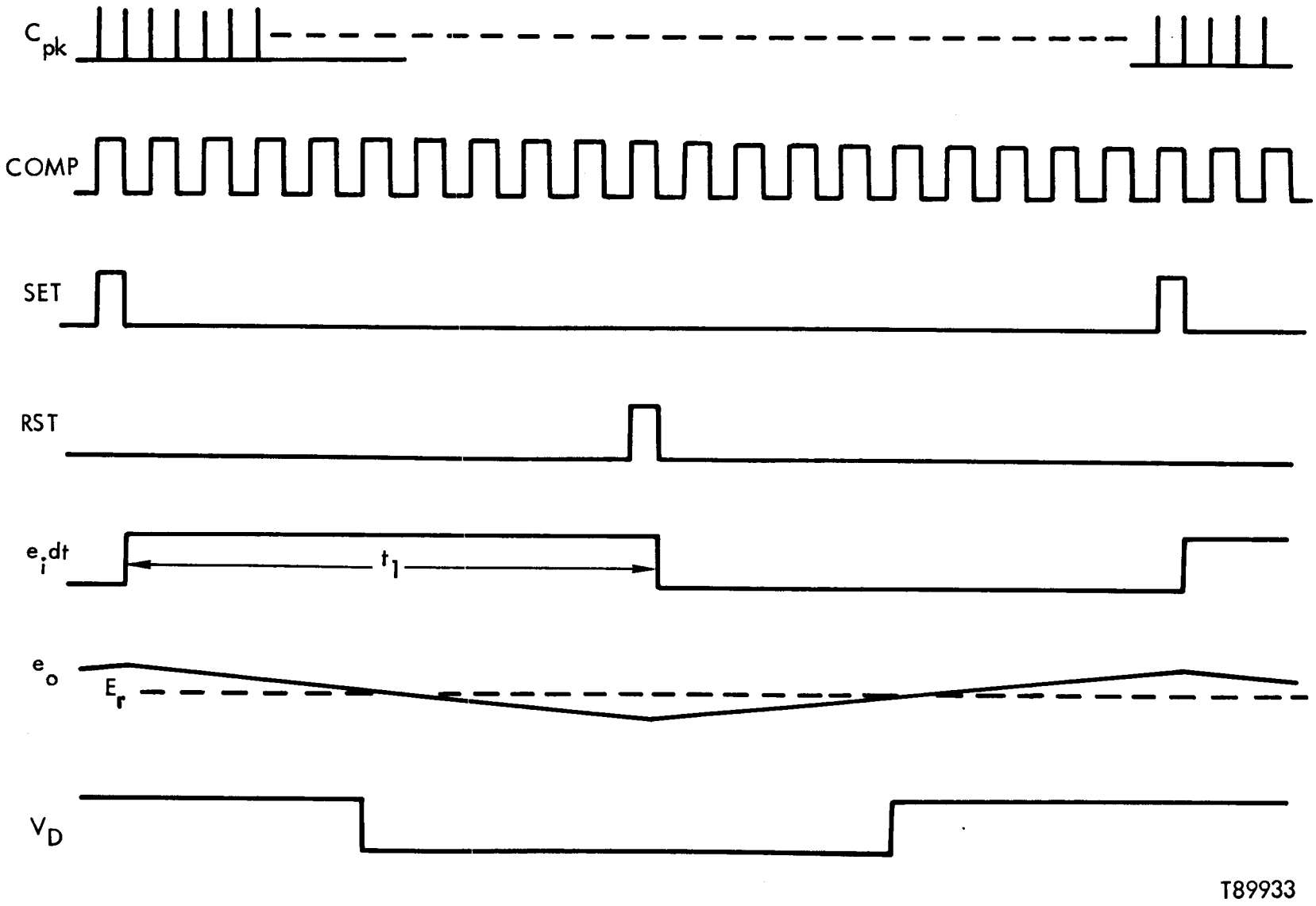

Figure 26. Timing Diagram and Voltage Waveforms for e_i = Full Scale

The output pulse train from the Reset Integrator is the most significant part of the solution. The integral term reflects the residue in the integrator and is less than the resolution of the A/D converter. Neglecting the quantization term and substituting equation (1) and (2) into the balance of (3) yields

$$\frac{1}{R_i C}\int e_i dt = N\left(\frac{E_r t_1}{R_f C}\right) \tag{4}$$

Differentiating equation (4) with respect to time and re-arranging to express the output pulse rate in terms of the input voltage gives

$$\frac{dN}{dt} = \left(\frac{R_f}{R_i}\right)\left(\frac{e_i}{E_r}\right)\frac{1}{t_1} \tag{5}$$

The terms in equation (5) define the major parameters which contribute to the scale factor of the A/D converter. Equation (5) is significant in that it says that the first order static accuracy of the scale factor is a function of the ratio of the source and feedback resistors, voltage reference and pulse width (clock frequency). Also, since all of the parameters except E_r are common and scaled for either input polarity the symmetry between positive and negative inputs is affected only by the differences in the two voltage references.

The foregoing discussion applies to the somewhat idealized condition where actual leakage currents and offsets of the integrator amplifier and feedback switches are ignored. These must be considered in any design where high accuracy is desired. A second area which must be considered relates to the dynamic errors such as switch drive feed-through, switch rise/fall time and turn-on/turn-off non-symmetry which affect the precision of the feed back pulse wave shape. The greatest error anticipated is the effect of positive-negative asymmetry in the precision pulse generator. This error is given by the following relationship:

$$\omega_E = \frac{\omega_m}{2F_+}\left(F_+ - F_-\right) \tag{6}$$

where

ω_E = effective equivalent gyro drift rate

ω_m = peak magnitude of assumed sinusoidal angular rate input

F_+ = positive scale factor of precision pulse generator

F_- = negative scale factor of precision pulse generator

During alignment it is assumed that $\omega_m = 360^o/hr$, $\frac{F_+ - F_-}{F_+} = 100$ ppm

Under these conditions

$$\omega_e = \frac{360}{2} \times 10^{-4} = 0.018^o/hr$$

This error results in a gyrocompass angular orientation error of approximately 0.1 degree.

This large error source is a distinct disadvantage that is not easily circumvented and, coupled with other inherent disadvantages, such as limited throughput rate, the Reset Integrator style of A/D converter was not chosen for application in the subject strapdown inertial system.

The A/D conversion technique which is judged most applicable, utilizes a Main A/D converter that is a high speed linear successive-approximation type which is described below. The overall conversion technique, that employs various peripheral technique to improve accuracy, will be detailed in later paragraphs.

Successive Approximation A/D Converter. - This type provides the binary equivalent of the ratio of the analog input signal and the D.C. Reference. Refer to the block diagram shown in Figure 27. The two signals (VA1 and VA2) are provided to the converter for comparison. One input, VA2, is attenuated by a factor KD through the ladder network and compared to the other input, VA1. In a sequence of successive steps, the feedback voltage, (KD) (VA2), is made to approximate the input voltage, VA1, where during each step the feedback voltage is changed in accordance with the result of the previous comparison between VA1 and (KD) (VA2). The amount by which the feedback voltage is increased or decreased is $V_R/2^{-i}$ where i defines the step in the operation. The output of the comparator systematically drives the logic, utilizing this successive approximation technique, until the digital feedback quantity to the ladder, KD, is of such value that the output of the comparator is at null. Hence, when the loop is forced to null:

$$VA1 = KD \times VA2 \qquad (7)$$

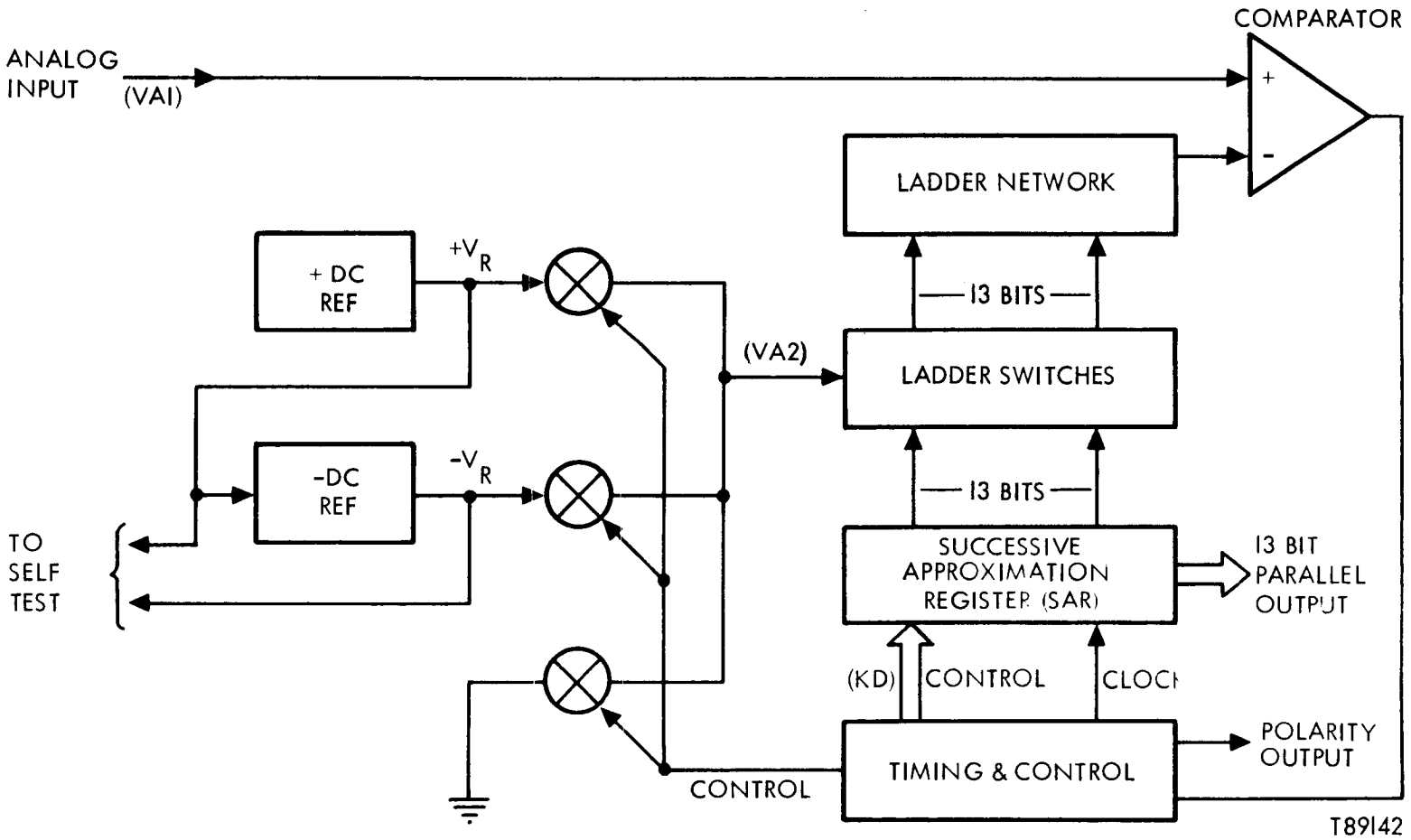

Figure 27. Block Diagram of Main A/D Converter

and

$$KD = \frac{VA1\ (Signal)}{VA2\ (Reference)} = \text{Digital Data.} \qquad (8)$$

Before the successive approximation conversion process starts the ladder network is grounded and the comparator used to determine the polarity of the input signal. This comparison is used as the most significant bit (MSB), bit 14, of the digital data and switches in the reference voltage which corresponds to the same polarity. This method of polarity and then magnitude conversion insures maximum linearity and accuracy about zero volts.

This converter constitutes what will be referred to in following paragraphs as the Main A/D converter while the overall conversion system will be denoted as the ADC. The ADC contains additional circuitry that increases the versitility and enhances the accuracy of the Main A/D. Error analyses were performed for the complete conversion system and are presented in the final paragraphs of this study. A general description of the ADC is given below.

Analog To Digital Conversion System. -The Analog to Digital Converter (ADC) performs the function of converting the Gyro, the Accelerometer, and the Temperature signals into digital data. Self-test signals are also converted to verify the integrity of the converter. The ADC block diagram is shown in Figure 28. All inputs are scaled and conditioned to be in a standard voltage range acceptable to the converter before being multiplexed into a high impedance buffer. The buffer outputs are switched into the Main A/D along with a Dither signal as required. The Main A/D performs a 14 Bit conversion (13 Bits magnitude and 1 Bit polarity) on the analog signal. The logic section performs the channel address decoding, the conversion timing and control functions and the summation and computational logic required to meet the required accuracy and resolution requirements.

The Main A/D is time shared by all of the conditioned analog input signals and alternates between inputs from channel A and channel B. The input channel selection logic is such that input signals are addressed alternately from MUX A and MUX B with MUX C being a sub-multiplexer of MUX A. (The Gyro inputs can be split between MUX A and B to allow a higher conversion rate on these inputs). The signal conditioning circuits are shown in Figure 29 and are mainly scaling resistors with only the temperature inputs requiring gain.

As the dynamic range at the input of the ADC would be somewhat limited, the scaling of the gyros is changed upon command of IMU digital logic testing the converter outputs. An A-C dither is also inserted into the input of the Main A/D to elevate the low rate signals to more readable levels. The dither

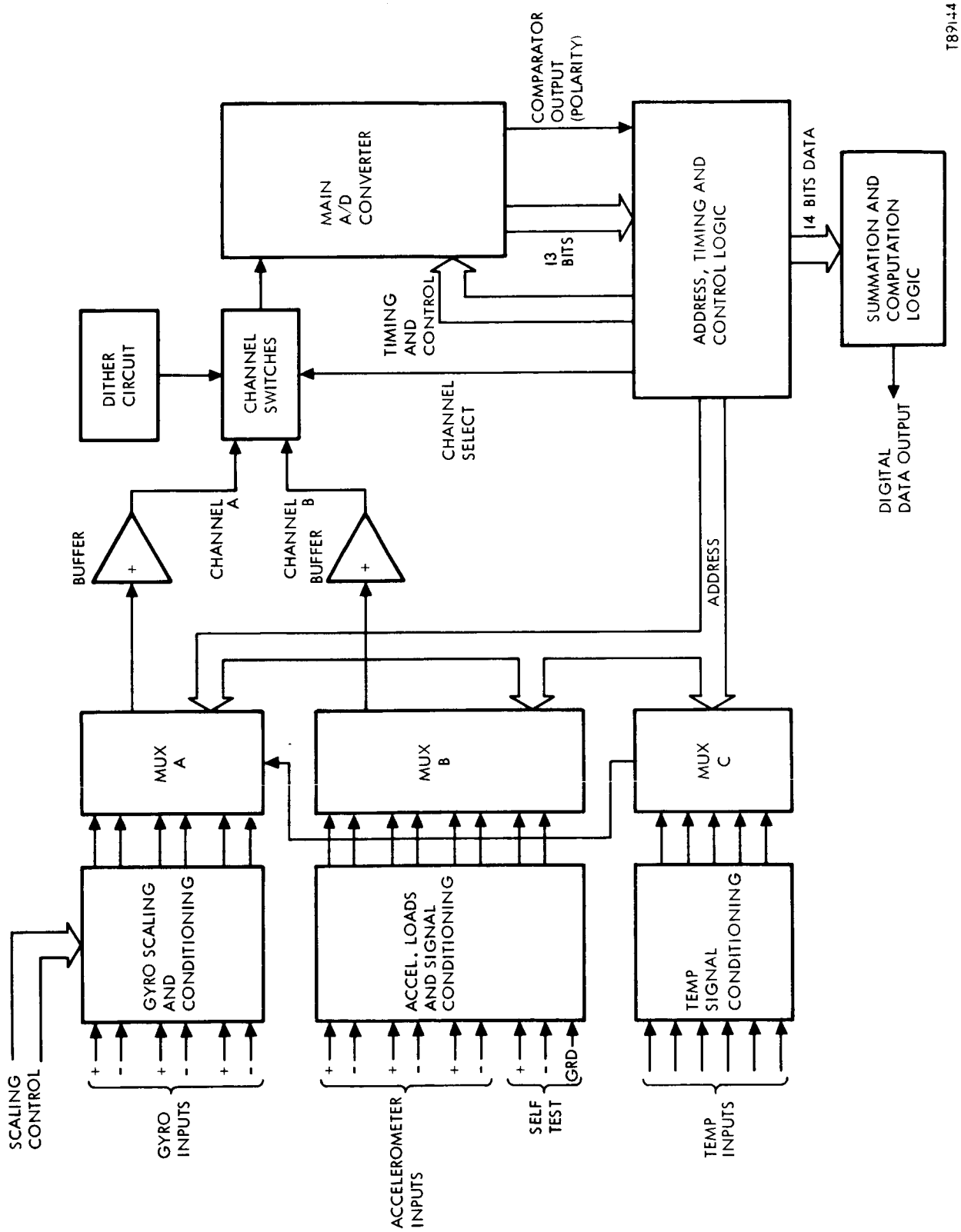

Figure 28. A/D Converter Block Diagram

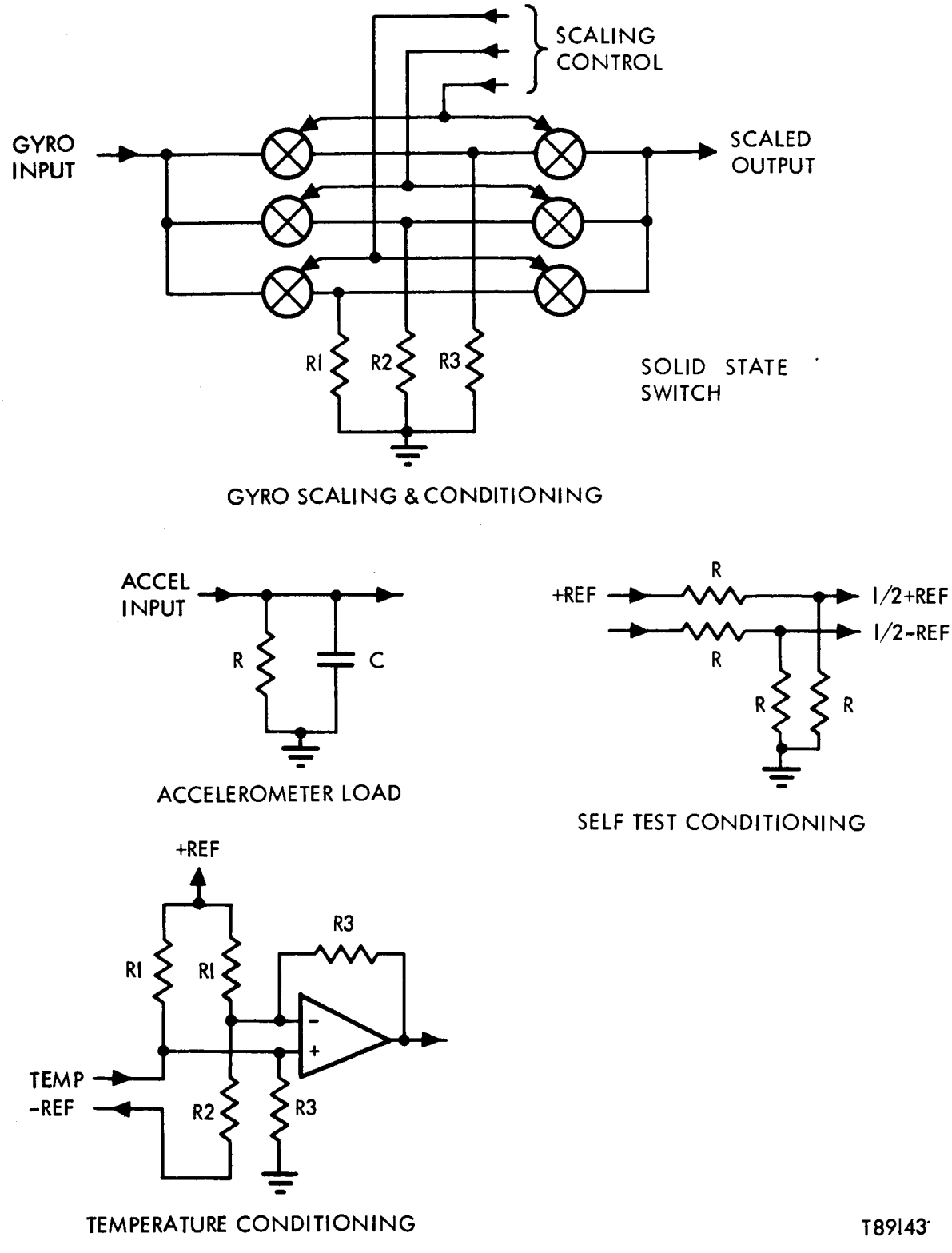

Figure 29. Scaling and Conditioning Circuits

also improves the linearity of the Main A/D, as the input signal follows the dither voltage resulting in an averaging of the signal over some part of the ADC input range.

To improve the effective resolution of the converter, averaging (buffer summing) is done on each high speed conversion channel before the data are transferred to the computer each problem cycle.

As symmetry of the scale factor is of great importance in a strapdown application, the gyro output is mechanized to have both a positive and negative torquing signal so that the difference of these two will eliminate the dither and any non-symmetry that may occur in either the gyro or ADC. This differencing is done in the computer.

An additional advantage of the proposed self-calibrating system is that the A/D scale factors and biases are also calibrated along with the instrument scale factors and biases as lumped effects so that any changes in these critical parameters with time, an inherent risk with long storage, may be compensated properly in the computer.

ADC Operation. - The A/D conversion methods are as described in the preceeding paragraphs. The analog inputs are all processed through a multiplexer unit and a high speed analog to digital converter. Timing signals from the IMU control logic are used to time the operations of the multiplexer and the Main A/D converter, as well as to provide sorting out and buffer summing of the various output signals between major computation iterations.

The accuracy of the A/D conversion is enhanced by two procedures: the introduction of a "dither" signal ahead of the Main A/D converter as a means for minimizing converter quantization errors and the averaging of a number of independent measurements in order to minimize the variance. As an additional procedure, the two reverse-polarity drive signals to each gyro and accelerometer torquer are converted to digital form separately and combined by computer program. This approach results effectively in a "common-mode rejection" of conversion bias.

The dither signal is a large amplitude triangular wave as compared to the quantization level of the A/D converter (LSB corresponds to about one millivolt). The slope of the dither signal is about $\pm$ 1 volt/ms = $\pm$ 1 mv/μs. Since the shortest interval between successive conversions of the same (equivalent) parameter (ω_R+ and ω_R- in this case) is two time slots or 65.2 microseconds, two successive readings for an unchanged signal level will differ by some 65 mv or, equivalentally, about 65 quantization units. This spread between successive converted values and the fact that the dither frequency is completely independent

of the data scanning (or any other) frequency is sufficient to establish the converted value as a random variable with a probability density function bounded by $\pm$ 1/2 LSB and distributed uniformly about a value corresponding to the true value of the input analog signal offset by the converter bias (all error sources other than quantization and converter bias are ignored here).

The most critical conversion process relates to the gyro signals, which must first be converted from analog currents to analog voltages by the use of precision resistors, and then to digital signals for subsequent computer processing. Two multiplexer input channels are utilized for the outputs from each gyro axis which are brought out in the form of a dual differential circuit, taking advantage of the gyro design which employs two push-pull torquer coils per gyro axis. A simplified block diagram of one gyro channel of A/D conversion is shown in Figure 30. The analog signal E_1 is ideally the same magnitude but the opposite polarity of the corresponding signal E_1. The timing of the multiplexer switching and A/D conversion is such that E_1 and E_1' are alternately sampled, converted and separately summed in the output registers labeled E_1 and E_1' in Figure 30.

The computer takes the algebraic difference between the E_1 and E_1' registers every major computation cycle, thus obtaining a measure of gyro angular rate over this constant time interval, equivalent to a small change in angular motion. This algebraic differencing process results in the elimination of the normal common mode errors due to the ADC voltage offset variation and due to the dither voltage, which is used to effectively eliminate the quantization error of the 14 bit Main A/D Converter. In addition, and of significance in the performance of this, as well as any other precision inertial digital output, is the fact that the above described algebraic differencing process provides an extremely symmetric output with respect to positive versus negative polarity inputs, resulting in negligible output rectification from this source. Actual test results show bias variations less than 1 ppm (parts per million) of full scale, a rectification error with an alternating peak voltage input of half full scale of less than 1 ppm, and a standard deviation from linearity error of 37 ppm over the full scale. If required, the bias error, which is almost entirely due to a small differential voltage bias of the multiplexer input pair for each gyro channel, can be effectively eliminated by periodically switching the connections of the input pair simultaneously, with a corresponding change in the polarity of the algebraic differencing process used for the output register, as described above.

ADC Error Analyses. -In the foregoing paragraphs a considerable concern was expressed relating to A/D conversion accuracy and error sources. In this section, error analyses are presented which will support Teledyne's selection of this technique for A/D conversion.

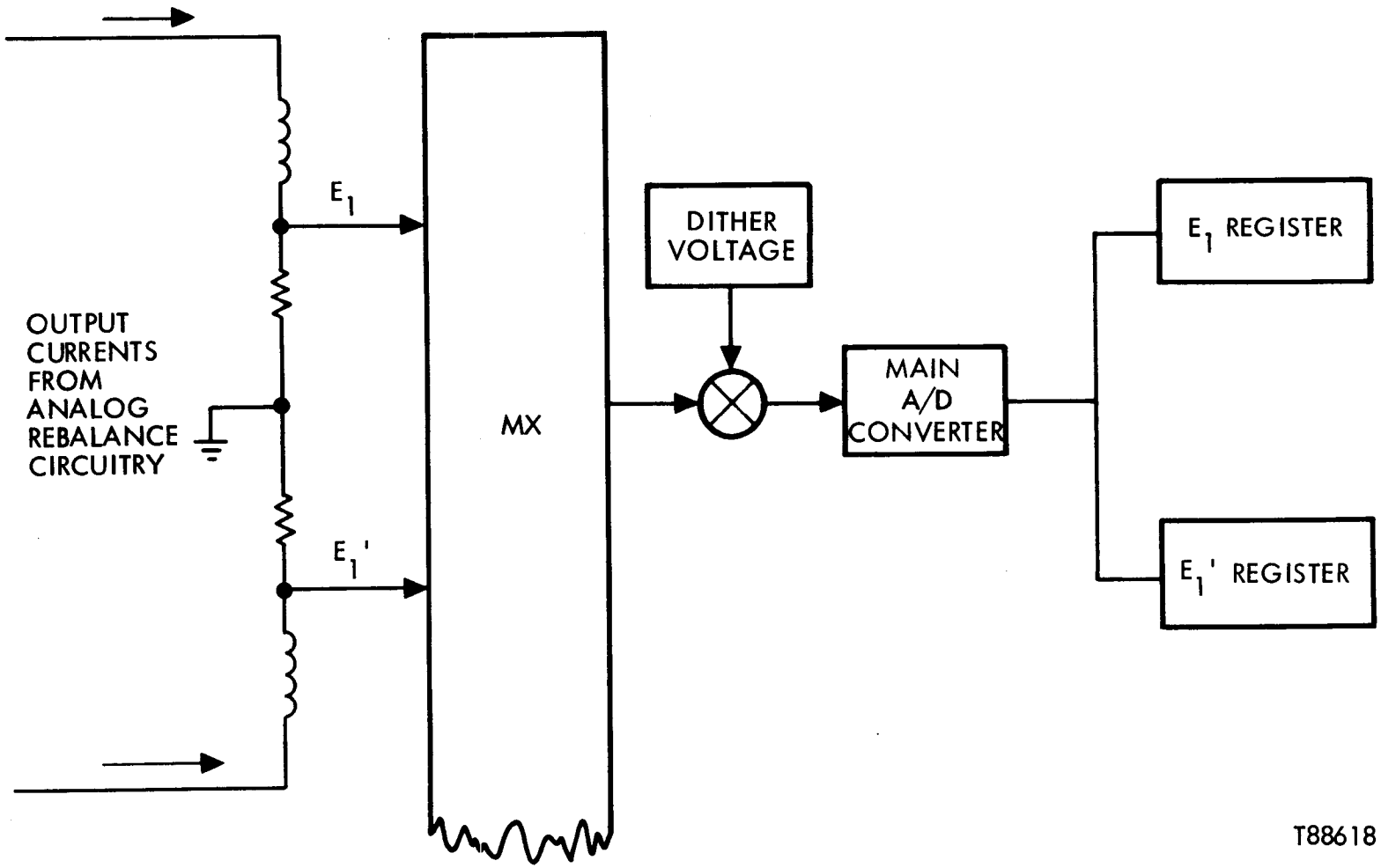

Figure 30. One Gyro Channel of A/D Conversion

Errors Due to Signal Unbalances. -In Figure 31 the voltage magnitude balance of the A/D converter input signals E_1 and E_1' are determined primarily by the resistor ratios R_2/R_1 and R_4/R_3, assuming the coil impedances are matched.

Let
$$E_1 = E_o (1 + \alpha) \tag{10}$$

$$E_1' = E_o (1 - \alpha) \tag{11}$$

In Figure 31, the system scale factor, defined as the physical angular rate of the gyro with respect to E_1 and E_1', is determined by a combination of gyro coil/magnetic/mechanical parameters and the values of the resistors R_3 and R_4. Thus, by varying the ratio R_4/R_3, both the output voltage balance and the scale factor balance are affected. By choosing the R_2/R_1 ratios correctly, it is possible to achieve both an ideal output voltage balance and an ideal scale factor balance. Since it is time consuming and expensive, however, to tailor each output circuit to the associated gyro in this manner, the following analysis has been performed to determine the allowable levels of output voltage and scale factor unbalance.

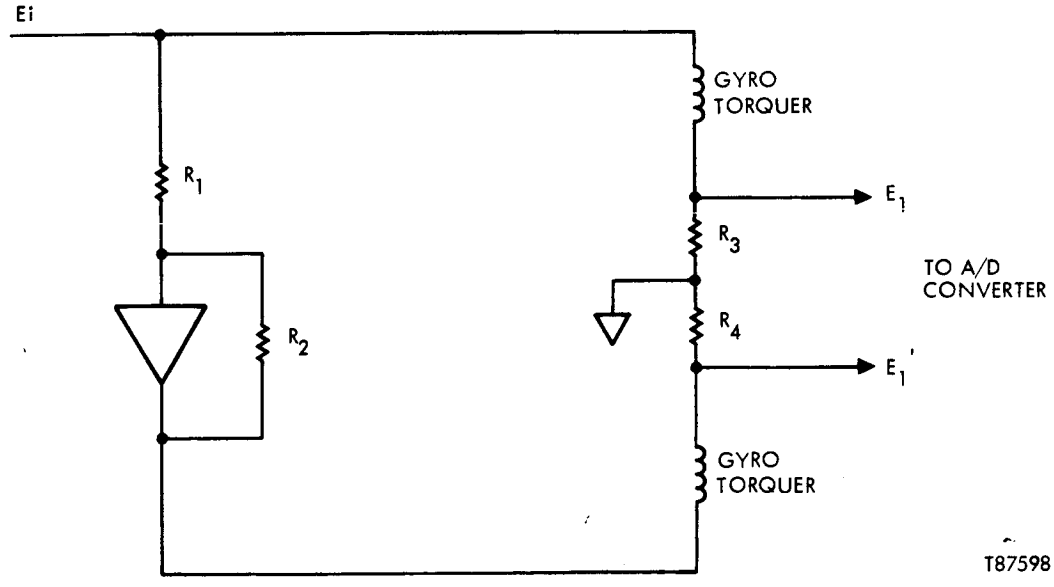

Figure 31. Simplified Gyro Torquing Circuitry

Assume that the error model of the A/D converter can be approximated by the block diagram depicted in Figure 32.

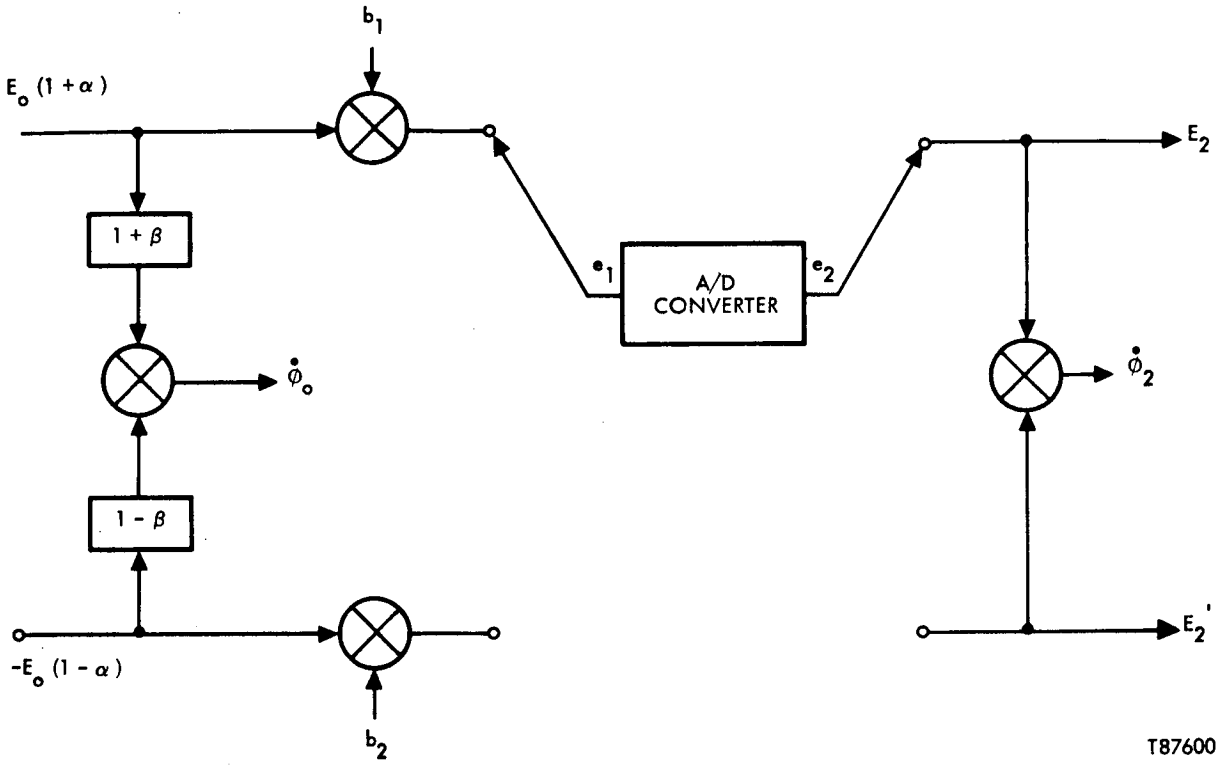

Figure 32. A/D Converter Error Block Diagram

2α	= voltage unbalance of input signals to the A/D converter
2β	= scale factor unbalance of input signals to the A/D converter
b_1, b_2	= multiplexer input channel bias voltages
e_1	= input analog signal to the A/D converter
e_2	= output digital signal of the A/D converter
$E_o(1+\alpha)$, $-E_o(1-\alpha)$	= input signals to the A/D converter
E_2, E_2	= output signals of the A/D converter
$\dot{\phi}_o$	= input angular rate to gyro
$\dot{\phi}_2$	= measured output rate from A/D converter, computer

let

$$e^2 = a_o + a_1 e_1 + a_2 e_1^2 + a_3 e_1^3 + \ldots\ldots\ldots + \text{quantization term} \qquad (12)$$

Neglecting the quantization term, and assuming the input $E_o(1+\alpha) + b_1$, and $-E_o(1-\alpha) + b_2$, as shown in Figure AD-8,

$$E_2 = a_o + a_1 [E_o(1+\alpha) + b_1] + a_2 [E_o(1+\alpha) + b_1]^2 + a_3 [E_o(1+\alpha) + b_1]^3$$

$$+ \ldots\ldots\ldots \text{ and} \qquad (13)$$

$$E_2' = a_o + a_1 [-E_o(1-\alpha) + b_2] + a_2 [-E_o(1-\alpha) + b^2]^2 + a_3 [-E_o(1-\alpha) + b_2]^3$$

$$+ \ldots\ldots\ldots \qquad (14)$$

so that $\dot{\phi}_2$ can be expressed as $\dot{\phi}_2 = E_2 - E_2'$ (15)

$$\dot{\phi}_2 = a_1 (b_1 - b_2) + a_2 (b_1^2 - b_2^2) + a_3 (b_1^3 - b_2^3)$$

$$+ E_o \left\{ 2a_1 + 2a_2 [b_1(1+\alpha) + b_2(1-\alpha) + 3a_3 [b_1^2(1+\alpha) + b_2^2(1-\alpha)] \right.$$

$$+ E_o^2 \left\{ a_2 [(1+\alpha)^2 - (1+\alpha)^2] + 3a_3 [b_1(1+\alpha)^2 - b_2(1-\alpha)^2] \right.$$

$$+ E_o^3 \left\{ a_3 [(1+\alpha)^3 + (1-\alpha)^3] \right.$$

plus higher order terms (16)

The error in the output,

$$\dot{\phi}_E = \dot{\phi}_2 - \dot{\phi}_o \qquad (17)$$

$$\dot{\phi}_E = \dot{\phi}_2 - E_o(2 + 2\alpha\beta) \quad \text{(Assuming } a_1 = 1) \qquad (18)$$

$$\dot{\phi}_E = (b_1 - b_2) + a_2 (b_1^2 - b_2^2) + a_3 (b_1^3 - b_2^3)$$

$$+ E_o \left\{ -2\alpha\beta + 2a_2 [b_1(1+\alpha) + b_2(1-\alpha)] + 3a_3 [b_1^2(1+\alpha) + b_2^2(1-\alpha)] \right.$$

$$+ E_o^2 \left\{ a_2 [(1+\alpha)^2 - (1-\alpha)^2] + 3a_3 [b_1(1+\alpha)^2 - b_2(1-\alpha)^2 \right.$$

$$+ E_o^3 \left\{ a_3 [(1+\alpha)^3 + (1-\alpha)^3] \text{ plus higher order terms} \right. \qquad (19)$$

An examination of equation (19) shows a zero signal input bias of approximately $b_1 - b_2$, a scale factor error approximately $-2\alpha\beta$, and a coefficient for E_o^2 of approximately $4a_2\alpha$. The latter coefficient results in a rectification factor of $2a_2\alpha$ relative to the peak value squared of an input sinusoid. Were the expression for $\dot{\phi}_E$ described by equation (19) to be carried out for more terms, additional rectification factors would appear, one for each even powered term of equation (12).

The preliminary conclusions to be drawn from all of the above are as follows:

1. The multiplexer differential bias, $b_1 - b_2$, should be maintained as low as possible, preferably on the order of 1 ppm or less.

2. The unbalance input voltage, 2α, should be maintained as low as possible, preferably on the order of 1.0% or less.

3. The scale factor unbalance, β, causes only the second order, constant scale factor change of $2\alpha\beta$, and is hence not critical, assuming α remains relatively constant.

4. Assuming the following values for the error parameters, the following errors ($\dot{\phi}_E$) result:

   let $b_1 - b_2$ = 5 ppm of full scale

   $\alpha = 0.01$

   $\beta = 0.03$

   $a_2 E_o$ (full scale) = 200 ppm of full scale

   Then Bias = approximately 5 ppm of full scale

   Scale factor constant error = approximately 300 ppm of full scale
   Rectification error for a sinusoidal input of peak magnitude E_S =

   approximately E_S/E_o x 2 ppm of E_S

   Maximum rectification error = approximately 2 ppm of full scale.

5. In the design of the caging amplifier and oven electrical components it should be satisfactory to specify tolerances for R_1, R_2, R_3, and R_4 which meet the above requirements and which will interface satisfactory with any gyro, assuming the usual computer calibration of overall scale factor.

6. It has been demonstrated that the effects of angular cross coupling errors of the torquers is negligible.

7. For the case where the input to the A/D converter can be represented by a constant plus a sinusoid, the following additional rectification term appears:

Let $E_o = E_K + E_S \sin w_o T$

$$E_o^3 = E_K^3 + 3E_K^2 E_S \sin w_o T + 3E_K E_S^2 \sin^2 w_o T + E_S^2 \sin^3 w_o T$$

In this expression the first term represents the nonlinear response to the constant input, and the third term represents a rectification term of magnitude.

$$\dot{\phi}_E = 3E_K E_S^2 a_3$$

Let $\frac{a^3 E_o^3}{E_o} = 150$ ppm

so that $\frac{\dot{\phi}_E}{E_o} = 3\,(a_e E_o^2)\,(\frac{E_K}{E_o})\,(\frac{E_S}{E_o})\,2$ (20)

for the case where

$$\frac{E_K}{E_o} = \frac{1}{20}, \quad \frac{E_S}{E_o} = \frac{1}{2}$$

$$\frac{\dot{\phi}_E}{E_o} = (3)\,(150\ \text{ppm})(\frac{1}{20})\,(\frac{1}{4})$$

$\frac{\dot{\phi}_E}{E_o}$ = approximately 6 ppm of full scale rectification error

Quantization Errors. -The Main A/D converter converts a signal having a triangular wave dither plus quantization noise and a bias into a train of digitized data whose time representation appears as in Figure 33.

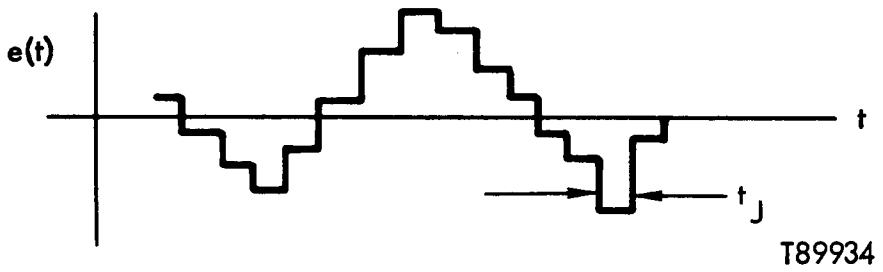

Figure 33. Digitized Data with Dither

The quantization noise, the bias, and triangular wave are uncorrelated with each other and their effects may be separately analyzed.

1. Dither Elimination

The dither signal is incorporated to make the very low levels of gyro bias (and the vehicle motion in quiescent flight) "visible" to an analog-to-digital converter whose least quantum of signal level is many times the biases to be measured.

While the dither is thus necessary, it must also be eliminated from the digitized data before computer processing so as not to introduce erroneous or extraneous effects which may be falsely attributed to instrument or system behavior.

To eliminate the dither from the data after conversion, a "common mode rejection" scheme is mechanized as shown in Figure 34, where the complementary polarities of the torquer signal are each mixed with the dither signal, converted, summed for a computer period (nominally 8 dither cycles) and then differenced.

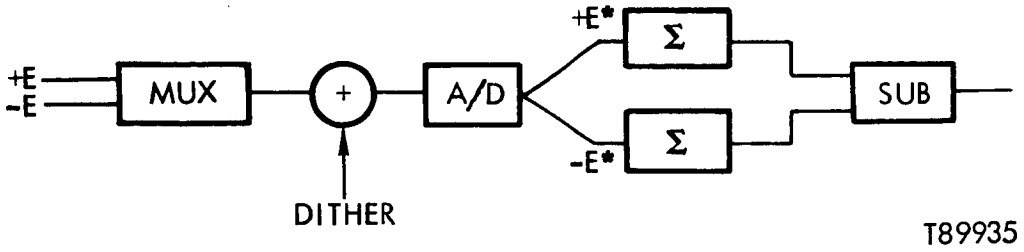

Figure 34. "Common Mode" Dither Mechanization

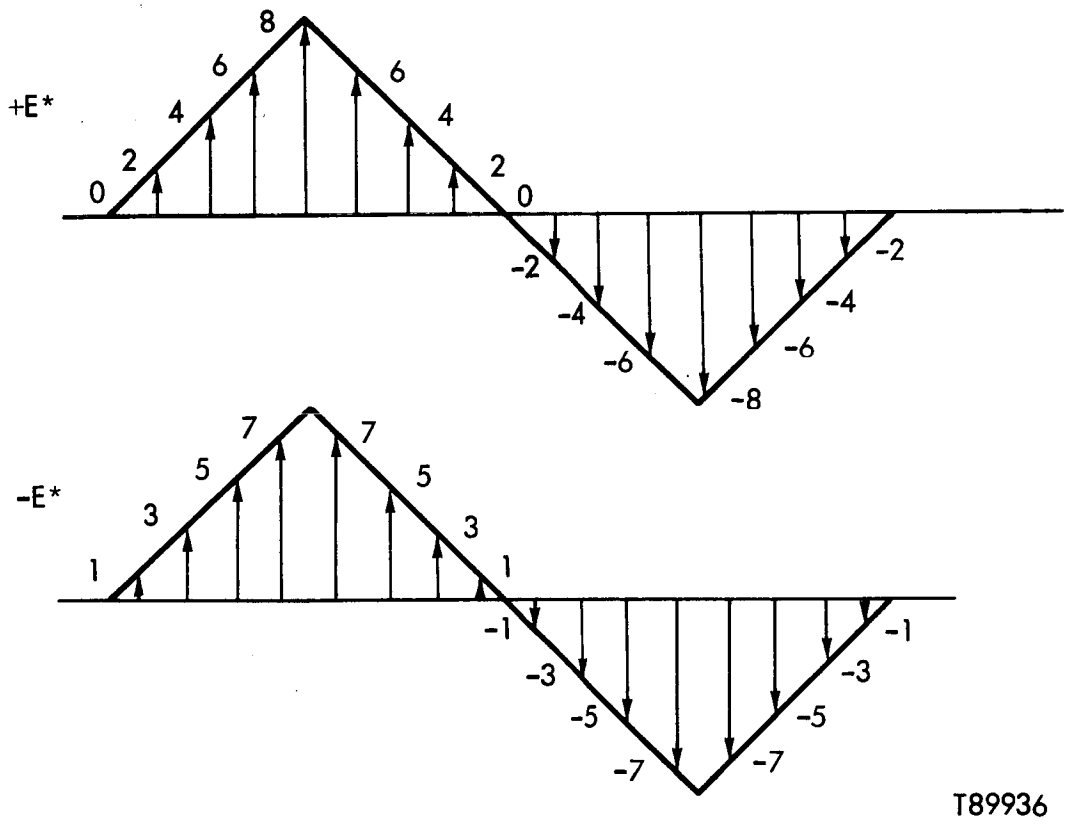

Figure 35. Typical Converted Waveforms of Dithered Signal

As seen in Figure 35, if the dither period is an exact multiple of the sample period, the sums of +E* and -E* will each (individually) total zero over a full dither cycle. Further, any bias in the dither will affect each equally and be cancelled when $\Sigma+ E^* - \Sigma-E^*$ is formed.

However, the converter has a finite resolution to each measurement such that a small numerical residual would surely arise systematically in each such sum over each cycle if perfect synchronism were used. Consequently, it is desirable to "detune" the dither and converter frequencies such that the converter "walks" across all levels of the dither signal, making these resolution residuals vary cyclically and average out. This detuning is done so the averaging is carried out rapidly over several machine cycles (in each of which there are approximately eight dither cycles).

2. Quantization Noise and Bias

The quantization error is a random "square wave" error having a uniform probability distribution over the range $\pm$ 1/2 LSB. Denote the half range by b. Then the variance in this quantization noise is

$$\sigma_N^2 = \frac{b^2}{3} \tag{21}$$

and the standard deviation in any one measurement is $b/\sqrt{3}$.

In a high-grade strapdown inertial system the following parameters are typical

A/D Converter 14 bits, 10 usec. /conversion.
Max range scaling $\pm 8^\circ$/sec.
Conversion rate per signal channel: 6,000/sec. = 100/computer cycle

Then

$$\text{LSB} = \frac{2 \times 8^\circ/\text{sec.}}{214} = 0.001^\circ/\text{sec.}, \quad b = 0.0005^\circ/\text{sec.}$$

$$\sigma_N = \frac{0.0005^\circ/\text{sec.}}{\sqrt{3}} = 0.00029^\circ/\text{sec.} = 1.05^\circ/\text{hr.}$$

During one machine cycle (1/60 sec.) there are 100 conversions in each channel, so the standard deviation of a rate measurement each machine cycle (after the subtraction +E* - -E*) is

$$\sigma_{N}^{1} = \frac{1.05^{\circ}/\text{hr.}}{\sqrt{200}} = 0.073^{\circ}/\text{hr.}$$

Averaged over, say, 2 seconds, during which there are 120 machine cycles

$$\sigma_{N}^{1}{}_{2\text{ sec.}} = \frac{0.073}{\sqrt{120}} = .0066^{\circ}/\text{hr.}$$

or, over 10 seconds:

$$\sigma_{N}^{1}{}_{10\text{ sec.}} = \frac{0.073}{\sqrt{600}} = 0.003^{\circ}/\text{hr.}$$

Thus, for all practical purposes the digital averaging process yields measurements with accuracies of very great precision with only several seconds of smoothing.

3. Instrument Calibration

To enhance the data smoothing during calibration, scaling may be changed. Since the quantization error varies directly with converter scaling, a factor of 2 or 3 change yields smoothed data accuracies compatible with the inherent instrument accuracies (0.001°/hr. 1σ random drift) using only 10 seconds of smoothing.

4. Long-Term Integration of Rate Data

If the rate data are integrated to generate attitude information, the picture for the error model is thus:

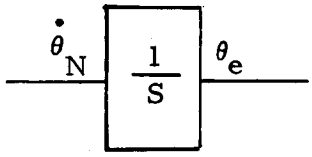

Here $\dot{\theta}_N$ has a deviation of 0.073°/hr. Integrated over time t the variance in the error is

$$\sigma_{\theta_e}^{2} = t \int_{-\infty}^{\infty} \phi_{\theta_N}(t)\, dt \qquad (22)$$

The autocorrelation ϕ_{θ_N} of the random pulse train has an integral $(\sigma_N^1)^2 \cdot T$ where T is the computer interval, 1/60 sec. Hence

$$\sigma_{\theta_e}^2 = t\,(\sigma_N^1)^2\,T \tag{23}$$

or

$$\sigma_{\theta_e} = \sqrt{t}\ 0.073\ \frac{\widehat{\text{sec.}}}{\text{sec.}}\sqrt{\frac{1}{60}}\ \text{sec. with t in secs.}$$

$$\sigma_{\theta_e} \cong 0.01\sqrt{t}\ \widehat{\text{sec.}}$$

For one hour (t = 3600), $\sigma_{\theta_e} = 0.6\ \widehat{\text{sec.}}$ Vectorially, the total tilt would not exceed 1 $\widehat{\text{sec.}}$ (1σ) at one hour or 2 $\widehat{\text{sec.}}$ (1σ) at four hours.

Errors Due To Circuit Characteristics. -Since the ADC consists of practical circuits containing non-ideal components it is important to consider the effects of various electrical characteristics of these circuits. Characteristics which affect the accuracy and/or stability of the ADC include offset voltage errors, scale factor errors, bias errors etc.

An error model for the ADC is presented in Appendix A5. Based on this model equations for the total output error are derived as a general case. Each circuit is then analyzed in detail for its various contribution to the general error. Finally these errors are to be tabulated and incorporated into this total output error equation. This table is repeated here as Table 27.

Conclusive Remarks. -After a review of the various analog-to-digital conversion techniques as described in this study, the method selected is an A/D system that utilizes a single high speed successive-approximation A/D converter in conjunction with additional hardware and software which act in concert to expand its input versatility and to enhance its accuracy. The foregoing error analyses illustrate that this technique may be applied with confidence to the strapdown inertial system and can be expected to provide the accurate conversions required in this application.

Table 27. Total Error Summary and Calculation

Error Parameter	Errors					
	Offset Voltage	Bias		Scale Factor		
				Absolute	Differential	
	E1	E1	$E1^2$	E2	E2	$E2^2$
	mv	mv	10-10V	mv	mv	10-10V
Input Multiplexer						
Bias: Initial	1.113					
Differential		0.0105	1.1			
Temperature		0.006	0.36			
Scale Factor:						
Absolute				0.0105		
Symmetry					0.005	0.25
Crosstalk-Differential:		0.011	1.21			
Input Buffer						
Input Current	Included In MUX					
Offset Voltage:						
Initial	6					
Drift	0.06					
CMRR:						
Linear				1.0		
Differential					0.1	100.
Open Loop Gain:						
Linear				1.0		
Differential					0.1	100.
PSRR:		0.0075	0.56			
Settling Time:		0			0	
MUX & Buffer						
MUX:						
Offset	0.0225					
Settling		0			0	
Buffer:						
Input Current	Included in MUX					
Offset Voltage:						
Initial	6					
Drift	0.06					

T89971

Table 27. Total Error Summary and Calculation (Continued)

Error Parameter	Errors: Offset Voltage E1	Bias: E1	Bias: $E1^2$	Scale Factor: Absolute E2	Scale Factor: Differential E2	Scale Factor: Differential $E2^2$
	mv	mv	10-10V	mv	mv	10-10V
MUX & Buffer (Continued)						
CMRR:						
Linear				1.0		
Differential					0.1	100.
Open Loop Gain:						
Linear				1.0		
Differential					0.1	100.
PSRR:		0.0075	0.56			
Differential Settling:					0.2	400.
Main A/D Converter						
Absolute Accuracy:				2		
Relative Accuracy:					2	40000
Differential Linearity:	Included in Rel.	Accuracy				
PSRR:		0.03	0.09			
Diff. Linearity Drift:					0.18	324.
Gain Drift:					0.3	900.
Offset Drift:	0.3					
Absolute Offset	10					
Absolute Gain:				10		
TOTAL	23.55 mv	0.045 mv	3.88 $x10^{-10}V$	16.01 mv	3.085 mv	42024 $x10^{-10}V$
RSS ERROR			0.02mv			2.1mv
RSS ERROR IN PPM OF FULL SCALE:			1 PPM			105PPM

From The Total Output Error Equation: $ET = \Sigma E1(N1N2)/2 + \Sigma E1$

The Total RSS Error Is: ET = 105 PPM + 1 PPM = 106 PPM

T89972

Although the basic successive-approximation technique is not new to Teledyne, the implementation described nevertheless represents a state-of-the-art conversion technique. Advances in semiconductor technology will no doubt enhance the accuracy and speed characteristics, however the greatest benefit will be in the condensed packaging that will result from new developments in LSI and Hybrid circuits. Thus redundant A/D conversion schemes become not only feasible but easily realized.

Compensation

Introduction

The purpose of this section is to present a detailed design and analysis of the gyro analog caging loop. The analysis makes use of the complex method [9] along with modified root locus and Bode plot techniques. Included are a discussion of the general loop configuration, design in the complex plane, transformation of the design into a physically realizable form, computer simulation and performance evaluation.

The function of the caging loop is to maintain the gyro rotor aligned with the set of orthogonal case fixed coordinates. This is accomplished by using the misalignment signals from the gyro pickoffs to provide the necessary currents to the torquer coils. This precesses the rotor such that the pickoff signals are driven to zero.

The caging loop contains a novel approach in that it not only uses the normal cross axis or gyroscopic torquing scheme but in addition uses some direct axis signal to increase the loop bandwidth and reduce the rotor hangoff angles during acceleration inputs.

Analysis

Basic Gyro Equation

The general open loop transfer function in case fixed coordinates can be expressed by the following equation as derived rigorously in [10]:

$$\Theta_{XY}(s) = \frac{\begin{array}{l} -\phi_{XY}(s)\,[F_1(s)\,\bar{\tau}_1(s-j2N) - \bar{F}_2(s-j2N)\,\tau_2(s)] \\ -\phi_{XY}(s-j2N)\,[F_2(s)\,\bar{\tau}_1(s-j2N) - \bar{F}_1(s-j2N)\,\tau_2(s)] \\ +M_{XY}(s)\,\bar{\tau}_1(s-j2N) - \bar{M}_{XY}(s-j2N)\,\tau_2(s) \end{array}}{\tau_1(s)\,\bar{\tau}_1(s-j2N) - \tau_2(s)\,\bar{\tau}_2(s-j2N)} \qquad (1)$$

where $\Theta_{XY}(s)$ is the gyro rotor to case offset angle and N is the rotor spin speed.

For the purposes of a caging loop design, (1) can be further reduced by making several simplifying assumptions:

1) Principal moments of inertia about rotor x and y axes are equal (A = B)

2) Principal moment of inertial about rotor spin axis z is twice the value of the principal moments of inertia about x and y (C = 2A = 2B)

3) Principal moments of inertia of the rotor are much larger than the principal moments of inertia of the gimbals (A, B, C $\gg A_n$, B_n, C_n)

4) The gyro is a symmetric, tuned, undamped instrument ($\tau_2(s) = \bar{\tau}_2(s-j2N)$ $= F_2(s) = \bar{F}_2(s-j2N) = 0$ and $N = \sqrt{K/J}$

Making use of these assumptions and substituting $\Omega_{XY}(s)$ for $s\phi_{XY}(s)$, (1) can be reduced to:

$$\theta_{XY}(s) = \frac{F_1(s)\,\Omega_{XY}(s) + M_{XY}(s)}{\tau_1(s)} \qquad (2)$$

where:

$\Omega_{XY}(s)$ = Input rate

$F_1(s) = -A\,(s-j2N)$

$\tau_1(s) = As(s-j2N)$

Defining:

$$\theta_{XY}(s) = \theta_X(s) + j\theta_Y(s) \qquad (3)$$

$$\Omega_{XY}(s) = \Omega_X(s) + j\Omega_Y(s) \qquad (4)$$

$$M_{XY}(s) = M_X(s) + jM_Y(s) \qquad (5)$$

Substituting (3) through (5) into (2), normalizing it, and equating the coefficients of real and imaginary quantities yields:

$$\theta_X(s) = \frac{-\Omega_{X(s)}}{s} + \frac{M_X(s)}{A(s^2+4N^2)} - \frac{2NM_Y(s)}{As(s^2+4N^2)} \tag{6}$$

$$\theta_Y(s) = \frac{-\Omega_{Y(s)}}{s} + \frac{2N\,M_X(s)}{As\,(s^2+4N^2)} - \frac{M_Y(s)}{A(s^2+4N^2)} \tag{7}$$

General Loop Configuration

Let $M_{XY}(s)$ in (2) be taken as the gyro restoring torque. Equations (6) and (7) show that $\theta_X(s)$ and $\theta_Y(s)$ are each dependent on both $M_X(s)$ and $M_Y(s)$. With this in mind, a feedback control system of the following general form will be assumed:

$$\begin{aligned} M_{XY}(s) &= \left[-G_1\,\theta_X(s) - G_2(s)\,\theta_Y(s)\right] + j\left[G_2(s)\,\theta_X(s) - G_1(s)\,\theta_Y(s)\right] \\ &= \left[-G_1(s) + j\,G_2(s)\right]\theta_X(s) + j\left[-G_1(s) + j\,G_2(s)\right]\theta_Y(s) \\ &= \left[-G_1(s) + j\,G_2(s)\right]\left[\theta_X(s) + j\,\theta_Y(s)\right] \\ &= G_{12}(s)\,\theta_{XY}(s) \end{aligned} \tag{8}$$

where:

$$G_{12}(s) = -G_1(s) + j\,G_2(s) \tag{9}$$

$$M_X(s) = -G_1(s)\,\theta_X(s) - G_2(s)\,\theta_Y(s) \tag{10}$$

$$M_Y(s) = +G_2(s)\,\theta_X(s) - G_1(s)\,\theta_Y(s) \tag{11}$$

Substituting (8) into (2) yields the following closed loop transfer function:

$$\theta_{XY}(s) = \frac{F_1(s)\ \Omega_{XY}(s) + G_{12}(s)\ \theta_{XY}(s)}{\tau_1(s)}$$

$$= \frac{F_1(s)\Omega_{XY}(s)}{\tau_1(s) - G_{12}(s)}$$

$$= \frac{F_1(s)\ \Omega_{XY}(s)}{\tau_1(s)\left[1 - \frac{G_{12}(s)}{\tau_1(s)}\right]} \qquad (12)$$

$G_{12}(s)$ represents the total feedback loop (i.e. gyro pickoff, AC amplifier, demodulator, D-C amplifier, compensation networks and gyro torquer). Separating $G_{12}(s)$ into several of its component parts gives the following block diagram:

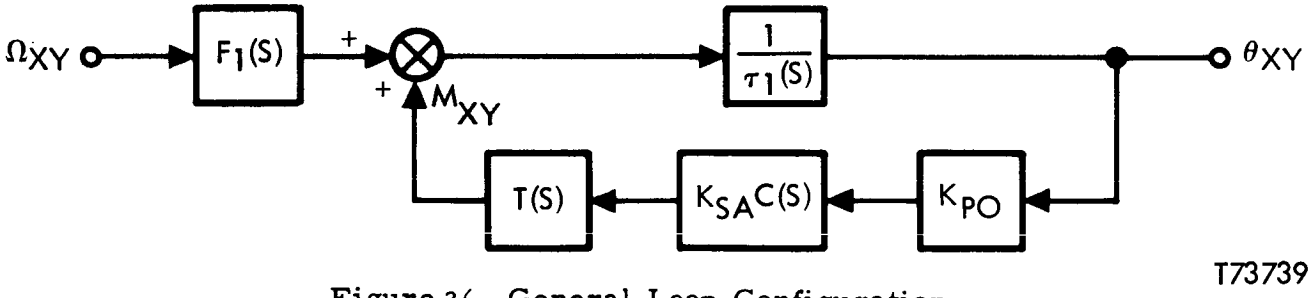

Figure 36. General Loop Configuration

where:

$G_{12}(s)$ = $K_{PO}K_{SA}C(s)\ T(s)$

K_{PO} = gyro pickoff gain

K_{SA} = required electronics gain

C(s) = required loop compensation

T(s) = Gyro Torquer

Closed Loop Analysis

In using the complex method of analysis and from the definition of $G_{12}(s)$ in (9), a transfer function which contains non-complex conjugate roots will be the result. Since the root locus technique of solving equations by finding points in the plane which satisfy the magnitude and phase criteria ($1 \angle 180^{\circ}$) is of a general enough nature, it is equally applicable to the above mentioned type of equation. The root locus is not only a convenient method of solving for the roots of the equation but also provides both stability and performance information of the closed loop system.

Since both K_{PO} and T(s) are known, only the $K_{SA}C(s)$ block needs to be designed.

$$K_{PO} = 130 \text{ volts/rad}$$

$$T(s) = \frac{K_T}{\frac{s}{\omega_T} + 1} = \frac{K_T \omega_T}{s + \omega_T}$$

where:

$$K_T = 7.5 \times 10^4 \text{ dyne-cm/volt}$$
$$\omega_T = 10^4 \text{ rad/sec}$$

Several constraints on the loop design partially dictate the form of C(s). First, it is desirable to drive the steady-state output errors (due to position and constant rate inputs) to zero. This requires at least one integration in the feedback. Second, the maximum transient error must be less than ± 5 mrad to prevent the rotor from hitting the stops. This governs the damping and bandwidth of the loop. Third, there are limitations placed on the feedback gain at spin frequency due to rectification effects. This requires a high attenuation notch filter at this frequency. Fourth, the loop response at gyro nutation frequency ($\approx 2N$) must either be less than unity or have the proper phase relationship to prevent instability. This further governs the damping and bandwidth of the loop.

Using the roots of $\tau_1(s)$ from (2) and the above constraints gives the root locus starting points as shown in Figure 37. For convenience, all break points will be normalized with respect to the spin frequency N (where N = 628 rad/sec).

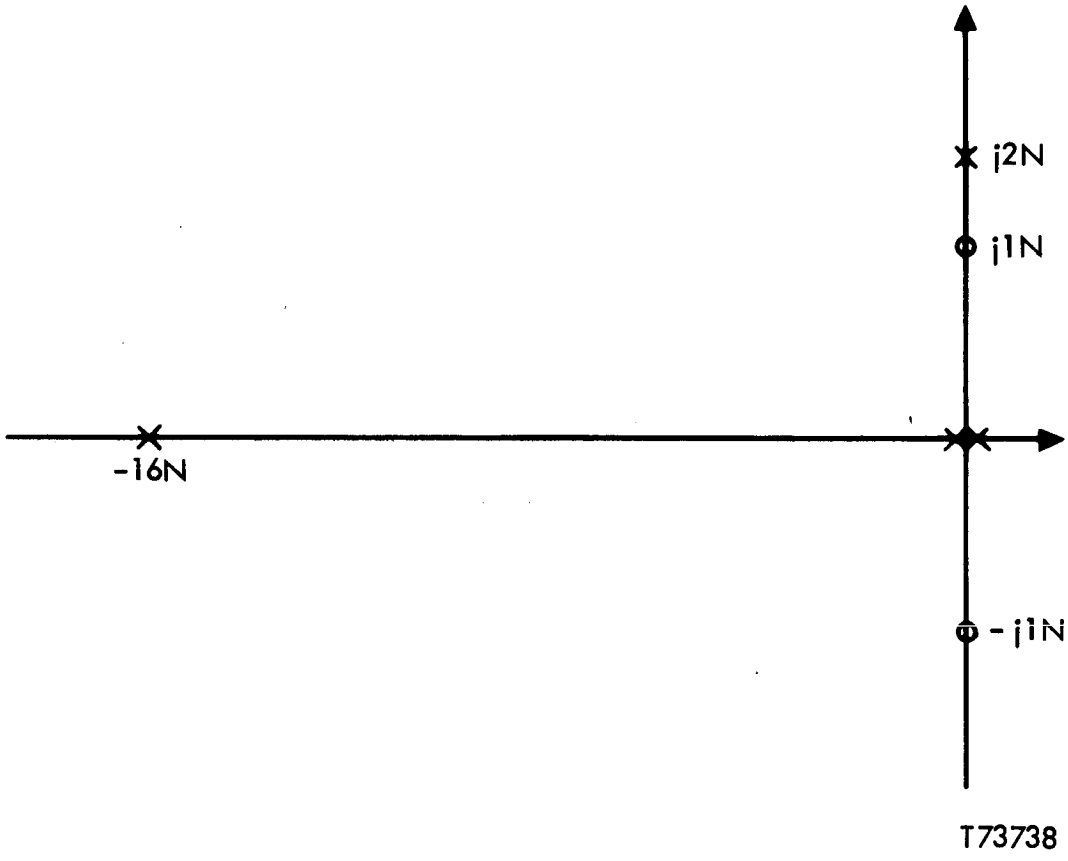

Figure 37. Root Locus Starting Points

By placing additional poles and zeros in the plane, the root locus can be drawn and evaluated. After several iterations, the following compensation was found to be near optimum.

$$K_{SA}C(s) = \frac{K'_{SA}\,(s^2 + N^2)\,(s + .35N)\,(s + .7N - j2N)\,(s + .8N - j.2N)}{s\,(s + 3N)^4} \tag{13}$$

The high frequency asymptotes are given by:

$$\sigma = -\frac{\sum_i Pi - \sum_i Zi}{P - Z} = -8.7N + j.1N$$

$$\alpha = \frac{180^\circ\,(2k + 1}{P - Z} = \pm 60^\circ, +180^\circ, \quad (k = 0, 1, 2, \ldots)$$

Where σ is the center of gravity, P_i and Z_i are the open loop pole and zero positions respectively, P is the number of poles, Z is the number of zeros, and α is the angle.

The root locus plots are given in two parts. Figure 38 contains the locus of the dominant roots (i.e. those near the origin). Figure 39 contains the locus of the high frequency roots. For the closed loop poles shown in Figures 38 and 39, the root locus gain is:

$$K_{RL} = 980\,N^3$$

The closed loop poles are located at :

$$s_1 = -.43N + j\,1.96N \qquad s_2 = -.65N + j\,.84N$$

$$s_3 = -.30N + j\,.36N \qquad s_4 = -.24N - j\,.64N$$

$$s_5 = -.53N - j\,.24N \qquad s_6 = -2.1N + j\,7.1N$$

$$s_7 = -2.05N - j\,7.3N \qquad s_8 = -19.3N + j\,.08N$$

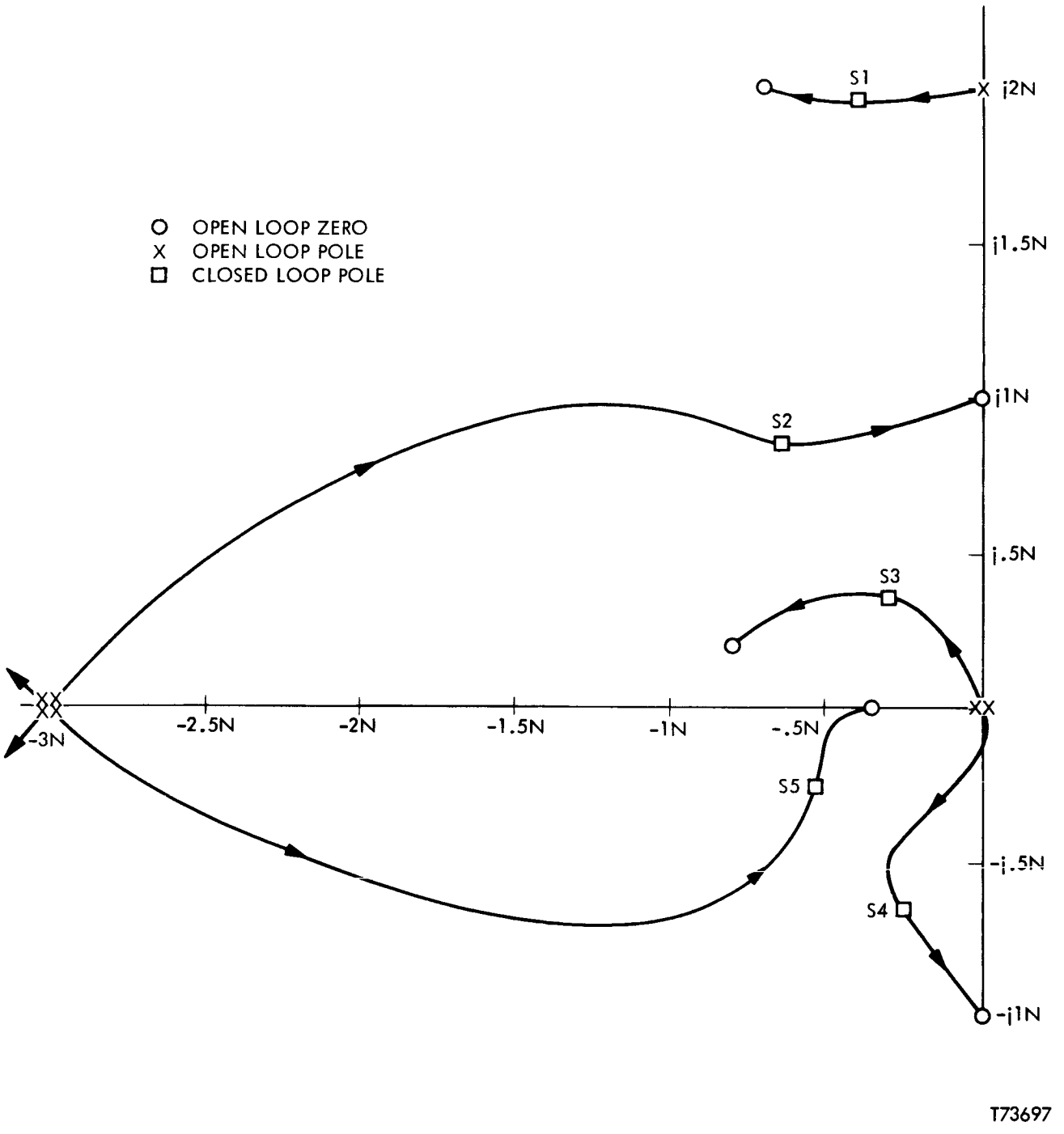

Figure 38. Root Locus (Low Frequency)

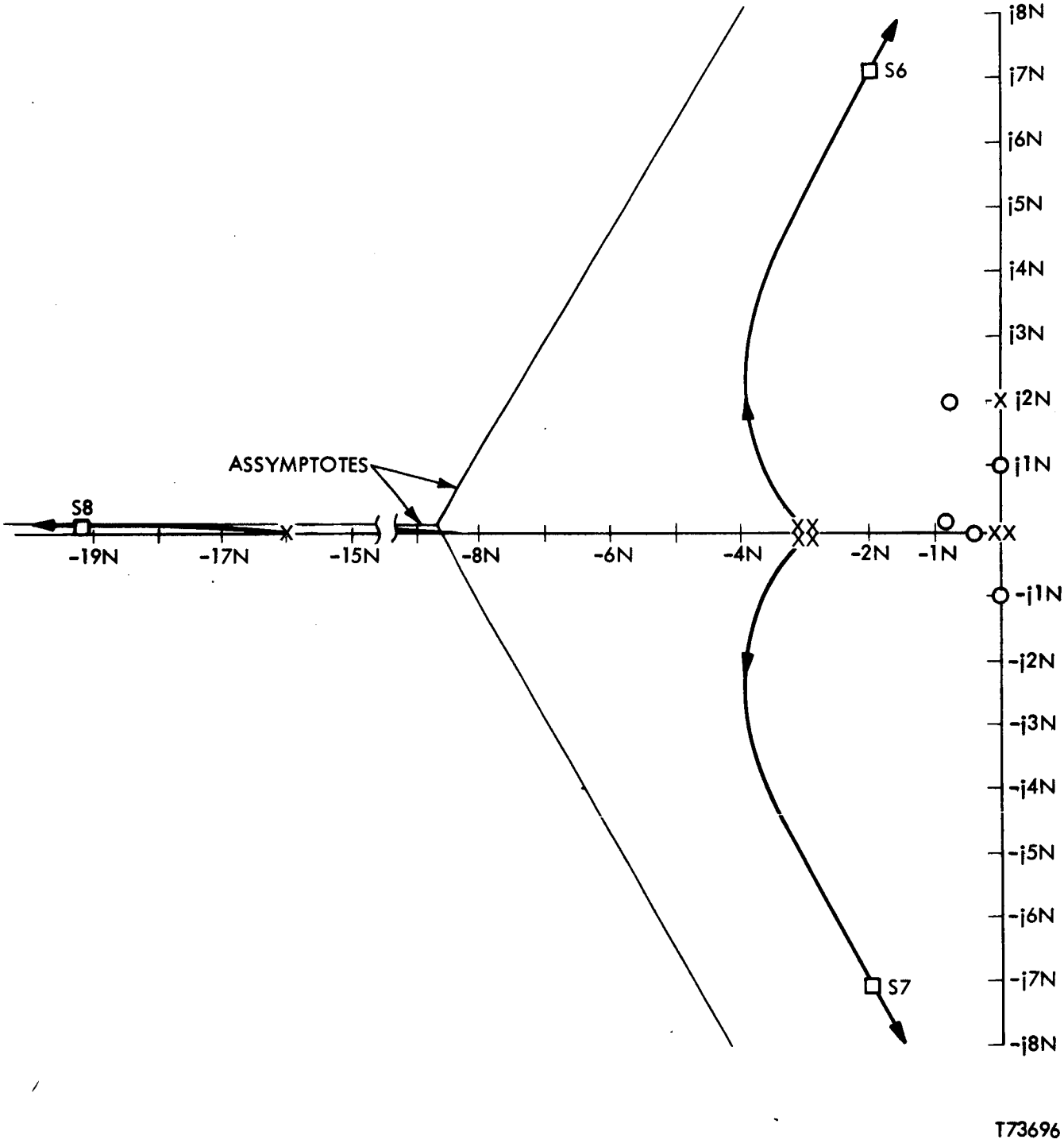

Figure 39. Root Locus (High Frequency)

Substituting the various functions into Figure 36 yields the following block diagram:

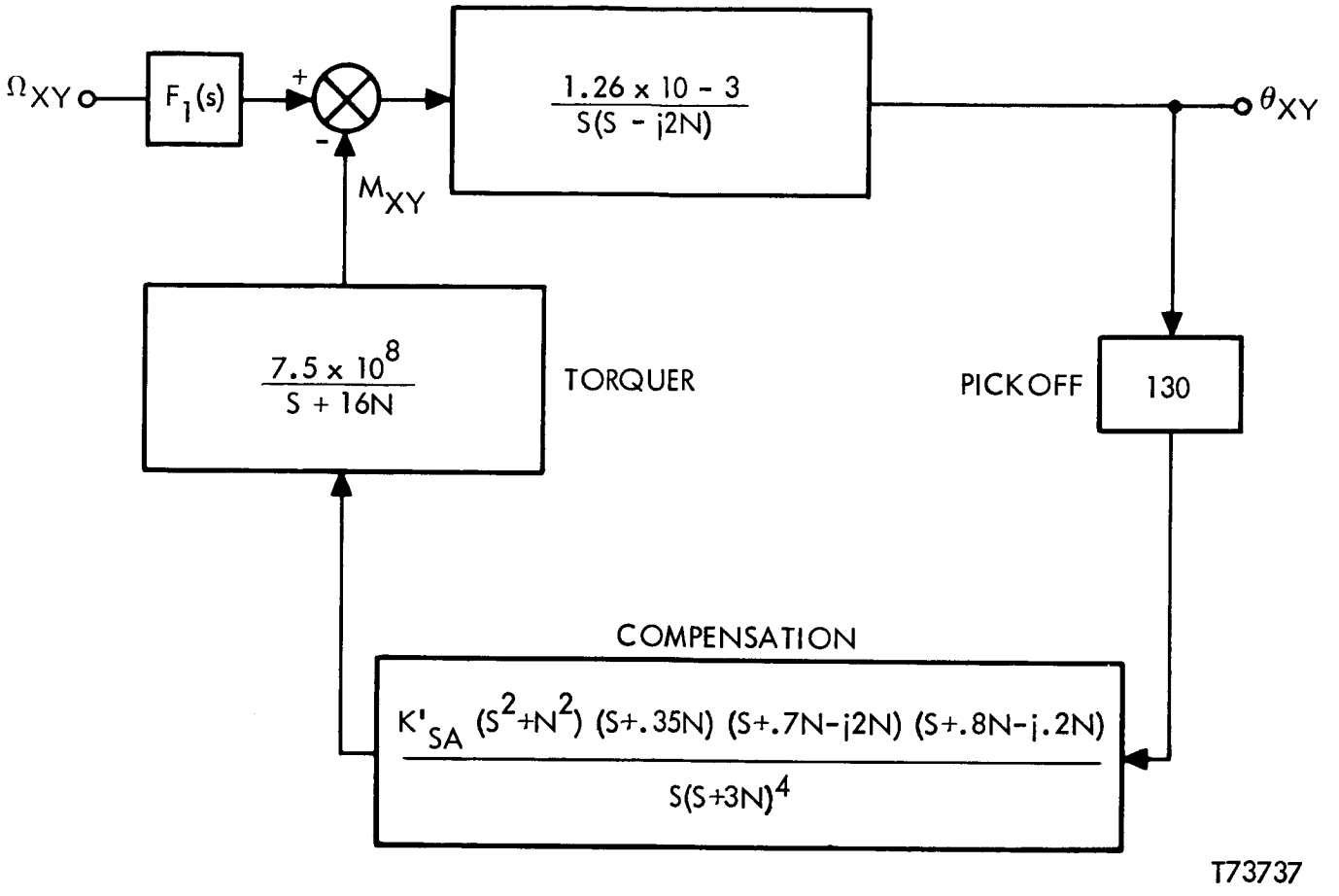

Figure 40. General Loop Transfer Functions

From Figure 40 and the root locus gain, the value of K'_{SA} can be readily obtained:

$$K_{RL} = 980\ N^3 = 1.23 \times 10^8\ K'_{SA}$$

$$K'_{SA} = 1.97 \times 10^3$$

In a strapdown application, the feedback torque M_{XY} indicates the movement of the gyro in inertial space. Ideally, M_{XY} should be equal to $F_1(s)\ \Omega_{xy}(s)$ under all conditions. From Figure 40:

$$\frac{M_{XY}}{F_1 \Omega_{XY}} = \frac{\dfrac{2.42 \times 10^{11} (s^2 + N^2)(s + .35N)(s + .7N - j2N)(s + .8N - j.2N)}{s^2 (s - j2N)(s + 3N)^4 (s + 16N)}}{1 + \dfrac{2.42 \times 10^{11} (s^2 + N^2)(s + .35N)(s + .7N - j2N)(s + .8N - j.2N)}{s^2 (s - j2N)(s + 3N)^4 (s + 16N)}}$$

$$= \frac{2.42 \times 10^{11} (s^2 + N^2)(s + .35N)(s + .7N - j2N)(s + .8N - j.2N)}{s^2 (s - j2N)(s + 3N)^4 (s + 16N) + 2.4 \times 10^{11} (s^2 + N^2)(s + .35N)(s + .7N - j2N)(s + .8N - j.2N)} \quad (14)$$

The roots of the denominator of Equation 14 are the closed loop poles given in Figures 38 and 39.

$$\frac{M_{XY}}{F_1 \Omega_{XY}} = \frac{2.42 \times 10^{11} (s^2 + N^2)(s + .35N)(s + .7N - j2N)(s + .8N - j.2N)}{(s + s_1)(s_4 + s_2) - - - - - (s + s_8)} \quad (15)$$

Letting $s = j\omega$, the closed loop response is given in Figure 41.

The 3dB bandwidth is 470 rad/sec with a phase angle of -98°. The peak overshot is +3.0 dB and occurs at 290 rad/sec.

Open Loop Analysis

In performing an open loop analysis (Bode plot) only positive frequencies are normally considered. This is due to the fact that the plot for $\omega \leq 0$ is a mirror image of the plot for $\omega \geq 0$. However in the case of nonsymmetric roots, this no longer holds. Therefore it is necessary to cover the full frequency range $-\infty \leq \omega \leq +\infty$.

It is also necessary to convert the transfer functions in Figure 5 from root locus form to standard form (i.e. $\tau s + 1$ or $\frac{s}{\omega} + 1$). This yields:

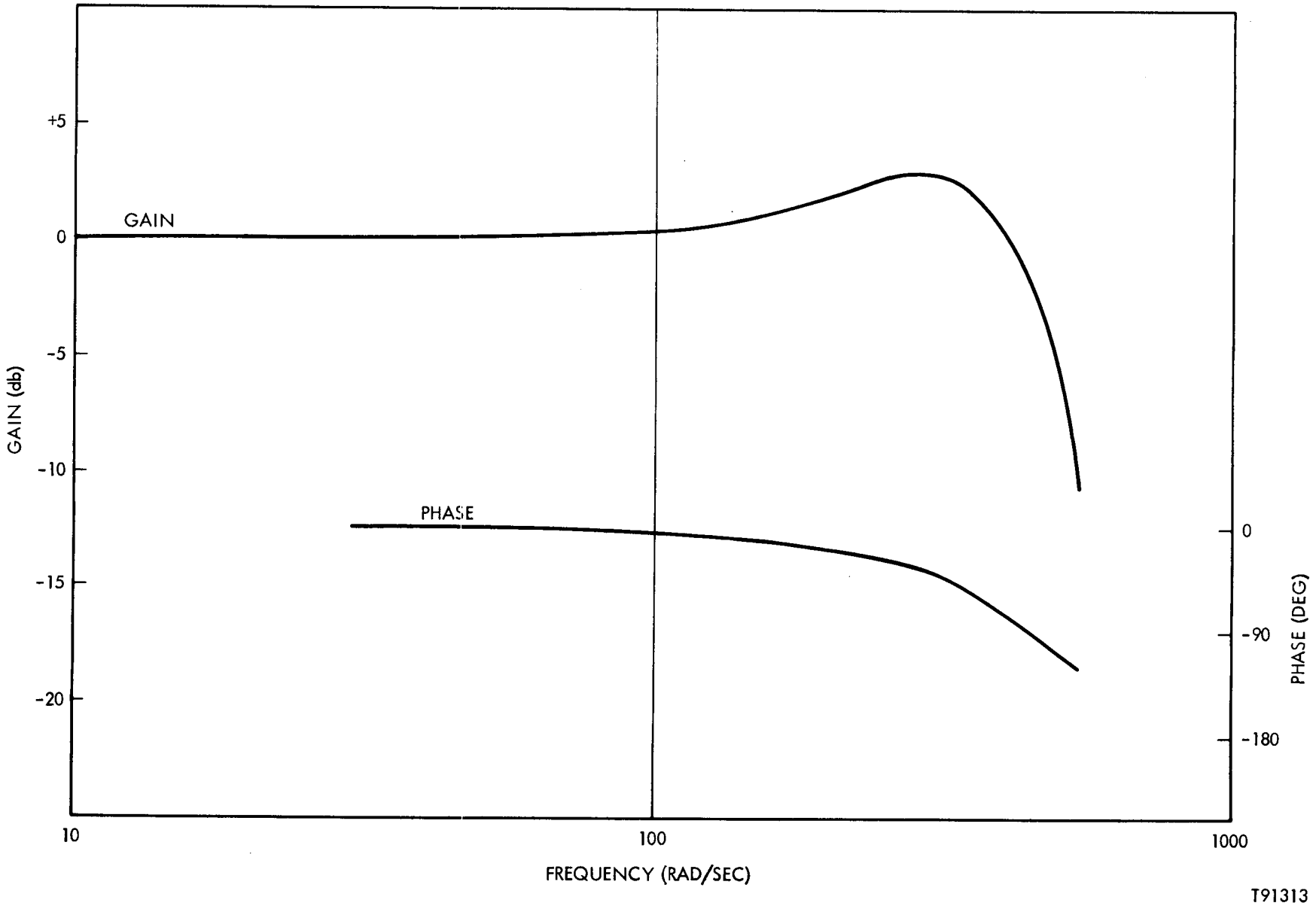

Figure 41. Closed Loop Response-Complex Form

$$\frac{1}{\tau_1(s)} = \frac{10^{-6}}{s\left(\frac{s}{j2N} - 1\right)} \tag{16}$$

$$T(s) = \frac{7.5 \times 10^4}{\left(\frac{s}{16N} + 1\right)} \tag{17}$$

$$K_{SA}C(s) = \frac{4.71\, K'_{SA}\left(\frac{s^2}{N^2} + 1\right)\left(\frac{s}{.35N} + 1\right)\left(\frac{s}{.7N - j2N} + 1\right)\left(\frac{s}{.8N - J.2N} + 1\right)}{s\left(\frac{s}{3N} + 1\right)^4} \tag{18}$$

From this form, the actual electronic gain (K_{SA}) needed can be calculated

$$K_{SA} = 4.71K'_{SA} = 9.3 \times 10^3$$

Letting $s = j\omega$, the plots for ω positive and negative are given in Figures 42 and 43.

For $\omega \geq 0$, the crossover occurs at 345 rad/sec with a phase margin of 63°.

For $\omega \leq 0$, the crossover occurs at 360 rad/sec with a phase margin of 40°.

Compensation Conversion

Next, it is necessary to convert the compensation from the complex form used thus far to a physically realizable form. From Figure 40 and equations (17) and (18):

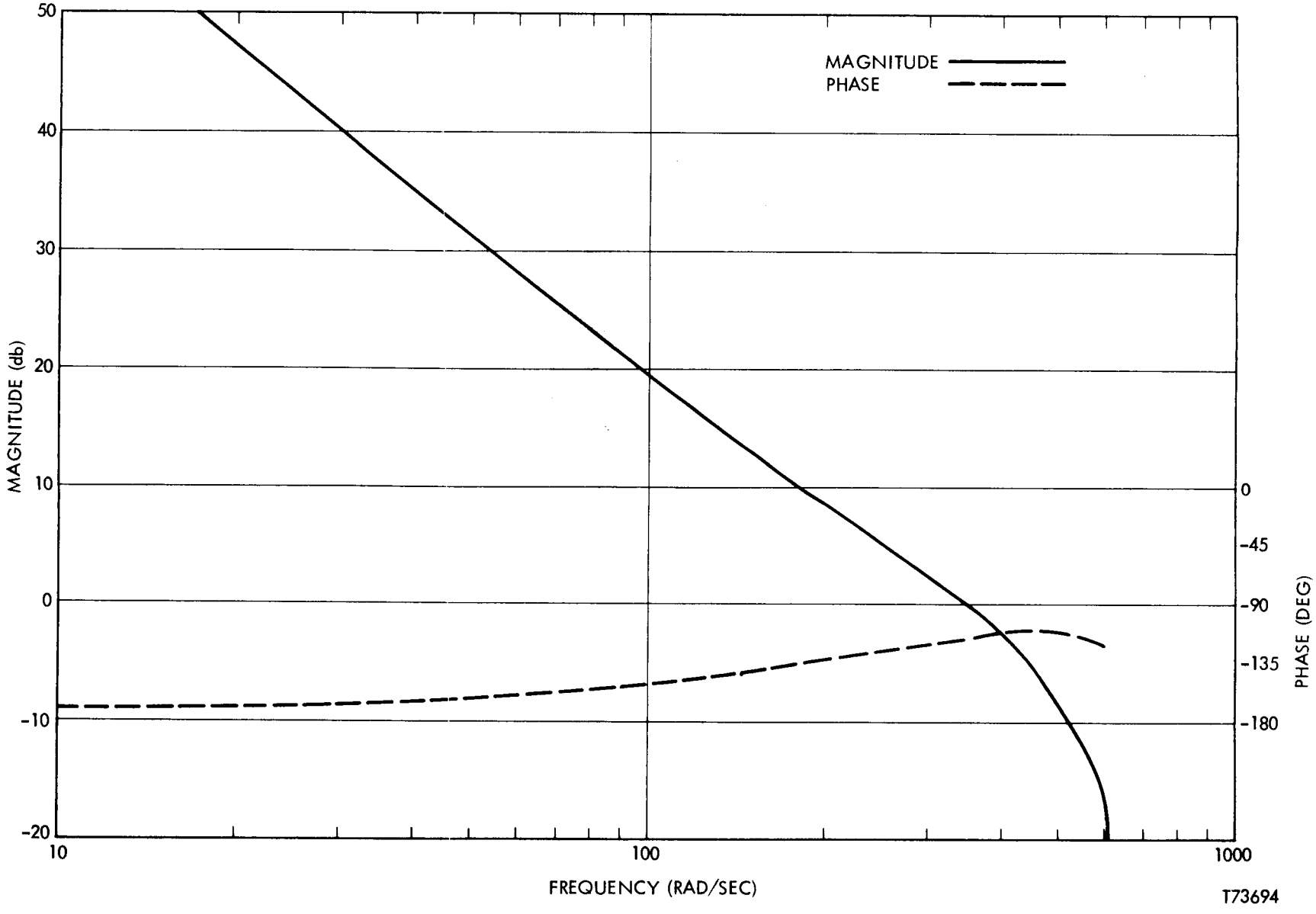

Figure 42. Open Loop Response (+ω)

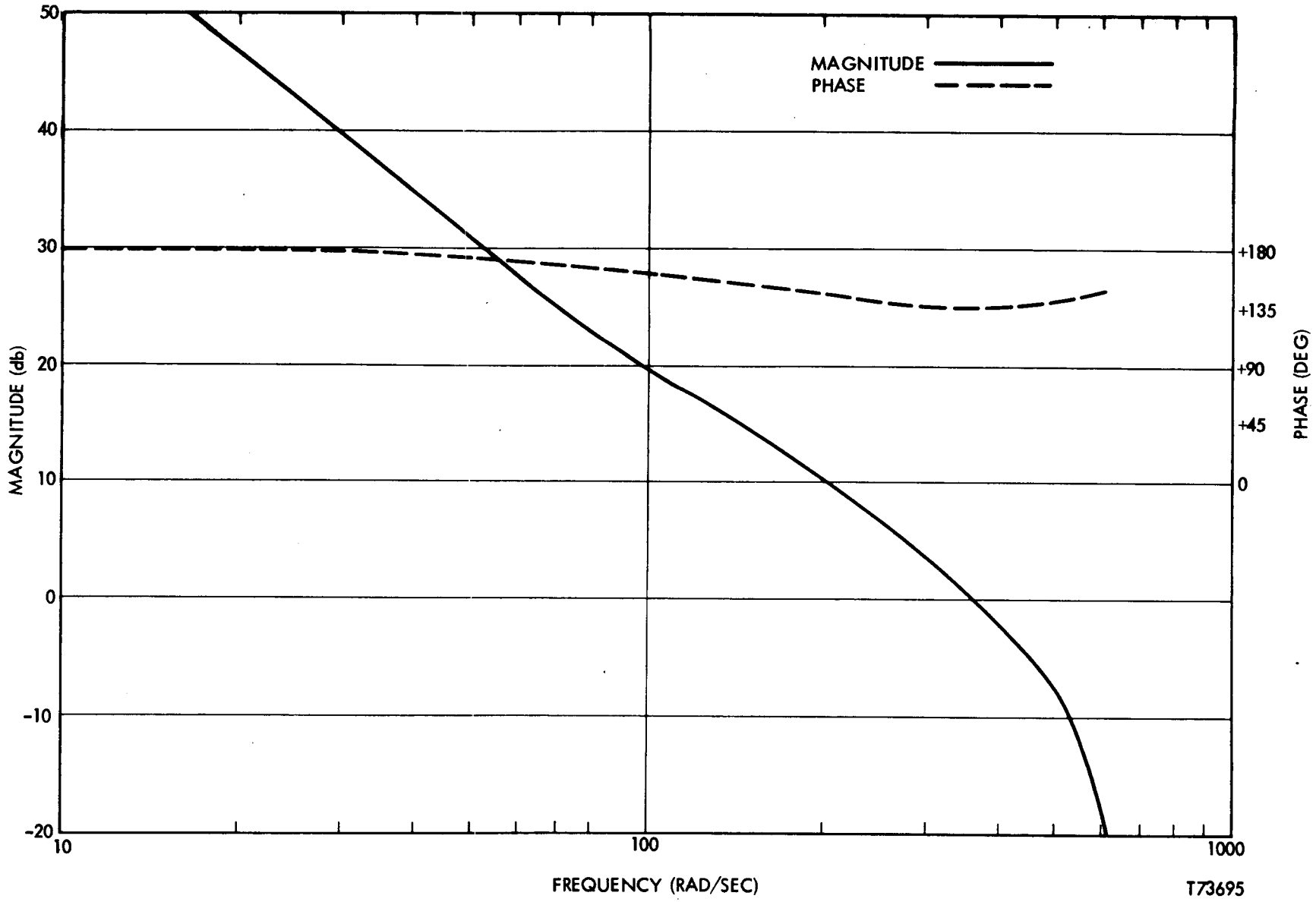

Figure 43. Open Loop Response (-ω)

$$G_{12}(s) = \frac{K_{PO} K_{SA} K_T \left(\frac{s^2}{N^2} + 1\right)\left(\frac{s}{.35N} + 1\right)\left(\frac{s}{.7N - j2N} + 1\right)\left(\frac{s}{.7N - j.2N} + 1\right)}{s\left(\frac{s}{3N} + 1\right)^4\left(\frac{s}{16N} + 1\right)}$$

$$= \frac{K'_{12}\left(s^2 + N^2\right)\left(s + .35N\right)\left(s + .7N - j2N\right)\left(s + .8N - j.2N\right)}{s\left(s + 3N\right)^4\left(s + 16N\right)}$$

$$= \frac{K'_{12}\left(s^2 + N^2\right)\left(s + .35N\right)\left[s^2 + \left(1.5N - j\,2.2N\right)s + \left(.16N^2 - j\,1.74N^2\right)\right]}{s\left(s + 3N\right)^4\left(s + 16N\right)} \tag{19}$$

$$= \frac{2160\, K_{PO} K_{SA} K_T \left(s^2 + N^2\right)\left(s + .35N\right)}{s\left(s + 3N\right)^4\left(s + 16N\right)}\left[\left(s^2 + 1.5Ns + .16N^2\right) - j\left(2.2Ns + 1.74N^2\right)\right] \tag{20}$$

From (9):

$$G_{12}(s) = -G_1(s) + j\,G_2(s)$$

Equating the real and imaginary parts of (9) and (20) yields:

$$G_1(s) = \frac{2160\, K_{PO} K_{SA} K_T \left(s^2 + N^2\right)\left(s + .35N\right)}{s\left(s + 3N\right)^4\left(s + 16N\right)}\left(s^2 + 1.5\,Ns + .16N^2\right)$$

$$= \frac{.092\, K_{PO} K_{SA} K_T \left(\frac{s^2}{N^2} + 1\right)\left(\frac{s}{.35N} + 1\right)\left(\frac{s^2}{.16N^2} + \frac{s}{.107N} + 1\right)}{s\left(\frac{s}{3N} + 1\right)^4\left(\frac{s}{16N} + 1\right)} \tag{21}$$

$$G_2(s) = \frac{2160\, K_{PO} K_{SA} K_T \left(s^2 + N^2\right)\left(s + .35N\right)}{s\left(s + 3N\right)^4\left(s + 16N\right)} \left(2.2Ns + 1.74N^2\right)$$

$$= \frac{1.01\, K_{PO} K_{SA} K_T \left(\frac{s^2}{N^2} + 1\right)\left(\frac{s}{.35N} + 1\right)\left(\frac{s}{.79N} + 1\right)}{s\left(\frac{s}{3N} + 1\right)^4\left(\frac{s}{16N} + 1\right)} \qquad (22)$$

From (10) and (11) the restoring torques are given by:

$$M_X(s) = -G_1(s)\ \theta_x(s) - G_2(s)\,\theta_y(s)$$

$$M_Y(s) = G_2(s)\,\theta_x(s) - G_1(s)\ \theta_y(s)$$

Substituting (21) and (22) yields:

$$M_X(s) = -\frac{.092\, K_{PO} K_{SA} K_T \left(\frac{s^2}{N^2} + 1\right)\left(\frac{s}{.35N} + 1\right)}{s\left(\frac{s}{3N} + 1\right)^4\left(\frac{s}{16N} + 1\right)} \left\{\left[\frac{s^2}{16N^2} + \frac{s}{.107N} + 1\right]\theta_x + 10.9\left[\frac{s}{.79N} + 1\right]\theta_y\right\}$$

$$M_Y(s) = \frac{.092\, K_{po} K_{sa} K_t \left(\frac{s^2}{N^2} + 1\right)\left(\frac{s}{.35N} + 1\right)}{s\left(\frac{s}{3N} + 1\right)^4\left(\frac{s}{16N} + 1\right)} \left\{-10.9\left[\frac{s}{.79_{2N}} + 1\right]\theta_x\right.$$

$$\left. - \left[\frac{s^2}{.16N^2} + \frac{s}{.107N} + 1\right]\theta_y\right\} \qquad (23)$$

The mechanization is shown in Figure 44.

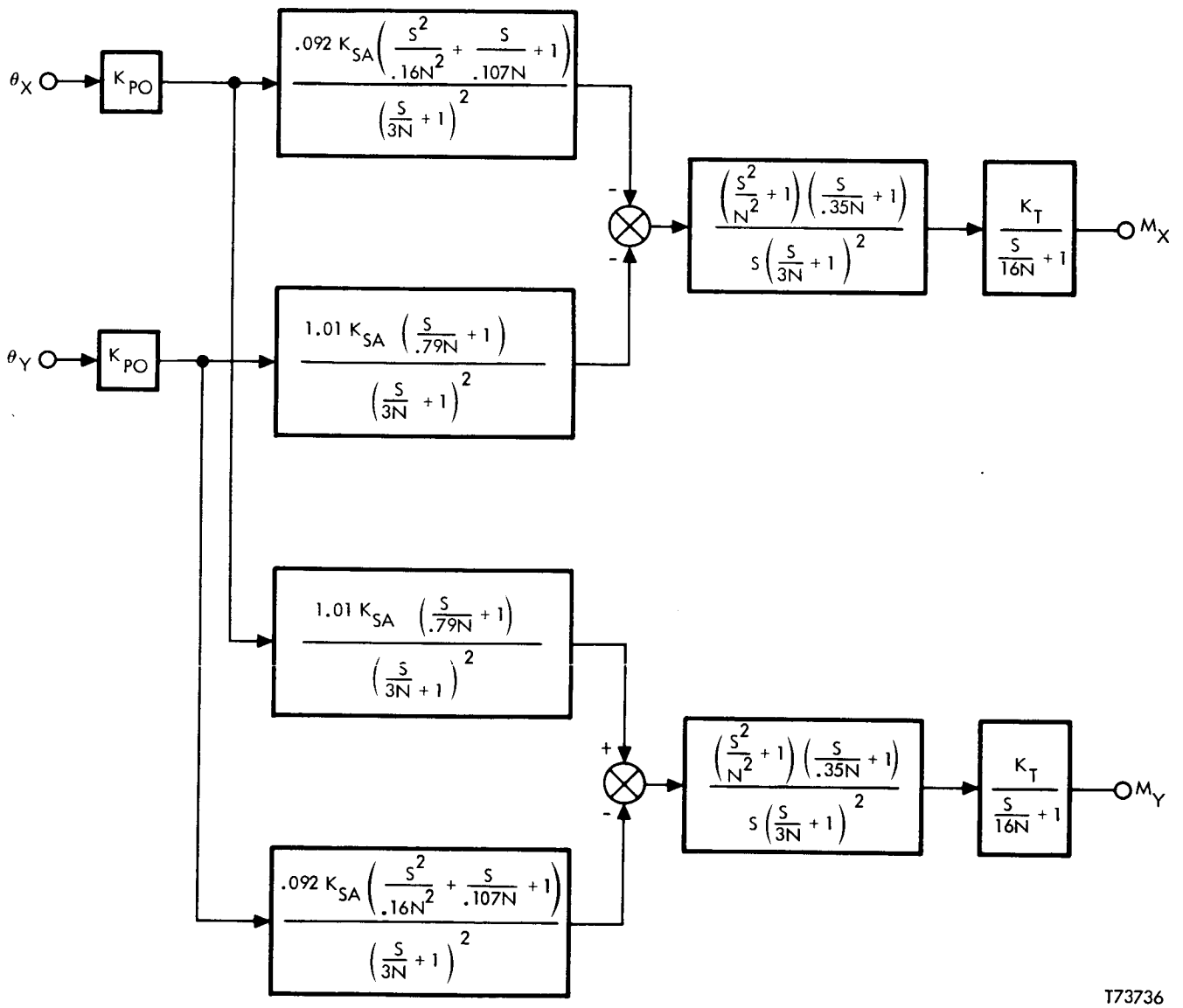

Figure 44. Caging Loop Mechanization

Computer Simulation

A two degree of freedom computer simulation using CSMP (Continuous System Modeling Program) was run to check the loop performance. From (2), (6), (7), (10) and (11) the following block diagram can be derived.

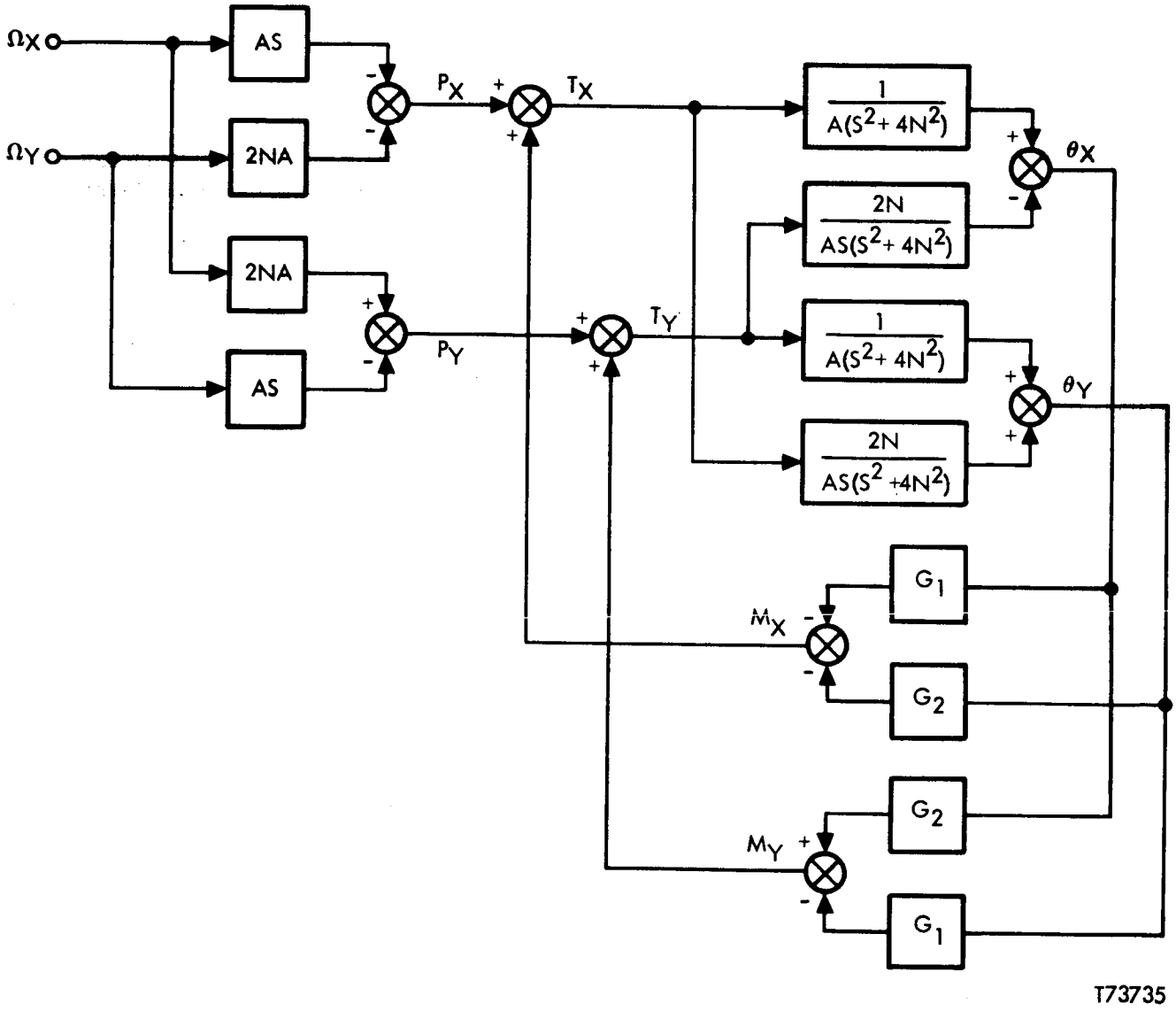

Figure 45. Block Diagram For Computer Simulation

G_1 and G_2 are given by (21) and (22).

Three types of inputs were used to test the loop response. The first was an acceleration input of 50 rad/sec^2 up to a steady state rate of 4 rad/sec along the X axis. Figure 46 shows the equivalent input torque T_{IN}, the feedback torque M_Y and the rotor hangoff angle θ_X vs time. The maximum and steady state value of θ_X during acceleration are 0.6 mrad and 0.54 mrad. θ_Y has a peak value of 0.08 mrad. Upon reaching a steady input rate, θ_X decays towards zero with a peak negative overshoot of 0.06 mrad. Figure 47 shows the torque error ($M_Y - T_{IN}$). The peak value is 8.7×10^{-4} dyne - cm. The net area under the curve is zero, indicating no accumulation of error due to acceleration and deceleration.

The second case was an acceleration input along both axes of 50 rad/sec^2 up to a steady state rate of 4 rad/sec. The resultant curves were essentially the same as in the single axis case with these exceptions. The peak hangoff angle was 0.72 mrad and the peak torque error was 9.3×10^4 dyne - cm. As in the first case, the net area under the torque error curve was zero.

The third case was a step disturbance in the rotor hangoff angle of 1 mrad. This is the same as a step change in the gyro case position. The response is given in Figure 48. The peak overshoot is 0.15 mrad.

Single Axis Transfer Functions

In addition to the time domain analysis and performance evaluation just described, it is also advantageous to use frequency domain analysis. While the complex method used thus far provides much useful information, it was found to be even more convenient to seperate the individual parameters of interest and express them as functions of the inputs about each axis (i.e. θ_X/Ω_X, θ_X/Ω_Y, M_X/Ω_X, M_X/Ω_Y, etc).

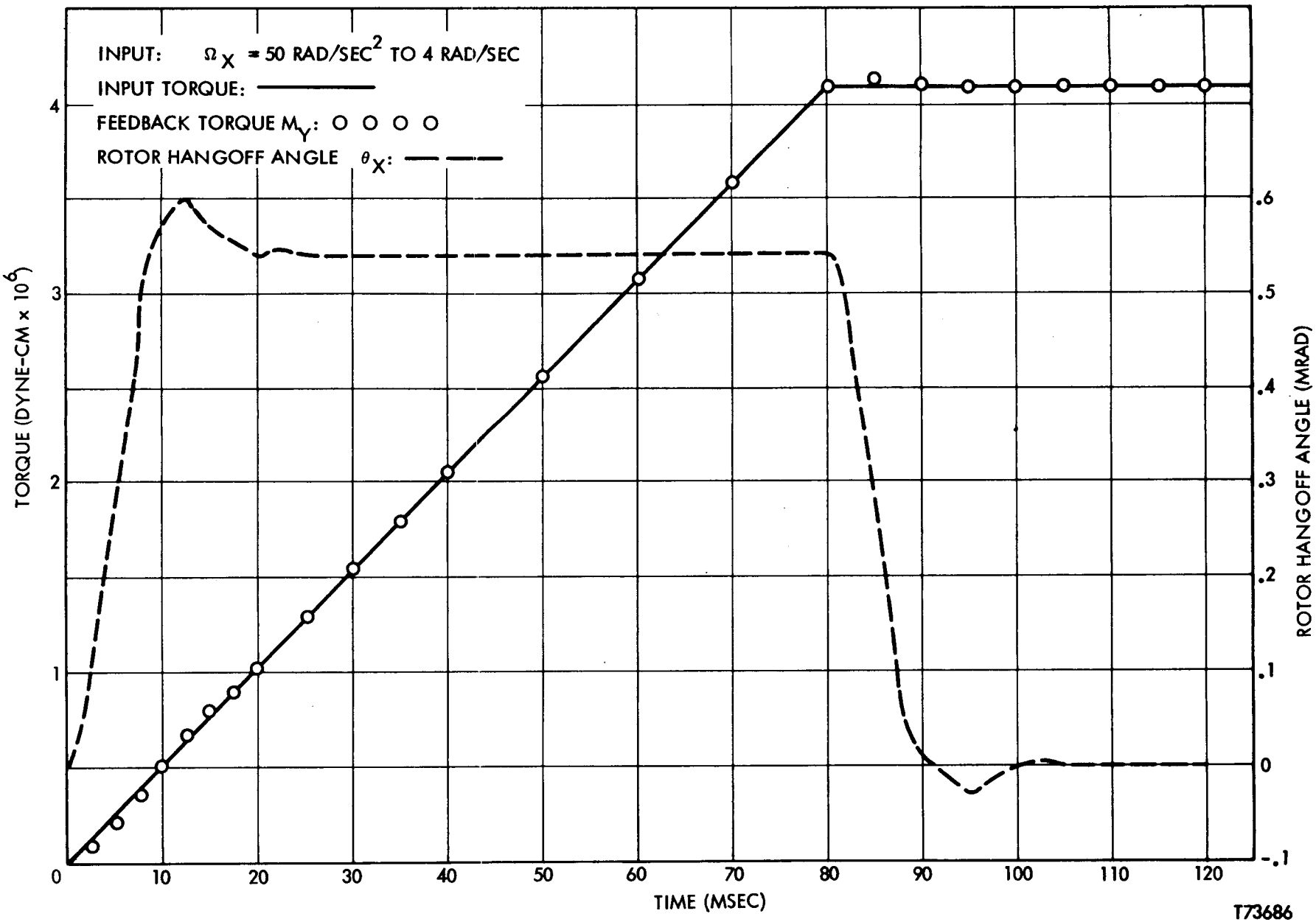

Figure 46. Loop Response Curves (Acceleration Input, One Axis)

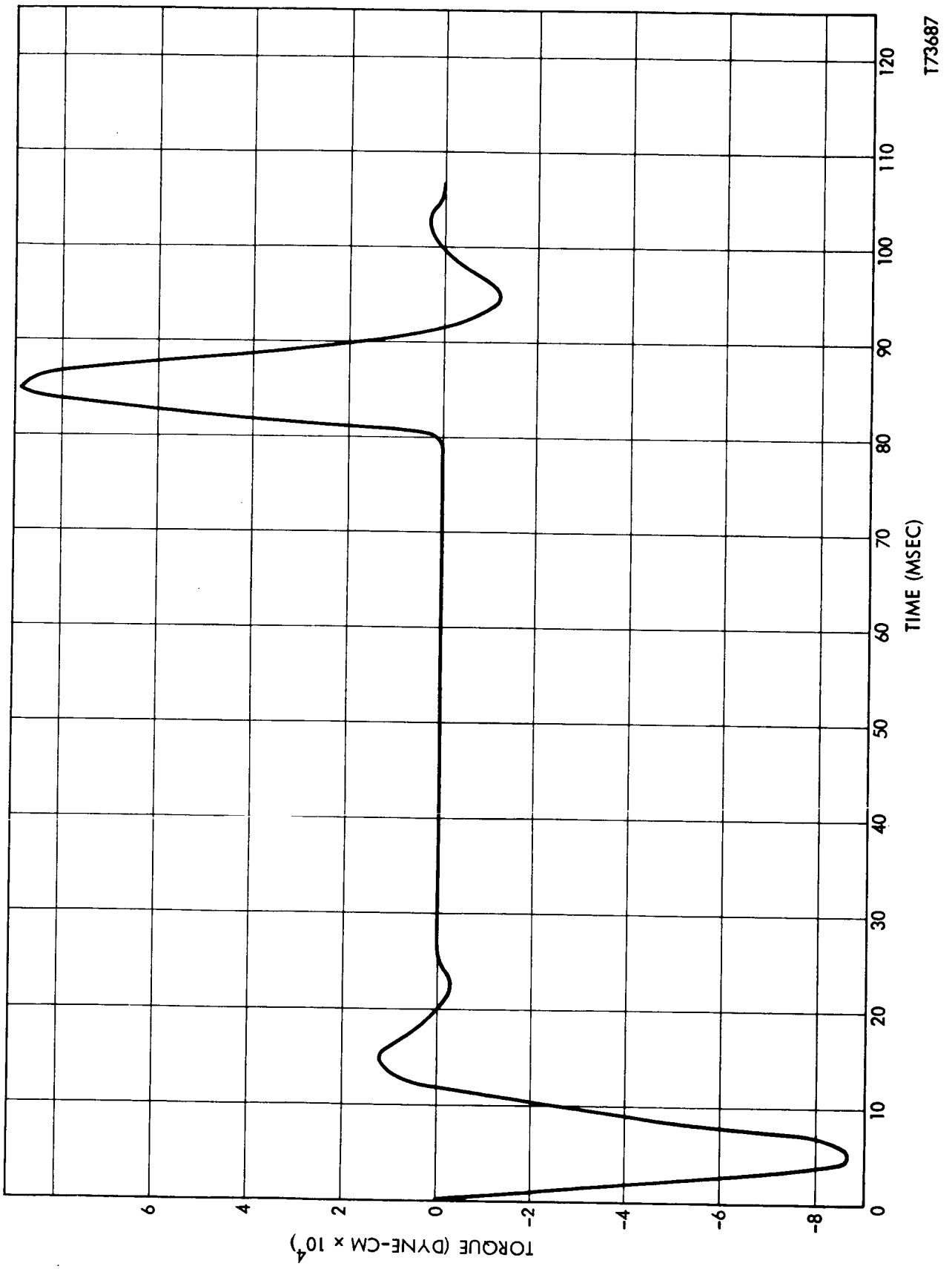

Figure 47. Torque Error (Acceleration Input, One Axis)

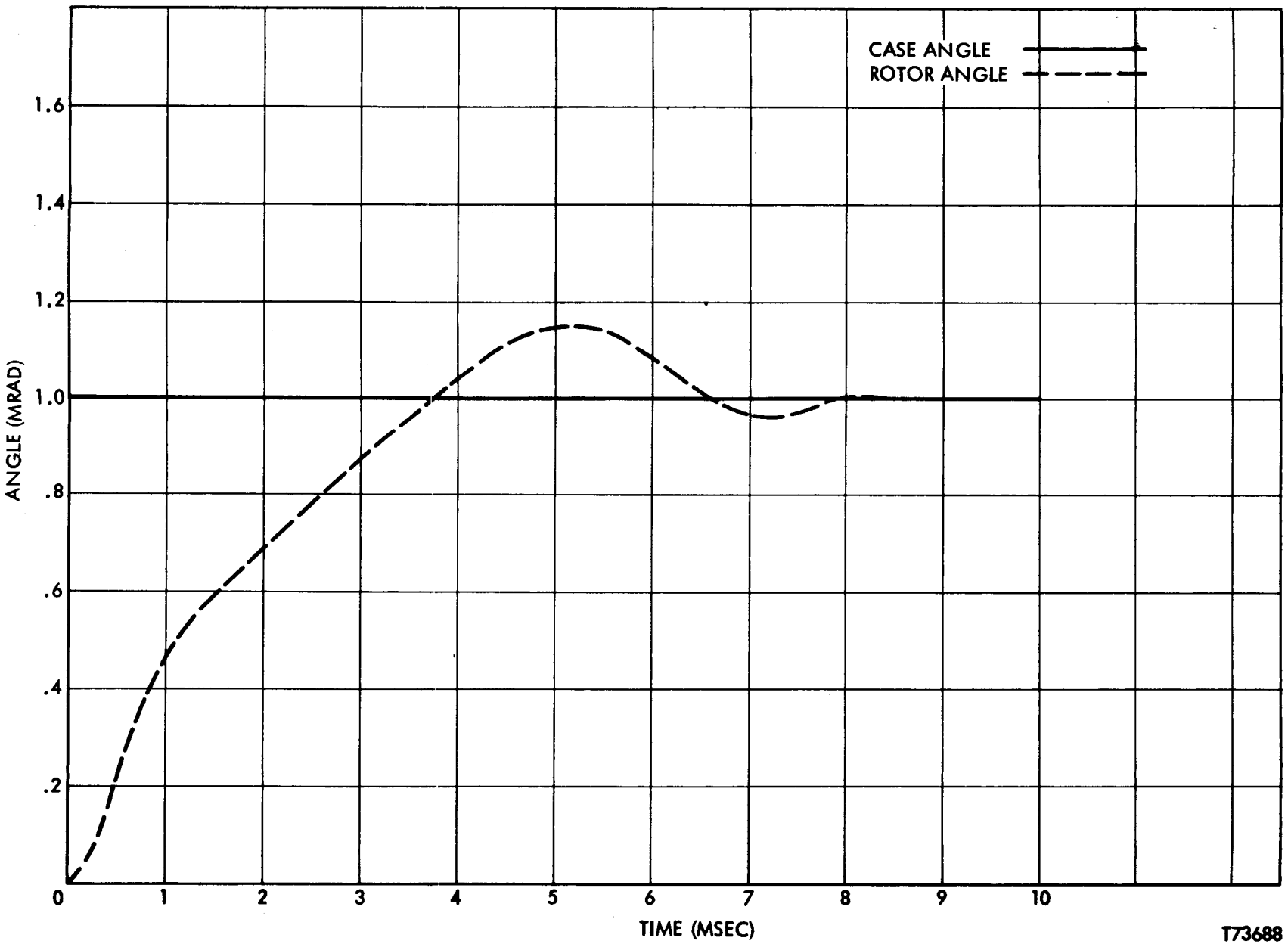

Figure 48. Step Input Response (One Axis)

From Figure 45, the following vector and matrix relationships can be obtained:

$$\underline{\theta} = \begin{bmatrix} \theta_X \\ \theta_Y \end{bmatrix} \qquad \underline{P} = \begin{bmatrix} P_X \\ P_Y \end{bmatrix}$$

$$\underline{\Omega} = \begin{bmatrix} \Omega_X \\ \Omega_Y \end{bmatrix} \qquad E = \begin{bmatrix} A_1 - A_2 & \\ A_2 & A_1 \end{bmatrix}$$

$$\underline{M} = \begin{bmatrix} M_X \\ M_Y \end{bmatrix} \qquad B = \begin{bmatrix} -As & -2NA \\ 2NA & -As \end{bmatrix}$$

$$\underline{T} = \begin{bmatrix} T_X \\ T_Y \end{bmatrix} \qquad G = \begin{bmatrix} -G_1 - G_2 & \\ G_2 - G_1 & \end{bmatrix}$$

where:

$$A_1 = \frac{1}{A(s^2 + 4N^2)}$$

$$A_2 = \frac{1}{As(s^2 + 4N^2)}$$

G_1 and G_2 are given by (21) and (22).

Next, several interrelationships can be obtained.

$$\underline{P} = B\underline{\Omega}$$

$$\underline{M} = G\underline{\theta}$$

$$\underline{T} = \underline{P} + \underline{M}$$

$$\underline{\theta} = E\underline{T}$$

$$= E(B\underline{\Omega} + G\underline{\theta}$$

$$= (I - EG)\, EB\underline{\Omega} \qquad (23)$$

$$\underline{M} = (I - EG)^{-1}\, GEB\underline{\Omega} \qquad (24)$$

I is the unit diagonal matrix and $(I - EG)^{-1}$ EB and $(I - EG)^{-1}$ GEB are defined as the transfer matrices.

Before calculating the transfer matrices, certain simplifications can be made. Note the relationships between A_1 and A_2 and between G_1 and G_2.

$$A_2 = \frac{2N}{s} A_1 \equiv H_A A_1$$

$$G_2 = \frac{2.2N\,(s + .79N)}{(s^2 + 1.5Ns + .16N^2)} G_1 \equiv H_G G_1$$

Consequently-

$$E = A_1 \begin{bmatrix} 1 & -H_A \\ H_A & 1 \end{bmatrix}$$

$$B = -As \begin{bmatrix} 1 & H_A \\ -H_A & 1 \end{bmatrix}$$

$$G = G_1 \begin{bmatrix} -1 & -H_G \\ H_G & -1 \end{bmatrix}$$

First it is seen that -

$$EB = -AA_1 s \begin{bmatrix} 1 + H_A^2 & 0 \\ 0 & 1 + H_A^2 \end{bmatrix}$$

$$-AA_1 s\,(1+H_A^2) = -As \left[\frac{1}{A(s^2 + 4N^2)}\right]\left[1 + \frac{4N^2}{s^2}\right] = -\frac{1}{s}$$

Therefore, $EB = -\frac{1}{s} I$

Continuing:

$$EG = A_1 G_1 \begin{bmatrix} -1 - H_A H_G & H_A - H_G \\ -H_A + H_G & -1 - H_A H_G \end{bmatrix}$$

$$= \begin{bmatrix} -A_1 G_1 (1 + H_A H_G) & A_1 G_1 (H_A - H_G) \\ -A_1 G_1 (H_A - H_G) & -A_1 G_1 (1 + H_A H_G) \end{bmatrix}$$

$$I\text{-}EG = \begin{bmatrix} 1 + A_1 G_1 (1 + H_A H_G) & -A_1 G_1 (H_A - H_G) \\ A_1 G_1 (H_A - H_G) & 1 + A_1 G_1 (1 + H_A H_G) \end{bmatrix}$$

$$[I\text{-}EG]^{-1} = \frac{\begin{bmatrix} 1 + A_1 G_1 (1 + H_A H_G) & A_1 G_1 (H_A - H_G) \\ -A_1 G_1 (H_A - H_G) & 1 + A_1 G_1 (1 + H_A H_G) \end{bmatrix}}{\left[1 + A_1 G_1 (1 + H_A H_G)\right]^2 + \left[A_1 G_1 (H_A - H_G)\right]^2}$$

Referring back to (23) and (24):

$$\begin{bmatrix} \theta_X \\ \theta_Y \end{bmatrix} = \frac{\begin{bmatrix} 1 + A_1 G_1 (1 + H_A H_G) & A_1 G_1 (H_A - H_G) \\ -A_1 G_1 (H_A - H_G) & 1 + A_1 G_1 (1 + H_A H_G) \end{bmatrix} \begin{bmatrix} \Omega_X \\ \Omega_Y \end{bmatrix}}{s\left\{\left[1 + A_1 G_1 (1 + H_A H_G)\right]^2 + \left[A_1 G_1 (H_A - H_G)\right]^2\right\}} \quad (25)$$

$$\begin{bmatrix} M_X \\ M_Y \end{bmatrix} = G_1 \frac{\begin{bmatrix} 1 + A_1G_1(1 + H_G^2) & H_G + A_1G_1H_A(1 + H_G^2) \\ -H_G - A_1G_1H_A(1 + H_G^2) & 1 + A_1G_1(1 + H_G^2) \end{bmatrix} \begin{bmatrix} \Omega_X \\ \Omega_Y \end{bmatrix}}{s\left\{\left[1 + A_1G_1(1 + H_AH_G)\right]^2 + \left[A_1G_1(H_A - H_G)\right]^2\right\}} \quad (26)$$

Since the transfer matrices are anti-symmetric (i.e. the off diagonal elements have opposite signs) certain relationships exist between the sets of transfer functions.

$$\theta_X/\Omega_X = \theta_Y/\Omega_Y$$

$$\theta_X/\Omega_Y = -\theta_Y/\Omega_X$$

$$M_X/\Omega_X = M_Y/\Omega_Y$$

$$M_X/\Omega_Y = -M_Y/\Omega_X$$

Therefore, only four closed loop transfer functions need to be calculated. From (25) and (26):

$$\frac{\theta_X}{\Omega_Y} = -\frac{1 + A_1G_1(1 + H_AH_G)}{\Delta} \quad (27)$$

$$\frac{\theta_X}{\Omega_Y} = -\frac{A_1G_1(H_A - H_G)}{\Delta} \quad (28)$$

$$\frac{M_X}{\Omega_X} = \frac{G_1\left[1 + A_1G_1(1 + H_G^2)\right]}{\Delta} \quad (29)$$

$$\frac{M_X}{\Omega_Y} = \frac{G_1\left[H_G + A_1G_1H_A 1 + H_G^2)\right]}{\Delta} \quad (30)$$

where: $\Delta = s\left\{\left[1 + A_1G_1(1 + H_AH_G)\right]^2 + \left[A_1G_1(H_A - H_G)\right]^2\right\}$

θ_X/Ω_Y and M_X/Ω_Y are the cross axis transfer functions and θ_X/Ω_X and M_X/Ω_X are the direct axis transfer functions.

Figure 49 gives the closed loop frequency response M_X/Ω_Y using (30). The 3 dB bandwidth is 475 rad/sec with a phase angle of -100°. The peak overshoot is +3.2 dB at 280 rad/sec. Comparing these values with those in Figure 41 shows very close correspondence between the two analytical approaches.

By using (27) through (30), it is possible to easily evaluate the effect on the loop response due to changes in the transfer functions of each individual stage. In addition, the equations are used to obtain the loop characteristic curves G_C, G_D, γ_C, γ_D used in the test section of this report.

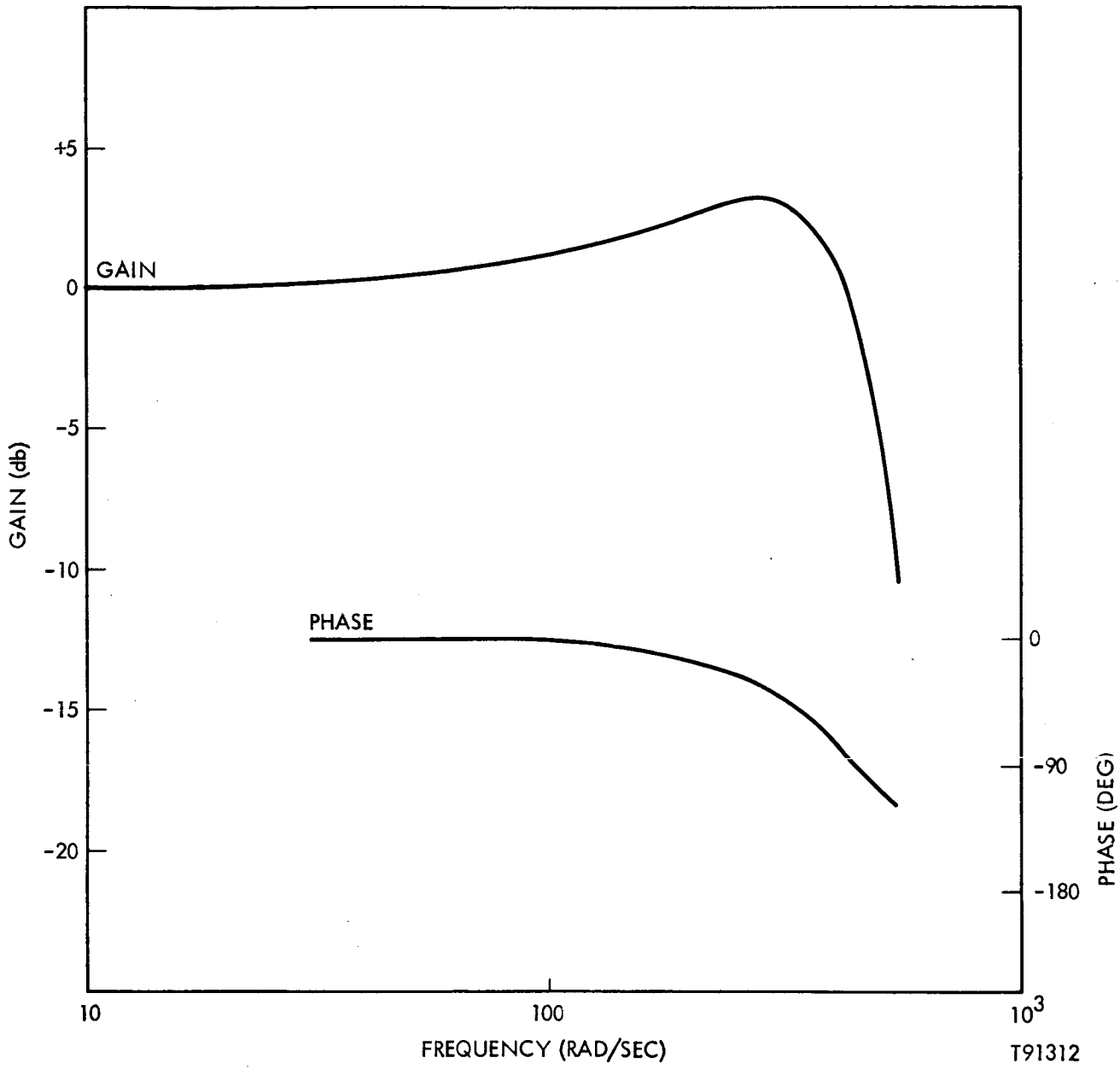

Figure 49. Closed Loop Response - Single Axis

This page intentionally left blank.

VI. SIMULATION AND TESTING

This section describes the simulation of the attitude computations which must be performed in a strapdown navigator, the self-alignment techniques which may be utilized to initialize the attitude computations, and the hardware tests which have been performed in order to obtain a realistic mathematical model of the two-degree-of-freedom dry tuned-gimbal instrument for use in the simulations.

The basic attitude computation simulation has been used extensively during the study in order to evaluate and trade-off various algorithms and techniques and to perform portions of the system error analysis. The simulation program is described in this section.

The alignment simulation is a covariance analysis simulation which is used to evaluate both optimal (Kalman Filter) and sub-optimal, fixed gain alignment techniques. A number of simulation runs are described and analyzed in this report.

The hardware tests have been utilized to verify theoretical results and substantiate the sensor models which have been used in the simulations. The agreement between theory and test data was generally good. Empirically derived servo loop parameters have been incorporated into the simulation.

Attitude Computations

Introduction. - A computer simulation program has been developed to evaluate alternative attitude computational schemes. The process is specifically structured to incorporate the design features of the two-degree-of-freedom dry tuned-gimbal gyro.

The major elements of the attitude simulation programs are

- Rate generation
- Gyro Model
- Analog to Digital
- Rate extraction
- Attitude Integration
- Statistical evaluations

The attitude computational process is illustrated in Figure 50.

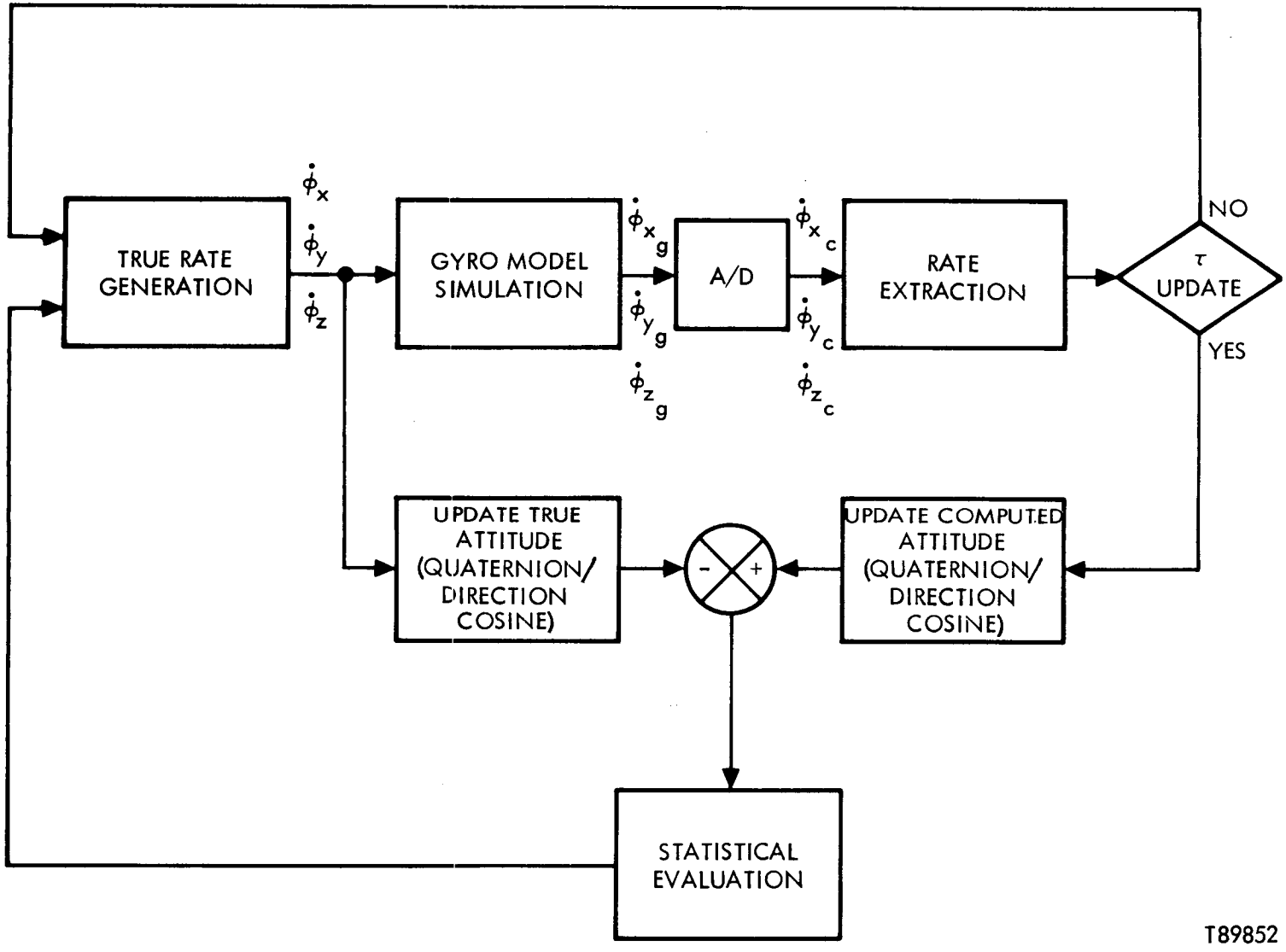

Figure 50. Attitude Computational Process

Rate Generation. - An attitude rate generation module was designed such that various vehicle dynamic effects can be evaluated. These different vehicle motions were simulated

- Coning
- Linear
- Static

The computation of the coning motion rates without the effects of a gimbal are given by

$$\dot{\phi}_x = (\omega_1 \cos\alpha_1 - \omega_1) - (\omega_2 \cos\alpha_2 - \omega_2)$$

$$\dot{\phi}_y = -\omega_1 \sin\alpha_1 \cos(\omega_1 t) - \omega_2 \sin\alpha_2 \cos(\omega_2 t)$$

$$\dot{\phi}_z = -\omega_1 \sin\alpha_1 \sin(\omega_1 t) - \omega_2 \sin\alpha_2 \sin(\omega_2 t)$$

where ω_1 and ω_2 are the coning rates and α_1 and α_2 are the coning angles. A typical example would be

$$\alpha_1 = 0.25^\circ$$

$$\alpha_2 = 5.0^\circ$$

$$\omega_1 = 0$$

$$\omega_2 = 10^\circ/\text{sec}$$

The coning motion example is illustrated in Figure 51.

The linear motion rates were simulated by applying the desired rate to each axis. A typical example is

$$\dot{\phi}_x = 10^\circ/\text{sec}$$

$$\dot{\phi}_y = 0^\circ/\text{sec}$$

$$\dot{\phi}_z = 0^\circ/\text{sec}$$

The static motion was simulated by maintaining the vehicle in a still position such that,

$$\dot{\phi}_x = 0$$

$$\dot{\phi}_y = 0$$

$$\dot{\phi}_z = 0$$

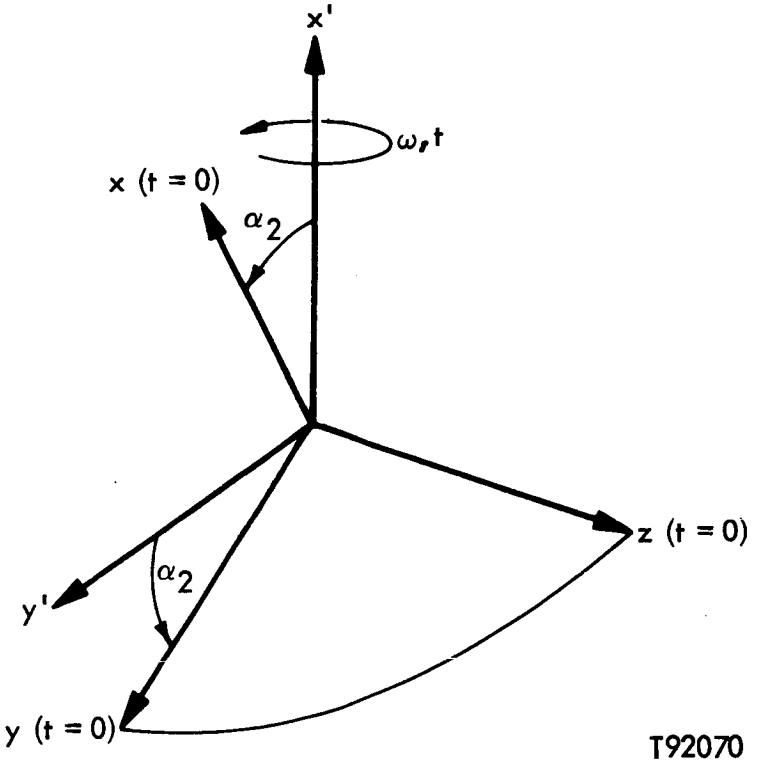

Figure 51. Coning Motions Example

Gyro Model. - The effects of a two degree of freedom dry-tuned gyro are taken into account by mathematical modeling [10]. The modification of the true system rates due to roll, pitch and yaw effects are incorporated. The processing equations are summarized as follows:

The effects of pitch and yaw are determined by the Z-gyro. The input angular rates $\dot{\phi}_x$, $\dot{\phi}_y$, and $\dot{\phi}_z$ are processed as follows. The Z-gyro torquer signals M_x^z and M_y^z are computed by

$$M_x^z = A\dot{\omega}_x + H\omega_y + (C-A)\omega_y\dot{\phi}_z - C\dot{\alpha}_t^z\omega_y$$

and

$$M_y^z = A\dot{\omega}_y - H\omega_x - (C-A)\omega_x\dot{\phi}_z + C\dot{\alpha}_t^z\omega_x$$

where

ω_x = True x-angular acceleration

ω_y = True y-angular acceleration

$\omega_x = \dot{\phi}_x + \dot{\theta}_x^z - \theta_y^z\dot{\phi}_z$ - x-angular rate

$\omega_y = \dot{\phi}_y + \dot{\theta}_y^z + \theta_x^z\dot{\phi}_z$ - y-angular rate

A = moment of inertia of the rotor about an axis perpendicular to the spin axis ($\cong$900).

H = Angular momentum of the rotor ($\cong 1 \times 10^6$).

C = moment of inertia of the rotor about the Z axis ($\cong$1600)

$\dot{\alpha}_t^z$ = motor torque angle about the Z axis

$\dot{\theta}_y^z$, $\dot{\theta}_x^z$, $\dot{\theta}_y^z$ = pickoff angles and rates from the Z gyro

The effects of roll are determined by the X-gyro. The M_y^x torque signals are computed by

$$M_y^x = A\dot{\omega}'_y + H\omega_z + (C-A)\omega_z - C\dot{\alpha}_t^x\omega_z$$

where

$\omega'_y = \dot{\phi}_y + \dot{\theta}_y^x - \theta_y^x\dot{\phi}_x$

$\omega_z = \dot{\phi}_z + \dot{\theta}_z^x + \theta_y^x\dot{\phi}_x$

$\dot{\alpha}_t^x$ = motor torque angle about the X axis

θ_y^x, $\dot{\theta}_y^x$, $\dot{\theta}_y^x$, θ_y^x = pickoff angles and rate from the x-gyro

The gyro output angular rates are obtained by scaling the gyro torquer signals as follows:

$\dot{\phi}_{x_g} = -M_y^z/H$

$\dot{\phi}_{y_g} = M_x^z/H$

and

$\dot{\phi}_{z_g} = M_y^x/H$

At this point in the simulation process, as indicated by Figure 50, the gyro output data is truncated and gyro noise is added.

Analog to Digital. - The gyro output is fed directly into the analog to digital (A/D) simulation process. The A/D process maintains a running average of the gyro output and has the capability of adding a dither motion to the signals if desired. The effects of scale factor and bias errors are also incorporated into the averaging process.

The process is modeled by

$$\dot{\phi}_{x_c} = \sum_{i=1}^{n} \left[\dot{\phi}_{x_g} + \dot{\phi}_{x_g} \eta_i^x + b^x + A \sin(\omega t_i) \right] / n$$

where

η_i = x-scale factor noise for each sample i

b_x = x-bias error

A = amplitude of the dither signal

ω = frequency of the dither signal

t_i = real time of the process

n = number of data points per sampling interval

The process is repeated for $\dot{\phi}_{y_c}$ and $\dot{\phi}_{z_c}$ but with different bias and scale factor parameters.

The output of the A/C converter is truncated to match the number of bits of the output word of the actual hardware.

Rate extraction. - Rate extraction is performed on the output A/D data before the quaternion update process is performed. Two input sums are maintained. The first is over the interval 0 to $\tau/2$. The second is over the interval 0 to τ. The time period τ corresponds to the duration of the current sampling interval t_k to t_{k+1}. The process is illuatrated in Figure 52.

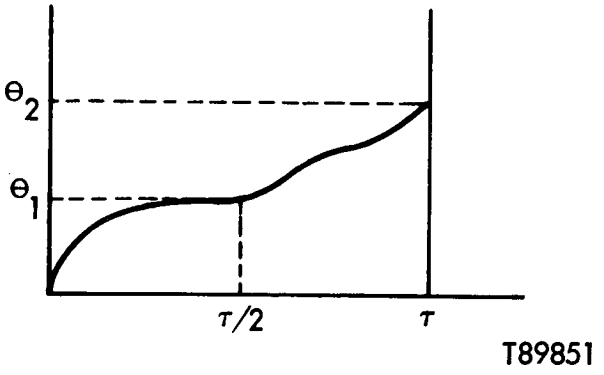

Figure 52. Output Pulse Sampling

The gyro and A/D output rates are assumed linear in time and thus modeled by

$$\omega(t) = \alpha + \beta t$$

Thus, the integrated value is obtained by

$$\theta(t) = \int_0^t \omega(\sigma)\, d\sigma = \alpha t + 1/2\beta t^2$$

where $\theta(0)$ is zero. Then

$$\theta_1 = \alpha(\tau/2) + 1/2\beta(\tau/2)^2$$

$$\theta_2 = \alpha(\tau) + 1/2\beta(\tau)^2$$

Solving for α and β we obtain

$$\alpha = \frac{1}{\tau}(4\theta_1 - \theta_2)$$

$$\beta = \frac{1}{\tau_2}(4\theta_2 - 8\theta_1)$$

Therefore, the values of ω at t_2, $t_{k+1/2}$, and t_{2+1} are given by

$$\omega(t_k) = (4\theta_1 - \theta_2)/\tau$$

$$\omega(t_k + 1/2\tau) = \theta_2/\tau$$

$$\omega(t_{k+1}) = (3\theta_2 - 4\theta_1)/\tau$$

The above computations are performed for each of the three A/D output rates.

The output of the rate extraction routines is truncated to simulate the word length of the operational implementation.

Attitude Integration. - The integration of the body attitude matrix can be performed by either a direction cosine or quaternion approach. Three different integration methods can be selected for each approach. The integration methods employed are

- 2nd order Runge-Kutta
- 2nd order State Transition
- 4th order Runge-Kutta

A detailed description of each approach as well as the integration method is contained in Section V.

The word length of the computer that will perform the operational attitude integration is simulated by a masking function on both the imput and output variables. The number of significant bits of the mantissa is specified by an input control word.

Statistical Evaluation. - The performance of the attitude computations can be evaluated by comparing the true quaternion and direction-cosine matrix with the computed quaternion and direction-cosine matrix. The performance can be evaluated for different vehicle rates, integration update interval, computational approach (quaternion or direction-cosine), integration method (2nd order Runge-Kutta, 2nd order State Transition, or 4th order Runge-Kutta), or hardware data word truncation.

The performance of the attitude computations was measured for both the quaternion and direction cosine mode of operation. The errors of the direction-cosine matrix (B)mode are

Scale
Skew
Drift

The three different errors result by considering how the original orthonormal unit vectors aligned to the body axis are transformed in time. The accuracy of the transformation process is a function of vehicle dynamics, integration interval, data accuracy, order of the integration algorithm, and word length of the computer.

The scale error measures how the vector lengths deviate from unity. The square of the column elements of B should equal unity. The scale error of B is computed by

$$\epsilon_i = \sqrt{b_{1i}^2 + b_{2i} + b_{3i}^2} - 1$$

where i corresponds to each column.

The skew errors are a measure of how the orthogonal triad described by B deviates from being mutually perpendicular. The error can be computed from the dot product of vector pairs. The small angular error is given by

$$\epsilon_i = \sin^{-1}\left(b_{1j}\, b_{1k} + b_{2j}\, b_{2k} + b_{3j}\, b_{3k}\right)$$

for i = 1 to 3

The subscripts j and k are by the following ordering

i	j	k
1	2	3
2	3	1
3	1	2

The skew errors can be approximated by

$$\epsilon_i = b_{1j}\, b_{1k} + b_{2j}\, b_{2k} + b_{3j}\, b_{3k}$$

The drift error measures the deviation of the computed attitude matrix B^c from its true attitude matrix B^o. If for the ideal case $B^c = B^o$, then

$$B^c(B^o)^T = I$$

and the off-diagonal terms are zero. In actual practice, $B^c \neq B^o$ so we get

$$B^c (B^o)^T = E$$

The off-diagonal elements of E provide a measure of the drift of B^c from B^o by

$$\epsilon_i = 1/2 \, (e_{kj} - e_{jk}) \quad \text{for } i = 1 \text{ to } 3$$

The values of k and j corresponding to i are determined the same as before.

The performance of the attitude computation using quaternion is measured in a similar manner. The scale error of the quaternion computations is computed directly by

$$\epsilon = \sqrt{b_0^2 + b_1^2 + b_2^2 + b_3^2} - 1$$

The skew and drift errors of the quaternion mode of attitude computations are computed by generating the corresponding direction-cosine matrix,

$$B^T = \begin{bmatrix} \left(b_0^2 + b_1^2 - b_2^2 - b_2^2\right) & 2\left(b_1 b_2 - b_0 b_3\right) & 2\left(b_1 b_3 + b_0 b_2\right) \\ 2\left(b_1 b_2 + b_0 b_3\right) & \left(b_0^2 - b_0^2 + b_2^2 - b_3^2\right) & 2\left(b_2 b_3 - b_0 b_1\right) \\ 2\left(b_1 b_3 - b_0 b_2\right) & 2\left(b_2 b_3 + b_0 b_1\right) & \left(b_0^2 - b_1^2 - b_2^2 + b_3^2\right) \end{bmatrix}$$

The skew and drift errors are computed in a same manner as the direction cosine method skew and drift errors.

The quaternion drift errors can be computed by an alternative method. The computed quaternion is given by

$$b_c = \begin{bmatrix} p_0 \\ p_1 \\ p_2 \\ p_3 \end{bmatrix}$$

The true attitude quaternion is given by

$$b^{o} = \begin{bmatrix} q_0 \\ q_1 \\ q_2 \\ q_3 \end{bmatrix}$$

Let any general quaternion be represented by

$$b = \begin{bmatrix} b_0 \\ b_1 \\ b_2 \\ b_3 \end{bmatrix}$$

Then the conjugate of b called b* is given by

$$b^{*} = \begin{bmatrix} b_0 \\ -b_1 \\ -b_2 \\ -b_3 \end{bmatrix}$$

If b^{o} is equal to b_c, then

$$b_c(b^{o}*) = \begin{bmatrix} 1 \\ 0 \\ 0 \\ 0 \end{bmatrix}$$

When b_c deviates from b^o we get

$$b_c(b^o)^* = \begin{bmatrix} 1 \\ \frac{\varphi_e}{2} \\ \frac{\varphi_n}{2} \\ \frac{\varphi_u}{2} \end{bmatrix}$$

where

φ_e = east drift error

φ_n = north drift error

φ_u = vertical drift error

Simulation Results

Two basic simulation error analysis were performed. Case 1 was a comparative analysis where various computer word length employed is the attitude were evaluated to determine how they affected the system performance for 4 different rate profiles. Case 2 demonstrates the drift of the attitude computations over an extended computational time.

Case 1

Case 1 consists of an analysis of the efforts of varying computer word lengths on performance for 4 different vehicle rates. The rates considered were

a a. Coning motion
Coning angle = 5^o
Coning rate 100^o/sec

b. Coning motion
Coning angle = 5^o
Coning rate = 10^o/sec

c. Linear motion
$\dot{\phi}_x = 100^o$/sec
$\dot{\phi}_y = \dot{\phi}_z = 0^o$.

d. Linear motion
$\dot{\phi}_x = 10^o$/sec
$\dot{\phi}_y = \dot{\phi}_z = 0^o$.

The number of bits in the mantissa of the computer word were:

16 bits
18 bits
20 bits
24 bits
28 bits

Case 1 Results

Tables 28 and 29 show attitude computation scale errors for the high coning motion rate. The performance does not show a sensitivity to input word length.

Tables 30 and 31 show the attitude computation scale errors for the low coning motion rate. The performance is not sensitive to input word length. However, the scale errors are reduced by about one half over to corresponding high coning motion scale errors.

Tables 32 and 33 show the attitude computation scale error for 10^{o}/sec linear motion. The performance is not sensitive to input word length.

Tables 34 and 35 show the attitude computation scale errors for 1^{o}/sec linear motion. The performance is not sensitive to input word length. The scale errors are not significantly reduced by the lower linear motion rate to 1^{o}/sec.

Tables 36 and 37 show the attitude computation skew errors for the high coning motion rate of 100^{o}/sec. The error are small for the direction-cosine method and are zero for the quaternion method. The skew errors for the direction cosine method are not sensitive to the input word length.

Tables 38 and 39 show that the skew errors for the low coning motion rate of 10^{o}/sec are zero for both methods.

Tables 40 through 43 show that the skew errors for linear motion is zero. The results were demonstrated for rates of both 10^{o}/sec and 1^{o}/sec.

Tables 44 and 45 demonstrate the effect of input word length on relative drift error for the high coning motion rate of 100^{o}/sec. The amount of drift error is very sensitive to the input word length. The results demonstrate that about 24 bits of precision are needed to adequately perform the attitude computations. The results were obtained by setting the computed attitude matrix B^{c} to correspond to the 16, 18, 20, and 24 bit word lengths. The ideal attitude matrix B^{o} was taken as the result of the 28 bit computations. Thus, the results do not measure absolute drift but only drift relative to the 28 bit input word length so that the effects of different word lengths can be assessed.

Tables 46 and 47 demonstrate the effects of the input word length on relative drift error for the low coning motion rate of 10^{o}/sec. The resulting errors are lower than the high coning motion drift errors. The sensitivity to word length is still presence but only 20 bits of precision is sufficient for the attitude computations.

Tables 48 and 49 demonstrate the effect of the input word length an relative drift error for linear motion rate of 10^{o}/sec on the ϕ_x axis. The results are sensitive to varying word lengths. Word lengths of 24 bits are needed to perform the attitude computations adequately.

Tables 50 and 51 demonstrate the effect of the input word length on the relative drift error for a linear motion rate of 1^{o}/sec on the ϕ_x asix. The drift errors are lower than the corresponding errors for the 10^{o}/sec linear motion drift errors. The results are sensitive to input word length with about 20 bits of precision needed to adequately perform the attitude computations.

Case 2

The purpose of Case 2 is to demonstrate the long term attitude matrix drift errors. A nominal coning motion rate was simulated. The coning angle was 1 degree with a rate of 100^{o} degrees per second. An attitude computation word length of 20 bits was employed. Figure 53 demonstrates the true drift error of the attitude computations as a function of time. The true attitude matrix B was computed directly from the rate generation routine and before any instrument errors were introduced. The computed attitude matrix B^{c} is corrupted by the 20 bit word length data, A/D, and rate extraction. The fourth order Runge-Kutta method was employed with a computation rate of 20 Hz.

The results demonstrate a periodic oscillation error of less than 0.04^{o}/hr. The period of the oscillation is about 4 seconds. This corresponds closely to coning rate of 100^{o}/sec. A definitive drift on the periodic oscillations can be seen. The amplitudes stay about the same but the maximum and minimum values increase in time. The rate of increase is about $.00008^{o}$/hr. Thus with proper smoothing on the periodic data the long term drift will be very small.

Table 28. Direction-Cosine Scale Errors for 100°/Sec Coning Motion

SCALE ERRORS (DEG/HR)

DIRECTION - COSINES

SECOND ORDER RUNGE-KUTTA

	X	Y	Z
16 Bits	0.1841	0.0645	0.0920
18 Bits	0.1841	0.0645	0.0920
20 Bits	0.1850	0.0645	0.0955
24 Bits	0.1850	0.0645	0.0955
28 Bits	0.1850	0.0645	0.0955

SECOND ORDER STATE TRANSITION

	X	Y	Z
16 Bits	-0.0645	-.058402	-0.0399545
18 Bits	-0.0630	-.063011	-0.040333
20 Bits	-0.0615	-.059938	-0.0399595
24 Bits	-0.0615	-.058402	-0.0368857
28 Bits	-0.0615	-.058402	-0.0353488

FOURTH ORDER RUNGE-KUTTA

	X	Y	Z
16 Bits	-0.032275	-0.032275	-0.032275
18 Bits	-0.033812	-0.032275	-0.029201
20 Bits	-0.032275	-0.029201	-0.030738
24 Bits	-0.029201	-0.033812	-0.032275
28 Bits	-0.027664	-0.033812	-0.032275

Table 29. Quaternion Scale Errors for 100^{o}/Sec Coning Motion

SCALE ERRORS (DEG/HR)

QUATERNIONS

SECOND ORDER RUNGE-KUTTA

	X	Y	Z
16 Bits	0.052255	0.049181	0.049181
18 Bits	0.046107	0.043033	0.046107
20 Bits	0.049181	0.046107	0.049187
24 Bits	0.052255	0.052255	0.052255
28 Bits	0.052255	0.052255	0.055328

SECOND ORDER STATE TRANSITION

	X	Y	Z
16 Bits	-0.1014347	-0.1014347	-0.1014347
18 Bits	-0.0876036	-0.0906774	-0.0906774
20 Bits	-0.0922143	-0.0937512	-0.0906774
24 Bits	-0.0922143	-0.0952882	-0.0922143
28 Bits	-0.0922143	-0.0937512	-0.0922143

FOURTH ORDER RUNGE-KUTTA

	X	Y	Z
16 Bits	-0.063013	-0.064550	-0.064550
18 Bits	-0.064550	-0.066087	-0.064550
20 Bits	-0.075308	-0.076845	-0.076845
24 Bits	-0.079919	-0.081456	-0.079919
28 Bits	-0.079919	-0.081456	-0.079919

DIRECT QUATERNION SCALE ERRORS

	Second Order Runge-Kutta	Second Order State Transition	Fourth Order Runge-Kutta
16 Bits	0.02766	0.0492	0.0307
18 Bits	0.02459	0.0446	0.0307
20 Bits	0.02459	0.0446	0.0369
24 Bits	0.0277	0.0446	0.0384
28 Bits	0.0277	0.0446	0.0384

Table 30. Direction-Cosine Scale Error for 10°/Sec Coning Motion

SCALE ERRORS (DEG/HR)

DIRECTION - COSINES

SECOND ORDER RUNGE-KUTTA

	X	Y	Z
16 Bits	-0.0245	-0.0307	-0.0261
18 Bits	-0.0231	-0.0307	-0.0246
20 Bits	-0.0231	-0.0307	-0.0246
24 Bits	-0.0231	-0.0307	-0.0246
28 Bits	-0.0231	-0.0307	-0.0246

SECOND ORDER STATE TRANSITION

	X	Y	Z
16 Bits	-0.0415	-0.0538	-0.0246
18 Bits	-0.0400	-0.0538	-0.0246
20 Bits	-0.0400	-0.0538	-0.0231
24 Bits	-0.0400	-0.0538	-0.0231
28 Bits	-0.0400	-0.0538	-0.0231

FOURTH ORDER RUNGE-KUTTA

	X	Y	Z
16 Bits	-0.0307	-0.0231	-0.0292
18 Bits	-0.0307	-0.0231	-0.0292
20 Bits	-0.0307	-0.0231	-0.0292
24 Bits	-0.0307	-0.0231	-0.0277
28 Bits	-0.0307	-0.0231	-0.0277

Table 31. Quaternion Scale Errors for 10°/Sec Coning Motion

SCALE ERRORS (DEG/HR)

QUATERNIONS

SECOND ORDER RUNGE-KUTTA

	X	Y	Z
16 Bits	-0.0630	-0.0615	-0.0630
18 Bits	-0.0676	-0.0676	-0.0676
20 Bits	-0.0676	-0.0676	-0.0676
24 Bits	-0.0676	-0.0676	-0.0676
28 Bits	-0.0676	-0.0676	-0.0676

SECOND ORDER STATE TRANSITION

	X	Y	Z
16 Bits	-0.0507	-0.0492	-0.0476
18 Bits	-0.0492	-0.0492	-0.0476
20 Bits	-0.0507	-0.0476	-0.0492
24 Bits	-0.0507	-0.0476	-0.0476
28 Bits	-0.0507	-0.0476	-0.0476

FOURTH ORDER RUNGE-KUTTA

	X	Y	Z
16 Bits	-0.0630	-0.0615	-0.0600
18 Bits	-0.0615	-0.0615	-0.0600
20 Bits	-0.0630	-0.0600	-0.0615
24 Bits	-0.0630	-0.0600	-0.0600
28 Bits	-0.0630	-0.0600	-0.0600

DIRECT QUATERNION SCALE ERRORS

	Second Order Runge-Kutta	Second Order State Transition	Fourth Order Runge-Kutta
16 Bits	-0.0307	-0.0231	-0.0292
18 Bits	-0.0323	-0.0231	-0.0292
20 Bits	-0.0323	-0.0231	-0.0292
24 Bits	-0.0323	-0.0231	-0.0292
28 Bits	-0.0323	-0.0231	-0.0292

Table 32. Direction-Cosine Scale Errors for 10°/Sec Linear Motion

SCALE ERRORS (DEG/HR)

DIRECTION - COSINES

SECOND ORDER RUNGE-KUTTA

	X	Y	Z
16 Bits	0.	-0.0261	-0.0261
18 Bits	0.	-0.0261	-0.0261
20 Bits	0.	-0.0277	-0.0277
24 Bits	0.	-0.0231	-0.0231
28 Bits	0.	-0.0231	-0.0231

SECOND ORDER STATE TRANSITION

	X	Y	Z
16 Bits	0.	-0.0430	-0.0430
18 Bits	0.	-0.0430	-0.0430
20 Bits	0.	-0.0353	-0.0353
24 Bits	0.	-0.0353	-0.0353
28 Bits	0.	-0.0353	-0.0353

FOURTH ORDER RUNGE-KUTTA

	X	Y	Z
16 Bits	0.	-0.0307	-0.0307
18 Bits	0.	-0.0307	-0.0307
20 Bits	0.	-0.0338	-0.0338
24 Bits	0.	-0.0369	-0.0369
28 Bits	0.	-0.0353	-0.0353

Table 33. Quaternion Scale Errors for 10^{o}/Sec Linear Motion

SCALE ERRORS (DEG/HR)

QUATERNIONS

SECOND ORDER RUNGE-KUTTA

	X	Y	Z
16 Bits	-.0630	-.0645	-.0645
18 Bits	-.0630	-.0645	-.0645
20 Bits	-.0584	-.0600	-.0600
24 Bits	-.0630	-.0630	-.0630
28 Bits	-.0615	-.0645	-.0645

SECOND ORDER STATE TRANSITION

	X	Y	Z
16 Bits	-.1122	-.1137	-.1137
18 Bits	-.1122	-.1137	-.1137
20 Bits	-.1030	-.1030	-.1030
24 Bits	-.1091	-.1091	-.1091
28 Bits	-.1091	-.1091	-.1091

FOURTH ORDER RUNGE-KUTTA

	X	Y	Z
16 Bits	-.0722	-.0722	-.0722
18 Bits	-.0722	-.0722	-.0722
20 Bits	-.0661	-.0661	-.0661
24 Bits	-.0615	-.0645	-.0645
28 Bits	-.0615	-.0645	-.0645

DIRECT QUATERNION SCALE ERRORS

	Second Order Runge-Kutta	Second Order State Transition	Fourth Order Runge-Kutta
16 Bits	-.0323	-.0569	-.0369
18 Bits	-.0323	-.0569	-.0369
20 Bits	-.0292	-.0523	-.0338
24 Bits	-.0323	-.0553	-.0292
28 Bits	-.0292	-.0553	-.0292

Table 34. Direction-Cosine Scale Errors for 1°/Sec Linear Motion

SCALE ERRORS (DEG/HR)

DIRECTION - COSINES

SECOND ORDER RUNGE-KUTTA

	X	Y	Z
16 Bits	0.	-.0261	-.0261
18 Bits	0.	-.0246	-.0246
20 Bits	0.	-.0246	-.0246
24 Bits	0.	-.0246	-.0246
28 Bits	0.	-.0246	-.0246

SECOND ORDER STATE TRANSITION

	X	Y	Z
16 Bits	0.	-.0292	-.0292
18 Bits	0.	-.0261	-.0261
20 Bits	0.	-.0261	-.0261
24 Bits	0.	-.0261	-.0261
28 Bits	0.	-.0261	-.0261

FOURTH ORDER RUNGE-KUTTA

	X	Y	Z
16 Bits	0.	-.0251	-.0251
18 Bits	0.	-.0251	-.0251
20 Bits	0.	-.0251	-.0251
24 Bits	0.	-.0251	-.0251
28 Bits	0.	-.0251	-.0251

Table 35. Quaternion Scale Errors for 1^{o}/Sec Linear Motion

SCALE ERRORS (DEG/HR)

QUATERNIONS

SECOND ORDER RUNGE-KUTTA

	X	Y	Z
16 Bits	-.0615	-.0615	-.0615
18 Bits	-.0599	-.0615	-.0615
20 Bits	-.0599	-.0615	-.0615
24 Bits	-.0599	-.0615	-.0615
28 Bits	-.0599	-.0615	-.0615

SECOND ORDER STATE TRANSITION

	X	Y	Z
16 Bits	-.0830	-.0861	-.0861
18 Bits	-.0830	-.0830	-.0830
20 Bits	-.0830	-.0830	-.0830
24 Bits	-.0830	-.0830	-.0830
28 Bits	-.0830	-.0830	-.0830

FOURTH ORDER RUNGE-KUTTA

	X	Y	Z
16 Bits	-.0676	-.0707	-.0707
18 Bits	-.0676	-.0676	-.0676
20 Bits	-.0676	-.0676	-.0676
24 Bits	-.0676	-.0676	-.0676
28 Bits	-.0676	-.0676	-.0676

DIRECT QUATERNION SCALE ERRORS

	Second Order Runge-Kutta	Second Order State Transition	Fourth Order Runge-Kutta
16 Bits	-.0307	-.0415	-.0338
18 Bits	-.0307	-.0415	-.0338
20 Bits	-.0307	-.0415	-.0338
24 Bits	-.0307	-.0415	-.0338
28 Bits	-.0307	-.0415	-.0338

Table 36. Direction-Cosine Skew Errors for 100°/Sec Coning Motion

SKEW ERRORS (DEG/HR)

DIRECTION - COSINES

SECOND ORDER RUNGE-KUTTA

	X	Y	Z
16 Bits	.000048	-.00058	.00015
18 Bits	.000048	-.00038	-.00014
20 Bits	.000024	.00019	-.00003
24 Bits	.000072	-.00019	-.00009
28 Bits	.000048	-.00058	-.00069

SECOND ORDER STATE TRANSITION

	X	Y	Z
16 Bits	-.00060	-.0032	.00010
18 Bits	-.00067	-.0031	-.00022
20 Bits	-.00070	-.0023	-.00027
24 Bits	-.00068	-.0031	-.00016
28 Bits	-.00070	-.0032	-.00076

FOURTH ORDER RUNGE-KUTTA

	X	Y	Z
16 Bits	.1245	.036	.00124
18 Bits	.1245	.036	.00128
20 Bits	.1245	.036	.00081
24 Bits	.1245	.035	.00114
28 Bits	.1245	.036	.00112

Table 37. Quaternion Skew Errors for 100°/Sec Coning Motion

SKEW ERRORS (DEG/HR)

QUATERNIONS

SECOND ORDER RUNGE-KUTTA

	X	Y	Z
16 Bits			
18 Bits			
20 Bits	ALL ZERO		
24 Bits			
28 Bits			

SECOND ORDER STATE TRANSITION

	X	Y	Z
16 Bits			
18 Bits			
20 Bits	ALL ZERO		
24 Bits			
28 Bits			

FOURTH ORDER RUNGE-KUTTA

	X	Y	Z
16 Bits			
18 Bits			
20 Bits	ALL ZERO		
24 Bits			
28 Bits			

Table 38. Direction-Cosine Skew Errors for 10^{o}/Sec Coning Motion

SKEW ERRORS (DEG/HR)

DIRECTION - COSINES

SECOND ORDER RUNGE-KUTTA

	X	Y	Z
16 Bits			
18 Bits			
20 Bits	ALL ZERO		
24 Bits			
28 Bits			

SECOND ORDER STATE TRANSITION

	X	Y	Z
16 Bits			
18 Bits			
20 Bits	ALL ZERO		
24 Bits			
28 Bits			

FOURTH ORDER RUNGE-KUTTA

	X	Y	Z
16 Bits			
18 Bits			
20 Bits	ALL ZERO		
24 Bits			
28 Bits			

Table 39. Quaternion Skew Errors for 10^{o}/Sec Coning Motion

SKEW ERRORS (DEG/HR)

QUATERNIONS

SECOND ORDER RUNGE-KUTTA

	X	Y	Z
16 Bits			
18 Bits			
20 Bits	ALL ZERO		
24 Bits			
28 Bits			

SECOND ORDER STATE TRANSITION

	X	Y	Z
16 Bits			
18 Bits			
20 Bits	ALL ZERO		
24 Bits			
28 Bits			

FOURTH ORDER RUNGE-KUTTA

	X	Y	Z
16 Bits			
18 Bits			
20 Bits	ALL ZERO		
24 Bits			
28 Bits			

Table 40. Direction-Cosine Skew Errors for 10°/Sec Linear Motion

SKEW ERRORS (DEG/HR)

DIRECTION - COSINES

SECOND ORDER RUNGE-KUTTA

	X	Y	Z
16 Bits			
18 Bits			
20 Bits	ALL ZERO		
24 Bits			
28 Bits			

SECOND ORDER STATE TRANSITION

	X	Y	Z
16 Bits			
18 Bits			
20 Bits	ALL ZERO		
24 Bits			
28 Bits			

FOURTH ORDER RUNGE-KUTTA

	X	Y	Z
16 Bits			
18 Bits			
20 Bits	ALL ZERO		
24 Bits			
28 Bits			

Table 41. Quaternion Skew Errors for 10^{o}/Sec Linear Motion

SKEW ERRORS (DEG/HR)

QUATERNIONS

SECOND ORDER RUNGE-KUTTA

	X	Y	Z
16 Bits			
18 Bits			
20 Bits	ALL ZERO		
24 Bits			
28 Bits			

SECOND ORDER STATE TRANSITION

	X	Y	Z
16 Bits			
18 Bits			
20 Bits	ALL ZERO		
24 Bits			
28 Bits			

FOURTH ORDER RUNGE-KUTTA

	X	Y	Z
16 Bits			
18 Bits			
20 Bits	ALL ZERO		
24 Bits			
28 Bits			

Table 42. Direction-Cosine Skew Errors for 1°/Sec Linear Motion

SKEW ERRORS (DEG/HR)

DIRECTION - COSINES

SECOND ORDER RUNGE-KUTTA

	X	Y	Z
16 Bits			
18 Bits			
20 Bits	ALL ZERO		
24 Bits			
28 Bits			

SECOND ORDER STATE TRANSITION

	X	Y	Z
16 Bits			
18 Bits			
20 Bits	ALL ZERO		
24 Bits			
28 Bits			

FOURTH ORDER RUNGE-KUTTA

	X	Y	Z
16 Bits			
18 Bits			
20 Bits	ALL ZERO		
24 Bits			
28 Bits			

Table 43. Quaternion Skew Errors for 1^{o}/Sec Linear Motion

SKEW ERRORS (DEG/HR)

QUATERNIONS

SECOND ORDER RUNGE-KUTTA

	X	Y	Z
16 Bits			
18 Bits			
20 Bits	ALL ZERO		
24 Bits			
28 Bits			

SECOND ORDER STATE TRANSITION

	X	Y	Z
16 Bits			
18 Bits			
20 Bits	ALL ZERO		
24 Bits			
28 Bits			

FOURTH ORDER RUNGE-KUTTA

	X	Y	Z
16 Bits			
18 Bits			
20 Bits	ALL ZERO		
24 Bits			
28 Bits			

Table 44. Direction-Cosine Drift Errors for 100°/Sec Coning Motion

DRIFT ERRORS (DEG/HR)

DIRECTION - COSINES

SECOND ORDER RUNGE-KUTTA

	X	Y	Z
16 Bits	-.0276	.8088	.8802
18 Bits	-.0063	.2063	.2338
20 Bits	-.0033	.0425	.0600
24 Bits	-.0001	.0017	.0021
28 Bits	0.	0.	0.

SECOND ORDER STATE TRANSITION

	X	Y	Z
16 Bits	-.0327	.8471	.9130
18 Bits	-.0080	.2165	.2453
20 Bits	-.0037	.0438	.0622
24 Bits	-.0002	.0019	.0024
28 Bits	0.	0.	0.

FOURTH ORDER RUNGE-KUTTA

	X	Y	Z
16 Bits	-.0326	.8464	.9131
18 Bits	-.0079	.2164	.2453
20 Bits	-.0037	.0439	.0618
24 Bits	-.0002	.0017	.0024
28 Bits	0.	0.	

Table 45. Quaternion Drift Errors for 100°/Sec Coning Motion

DRIFT ERRORS (DEG/HR)

QUATERNIONS

SECOND ORDER RUNGE-KUTTA

	X	Y	Z
16 Bits	-.0271	.8091	.8800
18 Bits	-.0063	.2065	.2337
20 Bits	-.0033	.0423	.0599
24 Bits	-.0001	.0022	.0027
28 Bits	0.	0.	0.

SECOND ORDER STATE TRANSITION

	X	Y	Z
16 Bits	-.0327	.8464	.9128
18 Bits	-.0080	.2170	.2457
20 Bits	-.0036	.0439	.0619
24 Bits	-.0001	.0023	.0018
28 Bits	0.	0.	0.

FOURTH ORDER RUNGE-KUTTA

	X	Y	Z
16 Bits	-.0326	.8469	.9133
18 Bits	-.0079	.2166	.2455
20 Bits	-.0037	.0439	.0615
24 Bits	-.0001	.0017	.0017
28 Bits	0.	0.	0.

Table 46. Direction-Cosine Drift Errors for 10°/Sec Coning Motion

DRIFT ERRORS (DEG/HR)

DIRECTION - COSINES

SECOND ORDER RUNGE-KUTTA

	X	Y	Z
16 Bits	.0018	.0971	.0113
18 Bits	.0003	.0252	.0028
20 Bits	0.	.0052	.0007
24 Bits	0.	.0002	0.
28 Bits	0.	0.	0.

SECOND ORDER STATE TRANSITION

	X	Y	Z
16 Bits	.0018	.1019	.0117
18 Bits	.0004	.0268	.0029
20 Bits	0.	.0056	.0007
24 Bits	0.	.0002	0.
28 Bits	0.	0.	0.

FOURTH ORDER RUNGE-KUTTA

	X	Y	Z
16 Bits	.0018	.1018	.0117
18 Bits	.0004	.0280	.0029
20 Bits	.0	.0056	.0007
24 Bits	0.	.0002	0.
28 Bits	0.	0.	0.

Table 47. Quaternion Drift Error for 10^{o}/Sec Coning Motion

DRIFT ERRORS (DEG/HR)

QUATERNIONS

SECOND ORDER RUNGE-KUTTA

	X	Y	Z
16 Bits	.0018	.0971	.0113
18 Bits	.0003	.0252	.0028
20 Bits	0.	.0053	.0007
24 Bits	0.	.0001	0.
28 Bits	0.	0.	0.

SECOND ORDER STATE TRANSITION

	X	Y	Z
16 Bits	.0018	.1018	.0017
18 Bits	.0004	.0268	.0029
20 Bits	0.	.0056	.0007
24 Bits	0.	.0002	0.
28 Bits	0.	0.	0.

FOURTH ORDER RUNGE-KUTTA

	X	Y	Z
16 Bits	.0018	.1017	.0117
18 Bits	.0004	.0267	.0029
20 Bits	0.	.0056	.0007
24 Bits	0.	.0001	0.
28 Bits	0.		0.

Table 48. Direction-Cosine Drift Error for 10°/Sec Linear Motion

DRIFT ERRORS (DEG/HR)

DIRECTION - COSINES

SECOND ORDER RUNGE-KUTTA

	X	Y	Z
16 Bits	-.3523	0. 0.	0. 0.
18 Bits	-.3523	0. 0.	0. 0.
20 Bits	-.0715	0.	0.
24 Bits	-.0023	0.	0.
28 Bits	0.	0.	0.

SECOND ORDER STATE TRANSITION

	X	Y	Z
16 Bits	-.3707	0.	0.
18 Bits	-.3707	0.	0.
20 Bits	-.0765	0.	0.
24 Bits	-.0023	0.	0.
28 Bits	0.	0.	0.

FOURTH ORDER RUNGE-KUTTA

	X	Y	Z
16 Bits	-.3713	0.	0.
18 Bits	-.3713	0.	0.
20 Bits	-.0768	0.	0.
24 Bits	-.0023	0.	0.
28 Bits	0.	0.	0.

Table 49. Quaternion Drift Error for 10°/Sec Linear Motion

DRIFT ERRORS (DEG/HR)

QUATERNIONS

SECOND ORDER RUNGE-KUTTA

	X	Y	Z
16 Bits	-.3531	0.	0.
18 Bits	-.3531	0.	0.
20 Bits	-.0726	0.	0.
24 Bits	-.0027	0.	0.
28 Bits	0.	0.	0.

SECOND ORDER STATE TRANSITION

	X	Y	Z
16 Bits	-.3715	0.	0.
18 Bits	-.3715	0.	0.
20 Bits	-.0772	0.	0.
24 Bits	-.0027	0.	0.
28 Bits	0.	0.	0.

FOURTH ORDER RUNGE-KUTTA

	X	Y	Z
16 Bits	-.3708	0.	0.
18 Bits	-.3708	0.	0.
20 Bits	-.0757	0.	0.
24 Bits	-.0015	0.	0.
28 Bits		0.	0.

Table 50. Direction-Cosine Drift Error for 1°/Sec Linear Motion

DRIFT ERRORS (DEG/HR)

DIRECTION - COSINES

SECOND ORDER RUNGE-KUTTA

	X	Y	Z
16 Bits	-.1475	0.	0.
18 Bits	-.0074	0.	0.
20 Bits	-.0074	0.	0.
24 Bits	-.0001	0.	0.
28 Bits	0.	0.	0.

SECOND ORDER STATE TRANSITION

	X	Y	Z
16 Bits	-.1554	0.	0.
18 Bits	-.0078	0.	0.
20 Bits	-.0078	0.	0.
24 Bits	-.0001	0.	0.
28 Bits	0.	0.	0.

FOURTH ORDER RUNGE-KUTTA

	X	Y	Z
16 Bits	-.1552	0.	0.
18 Bits	-.0077	0.	0.
20 Bits	-.0077	0.	0.
24 Bits	-.0001	0.	0.
28 Bits	0.	0.	0.

Table 51. Quaternion Drift Error for 1°/Sec Linear Motion

DRIFT ERRORS (DEG/HR)

QUATERNIONS

SECOND ORDER RUNGE-KUTTA

	X	Y	Z
16 Bits	-.1475	0.	0.
18 Bits	-.0073	0.	0.
20 Bits	-.0073	0.	0.
24 Bits	0.	0.	0.
28 Bits	0.	0.	0.

SECOND ORDER STATE TRANSITION

	X	Y	Z
16 Bits	-.1553	0.	0.
18 Bits	-.0078	0.	0.
20 Bits	-.0078	0.	0.
24 Bits	-.0001	0.	0.
28 Bits	0.	0.	0.

FOURTH ORDER RUNGE-KUTTA

	X	Y	Z
16 Bits	-.1552	0.	0.
18 Bits	-.0077	0.	0.
20 Bits	-.0077	0.	0.
24 Bits	0.	0.	0.
28 Bits	0.	0.	0.

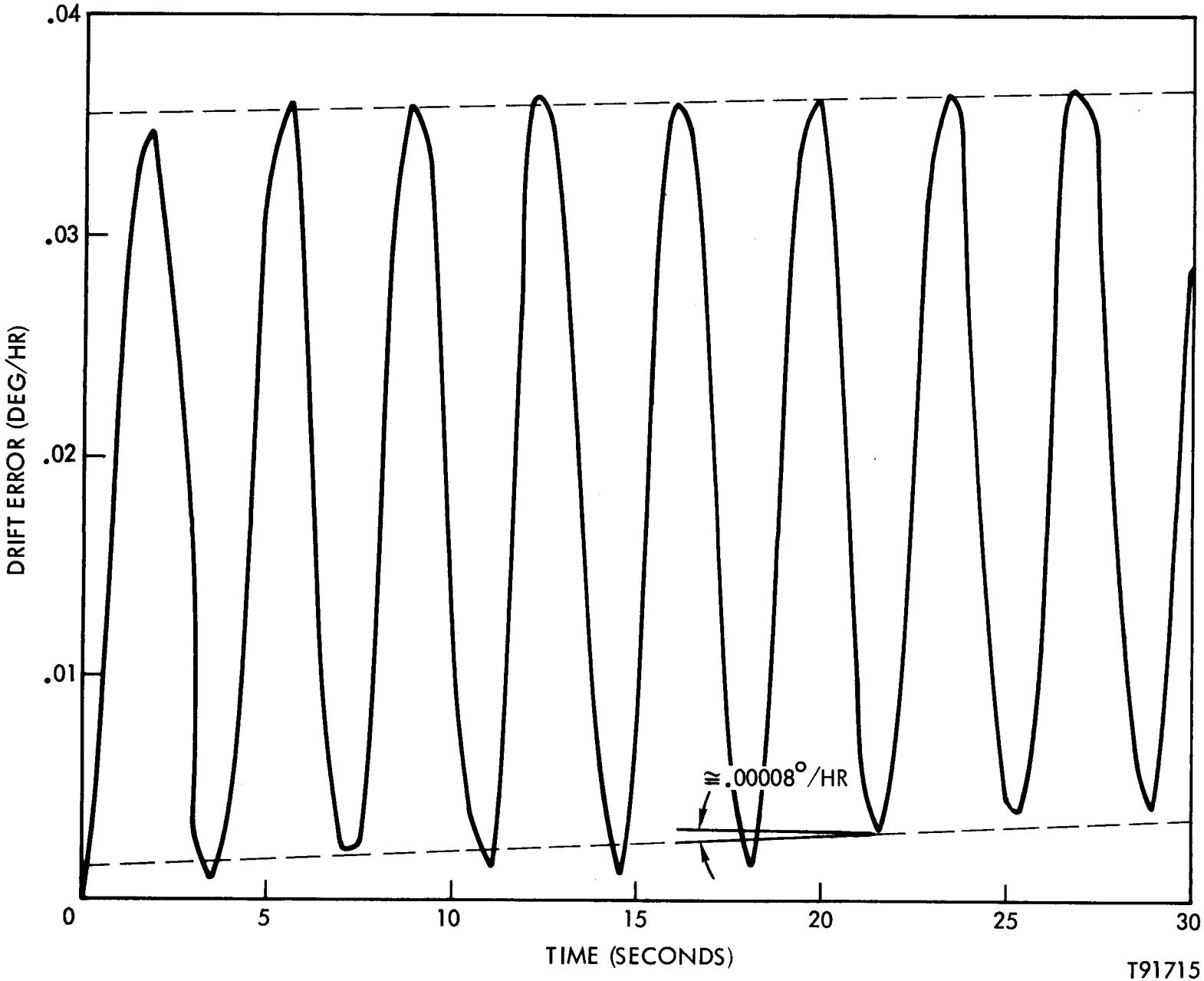

Figure 53. Long Term Attitude Computation Drift Error

Navigation. - The attitude computations are the most sensitive element of the overall strapdown Inertial navigation process. The attitude computations serve as a replacement for the gimbal that are present in non-strapdown systems.

A strapdown inertial simulation program has been designed which combines the attitude computations with the overall navigation process. The simulation program serves as both an evaluation and design tool. Figure 54 illustrates the processing flow of the simulation program. The major features of the program design are

Vehicle trajectory generation

Vehicle dynamic disturbances

Component error modeling

Statistical error analysis

The whole trajectory generation design will allow the evaluation of strapdown navigation systems on a global basis. The feature will allow the evaluation of navigation performance for predetermined scenarios where geographic points of destination are important.

The incorporation of vehicle dynamic disturbances will allow for a realistic assessment of these effects upon overall navigation accuracy. The design incorporates coning motions and pitch and roll variations.

The component error modeling will allow the evaluation of specified strapdown hardware configurations. The parameters associated with the component errors can be modified so that a specific design can be configured to optimally operate in a given environment. The component errors that are modeled are

Gyro errors

Analog to Digital errors

Rate extraction

Computation word length

Integration errors

Truncation errors.

The statistical error analysis entails the computation of the difference between computed navigation outputs and the true navigation positions. The true navigation position is derived directly from the trajectory computations. The computed navigation outputs are desired from the error corrupted system outputs. Thus a direct measurement of performance can be obtained.

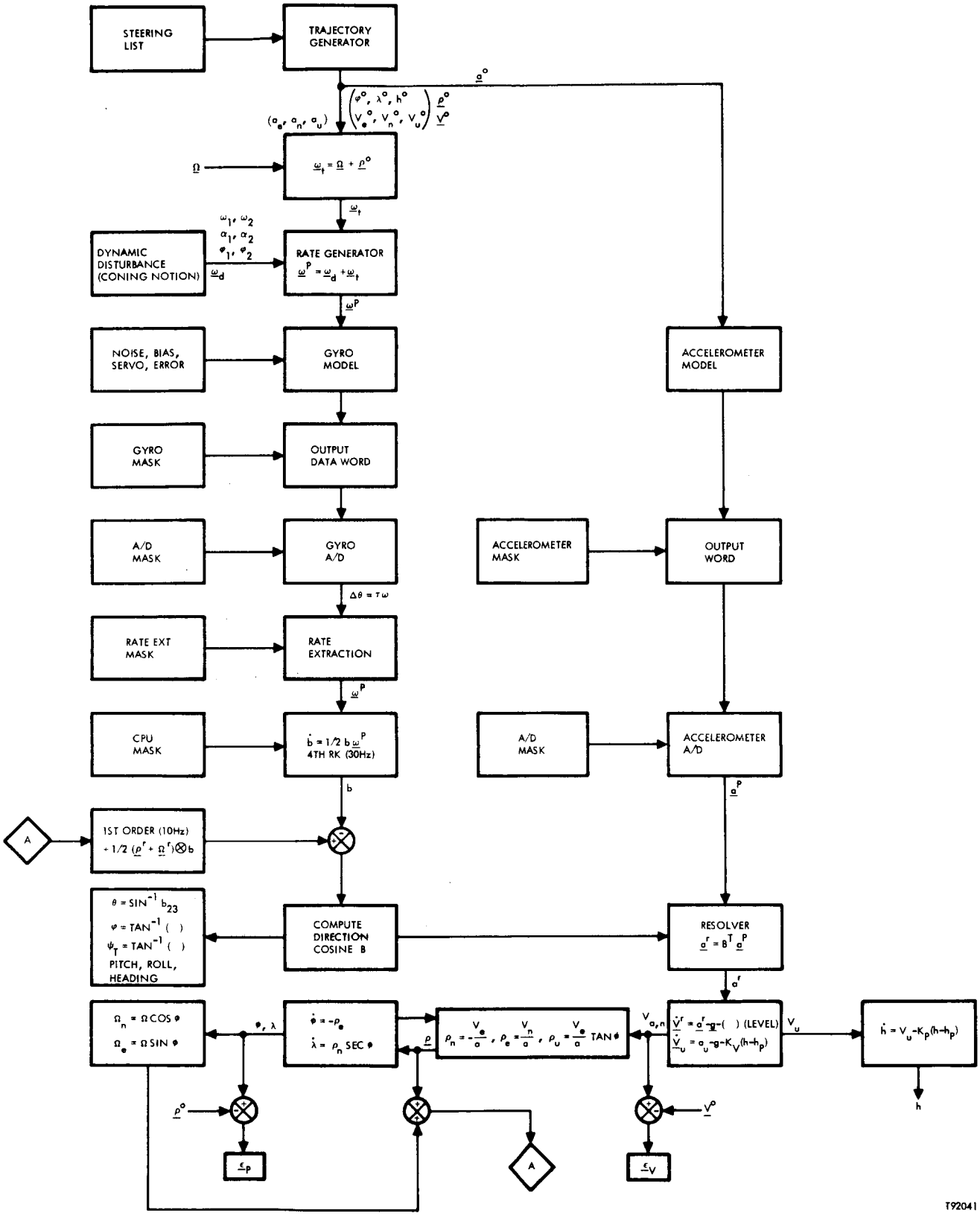

Figure 54. Processing Flow of the Simulation Program

Alignment

A generalized covariance analysis simulation computer program has been developed to evaluate both Kalman derived and predetermined fixed gains for leveling and gyrocompassing modes of operation. A system covariance matrix representing 18 error sources is propagated and filtered so that the overall system performance can be determined.

A set of 12 test cases were executed which provide a parametric prolife of system operation. Various disturbance amplitudes, frequencies, and time constants were evaluated with respect to a nominal system and environmental configuration.

An illustration of the alignment simulation processing is presented in Figure 55. The program operates by card input data that describes the environment and the mode of operation. Intermediate results are printed at selected time intervals and summary plots for attitude and azimuth errors are computed at the end of each simulation run.

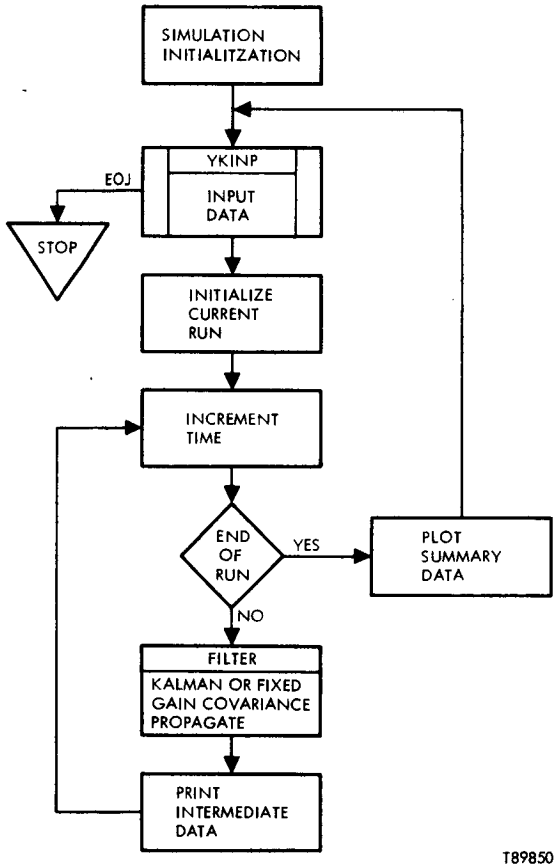

Figure 55. Alignment Simulation Flow

The system parameters were previously defined in Section V. The initial conditions for the system parameters for the nominal system and environmental configuration are:

Ω = earth rate (deg/hr)
= 15.07

g = gravitational acceleration (ft/sec^2)
= 32.

ψ = true north heading angle (deg)
= 0^o

Initial System Errors

φ_e = .001 (rad)

φ_n = .001 (rad)

φ_u = .01 (rad)

$\delta\omega_x$ = 5×10^{-8} (rad/sec)

$\delta\omega_y$ = 5×10^{-8} (rad/sec)

$\delta\omega_z$ = 5×10^{-8} (rad/sec)

δa_x = .0032 (ft/sec^2) ($\approx 10^{-4}$ g)

δa_y = .0032 (ft/sec^2) ($\approx 10^{-4}$ g)

δa_z = .0032 (ft/sec^2) ($\approx 10^{-4}$ g)

f_e = .0032 (ft/sec^2) ($\approx 10^{-4}$ g)

f_n = .0032 (ft/sec^2) ($\approx 10^{-4}$ g)

f_u = .0032 (ft/sec^2) ($\approx 10^{-4}$ g)

n_1 = .0032 (ft/sec^2) ($\approx 10^{-4}$ g)

n_2 = .0032 (ft/sec^2) ($\approx 10^{-4}$ g)

n_3 = .0032 (ft/sec^2) ($\approx 10^{-4}$ g)

n_4 = .0032 (ft/sec^2) ($\approx 10^{-4}$ g)

n_5 = 5×10^{-5} (rad/sec)

n_6 = 5×10^{-5} (rad/sec)

State Distrubances

$W_{\omega x}$	=	5×10^{-8}	(rad/sec)	
$W_{\omega y}$	=	5×10^{-8}	(rad/sec)	
$W_{\omega z}$	=	5×10^{-8}	(ft/sec^2)	
W_{ax}	=	.0032	(ft/sec^2)	
W_{ay}	=	.0032	(ft/sec^2)	
W_{az}	=	.0032	(ft/sec^2)	(Scaled down by the
W_{n1}	=	.0032	(ft/sec^2)	Correlation Time)
W_{n2}	=	.0032	(ft/sec^2)	
W_{n3}	=	.0032	(ft/sec^2)	
W_{n4}	=	.0032	(ft/sec^2)	
W_{n5}	=	5×10^{-5}	(rad/sec)	
W_{n6}	=	5×10^{-5}	(rad/sec)	

State Error Inverse Correlation Time

$\alpha_{\omega x}$	=	$.1\ (sec)^{-1}$
$\alpha_{\omega y}$	=	$.1\ (sec)^{-1}$
$\alpha_{\omega z}$	=	$.1\ (sec)^{-1}$
α_{ax}	=	$.1\ (sec)^{-1}$
α_{ay}	=	$.1\ (sec)^{-1}$
α_{az}	=	$.1\ (sec)^{-1}$
α_{n1}	=	$.1\ (sec)^{-1}$
α_{n2}	=	$.1\ (sec)^{-1}$
α_{n3}	=	$.1\ (sec)^{-1}$
α_{n4}	=	$.1\ (sec)^{-1}$
α_{n5}	=	$.1\ (sec)^{-1}$
α_{n6}	=	$.1\ (sec)^{-1}$

Time Parameters

τ	=	1 (sec)
TSTOP	=	Total Simulation Time (15 min)
t	=	present time (TF) minus initial time (T0)

Observation Errors

$V_{ae} = .0032 \quad (ft/sec^2) \quad (\approx 10^{-4} g)$

$V_{an} = .0032 \quad (ft/sec^2) \quad (\approx 10^{-4} g)$

$V_{\omega e} = 4.85 \times 10^{-8} \quad (rad/sec) \quad (\approx .01^{o}/hr)$

$V_{fe} = .00032 \quad (ft/sec^2) \quad (\approx 10^{-5} g)$

$V_{fn} = .00032 \quad (ft/sec^2) \quad (\approx 10^{-5} g)$

$V_{fu} = .00032 \quad (ft/sec^2) \quad (\approx 10^{-5} g)$

Fixed Gains

$K_x = 1 / (\tau_L g)$

$K_y = -1 / (\tau_L g)$

$K_z = 0$

$K_{fn} =$ } Variable

$K_{fe} =$ } Variable

$K_{fu} =$ } Variable

State Disturbance Period

$\omega_{dax} = 60. \quad (sec)$

$\omega_{day} = 60. \quad (sec)$

$\omega_{d\omega x} = 60. \quad (sec)$

Several variations of the nominal system and environmental configuration were run. A total of 12 cases were evaluated.

CASE 1 - Nominal System and Environmental Model

CASE 2 - 10^{-3}g disturbance amplitudes test

CASE 3 - 10^{-2}g disturbance amplitude test

CASE 4 - 10^{-3}g disturbance amplitude
5×10^{-3} rate amplitude
0.1 rad/sec disturbance frequency
1 min disturbance time constant

CASE 5 - 10^{-3}g disturbance amplitude
5×10^{-4} rate amplitude
0.1 rad/sec disturbance frequency
1 min disturbance time constant

CASE 6 - 10^{-3}g disturbance amplitude
5×10^{-3} rate amplitude
1.0 rad/sec disturbance frequency
1 min disturbance time constant

CASE 7 - 10^{-3}g disturbance amplitude
5×10^{-3} rate amplitude
.01 rad/sec disturbance frequency
1 min disturbance time constant

CASE 8 - 10^{-3}g disturbance amplitude
5×10^{-3} rate amplitude
.1 rad/sec disturbance frequency
10 min disturbance time constant

CASE 9 - 10^{-3}g disturbance amplitude
5×10^{-3} rate amplitude
.1 rad/sec disturbance frequency
.1 min disturbance time constant

CASE 10 - 10^{-2}g disturbance amplitude
5×10^{-3} rate amplitude
.1 rad/sec disturbance frequency
1 min disturbance time constant

CASE 11 - Same as CASE 4 except
.25g disturbance amplitude
17.5 Hertz disturbance frequency

CASE 12 - Fixed gain processing of CASE 13

A parametric analysis can be performed by comparing various cases which have been run. Cases 1, 2, and 3 may be used to examine the effects of disturbance acceleration amplitudes. Variations in east, north, and azimuth alignment for these cases are shown in Figures 56A, 56B, and 56C, respectively Figures 57A, 57B, and 57C similarly show the effects of disturbance frequency on alignment, as derived from cases 4, 6, and 7. The effects of varying the disturbance noise time constant are derived from cases 4, 8, and 9 and shown in Figures 58A, 58B, and 58C. All of the curves of Figures 56, 57, and 58 are for Kalman filtered alignment. Finally, Figures 60A, 60B, and 60C show the insensitivity fo alignment to variation in rate disturbance amplitudes, The Kalman filter essentially ignores the rate information which is available ($\hat{\varphi}_u$ in Section V) and uses only acceleration - derived data.

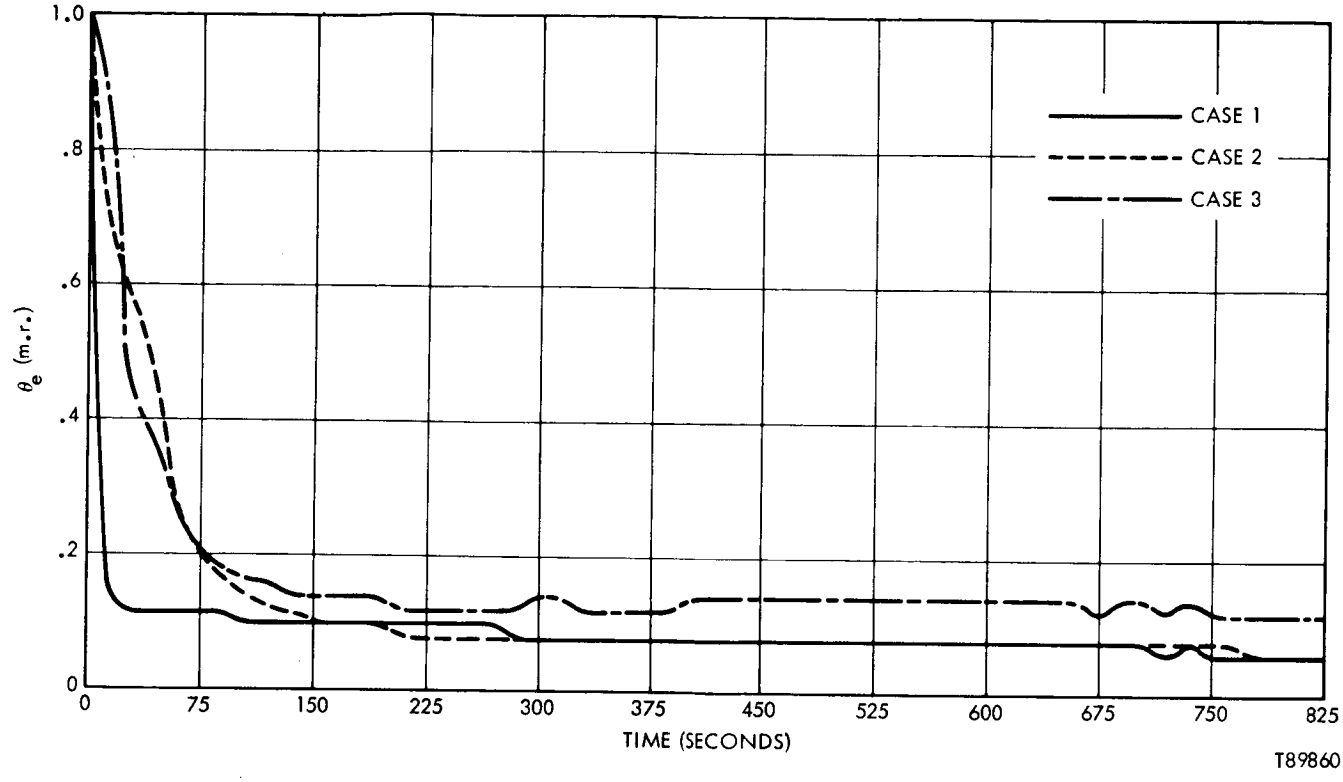

Figure 56A. East Axis Alignment for Varying Disturbance Accelerations

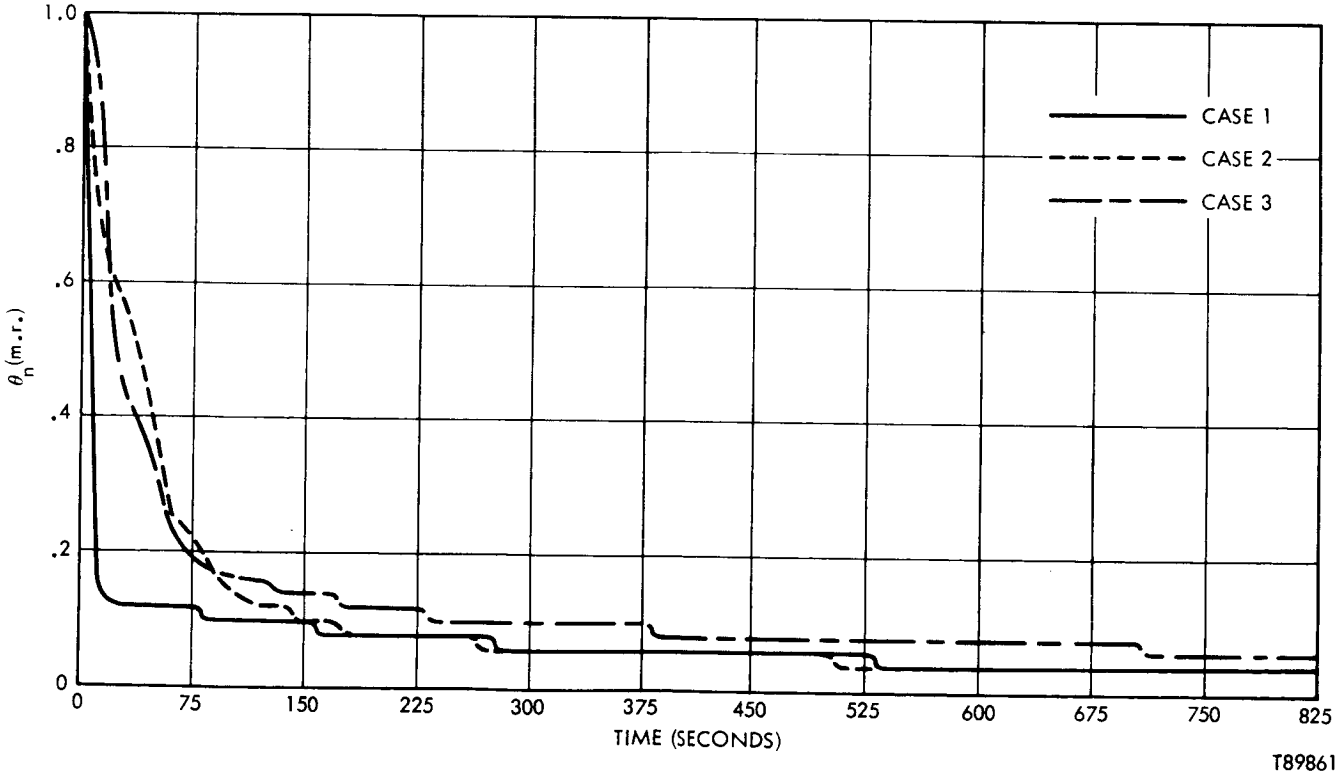

Figure 56B. North Axis Alignment for Varying Disturbance Accelerations

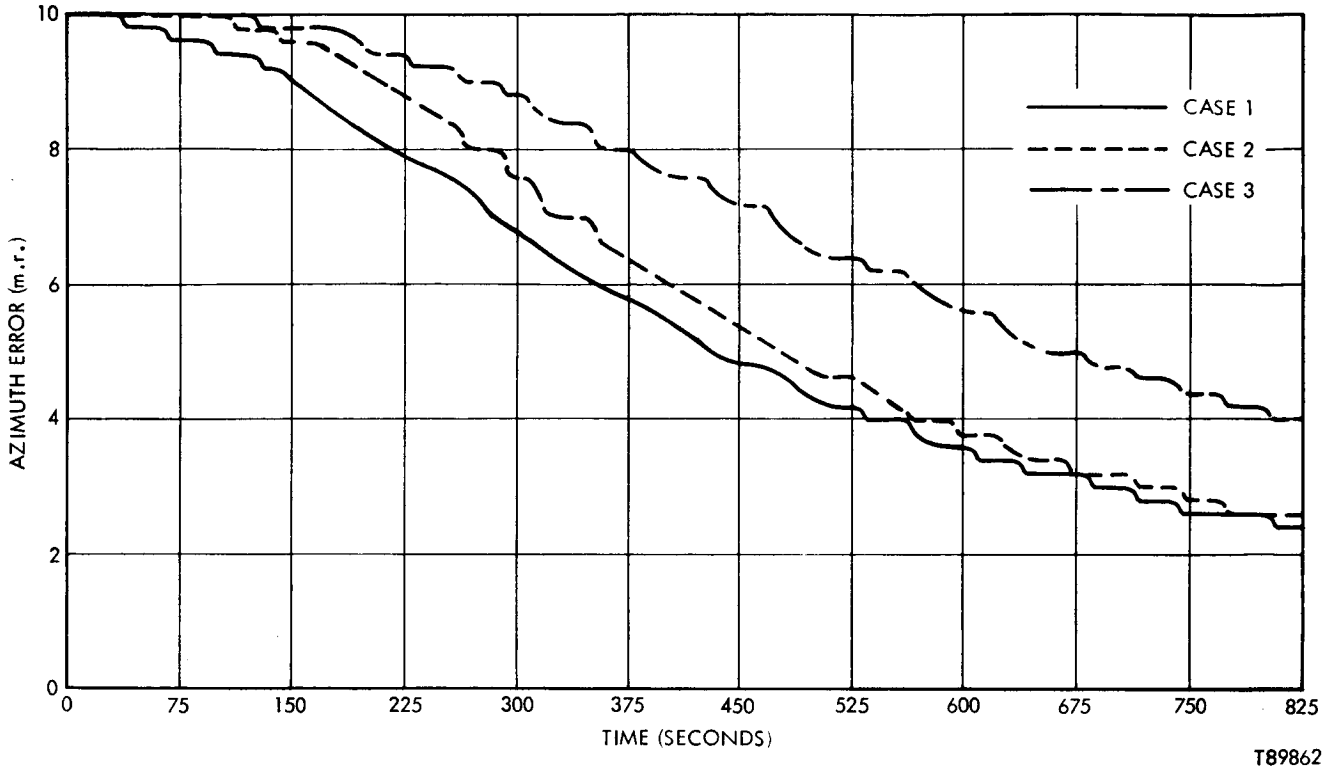

Figure 56C. Azimuth Alignment for Varying Disturbance Accelerations

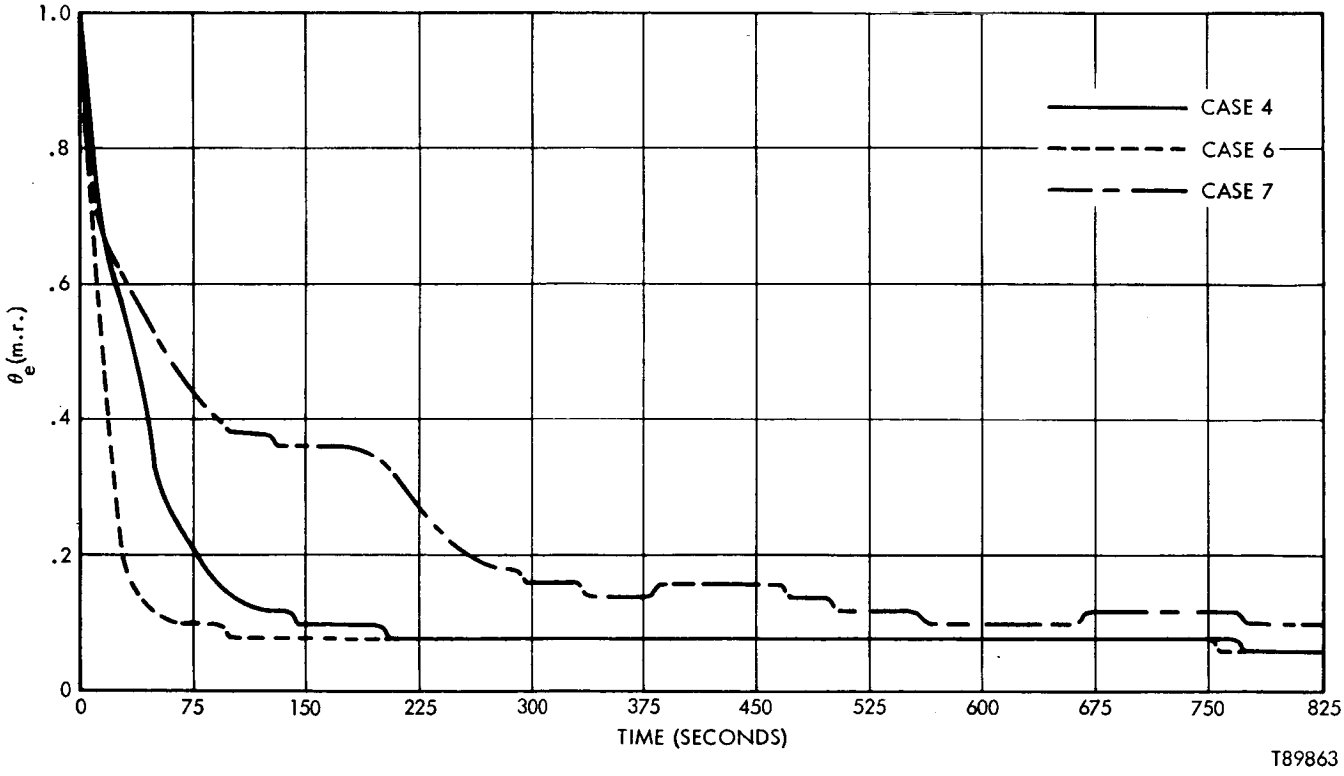

Figure 57A. East Axis Alignment for Varying Disturbance Frequency

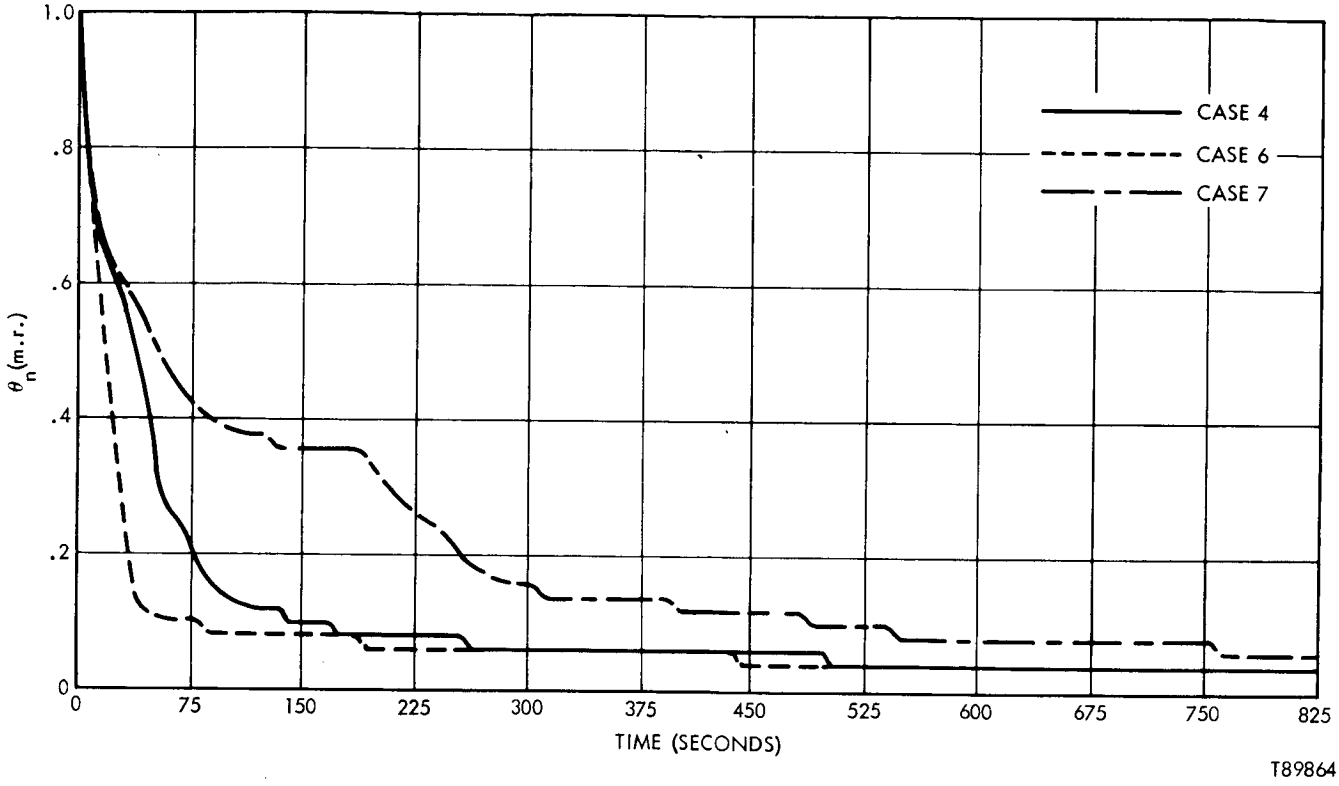

Figure 57B. North Axis Alignment for Varying Disturbance Frequency

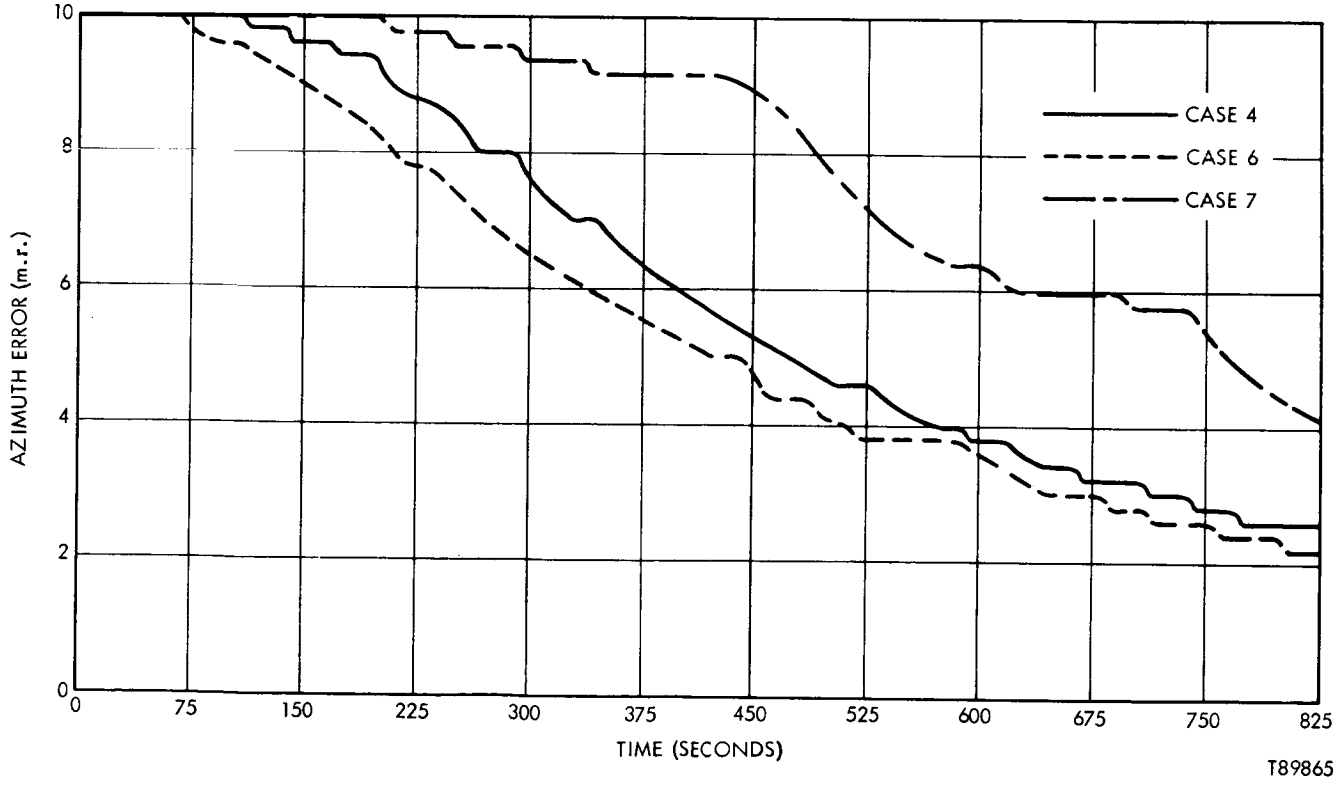

Figure 57C. Azimuth Axis Alignment for Varying Disturbance Frequency

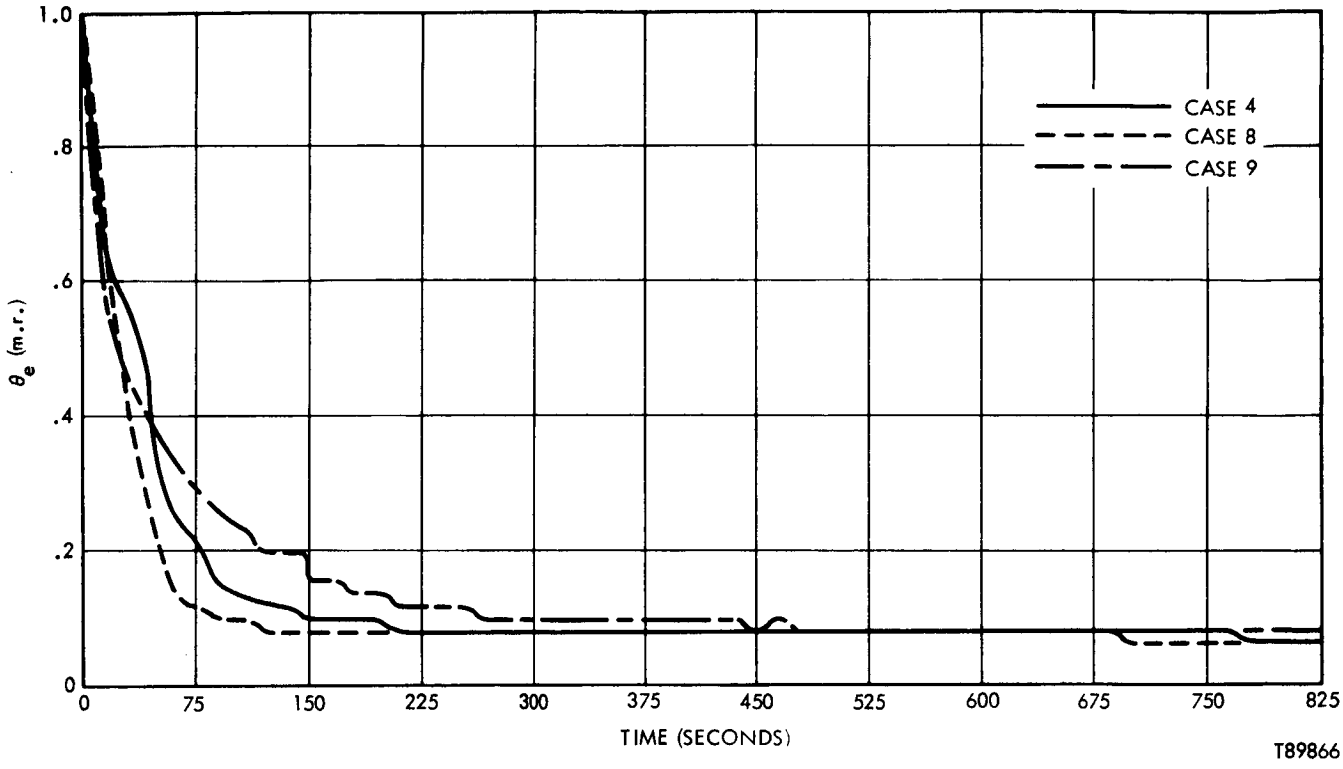

Figure 58A. East Axis Alignment for Varying Disturbance Time Constants

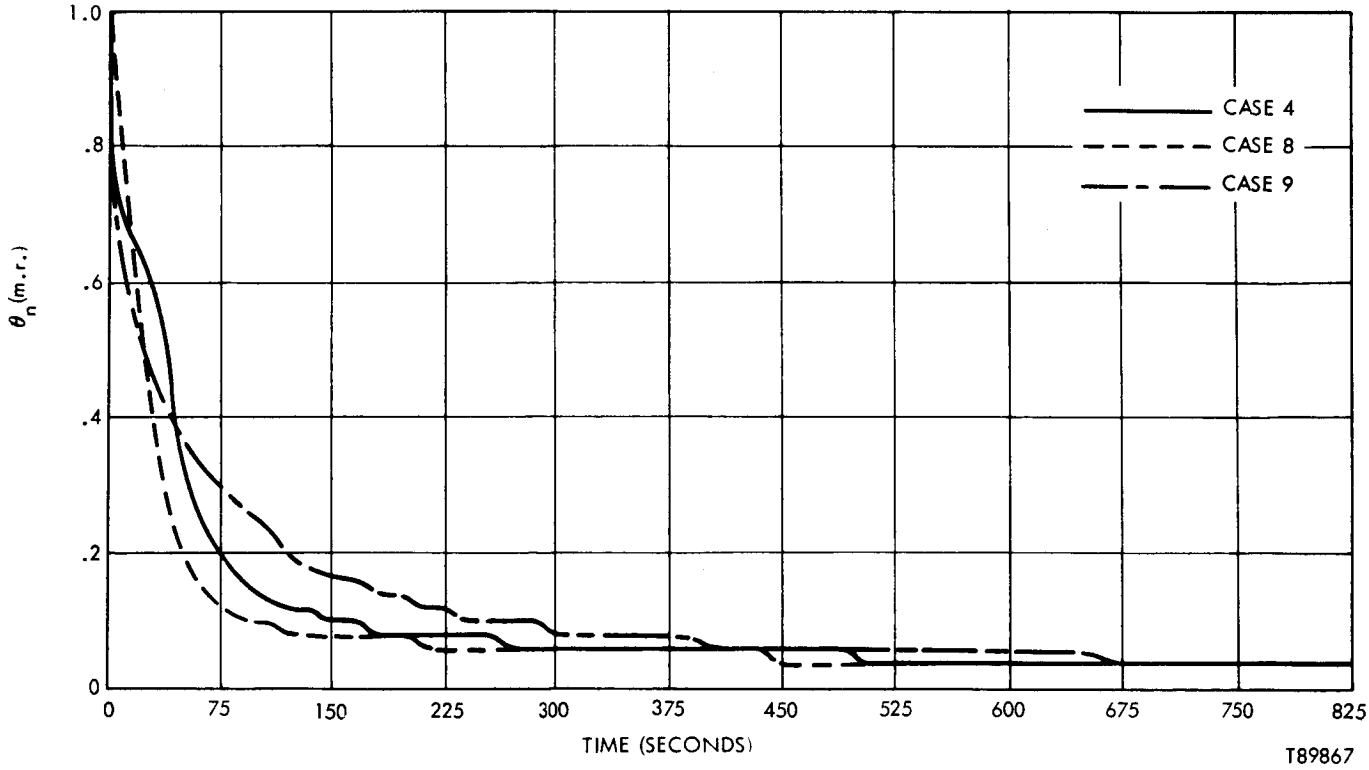

Figure 58B. North Axis Alignment for Varying Disturbance Time Constants

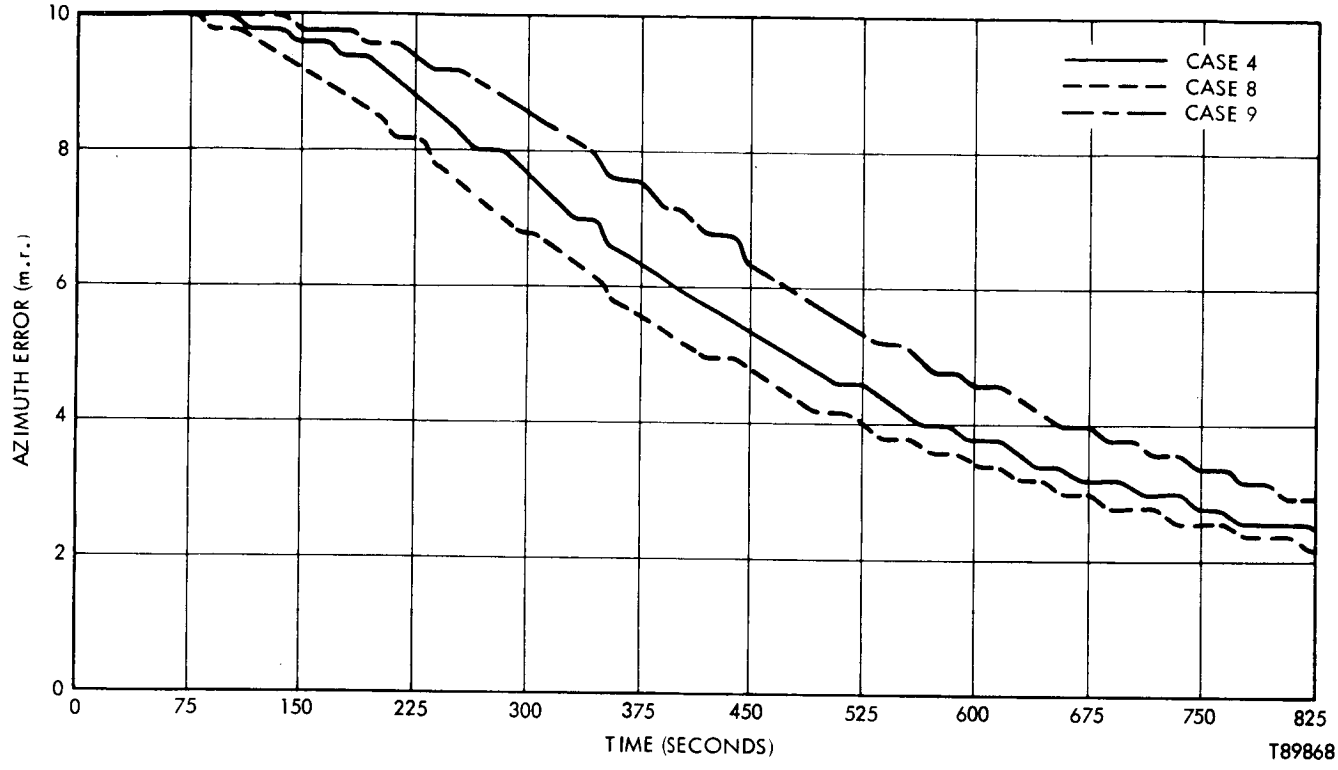

Figure 58C. Azimuth Alignment for Varying Disturbance Time Constants

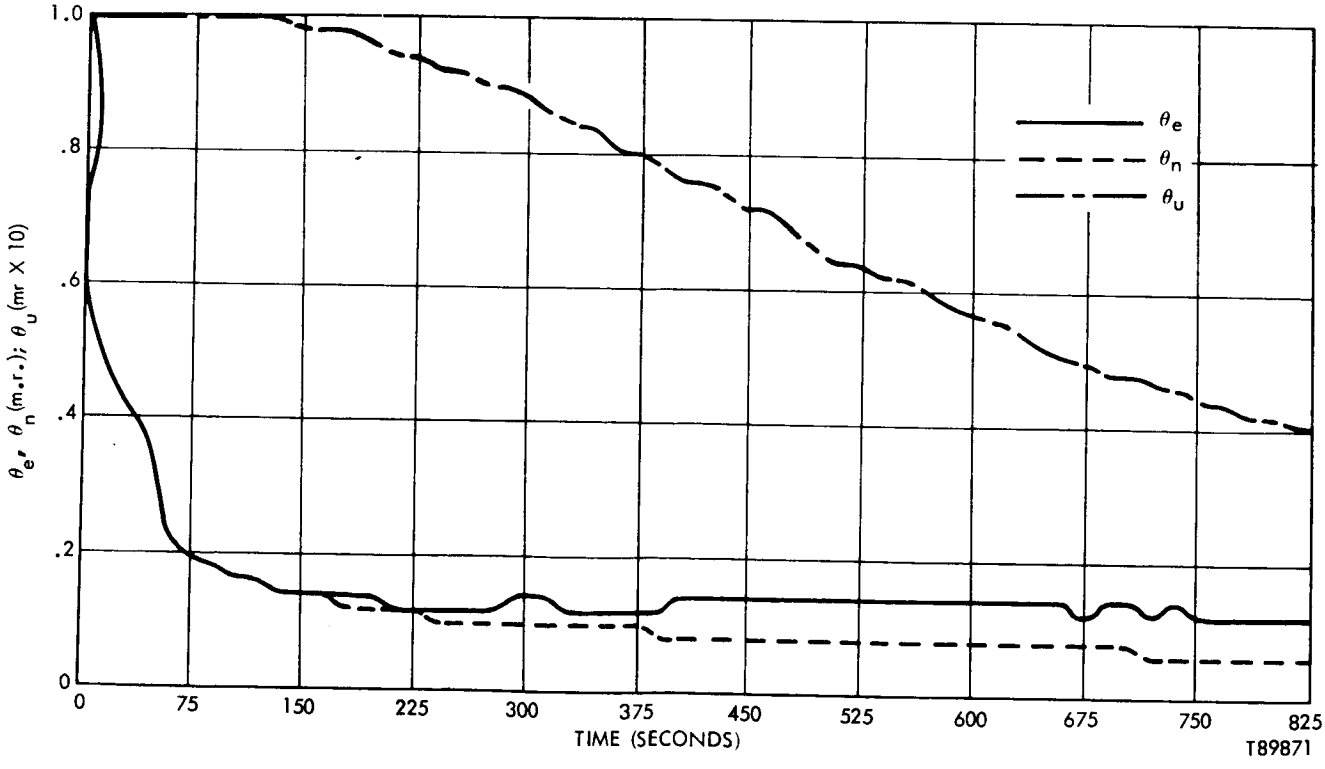

Figure 59. Alignment for High Disturbance Levels (Case 10)

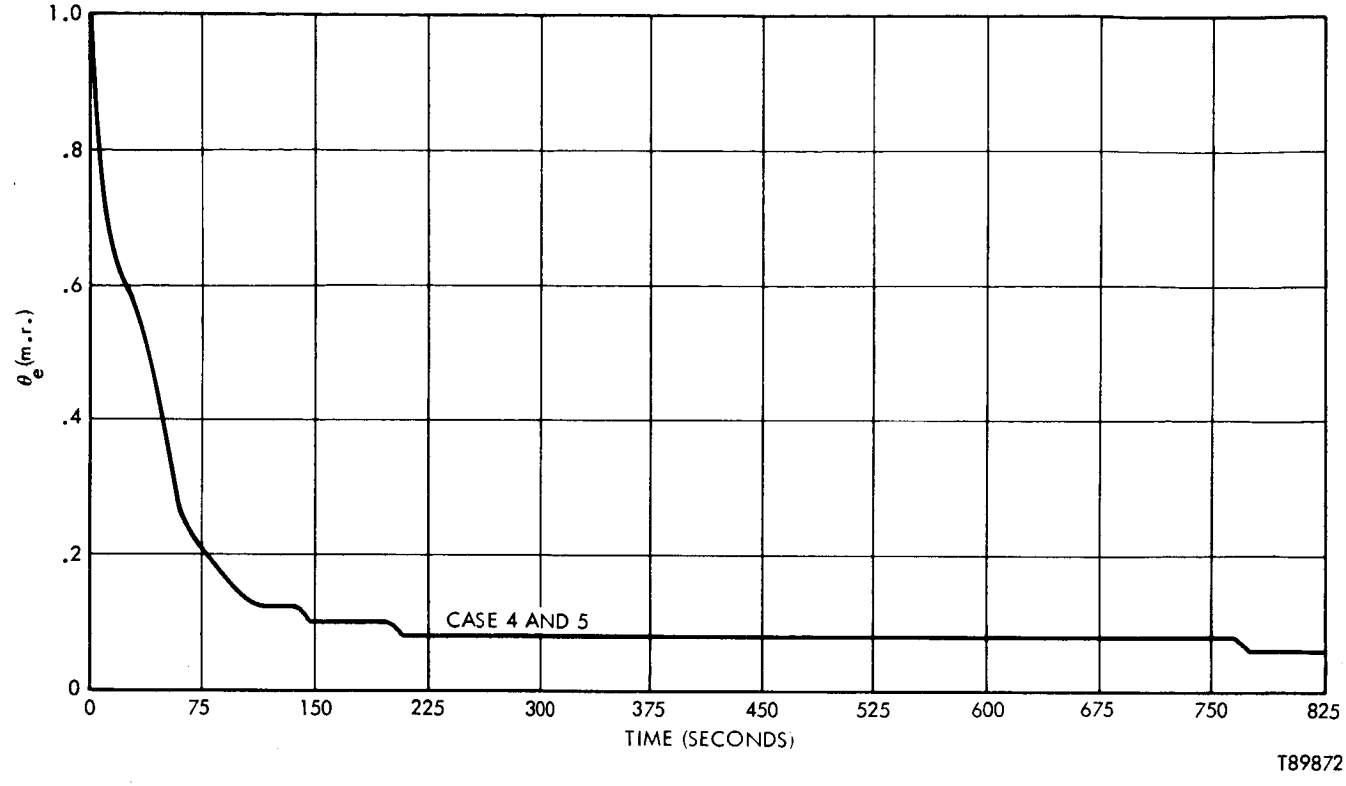

Figure 60A. East Axis Alignment for Varying Disturbance Frequencies

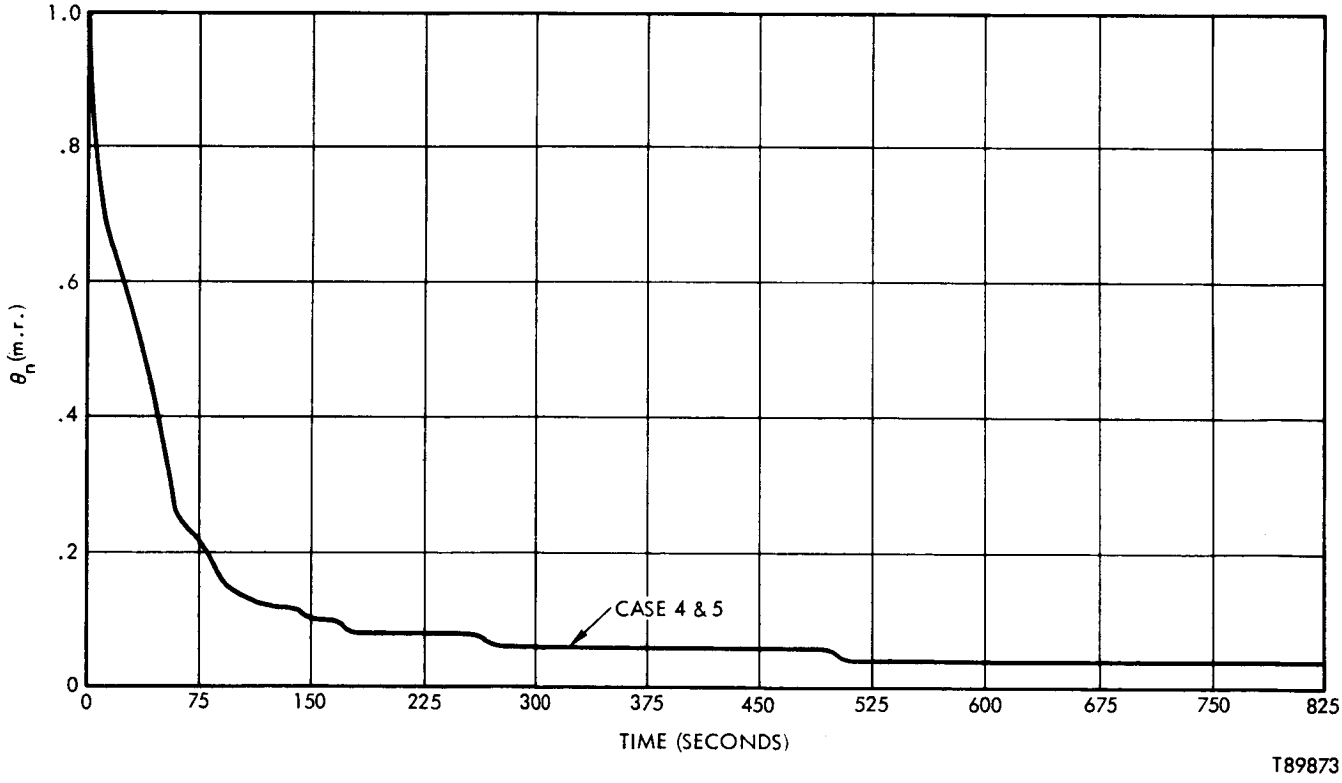

Figure 60B. North Axis Alignment for Varying Disturbance Frequencies

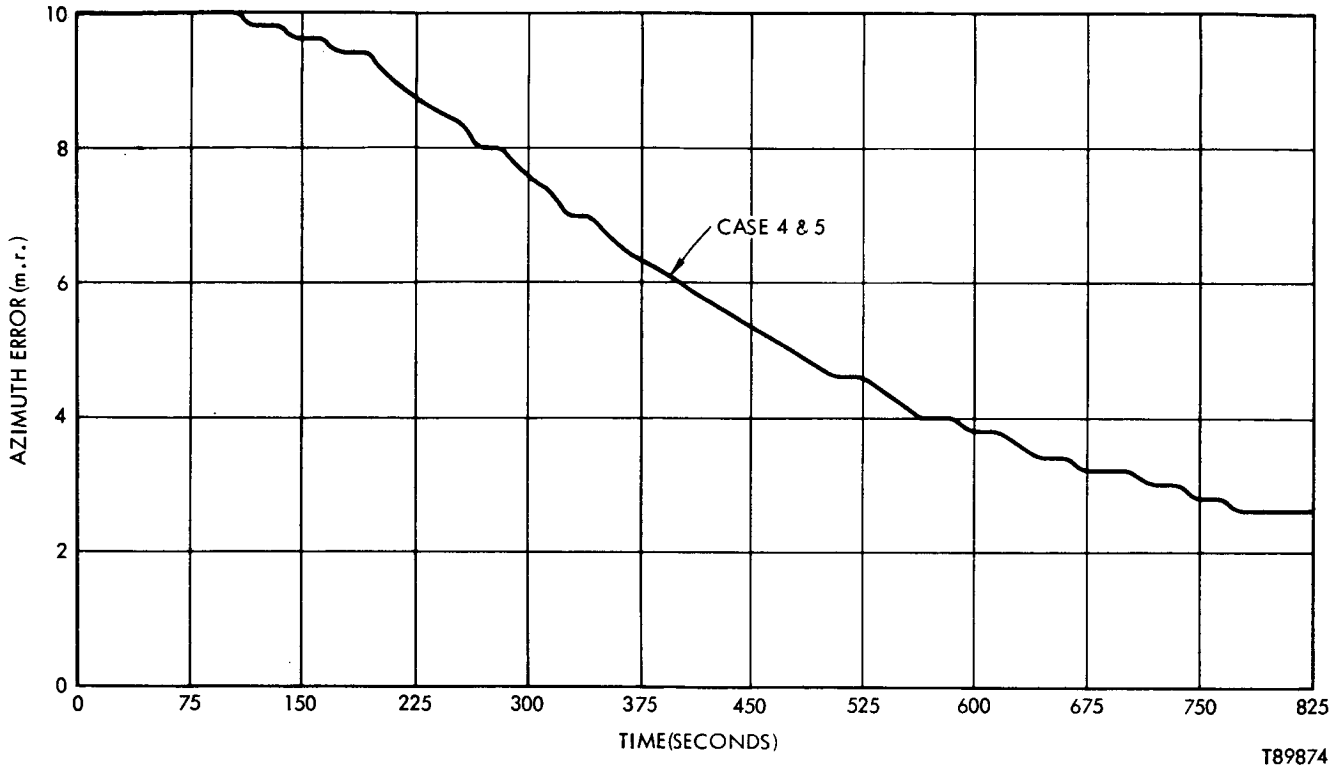

Figure 60C. Azimuth Axis Alignment for Varying Disturbance Frequency

Compensation Simulation

Introduction - A two degree-of-freedom dry-tuned gyro compensation algorithm has been developed to account for repeatable instrument errors. The magnitude of the errors vary as a function of changing vehicle dynamics.

Discussion - A computer simulation program has been developed to evaluate the compensation algorithm for varying vehicle dynamics. The overall processing flow is illustrated in Figure 61. Two stages of compensation are performed. The first is partial compensation is where the computed angular increment

$$\phi_{XYC(i)} = \phi_{XC(i)} + i\,\phi_{YC(i)}$$

is determined by

$$\phi_{XYC(i)} = \frac{i}{H}\int_{t_{i-1}}^{t_i} T_{XY}(t)\,dt - \frac{iA}{\tau H}\left[\phi_{XYC}(i-1) - \phi_{XYC}(i-2) + \phi_{XYC}(i-3)\right]$$

$$+\frac{(A-C)}{\tau H}\left[\left(\phi_{ZFC}(i-1) - \phi_{ZFC}(i-2)\right)\left(\phi_{XYC}(i-1) - \phi_{XYC}(i-2)\right)\right]$$

$$-\frac{1}{\tau_n}\left[\left(\tilde{\phi}_Z(i-1) - \tilde{\phi}_Z(i-2)\right)\left(\phi_{XYC}(i-1) - \phi_{XYC}(i-2)\right)\right]$$

where

ϕ_{ZFC} = computed angular increment about the spin axis

$\tilde{\phi}_Z$ = measured phase angle of spin axis pickoff system

$$= \int_{t_{i-1}}^{t_i} \dot{\phi}_{G_Z}\,dt$$

T_{XY} = $T_X + i\,T_Y$ = XY - gyro torque

i = $\sqrt{-1}$

H = C

n = mechanical synchronous speed of the rotor with respect to the instrument cases

C = polar moment of inertia of the gyro rotor

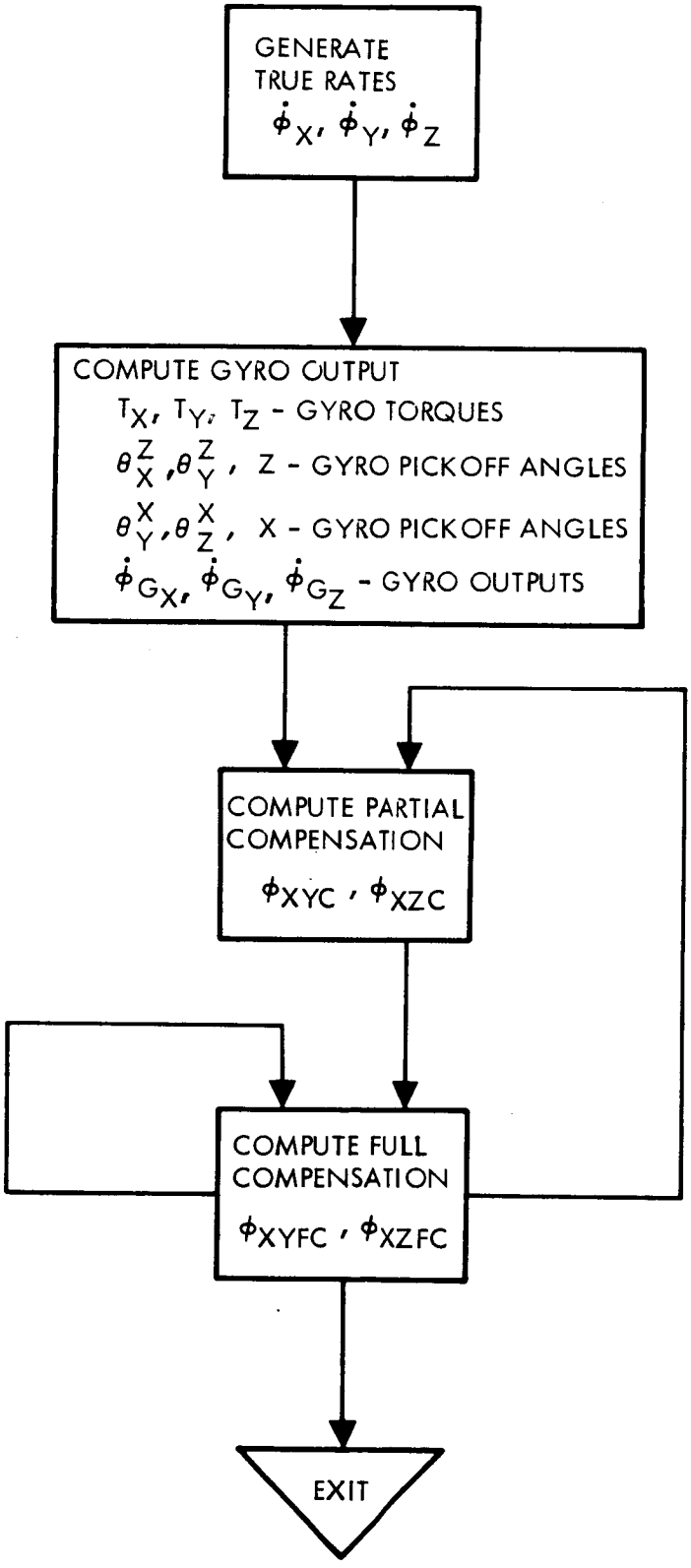

Figure 61. Overall Compensation Flow

A = Transverse moment of inertia of the gyro rotor

τ = $t_i - t_{i-1}$

The corresponding compensated angular input with respect to the instrument case is given by

$$\phi_{XYFC}(i) = \phi_{XYC}(i) - \frac{i}{2}\left[\left(\phi_{ZFC}(i-1) - \phi_{ZFC}(i-2)\right)\left(\tilde{\theta}_{XY}(i-1) - \tilde{\theta}_{XY}(i-2)\right)\right]$$

$$- \left[\tilde{\theta}_{XY}(i-1) - \tilde{\theta}_{XY}(i-2)\right]$$

where $\tilde{\theta}_{XY} = \tilde{\theta}_X + i\,\tilde{\theta}_Y$

= measured gyro pickoff angle

The processing flow is illustrated in Figure 62. The compensated angular input should approach the true angular input when all the systematic instrument errors are accounted for such that

$$\phi_{XYFC} \rightarrow \phi_{XY}$$

and

$$\phi_{XZFC} \rightarrow \phi_{XZ}$$

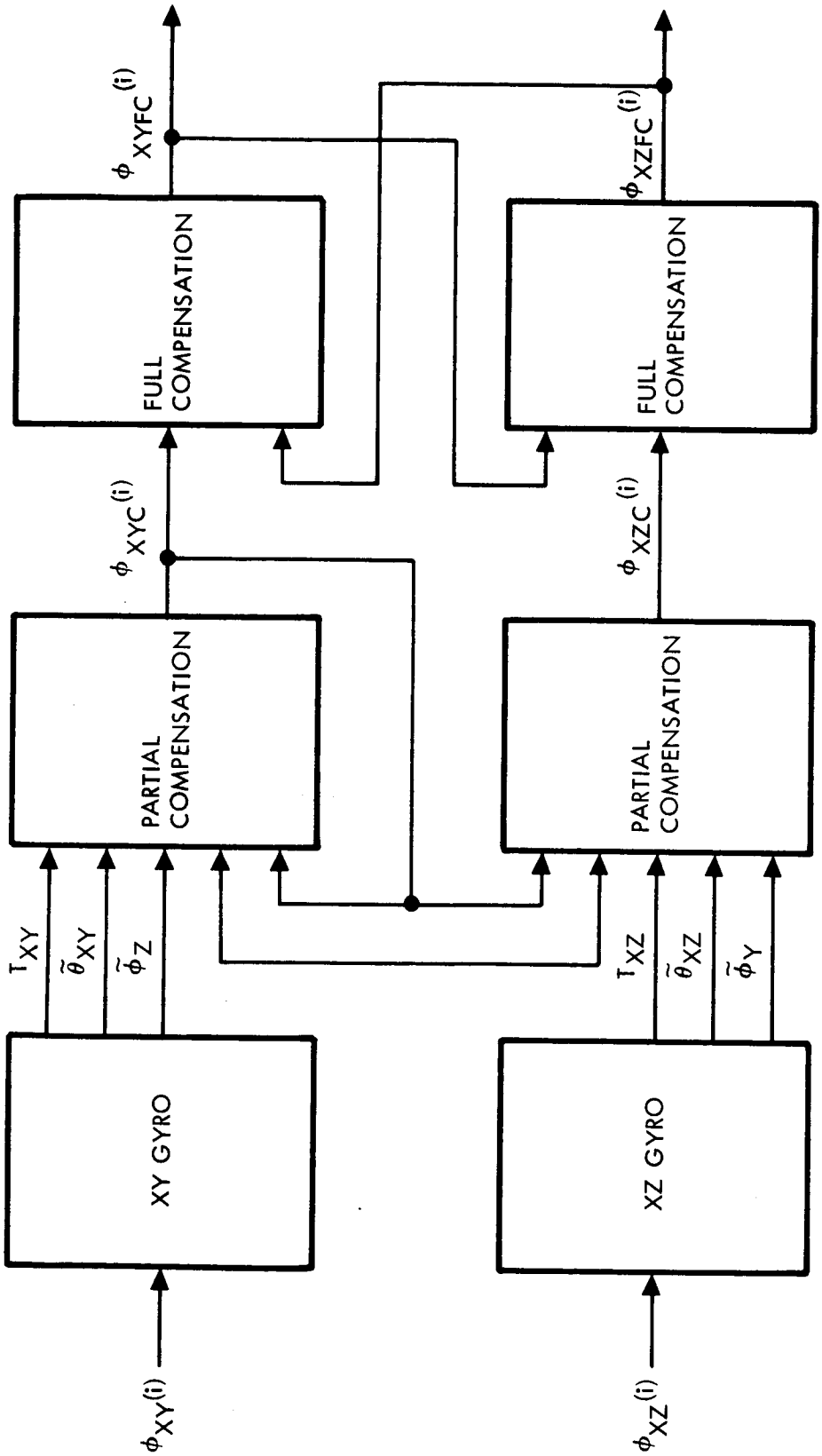

Figure 62. Detail Compensation Diagram

Hardware Tests

Introduction. - The purpose of the hardware tests was to determine 1) The rectification characteristics of angular inputs, applied about the spin axis and one of the input axis, throughout the frequency range of the gyro servo loop, and 2) the sensitivity to translational inputs through the frequency range of 15-95 Hz. In addition, the characteristics of the servo loop were measured for component modeling purposes.

Gyro/Servo Frequency Response Characteristics. - The servo loop characteristics shown in Figure 63 were obtained by mounting a gyro to the angular shaker with the gyro spin axis horizontal and one of the input axes parallel to the shaker axis. An accelerometer was mounted to the shaker in such a manner as to read tangential acceleration. The accelerometer output was then measured with a wave analyzer and was also displayed on an oscilloscope, along with the pickoff signals, to determine the servoloop parameters G_c, G_d, ξ_c, and ξ_d as defined in [10]. Peak angular rate was determined and maintained constant throughout the tests in two ways. For frequencies of 10 Hz or less, the gyro torquing current was used as a direct measure of rate. For frequencies above 10 Hz, the accelerometer output was used and rate was determined from the relationship

$$\dot{\theta} = \frac{\ddot{\theta}}{\omega} = \frac{a_T}{R_\omega} \quad \text{where}$$

$\dot{\theta}$ = angular rate

$\ddot{\theta}$ = angular acceleration

a = tangential acceleration

R_T = radius of accelerometer from shaker axis

ω = frequency of shake

The angular displacements of the rotor to case were measured at the pickoff demodulator output with a wave analyzer. Phase shift between torquing current and rotor displacement relative to the rate input were measured with the oscilloscope.

The results of these tests were in close agreement with the theoretically derived results. These parameters have subsequently seen incorporated into the simulation model.

Low Frequency Rectification. - The rectification coefficients shown in Figure 64 were obtained by mounting the gyro with its spin axis and one input axis at 45^o to the shaker axis. The other gyro input axis was perpendicular to the

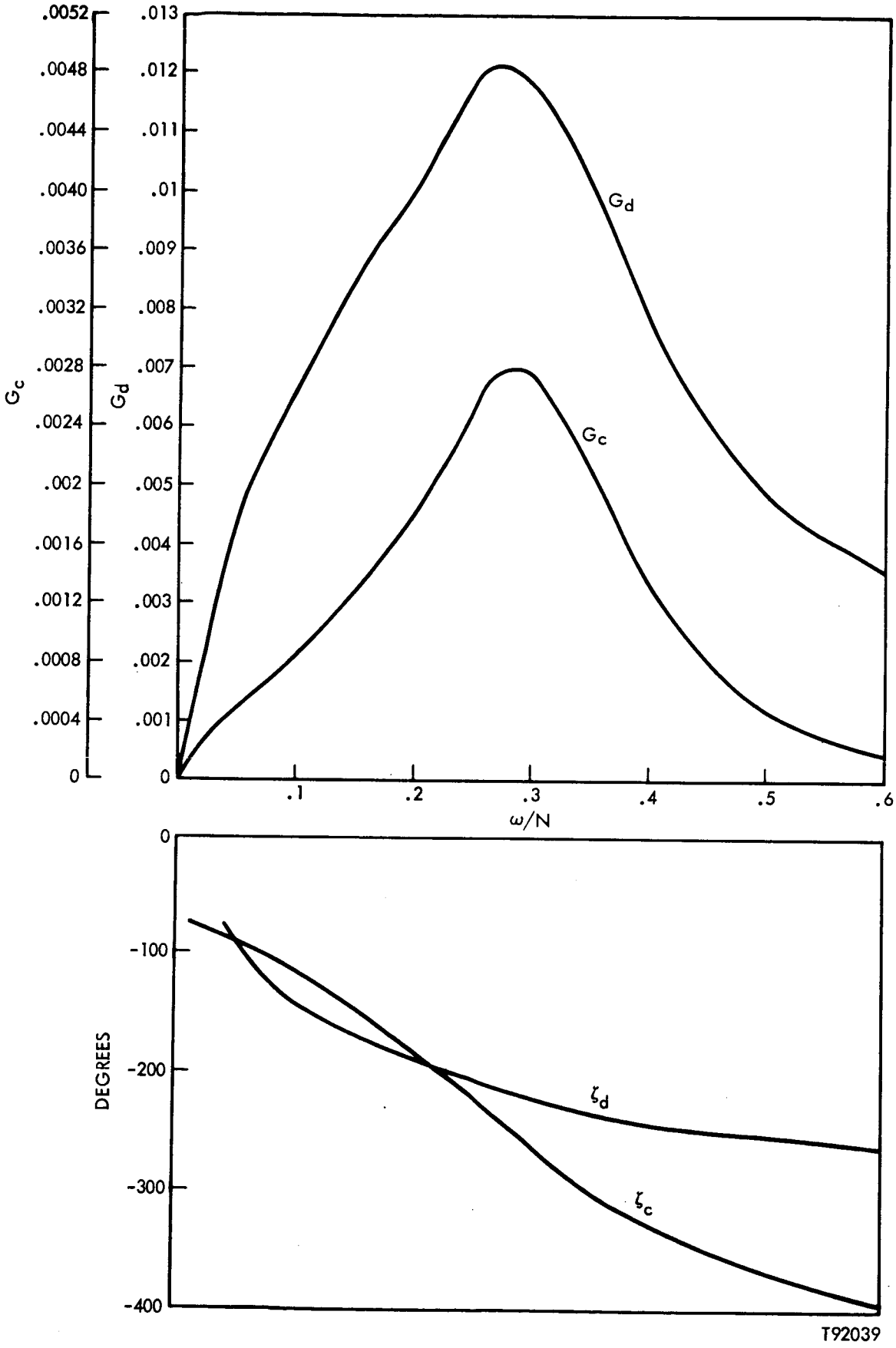

Figure 63. Servo Loop Characteristics

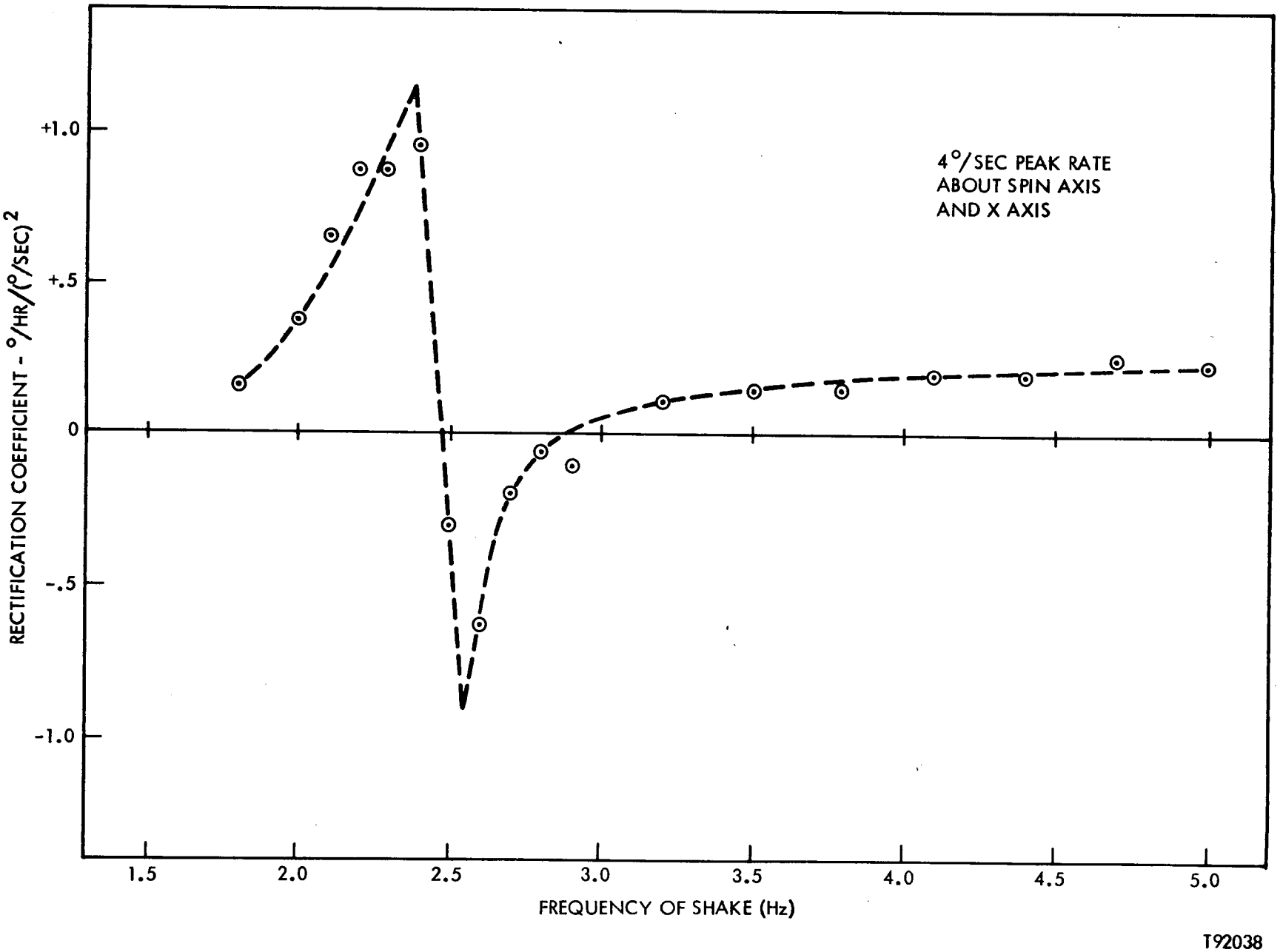

Figure 65. Low Frequency Rectification

shaker axis and thus was not subjected to any rate. Angular rate was measured and maintained constant at 4^{o}/sec during this test by monitoring the gyro torquer current. The rectification coefficients obtained apply to the operating condition when the gyro spin motor is excited sinusoidally with 3ϕ, 35V RMS line/line power.

The relationship between motor hunting frequency, time constant and excitation voltage is shown in Figure 65. These motor characteristics were measured just prior to performing the low frequency tests.

High Frequency Rectification. - The high frequency rectification tests were performed with the gyro in the same orientation as used for the low frequency tests. The input rate at the shaker was maintained at 5.65^{o}/sec peak (4^{o}/sec about the gyro axes) throughout the test.

The results of these tests showed the same general relationship between rectification error and shake frequency as that predicted analytically in [10] and simulated as described elsewhere in this report. The measured magnitude of this rectification error was significantly higher than that predicted theoretically, however.

As a result of this apparent discrepancy the tests were repeated. It was then observed that a rectification term exists which is independent of the motion of the gyro about its spin axis but dependent upon the magnitude of the torquer currents at the various frequencies. After further examination of this effect it was determined that essentially all of this rectification was the result of a non-linear output instrumentation circuit used to measure the average current.

The fact that almost no measureble rectification exists for a well instrumented test setup using large values of torquer current in each axis with a variable phase relationship has verified that no rectification terms beyond those analyzed and listed in [10] exist in the gyro design and that the theoretically derived results and simulation models are valid.

Sensitivity to Translational Inputs. - The instrument was mounted on a translational shaker and subjected to vibration along the spin axis as well as perpendicular to spin axis. The input was .15g's RMS through the frequency range of 15-95 Hz. Gyro drift rate was monitored during each test yielding the data shown in Figures 66 and 67. These results demonstrate that no significant sensitivity to translation vibrations, such as those which would be produced by vehicle rotor motions, are present in the instrument.

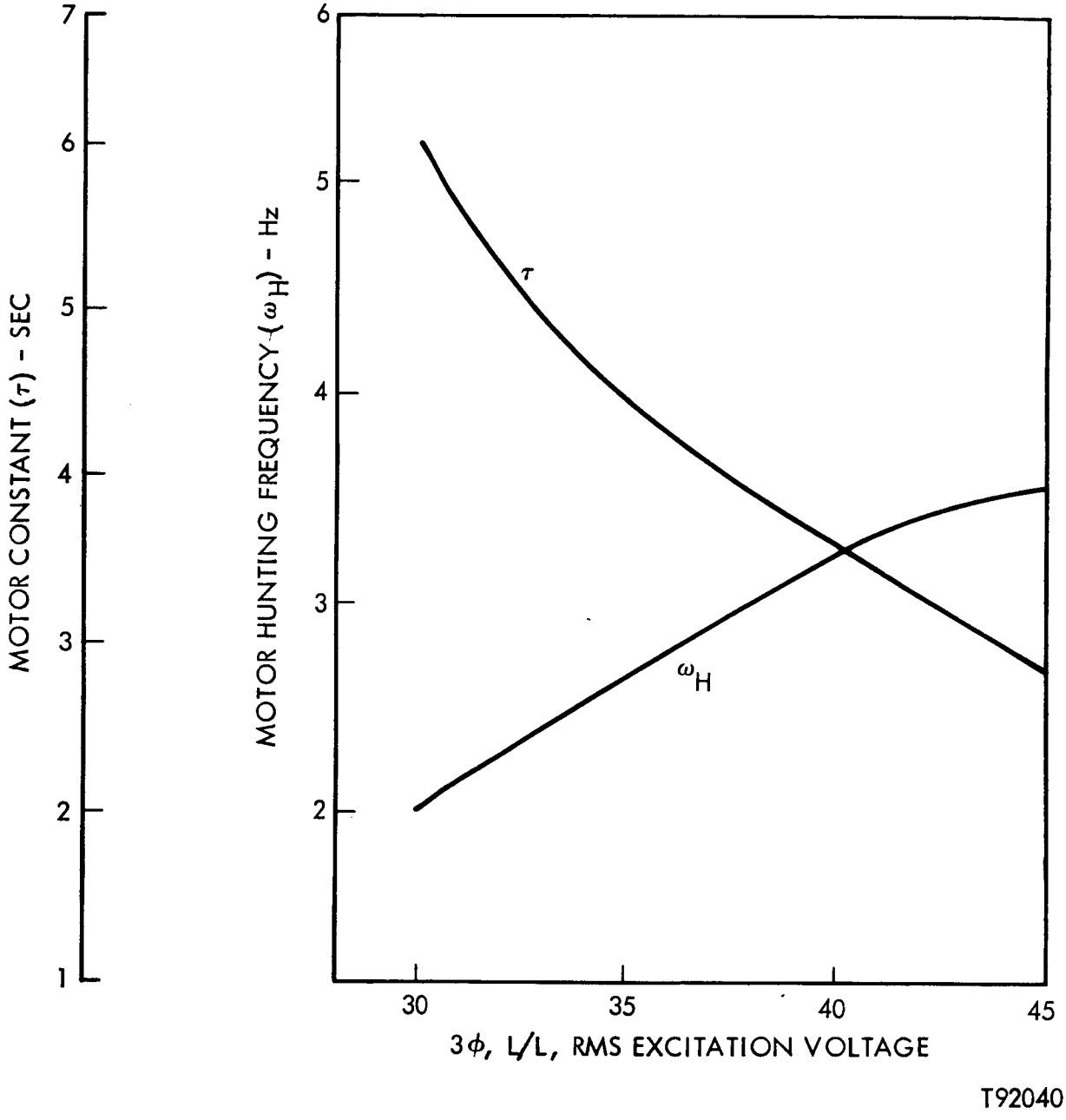

Figure 65. Gyro Spin Motor Dynamic Characteristics

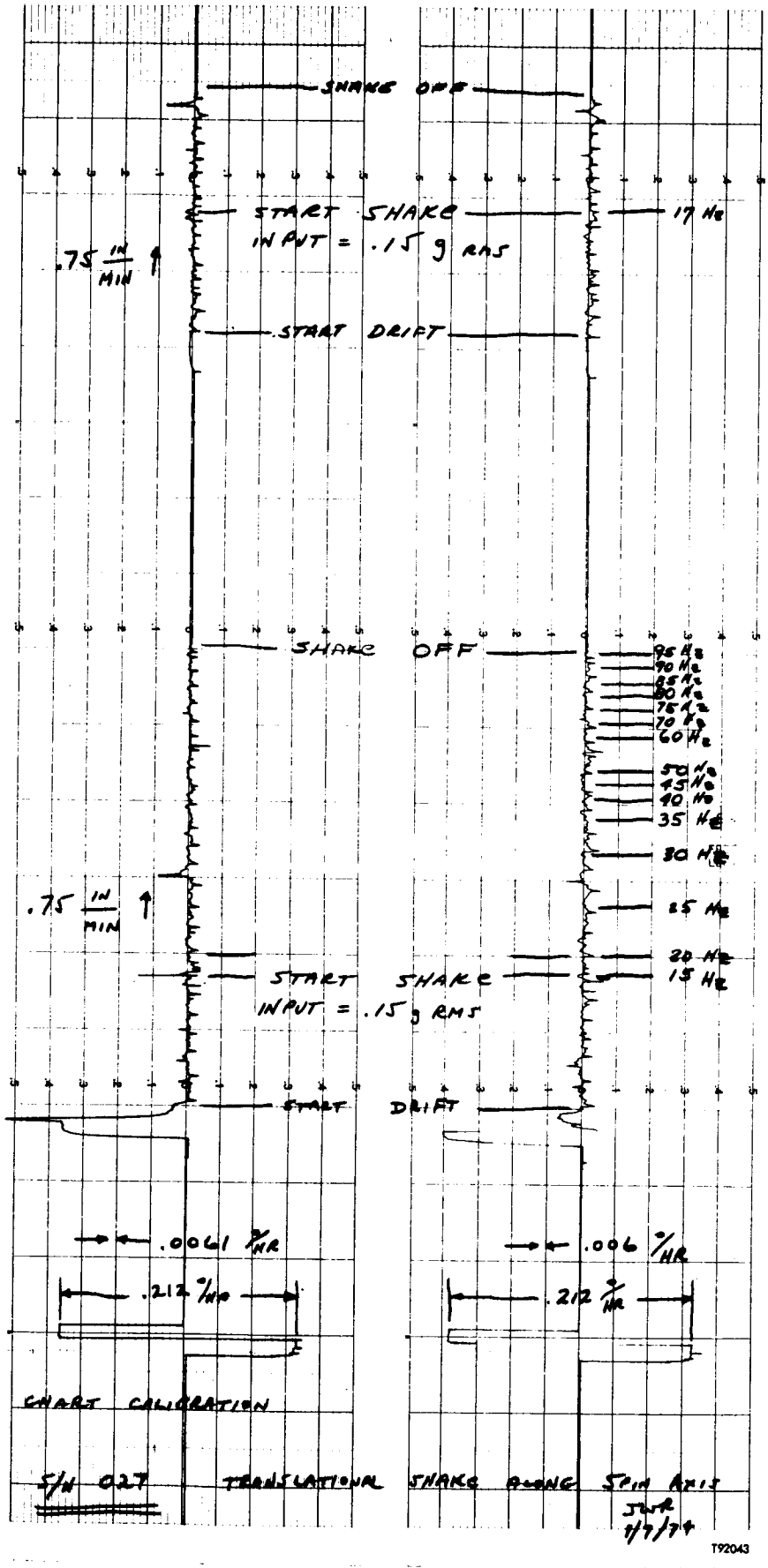

Figure 66. Translational Shake Along Spin Axis

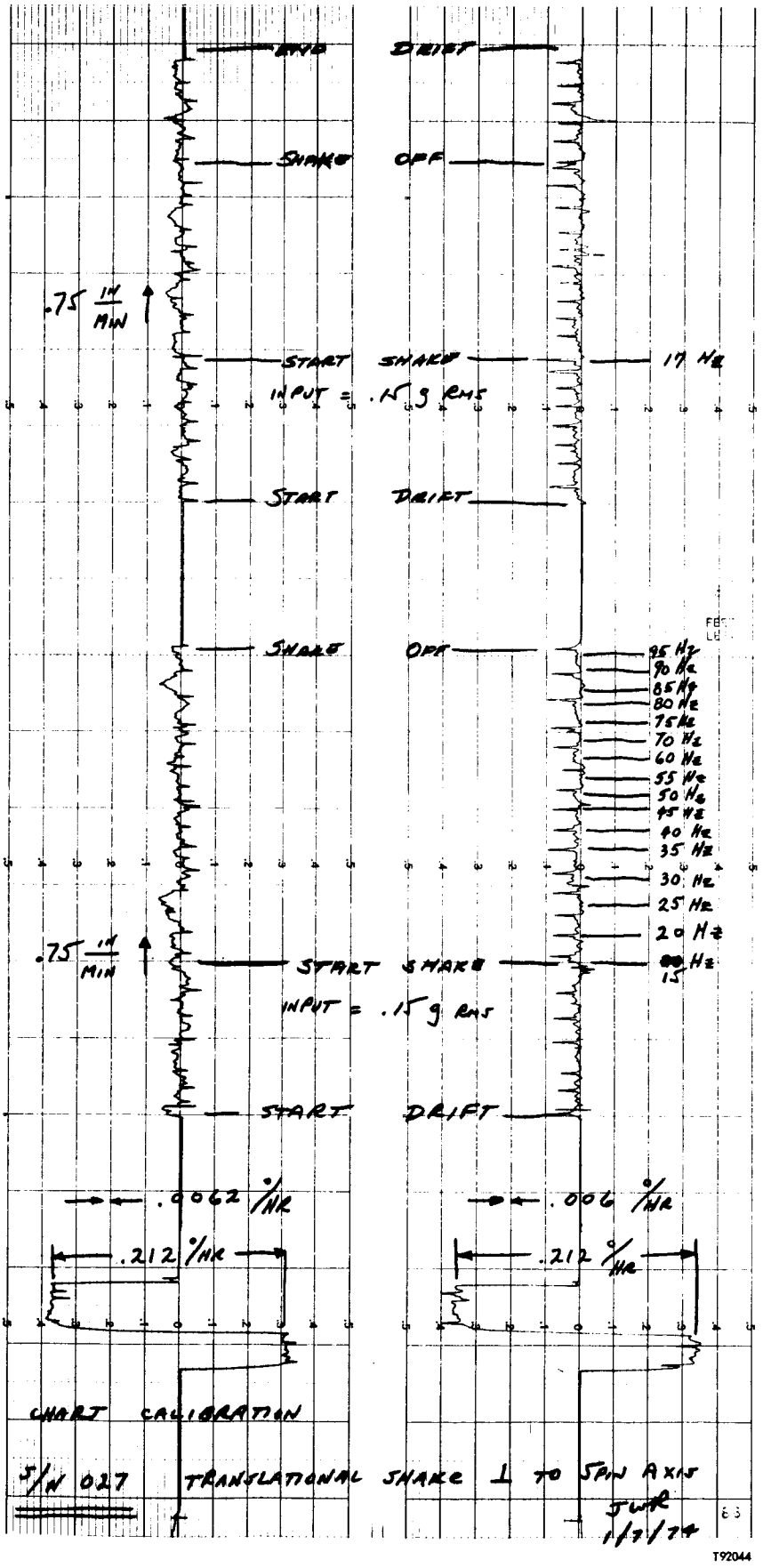

Figure 67. Translational Shake Normal to Spin Axis

This page intentionally left blank.

VII. ANALYSIS AND INTERPRETATION OF RESULTS

The primary goal of this study was to examine the applicability of two-degree-of-freedom dry tuned-gimbal instruments to strapdown navigation. This applicability is judged primarily by three performance factors: cost, reliability, and accuracy. Accuracy, once the basic sensors are specified, is largely dependent upon the software mechanization and the hardware/software interface. Thus accuracy may, to a large extent, be considered separately from cost and reliability.

The major emphasis of the first half of the study, beyond the specification of the study goals, was in the areas of cost and reliability. The most important results of this portion of the study are summarized by the cost-reliability curve derived in Section IV and repeated here for convenience as Figure 68.

A conventional strapdown mechanization was first examined using various levels of redundancy. The worst-case and best-case cost vs reliability curves for such a system are shown on the right in Figure 66. In a non-redundant configuration, indicated by the uppermost points on the curves, the system cost is somewhat less than the $50K which was established as a goal. The corresponding failure probability, however, far exceeds the goal of 10^{-6} per half hour. As various levels of redundancy are incorporated the reliability improves and the cost increases. The reliability goal is not achieved until the system cost has increased to approximately $85K.

The apparent inability of the conventional strapdown mechanization to simultaneously meet both the cost and reliability goals led to an investigation of possible alternative system configurations. The portion of the conventional system which was found most amenable to modification was the analog electronics package which contains the gyro and accelerometer caging loops and other associated sensor instrument control functions. This package represents a substantial portion of system cost and also contributes significantly to the system failure probability. Although historically these instrument control functions have been performed in analog electronics, both in strapdown and gimbal systems, there is no fundamental reason why they cannot be mechanized in a digital processor. This is particularly true when the multiplexed direct analog-to-digital converter described in Section V is used, since it obviates the necessity for separate converters for each signal. The transfer of the sensor control functions to the digital processor was made the basis of the "All-Digital" alternative to the conventional mechanization.

Another area of potential cost saving and reliability improvement centers around the measurement of acceleration. The conventional mechanization includes separate accelerometers for this function with the attendant cost and reliability

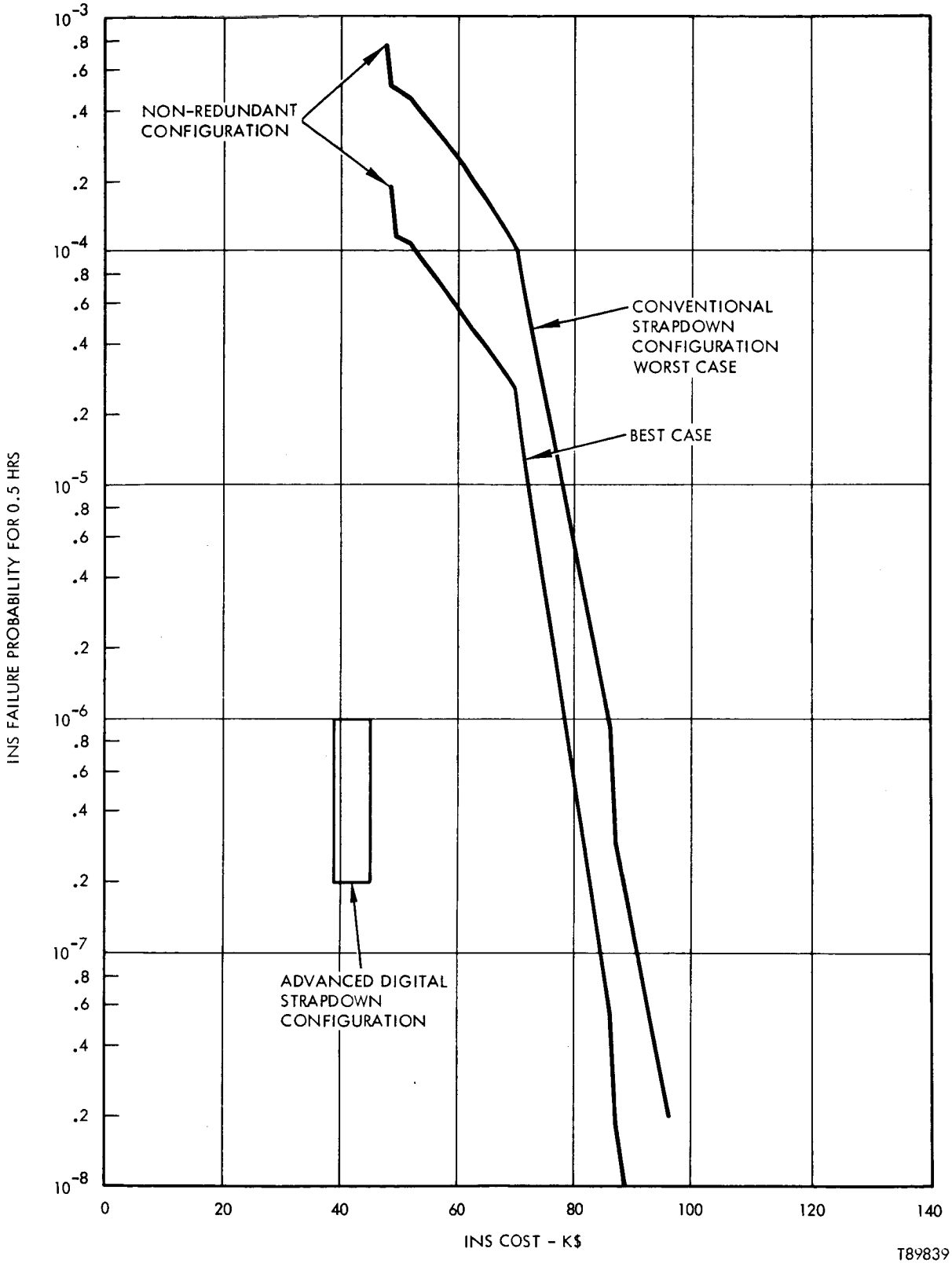

Figure 68. Cost-Reliability Tradeoff

penalties. The use of pendulous gyros to replace the accelerometers is feasible but, since one additional gyro axis must be added to the system for each accelerometer removed, the cost-reliability improvement does not appear to be significant. The spin-coupled gyro accelerometer (SCAG) described in Section IV, however, provides two axes of rate and two axes of acceleration information simultaneously. The SCAG is mechanically essentially the same instrument as the conventional dry tuned-gimbal byroscope, so the measurement of acceleration is obtained "free" in terms of cost and reliability at the instrument level (control functions are still required, of course). Hence utilization of the SCAG instrument appears to be another beneficial departure from the conventional strapdown design in terms of meeting the performance goals of the study.

A second baseline system was configured for the study, consisting of the All-Digital approach in conjunction with the SCAG instrument with full parallel triple redundancy. As indicated in Figure 68, this configuration appears to meet both the cost and reliability goals of the study.

A comprehensive system error analysis was conducted in order to evaluate the effects of sensor, computational, and approximation errors. Both analytical and simulation results were utilized for this analysis. It was concluded that the overall system accuracy was far in excess of the required 3 nautical miles per hour.

A detailed mechanization analysis was performed in order to obtain an appropriate set of equations to solve the strapdown navigation problem. Alternative mechanizations and algorithms were traded off in order to arrive at a set of equations which appears optimal for the VTOL application.

A detailed analysis of servo compensation requirements for the TDF strapdown gyro was performed. Although this was done for a conventional analog design it may be used as the basis for the all-digial approach as well.

It was concluded that alignment can be accomplished to the required accuracy within the 10 minute goal which had been established. The use of fixed-gain alignment filtering rather than Kalman filtering, appears to yield satisfactory results while minimizing the computational burden.

The hardware tests which have been conducted have demonstrated general agreement with analytically-derived results, but showed some variation in detail. The results of these tests was used to modify the simulation models in order to to make them as realistic as practical.

A cost of ownership analysis was performed. This analysis concluded that life cycle costs for a strapdown inertial navigator using the TDF dry tuned gyro are significantly lower than those accrued by its gimbaled counterpart which was used as a reference baseline for comparison. The low cost of ownership is one of the key

advantages of the dry gyro strapdown system over other inertial systems either strapdown or gimbal.

An estimate of the overall computational requirements was performed. It was concluded that a non-redundant system would require between 2000 and 2500 words of memory. Thus even allowing for auxiliary computations, such as flight control functions, a 4K memory would be sufficient. The incorporation of redundancy of any sort would apparently require more than 4K of memory for a conservative (i.e. low risk) design. Full fail-op/fail-op capability would be easily accommodated by an 8K memory. The computer speed afforded by the TDY-43 computer and high-speed versions of the TDY-52 assures that computer timing is not a problem for the selected 30 Hz computational frequency.

Although flight control mechanizations have not been specifically analyzed during the study, an important feature of strapdown inertial systems is the ability to provide highly accurate attitude information as well as body axis components of angular rate and linear acceleration for use in flight control computations. (Gimbaled systems provide attitude information which is limited in accuracy by the gimbal readout devices-synchros or resolvers-and do not provide the required angular rate components or body axis accelerations.)

Risk Considerations - The risk associated with the use of conventional sensors - the TDF dry tuned-gimbal gyro and conventional linear accelerometers-is small. These instruments have been extensively tested and are currently being used in a number of applications. The use of pendulous TDF gyros to provide acceleration and angular rate information has also been demonstrated in one systems application by the contractor, but this approach must be considered to be somewhat riskier than the conventional approach. The SCAG instrument has not yet been developed and thus probably represents an unacceptably high risk for the current application.

The TDY-43 computer has virtually no risk associated with it as it has been in production for some time and is in use in a variety of applications. The TDY-52 series of computers represents moderate risk as it represents current state-of-the-art. It has been concluded, however, that the TDY-52 is appropriate for use in the current application, however, and that the risk is more than outweighed by the cost advantages and design flexibility which it affords.

A third major risk consideration involves the "all-digital" concept. It appears from the results of this study that this approach is very desirable from the cost/reliability standpoint. It does, however, have associated with it a moderate risk factor. It is recommended that the viability of this concept be studied further and demonstrated prior to its inclusion in a system design.

Summary - It is the conclusion of this study that a redundant strapdown inertial navigation system employing the two-degree-of freedom dry tuned-gimbal gyroscope is an extremely attractive solution to the VTOL navigation problem which has been considered. Full fail-op/fail-op capability can be provided using the "all-digital" approach with conventional sensors for 50 to 60 thousand dollars in quantity. Such a system exceeds the reliability goal of 10^{-6} failure rate per half hour at a cost which is only slightly in excess of the goal of 50 thousand dollars per system. The cost and reliability goals can be met simultaneously by employing the SCAG instrument, but there is a substantial risk associated with such a configuration since that sensor has not yet been fully developed.

The third major performance parameter which was considered was accuracy. The study has concluded that the strapdown system is capable of accuracy well in excess of the 3 nautical mile per hour goal. This higher accuracy is attained without substantial effect on either cost of reliability.

REFERENCES

[1] Wilcox, James C. "A New Algorithm for Strapped-Down Inertial Navigation", IEEE Trans Aero Elec Systems; Vol AES-3, No. 5, Sept. 1967, pp, 796-802.

[2] McKern, Richard A. "A Study of Transformation Algorithms for Use in a Digital Computer", Master's Thesis, MIT, 1968.

[3] Koenike, E. J., and D. R. Downing, "Evaluating Strapdown Algorithms: A Unified Approach" NASA Electronics Research Center.

[4] " A Study of the Critical Computational Programs Associated with Strapdown Inertial Navigation Systems", NASA CR-968, United Aircraft Corporation.

[5] Sullivan, J. J., "Evaluation of the Computational Errors of Strapdown Navigation Systems", AIAA Journal, Vol 6, No. 2, February 1968, pp 312-319.

[6] Halamandaris, H., "Strapdown Inertial Navigation Practical Considerations", Proc Inst of Navigation Aerospace Meeting, March 1973.

[7] Rabiner, L. R. and C. M. Rader, Digital Signal Processing, IEEE Press, New York, 1972, pp 43-65 and pp 361-368.

[8] Gold, B. and C. M. Rader, Digital Processing of Signals, McGraw-Hill, New York, 1969, Chap 4.

[9] Lipman, J. S., "Application of the Complex Method to Transform Analysis of Spinning Systems with Rotating Non-Symmetries", Proc 1968. Joint Auto Control Conf., Ann Arbor, Mich.

[10] Craig, R. J. G., "Dynamically Tuned Gyros in Strapdown Systems", Proc 1972 AGARD Conf on Inertial Navigation Components and Systems, Florence, Italy.

[11] _____, "Theory of Operation of an Elastically Supported, Tuned Gyroscope", IEEE Trans Aero Elec Systems, Vol AES-8, May, 1972, pp. 280-288.

[12] Ickes, B. P., "A New Method for Performing Digital Control System Attitude Computations Using Quaternions", Proc 1968 Joint Auto. Control Conf.

[13] Robinson, Alfred C., "On the Use of Quaternions in Simulation of Rigid-Body Motion", Wright Air Development Center Technical Report WADC 58-17, 1958.

[14] Klein, F., Nichteuklidische Geometrie, Chelsea, London, 1927, pp 238-241.

[15] Pitman, G. R. Jr., Inertial Guidance, Wiley, New York, 1962.

[16] Britting, K. R., Inertial Navigation Systems Analysis, Wiley, New York, 1971.

[17] Cannon, R. H. Jr., "Alignment of Inertial Guidance Systems by Gyrocompassing - Linear Theory", Journal Aerospace Sciences, Vol 28, No. 11, Nov. 1961.

[18] Gilmore, J. P. "A Non-Orthogonal Gyro Configuration", Master's Thesis, MIT, 1967.

This page intentionally left blank

A1 - FAILURE RATE ANALYSIS FOR THE INS POWER SUPPLY

SUMMARY

The operating failure rate for an INS power supply is 5.177 failures per 10^6 hours while the non-operating failure rate for the INS power supply is 1.091 failures per 10^6 hours. The failure rates are the same for both a two and three gyro INS.

The failure rates presented in the following tables and used for the individual components are those in Table II - 1 (Preferred failure rates for electronic piece parts) of the "Handbook of Piece Part Failure Rates," June 22, 1970, Martin Marietta, document.

ANALYSIS

FAILURE RATES OF INDIVIDUAL CIRCUITS OF INS POWER SUPPLY

	Circuit	Failure Rate (Failures/10^6 hrs) Operating	Non-Operating
I	DC to DC Converter	0.390	0.0370
II	+30 Volt DC Regulator	0.448	0.0792
III	-30 Volt DC Regulator	0.448	0.0792
IV	+ Spin Supply Regulator	0.412	0.0702
V	- Spin Supply Regulator	0.412	0.0702
VI	HI/LO Spin Switch	0.122	0.0370
VII	+15 Volt DC Precision Regulator	0.390	0.087
VIII	-15 Volt DC Precision Regulator	0.403	0.088
IX	+5 Volt DC Regulator	0.284	0.0502
X	Pickoff Excitation Filter & Power Amp.	0.458	0.0682
XI	Precision AC to DC Converter & Multiplier	0.180	0.0812
XII	Phase Splitter & Countdown	0.210	0.1400
XIII	Digital Countdown & Logic Reset	0.141	0.0836
XIV	Spin Motor Power Switch (3 each)	0.879	0.120
	Total	5.177	1.091

FAILURE ANALYSIS OF INDIVIDUAL CIRCUITS OF INS POWER SUPPLY

I DC to DC CONVERTER

COMPONENT	QTY	PART FAILURE RATE (Failures/10^6 Hrs)		TOTAL FAILURE RATE (Failures/10^6 Hrs)	
		Operating	Non-Operating	Operating	Non-operating
Transistor (Power)	2	0.10	0.01	0.200	0.020
Diode (Power)	8	.006	.001	.048	.008
Resistor, W. W. (Power)	4	0.003	0.001	0.012	0.004
Capacitor, Tantalum	4	0.020	0.001	0.080	0.004
Transformer	1	0.050	0.001	0.050	0.001
			Totals	0.390	0.037

II +30 VOLT DC REGULATOR

COMPONENT	QTY	PART FAILURE RATE (Failures/10^6 Hrs)		TOTAL FAILURE RATE (Failures/10^6 Hrs)	
		Operating	Non-Operating	Operating	Non-Operating
Transistor (Power)	2	0.100	0.010	0.200	0.020
Transistor (NPN small signal)	3	0.010	0.002	0.030	0.006
Diode (Power)	1	.006	.001	.006	.001
Diode (General)	1	0.006	0.001	0.006	0.001
Diode (Ref. Zener)	3	0.020	0.005	0.060	0.015
Resistors	14	0.003	0.001	0.042	0.014
Capacitors (Ceramic)	1	0.004	0.0002	0.004	0.0002
Capacitors (Tantalum)	1	0.020	0.001	0.020	0.001
Microcircuit, Linear	1	0.030	0.020	0.030	0.020
Choke	1	0.050	0.001	0.050	0.001
			Totals	0.448	0.0792

III -30 VOLT DC REGULATOR

(Same as +30 Volt DC Regulator)

	(Failures/10^6 Hrs)	
	Operating	Non-Operating
Totals	0.448	0.0792

IV + SPIN SUPPLY REGULATOR

COMPONENTS	QTY	PART FAILURE RATE (Failures/10^6 Hrs)		TOTAL FAILURE RATE (Failures/10^6 Hrs)	
		Operating	Non-Operating	Operating	Non-Operating
Transistor (Power)	2	0.100	0.010	0.200	0.020
Transistor (small signal)	2	0.010	0.002	0.020	0.004
Diode (Power)	1	.006	.001	.006	.001
Diode (Ref. Zener)	2	0.020	0.005	0.040	0.010
Diode (General)	1	0.006	0.001	0.006	0.001
Resistors	12	0.003	0.001	0.036	0.012
Capacitor, Ceramic	1	0.004	0.0002	0.004	0.0002
Capacitor, Tantalum	1	0.020	0.001	0.020	0.001
Microcircuit, Linear	1	0.030	0.020	0.030	0.020
Choke	1	0.050	0.001	0.050	0.001
			Totals	0.412	0.0702

V - SPIN SUPPLY REGULATOR

(Same as + Spin Supply Regulator)

	(Failure Rate/10^6 Hrs)	
	Operating	Non-Operating
Totals	0.412	0.0702

VI HI/LO SPIN SWITCH

COMPONENT	QTY	PART FAILURE RATE (Failures/10^6 Hrs)		TOTAL FAILURE RATE (Failures/10^6 Hrs)	
		Operating	Non-Operating	Operating	Non-Operating
Transistor (NPN, Si)	1	0.010	0.002	0.010	0.002
Transistor (PNP, Si)	2	0.020	0.002	0.040	0.004
Diode (General)	3	0.006	0.001	0.018	0.003
Resistor	8	0.003	0.001	0.024	0.008
Microcircuit, Digital	1	0.030	0.020	0.030	0.020
			Totals	0.122	0.037

VII +15 VOLT DC PRECISION REGULATOR

COMPONENT	QTY	PART FAILURE RATE (Failures/10^6 Hrs)		TOTAL FAILURE RATE (Failures/10^6 Hrs)	
		Operating	Non-Operating	Operating	Non-Operating
Transistor (Power)	1	0.100	0.010	0.100	0.010
Transistor (NPN, Si)	2	0.010	0.002	0.020	0.004
Transistor (PNP, Si)	1	0.020	0.002	0.020	0.002
Diode (Power)	1	.006	.001	.006	.001
Diode (Ref. Zener)	2	0.020	0.005	0.040	0.010
Diode (General)	1	0.006	0.001	0.006	0.001
Resistor	16	0.003	0.001	0.048	0.016
Capacitor (Ceramic	5	0.004	0.0002	0.020	0.001
Capacitor (Tantalum)	1	0.020	0.001	0.020	0.001
Microcircuit, Linear	2	0.030	0.020	0.060	0.040
Choke	1	0.050	0.001	0.050	0.001
			Totals	0.390	0.087

VIII -15 VOLT DC PRECISION REGULATOR

COMPONENT	QTY	PART FAILURE RATE (Failures/10^6 Hrs)		TOTAL FAILURE RATE (Failures/10^6 Hrs)	
		Operating	Non-Operating	Operating	Non-Operating
Transistor (Power	1	0.100	0.010	0.100	0.010
Transistor (NPN, Si)	1	0.010	0.002	0.010	0.002
Transistor (PNP, Si)	2	0.020	0.002	0.040	0.004
Diode (Power)	1	.006	.001	.006	.001
Diode (Ref. Zener)	2	0.020	0.005	0.040	0.010
Diode (General)	1	0.006	0.001	0.006	0.001
Resistor	17	0.003	0.001	0.051	0.017
Capacitor (Ceramic)	5	0.004	0.0002	0.020	0.001
Capacitor (Tantalum)	1	0.020	0.001	0.020	0.001
Microcircuit, Linear	2	0.030	0.020	0.060	0.040
Choke	1	0.050	0.001	0.050	0.001
			Totals	0.403	0.088

IX +5 VOLT DC REGULATOR

COMPONENT	QTY	PART FAILURE RATE (Failures/10^6 Hrs)		TOTAL FAILURE RATE (Failures/10^6 Hrs)	
		Operating	Non-Operating	Operating	Non-Operating
Transistor (Power)	1	0.100	0.010	0.100	0.010
Transistor (PNP, Si)	1	0.020	0.002	0.020	0.002
Transistor (NPN, Si)	1	0.010	0.002	0.010	0.002
Diode (Power)	1	.006	.001	.006	.007
Diode (Ref. Zener)	1	0.020	0.005	0.020	0.005
Resistor	8	0.003	0.001	0.024	0.008
Capacitor (Ceramic)	1	0.004	0.0002	0.004	0.0002
Capacitor (Tantalum)	1	0.020	0.001	0.020	0.001
Microcircuit, Linear	1	0.030	0.020	0.030	0.020
Choke	1	0.050	0.001	0.050	0.001
			Totals	0.284	0.0502

X PICKOFF EXCITATION FILTER & POWER AMP

COMPONENT	QTY	PART FAILURE RATE (Failures/10^6 Hrs)		TOTAL FAILURE RATE (Failures/10^6 Hrs)	
		Operating	Non-Operating	Operating	Non-Operating
Transistor (Power)	2	0.100	0.010	0.200	0.020
Transistor (PNP, Si)	2	0.020	0.002	0.040	0.004
Transistor (NPN, Si)	2	0.010	0.002	0.020	0.004
Diode (General)	2	0.006	0.001	0.012	0.002
Resistor	14	0.003	0.001	0.042	0.014
Capacitor (Ceramic)	6	0.004	0.0002	0.024	0.0012
Capacitor (Tantalum)	2	0.020	0.001	0.040	0.002
Inductor	1	0.050	0.001	0.050	0.001
Microcircuit, Linear	1	0.030	0.020	0.030	0.020
			Totals	0.458	0.0682

XI PRECISION AC TO DC CONVERTER & MULTIPLIER

COMPONENT	QTY	PART FAILURE RATE (Failures/10^6 Hrs)		TOTAL FAILURE RATE (Failures/10^6 Hrs)	
		Operating	Non-Operating	Operating	Non-Operating
Diode (General	2	0.006	0.001	0.012	0.002
Resistor	18	0.003	0.001	0.054	0.018
Capacitor (Ceramic)	6	0.004	0.0002	0.024	0.0012
Microcircuits, Linear	3	0.030	0.020	0.090	0.060
			Totals	0.180	0.0812

XII PHASE SPLITTER AND COUNTDOWN

COMPONENT	QTY.	PART FAILURE RATE (Failures/10^6Hrs)		TOTAL FAILURE RATE (Failures/10^6Hrs)	
		Operating	Non-Operating	Operating	Non-Operating
Microcircuit, Digital	7	0.030	0.020	0.210	0.140
			Totals	0.210	0.140

XIII DIGITAL COUNTDOWN & LOGIC RESET

COMPONENT	QTY.	PART FAILURE RATE (Failures/10^6Hrs)		TOTAL FAILURE RATE (Failures/10^6Hrs)	
		Operating	Non-Operating	Operating	Non-Operating
Microcircuit (Digital)	4	0.030	0.020	0.120	0.080
Resistor	3	0.003	0.001	0.009	0.003
Capacitor (Ceramic)	3	0.004	0.0002	0.012	0.0006
			Totals	0.141	0.0836

XIV SPIN MOTOR POWER SWITCH (3 EACH)

COMPONENT	QTY	PART FAILURE RATE (Failures/10^6Hrs)		TOTAL FAILURE RATE (Failures/10^6Hrs)	
		Operating	Non-Operating	Operating	Non-Operating
Transistor (Power)	2	0.100	0.010	0.200	0.020
Transistor (NPN, Si)	4	0.010	0.002	0.040	0.008
Transistor (PNP, Si)	1	0.020	0.002	0.020	0.002
Diode (Power)	1	.006	.001	.006	.001
Resistor	9	0.003	0.001	0.027	0.009
			Totals	0.293	0.0400
		For All 3:	TOTALS	0.879	0.120

This page intentionally left blank

A2 - FAILURE ANALYSIS FOR THE ISOLATION AMPLIFIERS AND CAGING CIRCUITS

INTRODUCTION

The block diagram for the isoamp and caging circuit is shown in Figure 1. The schematics for the block are in Figures 2 through 5.

The isoamp is an impedance matching device between the gyro pickoff output and the caging circuit input. The caging circuit output provides the current for the gyro torquer coils.

SUMMARY

The operating failure rate for the isoamps and caging circuits for both axis of a single gyro is 2.2550 failures per million hours. The operating failure rate for these circuits for a two gyro INS is 4.5100 failures per million hours and 6.7650 failures per million hours for a three gyro INS. The non-operating failure rate for the isoamps and caging circuit for both axes of a single gyro is 0.5708 failures per million hours. The non-operating failure rate for these circuits for a two gyro INS is 1.1416 failures per million hours and 1.7124 failures per million hours for a three gyro INS.

The results of the failure analysis are contained in the following tables.

ANALYSIS

Failure Rates for the Caging Circuit and Isoamps for Each Gyro:

	Block	Failure Rate (failures/10^6 hrs) Operating	Non-Operating
I.	Isoamps	0.206	0.0592
II.	AC Amp and Demod	0.181	0.0828
III.	Filter	0.146	0.0528
IV.	Direct Axis Compensation	0.264	0.1008
V.	Cross Axis Compensation	0.234	0.0976
VI.	Integrator and DC Amp	0.124	0.0500
VII.	Power Amp	1.100	0.1276
	Total Per Gyro	2.2550	0.5708
	Total 2 Gyros	4.5100	1.1416
	Total 3 Gyros	6.7650	1.7124

Failure Analysis of the Caging Circuits and Isoamps for the ARU:

I. Isoamp (2 each)

COMPONENT	Qty	Part Failure Rate (failures/10^6 hrs)		Total Failure Rate (failures/10^6 hrs)	
		Oper	Non Oper	Oper	Non Oper
Op. Amp	1	0.030	0.020	0.030	0.020
Resistors	7	0.003	0.001	0.021	0.007
Capacitor, Tantalum	2	0.020	0.001	0.040	0.002
Capacitor, Ceramic	3	0.004	0.0002	0.012	0.0006
		TOTAL		0.103	0.0296
		TOTAL (2 ea)		0.206	0.0592

II. AC Amp and Demod

COMPONENT	Qty	Part Failure Rate (failures/10^6 hrs)		Total Failure Rate (failures/10^6 hrs)	
		Oper	Non Oper	Oper	Non Oper
Op Amp	2	0.030	0.020	0.060	0.040
Resistor	10	0.003	0.001	0.030	0.010
Capacitor, Ceramic	14	0.004	0.0002	0.056	0.0028
MOS, Analog Switch	1	0.035	0.030	0.035	0.030
		TOTAL		0.181	0.0828

III. Filter (2 each)

COMPONENT	Qty	Part Failure Rate (failures/10^6 hrs)		Total Failure Rate (failures/10^6 hrs)	
		Oper	Non Oper	Oper	Non Oper
Op Amp	1	0.030	0.020	0.030	0.020
Resistor	5	0.003	0.001	0.015	0.005
Capacitor, Polystyrene	3	0.004	0.0002	0.012	0.0006
Capacitor, Ceramic	4	0.004	0.0002	0.016	0.0008
		TOTAL		0.073	0.0264
		TOTAL (2 ea)		0.146	0.0528

IV. Direct Axis Compensation (2 each)

COMPONENT	Qty	Part Failure Rate (failures/10^6 hrs)		Total Failure Rate (failures/10^6 hrs)	
		Oper	Non Oper	Oper	Non Oper
Op Amp	2	0.030	0.020	0.060	0.040
Resistor	8	0.003	0.001	0.024	0.008
Capacitor, Ceramic	12	0.004	0.0002	0.048	0.0024
		TOTAL		0.132	0.0504
		TOTAL (2 ea)		0.264	0.1008

V. Cross Axis Compensation (2 each)

COMPONENT	Qty	Part Failure Rate (failures/10^6 hrs)		Total Failure Rate (failures/10^6 hrs)	
		Oper	Non Oper	Oper	Non Oper
Op Amp	2	0.030	0.020	0.060	0.040
Resistor	7	0.003	0.001	0.021	0.007
Capacitor, Ceramic	9	0.004	0.0002	0.036	0.0018
		TOTAL		0.117	0.0488
		TOTAL (2 ea)		0.234	0.0976

VI. Integrator and DC Amp (2 each)

COMPONENT	Qty	Part Failure Rate (failures/10^6 hrs)		Total Failure Rate (failures/10^6 hrs)	
		Oper	Non Oper	Oper	Non Oper
Op Amp	1	0.030	0.020	0.030	0.020
Resistor	4	0.003	0.001	0.012	0.004
Capacitor, Ceramic	4	0.004	0.0002	0.016	0.0008
Capacitor, Polystyrene	1	0.004	0.0002	0.004	0.0002
		TOTAL		0.062	0.025
		TOTAL (2 ea)		0.124	0.050

VII. Power Amp (2 each)

COMPONENT	Qty	Part Failure Rate (failures/10^6 hrs)		Total Failure Rate (failures/10^6 hrs)	
		Oper	Non Oper	Oper	Non Oper
Transistor (Power)	4	0.100	0.010	0.400	0.040
Transistor (Small Signal)	2	0.010	0.002	0.020	0.004
Diode (Med. Power)	2	0.006	0.004	0.012	0.002
Resistor	14	0.003	0.001	0.042	0.014
Capacitor, Tantalum	2	0.020	0.001	0.040	0.002
Capacitor, Ceramic	9	0.004	0.0002	0.036	0.0018
		TOTAL		0.550	.0638
		TOTAL (2 ea)		1.100	0.1276

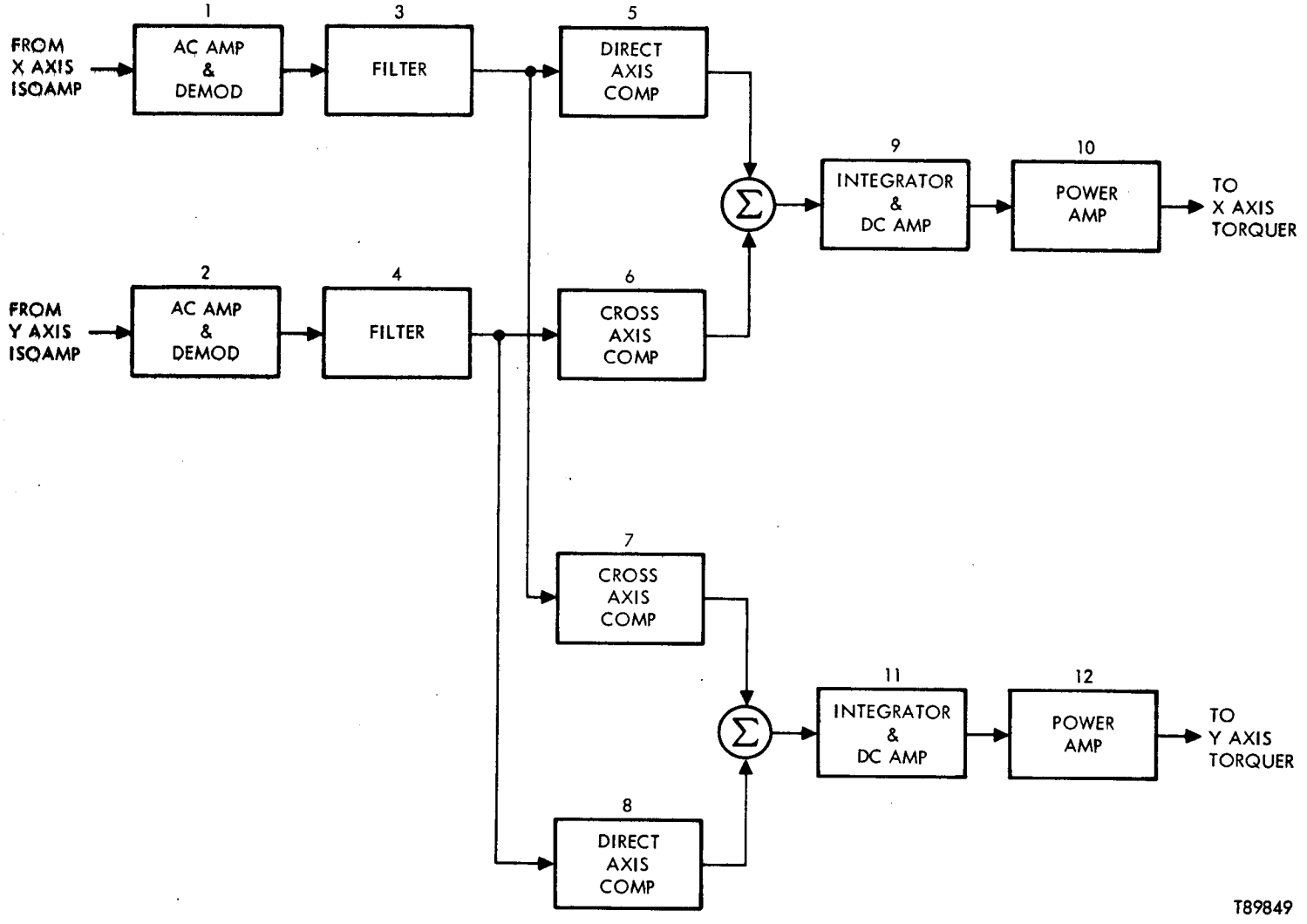

Figure 1. Caging Circuit Block Diagram for each Strapdown Gyro

Part Population for Failure Rate Analysis Each Gyro:

Isoamp (2 each)

Component	Qty
Operational Amplifier	1
Resistor, Variable	2
Resistor, Carbon	5
Capacitor, Tantalum	2
Capacitor, Ceramic	3

1, 2 AC Amp and Demod (total)

Component	Qty
Operational Amplifier	2
Resistor, Carbon	10
Capacitor, Ceramic	14
MOS, Analog Switch	1

3, 4 Filter (2 each)

Component	Qty
Operational Amplifier	1
Resistor, Carbon	2
Resistor, Wirewound	3
Capacitor, Polystyrene	3
Capacitor, Ceramic	4

5, 8 Direct Axis Compensation (2 each)

Component	Qty
Operational Amplifier	2
Resistor, Carbon	8
Capacitor, Ceramic	12

6, 7 Cross Axis Compensation (2 each)

Component	Qty
Operational Amplifier	2
Resistor, Carbon	7
Capacitor, Ceramic	9

9, 11 Integrator and DC Amp (2 each)

Component	Qty
Operational Amplifier	1
Resistor, Carbon	4
Capacitor, Ceramic	4
Capacitor, Polystyrene	1

10, 12 Power Amp (2 each)

Component	Qty
Transistor (power)	2
Transistor (medium power)	2
Transistor (small signal)	2
Diode, Medium Power	2
Resistor, Carbon	14
Capacitor, Tantalum	2
Capacitor, Ceramic	9

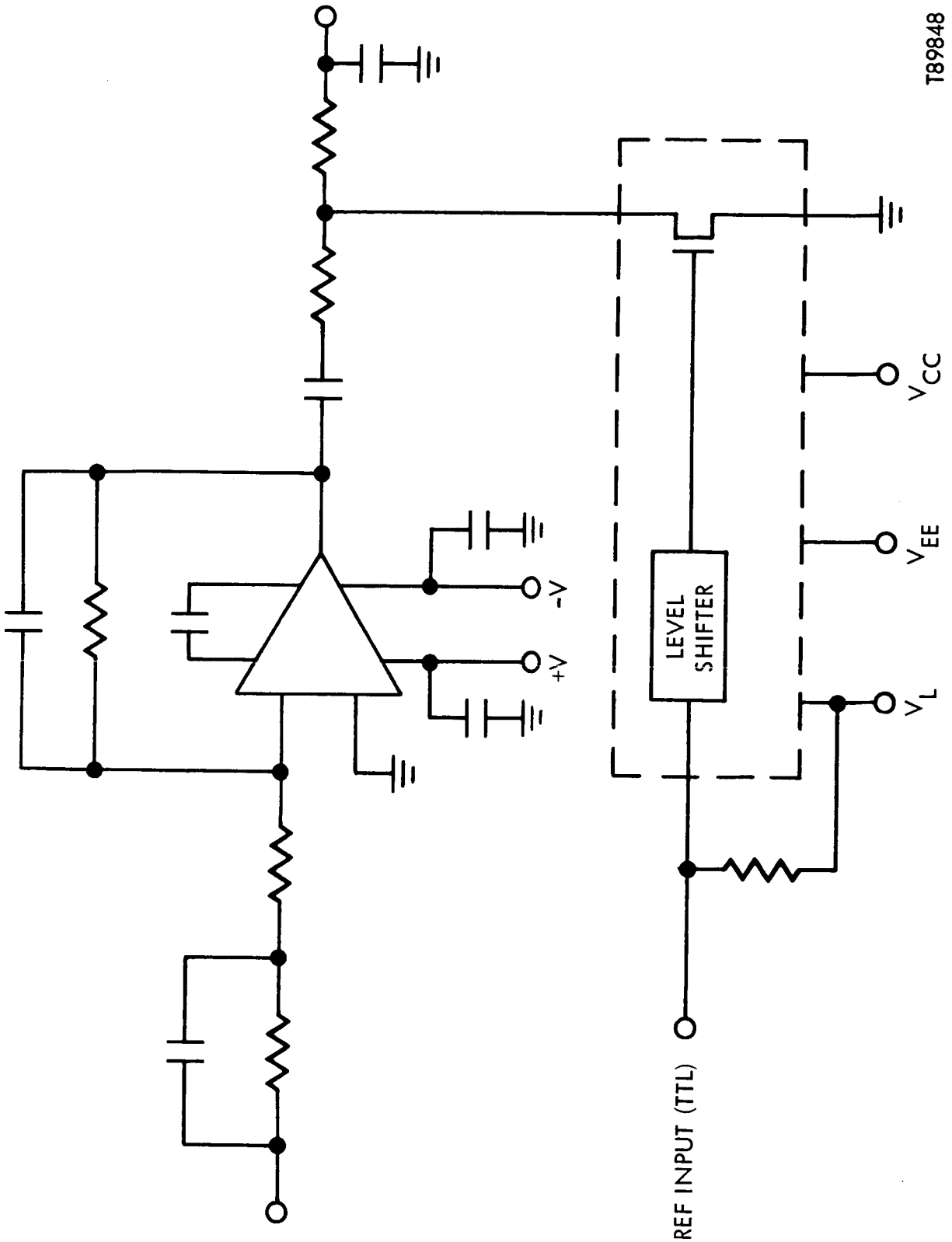

Figure 2. AC Amp & Demod

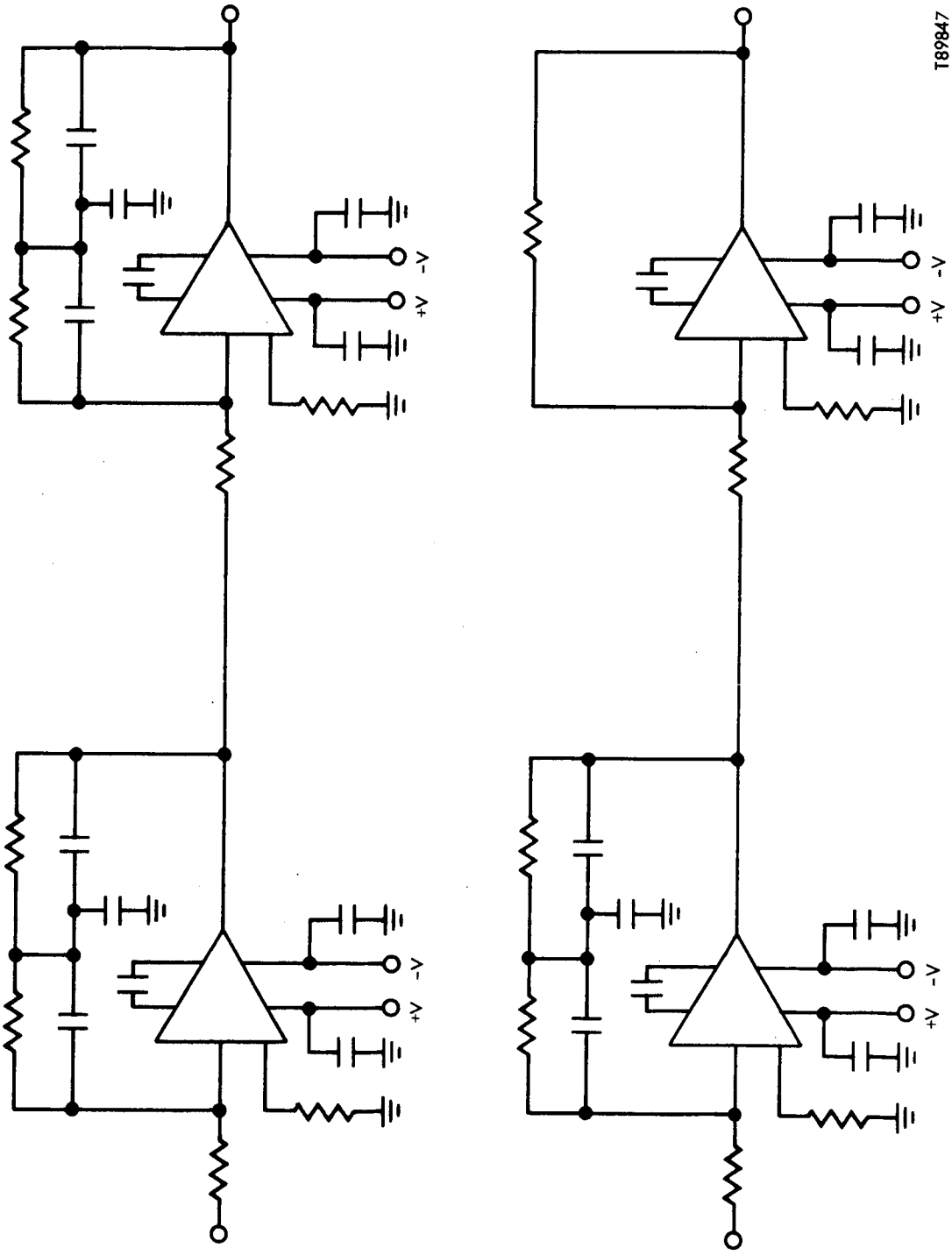

Figure 3. Direct and Cross Axis Compensation

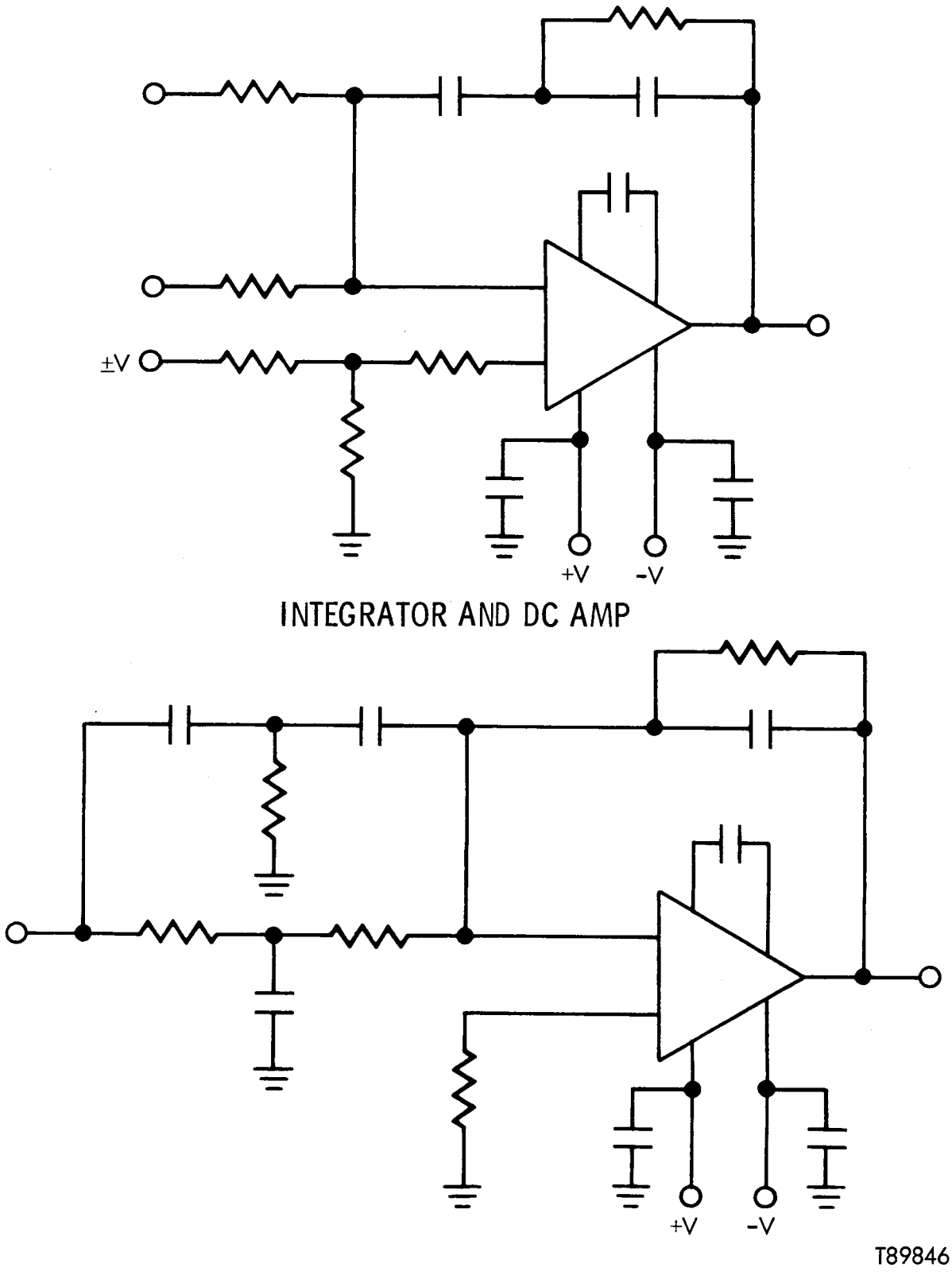

Figure 4. Filter

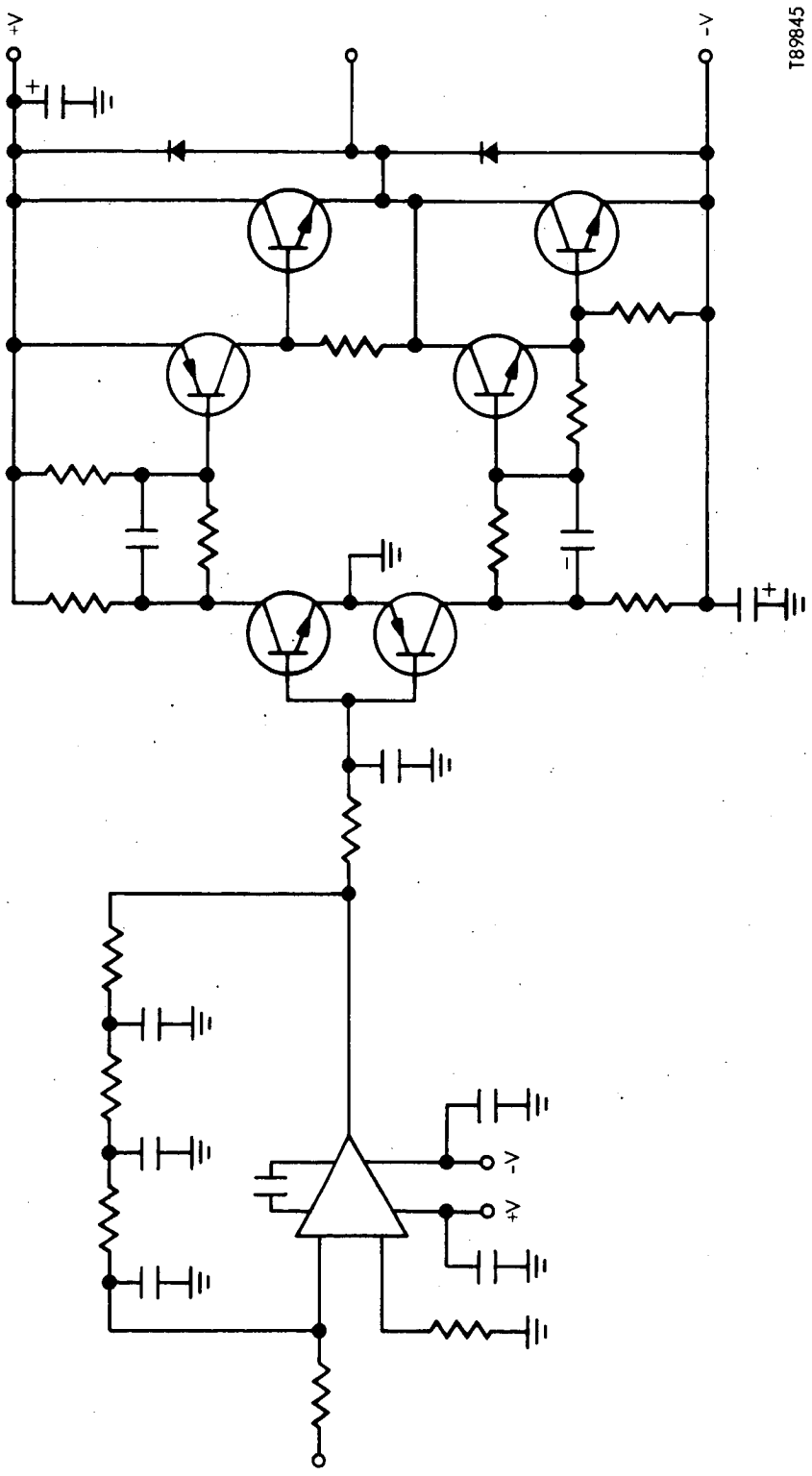

Figure 5. Power Amp

This page intentionally left blank

A3 - FAILURE RATE FOR A/D CONVERTER AND SCALE FACTOR TEMPERATURE COMPENSATION

I. SUMMARY

The failure rate for the A/D converter and temperature compensation is:

$$\text{Failure Rate} = 9.757 \text{ failures}/10^6 \text{ hours total}$$
$$= 3.252 \text{ failures}/10^6 \text{ hours per channel}$$

II. GENERAL DESCRIPTION

The A/D converter and temperature compensation is described for the purpose of failure rate analysis by its parts list. The parts list for the three channel (two gyro) version is in the following pages. As there is one A/D and temperature compensation circuit per axis, the number of parts and the failure rate can be multiplied by two for the six channel (three gyro-redundant axes) configuration.

PARTS LIST

A/D CONVERTER AND TEMPERATURE COMPENSATION

(THREE AXIS VERSION)

Resistor, Composition	1/4 watt 5%	SV92RCR	240
Resistor, Composition	1/2 watt 5%	SV92RCR	35
Resistor, Composition	1 watt 5%	SV92RCR	33
Resistor, Wire Wound	2 watt	SV92RWR	6
Resistor, Wire Wound	5 watt	SV92RWR	4
Resistor, Wire Wound	10 watt	SV92RWR	3
Resistor, Metal Film	1/8 watt 1%	SV92RN	18
Resistor, Metal Film	1/4 watt 1%	SV92RN	3
Resistor, Metal Film	1/2 watt 1%	SV92RN	6
Resistor, Precision	1/8 watt .01%	SV92RBR	8
Resistor, Precision	1/4 watt .01%	SB92RBR	8
Resistor, Precision	1/2 watt .01%	SV92RBR	9
Capacitor, Ceramic	200 pf - .01 μfd	SV90DM29014	35
Capacitor, Ceramic	.01 - .01 μfd	SV90DM29014	30
Capacitor, Teflon	2 μfd	SV90D1	3
Capacitor, Polycarbonate	.022 μfd 100V	SV90D1	28
Capacitor, Solid Tantalum	15 μf 20V	SV90DM39003	30
Diode, Reference	1N4579A	SV1N4565A	1
Diode, Low Leakage	1N3595	SV1N3595	4
Diode, General Purpose	1N5252	SV1N5252	5
Diode, Fast	1N4148	SV1N4148	75
Diode, Fast	1N5417	SV1N5417	24
Transistor, NPN	2N2222A	SV2N2222A	94
Transistor, PNP	2N2907A	SV2N2907A	58
Transistor, PNP	2N5153	SV2N5153	8
Transistor, NPN	2N5154	SV2N5154	9
Transistor, PNP	2N2946A	SV2N2946A	10
Amplifier, I. C.	LM101A	SV99D101A	14

Comparator, I. C.	710	SV99D710	6
Flip Flop, I. C.	SN54L73T	SV99D54	34
Flip Flop, I. C.	SN5473S	SV99D54	3
2 Input Nand Gate, I. C.	SN54L00T	SV99D54	22
3 Input Nand Gate, I. C.	SN54L10T	SV99D54	18
8 Input Nand Gate, I. C.	SN54L30T	SV99D54	6
Magnetic Modulator (Special)			3
5KC Inverter Transformer (Special)			1

III. FAILURE RATE ANALYSIS

The magnetic modulator is a special device that consists of six coils wound on two permaloy 80 cores. In the failure rate analysis, the failure rate for the magnetic modulator will be that of six coils. The failure rate per coil is 0.03 failures/10^6 hrs.

The failure rates are:

Part	Qty	Part Failure Rate (FR/10^6 hrs)	Total Failure Rate (FR/10^6 hrs)
Resistors	373	.003	1.119
Capacitor, Tantalum	30	.020	0.600
Capacitor, Other	96	.004	0.384
Diode	109	.006	0.654
Transistor, Low Power	162	.010	1.620
Transistor, Power	17	.100	1.700
Integrated Circuits	103	.030	3.090
Transformer	1	.050	0.050
Magnetic Modulator	3	.180	0.540
		TOTAL	9.757

The failure rate for the A/D converter and temperature compensation is:

$$\text{Failure Rate} = 9.757 \text{ failure}/10^6 \text{ hours total}$$

$$= 3.252 \text{ failures}/10^6 \text{ hours per channel}$$

A4 - PROBABILITY OF FAILURE FOR TELEDYNE'S STRAPDOWN GYRO

A4.1 - PROBABILITY OF FAILURE FOR THE COILS IN TELEDYNE'S STRAPDOWN GYRO

SUMMARY

Table 1 below lists the sources of failure, the failure rates, and the total failure rates for Teledyne's Strapdown Gyro.

Table 1. Table of Failure Rates for Strapdown Gryo

Source of Failure	Section of Report Where Considered	Operating Failure Rate (10^{-6}/Hr)
Coils	A	0.450
Bearings	B	0.30
Mechanical Parts	C	0.233
Cement Joints	D	0.002
Total		.985

The failure rates are based on handbook values where applicable, test data, and certain assumptions. In all cases the assumptions tend to be conservative and worst case. The rule of thumb has been to assume the one sigma value of a parameter to be equal to or greater than the worst observed value.

The coil and hermetic connector failure rates are based on handbook values. The bearing failure rates are derived from emperical equations using worst case conditions and are higher than comparable handbook values. The flexure and cement failure rates are based on failure tests performed in the laboratory.

It is estimated that the failure rates for a flexure suspended, dry gyro is at least a factor of three better than a floated gyro. This is because there are no bias shifts due to flex lead spring rate changes in a dry gyro, and no fluid associated problems such as bubbles and corrosion. Also the sensitivity to bearing anomolies in a flexure suspended gyro is much less than in a floated gyro.

1. INTRODUCTION

The purpose of this section is to establish the failure rates for the gyro coils in the Teledyne strapdown gyro. For the purpose of establishing a failure rate from existing literature, a study of the characteristics of the gyro coils is made and the gyro coils are compared to coils listed in available literature.

2. SUMMARY

The failure rates for the gyro coils are shown below in Table 1.

Coil	No of Coils	Failure Rate Per Coil (10^6 hrs)	Total Failure Rate (10^6 hrs)
Torquer	4	.03	.120
Pickoff	8	.03	.240
Motor	3	.03	.090
TOTAL	15		.450

Table 1

The failure rates for the gyro coils are derived in paragraph 3 of this section.

The following assumptions are made:

ASSUMPTIONS

A) The types of failures associated with gyro coils are opens and shorts.

B) All of the gyro coils fall into the broad category of motor winding coils.

3. DESCRIPTION AND FAILURE ANALYSIS FOR EACH OF THE THREE TYPES OF COILS

A. General Description

Coil Type	No of Coils	No of Turns (ea)	Wire Size	Resistance (ea)	Insulation Type	Temp Rating	Max Current Subject
Torquer Coil	4	209	30 AWG	8 - 10Ω	MIL-W-583 Class 155	155°C	4.8 amps
P.O. Coil	4 (pri) 4 (sec)	280-281 400-401	40 AWG 40 AWG	16 - 21Ω 27 - 31Ω	MIL-W-583 Class 155	155°C	1.0 ma rms
Motor	3	560	31 AWG	11 - 12Ω	MIL-W-583 Class 155	155°C	0.6 amps rms

B. Failure Analysis - The types of failures associated with gyro coils will be broken down into the classifications of "opens" and "shorts". The types of coils used in the gyro all fall into the broad category of motor winding coils. The mean generic failure rate for the gyro coils is as follows:

COILS MOTOR WINDING

	Mean Generic Failure Rate ($FR/10^6$ hrs)
Short	0.021
Open	0.009
TOTAL	0.030

The gyro coils failure rates are:

Coil Type	No of Coils	F.R. for Open ($FR/10^6$ hrs)	F.R. for Short ($FR/10^6$ hrs)	Total Failure Rate ($FR/10^6$ hrs)
Torquer	4	0.036	0.084	0.120
Pick-Off	8	0.072	0.168	0.240
Motor	3	0.027	0.063	0.090

Temperature - The maximum temperature in any of the gyro coils will be at the torquer coils. The highest temperature of the torquer coils will be $180^{\circ}F$. The lowest temperature on all coils will be $0^{\circ}F$.

A4.2 - PROBABILITY OF FAILURE FOR THE BALL BEARINGS IN THE TELEDYNE STRAPDOWN GYRO

INTRODUCTION

This section analyzes the gyro bearing and derives a failure rate.

All aspects of bearing life are examined, including the environmental considerations that apply to the mission.

SUMMARY

The bearing failure rate is 0.3 failures/10^6 hours and was determined on the following basis:

I. The attached analysis yields a design fatigue life of 235,000 hours, or, .145 failures/10^6 hours/bearing when a total operating time of 2,000 hours is assumed. This failure rate is a "worst case" number and is supported by the following data taken from Reference 5, specifically:

   A. Bearing Generic Failure Rate = .011 failures/10^6 hours

   B. Bearing Hi-Rel Failure Rate for Motor Driven Switches = .11 failures/10^6 hours

II. The bearing failure rate of 0.3 failures/10^6 hours was arrived at after careful consideration of the effects of the following on design fatigue life.

   A. Oil degradation as a function of viscosity, volatility, oxidation, chemical compatibility, heat compatibility, lubricity, and wettability.

B. Ball retainer degradation

C. Load capability

D. Bearing installation

III. The instrument design is unique in that its performance is not affected by such typical bearing problems like "torque jogs" (oil migration in the bearings), axial instability of the of the retainer, or minor changes in preload, all of which are very significant problems for typical "floated " gyro designs.

DESCRIPTION OF BEARING

The bearing design is described in the attached design control drawing 8005434, and consists basically of a modified deep grooved, angular contact R-4 bearing, with a separable inner ring. Bearing tolerances are ABEC 7P with tightened tolerances on ball geometry, and an additional "radial runout" requirement (measured as a functional bearing assembly) which minimizes bearing generated vibration and promotes life.

NEXT ASSY	USED ON

LTR	DESCRIPTION	DATE	APPROVED

APR 23 1971

DESIGN CONTROL DRAWING

UNLESS OTHERWISE SPECIFIED
ALL DIMENSIONS ARE
IN INCHES

XX	± .01
XXX	± .005
FRACTIONS	± 1/64

CONTR NO.

APPROVALS DATE

DRAWN

CHECKED

APPROVAL

APPROVAL

DESIGN ACTIVITY APPROVAL

CONTRACTOR APPROVAL

322

TELEDYNE SYSTEMS CORPORATION
HAWTHORNE, CALIFORNIA

BEARING, BALL -
PRECISION INSTRUMENT

SIZE	CODE IDENT NO.		REV
A	27033	XX8005434	

SCALE DO NOT SCALE DRAWING SHEET 1 of 3

DESCRIPTION

The ball bearing delineated in this document shall be a deep grooved angular contac bearing with a separable inner ring.

BEARING ASSEMBLY

The angle on contact shall be $22^{\circ} \pm 2^{\circ}$ with an axial load of 3.0 ± 0.1 pounds.

Radial runout of the assembled bearing under a 3 pound axial thrust load shall be 50 micro-inches, total indicated reading. Radial runout to be measured at the stationary outside diameter of the outer ring as the inner ring rotates.

RINGS

Inner and outer ring ball raceways to be round within 50 micro-inches.

Cross-race radius of curvature of the inner and outer ring ball raceways shall be 57% of the ball diameter.

BALLS

Ball size to be 3/32 diameter. Size variation in any one bearing to be 5 micro-inches maximum. All balls to be spherical within 5 micro-inches.

Quantity of balls to be per tabulation in figure 1.

MATERIAL

Rings - SAE 52100 Chromium Steel
Balls - SAE 52100 Chromium Steel
Retainer - Phenolic Laminate

LUBRICATION

KRYTOX 143 AC Fluorinated oil

TOLERANCES

ABEC 7P, unless otherwise specified.

PACKAGING

Each bearing shall be individually packed in a sealed plastic envelope with an excess of lubricant.

Each plastic envelope to be sealed in a metal foil envelope per MIL-B-131, Class

Mark each package with the bearing manufacturer's name and part number, lubricant, customer's part number and date of package.

TABULATION	
DASH NO.	QTY OF BALLS
1	7
2	8
3	9

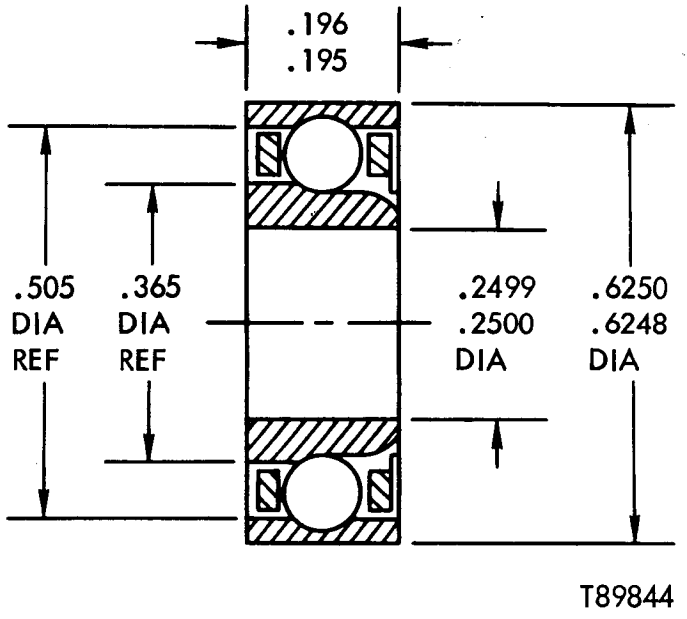

Figure 1.

I. STRAPDOWN GYRO BALL BEARING FAILURE ANALYSIS

The following analysis is based on the following assumptions:

A. A pair of bearings, described in Teledyne Drawing 8005434-2 will be assembled with an axial preload of 2.5 $\pm$ .1 pounds.

B. The bearings will operate in a sealed, clean environment consisting of dry air at a pressure of 6.5 to 8.5 mm Hg absolute over the temperature range of 0°F to 180°F.

C. The non-operating environment will consist of a sealed clean atmosphere of dry air at a pressure of 6.0 to 10.5 mm Hg absolute over the temperature range of -35°F to 285°F.

II. POTENTIAL SOURCES OF BEARING FAILURE

A. Fatigue Life of Bearing Rings and Balls - The "Design Fatigue Life", as defined by the Barden Corporation (Reference 1), is the number of hours a bearing will operate, at a given speed and load, before the first evidence of spalling or flaking of raceways or balls becomes apparent. It is considered to be the life which will be exceeded by 90% of a group of identical bearings operating under identical speed/load conditions. "Mean Fatigue Life" is approximately five times the "Design Fatigue Life". For purposes of this analysis, the worst case, or "Design Fatigue Life" will be considered.

Since the rotating shaft and sensitive element of the gyro is very well balanced dynamically (less than 1.0 mg - cm), the spin frequency vibration to the bearings is so small that their will be no effect on design fatigue life.

Then for the design configuration shown, the radial loading of the bearings will be as follows:

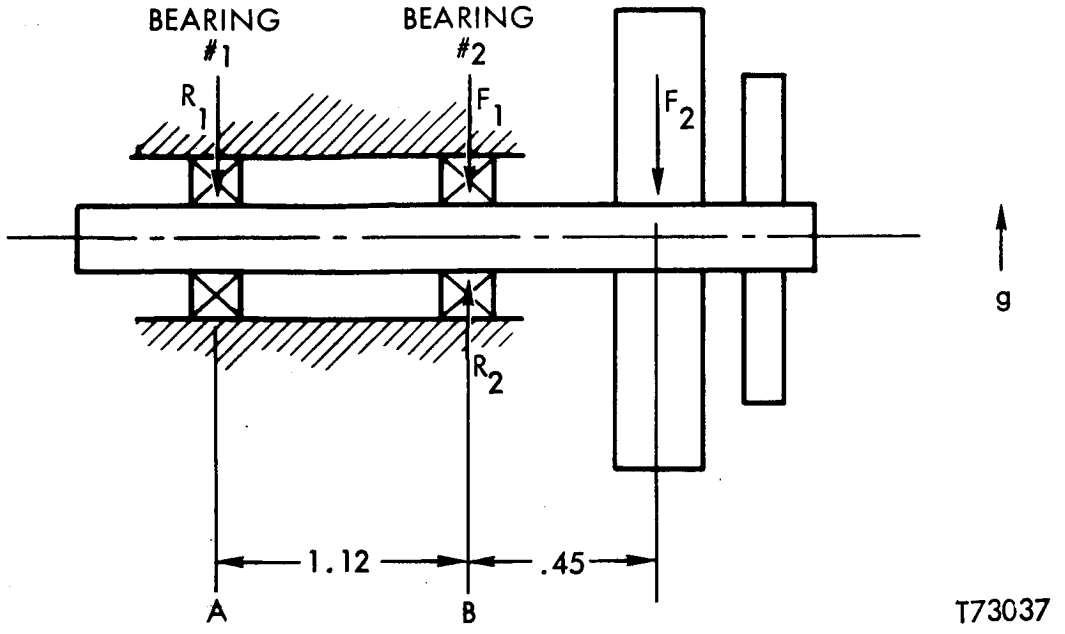

F_1 = Radial force due to non-gimballed rotating parts - 56 gms.

F_2 = Radial force due to gimballed rotor - 261 gms.

R_1 = Force exerted by bearing #1

R_2 = Force exerted by beqring #2

$\Sigma M_B = 0 = 261\ (.45) - R_1\ (1.12)$

$\therefore R_1 = 104.7$ gms = .231 pounds

$\therefore R_2 = 104.7 + 56 + 261 = 422$ gms = .93 pounds

Since bearing #2 is exposed to the larger load, it will be used for the analysis.

Then in accordance with Reference 1, the design fatigue life will be

$$L_D = 500 \left(\frac{C_S}{P}\right)^3 = 500 \left[\frac{C_S}{X\left(R_h + 1.2\, R_s\right) + YT}\right]^3 .$$

where L_D = Design fatigue life in hours

C_S = Dynamic radial load rating = 29 pounds

R_h = Radial load (case fixed) = .93 pounds

R_s = Radial load (dynamic unbalance) = 0

X = From chart A for 22° brg. = .42

T = Thrust load (preload + rotor wt.) = 3.22 pounds

and Y = From chart B for $\frac{T}{ZD^2} = 45.8$ = 1.04

where $\frac{T}{ZD^2} = \frac{3.22}{.0703} = 45.8$

Evaluating,

$$L_D = 500 \left[\frac{29}{.42\ (.93 + 0) + 1.04\ (3.22)}\right]^3$$

L_D = 235,000 hours (worst case design fatigue life)

Note: Mean Design Life (as explained earlier) = 5 (235,000) = 1,175,000 hrs.

Then the failure rate can be calculated as follows. Using the calculated values for the 90% probable fatigue life and the 50% probable fatigue life, the one sigma value can be calculated - assuming a normal distribution

$$L_\sigma = \frac{L_M - L_{90}}{1.3}$$

Where

L_M = Mean fatigue life (50%)

= 1.175×10^6 hours

L_{90} = 90% prob. fatigue life

= 2.35×10^5 hours

L_σ = One sigma value of fatigue life distribution

= 7.25×10^5 hours

Using these values of L_M and L_σ the probability of bearing failure in the first 2000 hours of operation can be calculated taking the integral of the fatigue life distribution between zero and 2000 as follows:

$$P(2000) = \frac{1}{P_\sigma \sqrt{2\pi}} \int_0^{2000} e - \frac{(P - P_M)^2}{P_\sigma^2} \, dP$$

For convenience in evaluating this integral substitute the following

$$u = \frac{P - P_M}{P_\sigma}$$

$$du = - \frac{dP}{P_\sigma}$$

and the new limits become

$$u_{lower} = \frac{P_M}{P_\sigma}$$

$$= - 1.62$$

$$U_{upper} = \frac{P_M}{P_\sigma} + \frac{2,000}{P_\sigma}$$

$$= - 1.62 + .00275$$

This integral is easily evaluated from Table 26.1 of Reference 4 by extrapolating between 1.62 and 1.64 which gives

$$P(2000) = 2.9 \times 10^{-4}$$

The probability between these limits is approximately linear so a failure rate for the first 2,000 hours of bearing operating can be established by dividing P (2,000) by 2,000 hours

$$F_R = \frac{P(2000)}{2000}$$

$$= .145 \times 10^{-6} \text{ failures/hour}$$

Note: This number is a worst case consideration and assumes all operation in a 1 g field.

B. Oil Degradation - The following discussion is based on data supplied by E.I. DuPont (Reference 2) and heat compatability tests performed at Teledyne Systems (Reference 3).

The bearing oil used is E.I. DuPont's "Krytox 143 AC Fluorinated Oil". It was selected after careful examination of the following major oil properties, all of which directly contribute to oil life.

1. Heat Compatibility - Krytox 143 AC is suitable for use with the 52100 steel, used in the bearing, at temperatures up to 550°F. This has been substantiated, in part, by heat compatibility tests run at Teledyne Systems (Reference 3) in which exposure for in excess of 400 hours at 325°F showed no detectable change in oil characteristics.

2. Lubricity, Wettability - "Four-Ball Wear Tests" have demonstrated superior load carrying ability and lubricity of Krytox 143 AC oil when compared to various other oils (Reference 2, pages 4 - 7). In addition, the low surface tension of the oil promotes wetting of the surface and aids its lubricating properties. The oil is not as susceptible to migration as silicone oils and once applied to a surface, resist removal, as they are relatively insoluble in most solvents (Reference 2, page 12).

3. Oxidation, Chemical Inertness - Krytox oils are not subject to oxidation below their thermal decomposition temperatures, which has been found to be above 670°F. The oil is essentially chemically inert at temperatures below 550°F (Reference 2, page 3).

4. Viscosity, Volatility - The viscosity of Krytox 143 AC oil is approximately 50% higher (26 centistokes at 210°F) than Kendall KG-80 oil (15.7 centistokes at 210°F) which, to date, is an accepted gyro spin bearing oil used in inertial quality gyros. This increase in viscosity results in increased load carrying ability, resulting in less wear rate and subsequent increase in life of the bearing. Change in viscosity with temperature is comparable to that of Kendall KG-80 oil.

The volatility of Krytox 143 AC is also less than Kendall KG-80 oil. Since the gyro is evacuated and sealed with an absolute pressure of 10 mm Hg at 250°F, the resulting pressure variation as a function of temperature change, will be as listed below:

Temperature (°F)	Non-Operating		Operating	
	-35	285	0	140
Atmospheric pressure seen by bearings (mm Hg absolute)	6.0	10.5	6.5	8.5

The vapor pressure characteristics of the oils discussed are:

Oil	*Vapor Pressure @ 400°F (mm Hg. absolute)
Krytox 143 AC	0.3
Kendall KG-80	0.6

* Data on vapor pressure of Krytox 143 AC at temperatures less than 400°F was not available.

Examination of the above tabular data shows that the vapor pressure of Krytox 143 AC oil is far below the pressures seen by the bearings at comparable temperatures. A lack of vapor pressure data at lower temperatures prevents a direct comparison of pressures, but if the instrument were to be heated to 400°F, the pressure seen by the bearing oil would be 12.7 mm Hg absolute compared to a vapor pressure of only 0.3 mm Hg for Krytox 143 AC.

C. Ball Retainer Degradation - The material of the ball retainer is linen base phenolic. Tests run at Teledyne Systems (Reference 3) revealed that the retainers discolored when exposed to 300°F for 400 hours, but no physical degradation was observed visually and no physical distortion was detectable. Bearings with these retainers are presently operating in an instrument after having been exposed to 300 - 325°F for in excess of 400 hours. Discussions with the Barden Corporation concerning the optimum retainer material for the current application resulted in the conclusion and recommendation, by Barden, that phenolic retainers should be used as they appear to be the best overall material for the application.

D. Load Capability - Conversations with the Barden Corporation (H. Williams) have established that the dynamic radial load capability of the bearing is in excess of 112 pounds (see "attached" statement from Barden Corporation, Reference 6) and that no bearing damage will be incurred in the form of changes in vibration or life expectancy as a result of the shock loading requirements of the current application.

E. Bearing Installation - Since life and bearing performance are very dependent on preload and alignment, considerable care is exercised, during installation, to assure that the proper preload and alignment are achieved.

The bearings are installed in the case assembly with the use of a high temperature epoxy adhesive. Preload is achieved by loading the inner rings axially with a known "dead weight" force and simultaneously curing the adhesive. The assembly is cured with the outer rings rotating slowly to allow proper ball distribution, and aid in achieving alignment. Alignment is achieved through the use of precision parts and tooling to achieve face runout relative to spin axis of .0002 maximum for any one ring. Curing is done at a temperature which assures thermal stabilization of all parts prior to cement hardening to assure correct preload after cure. A post

cure minimizes any potential possibility of creep with time/temperature which would tend to change preload. Further, all bearing inner ring joints are subjected to proof loads in excess of those seen during the mission, to assure the structural integrity of the bearing installation.

III. REFERENCES

1. Barden Corporation, Engineering Catalog G-3, pages 22, 23, 60 - 63

2. E. I. DuPont De Nemours and Company, Petroleum Chemicals Division, Technical Bulletin #L-5 (Krytox Fluorinated Lubricants)

3. J. Ritter, "Heat Compatibility of Materials in the Teledyne Strapdown Gyro", Teledyne Systems Company

4. M. Abramowitz and I. A. Stegun, "Handbook of Mathematical Functions", National Bureau of Standards

5. Report T-70-48891-007, "Handbook of Piece Part Failure Rates (Long Life Space Vehicle Investigations)", dated 22 June 1970.

A4.3 - PROBABILITY OF FAILURE OF THE MECHANICAL PARTS IN TELEDYNE'S STRAPDOWN GYRO

INTRODUCTION

The purpose of this report is to obtain a failure rate or probability of failure of the mechanical parts in the gyro. The results of this report will be used to help establish a failure rate for the gyro.

SUMMARY

The significant failure rates for the mechanical elements in the gyro are summarized in the following table:

Element Description	Number of Elements Per Gyro	Failure Rate of a Single Element (failures/hr)	Total Failure Rate (failures/hr)
Gyro Flexure	12	$.021 \times 10^{-6}$	$.175 \times 10^{-6}$
Gimbal Pin Joint	12	$.007 \times 10^{-6}$	$.058 \times 10^{-6}$
	TOTAL		$.233 \times 10^{-6}$

The flexure failure rate is based on flexure buckling as measured in tests, assuming a normal distribution to calculate the probability of failure at low stress levels. The gimbal pin joint is based on calculated stress using worst case approximations, and also assumes a normal distribution.

The maximum load is assumed to be 120 g's.

None of the other gyro stresses are large enough to warrant calculating a failure probability.

Section 1 contains the description and failure analysis of the gyro flexure.

Section 2 contains the description and failure analysis of the gimbal pin joint.

1.0 DESCRIPTION AND PROBABILITY OF FAILURE OF THE GYRO FLEXURES

The 12 flexures used in this gyro are each made of two crossed hinges as shown schematically in Figure 1 below.

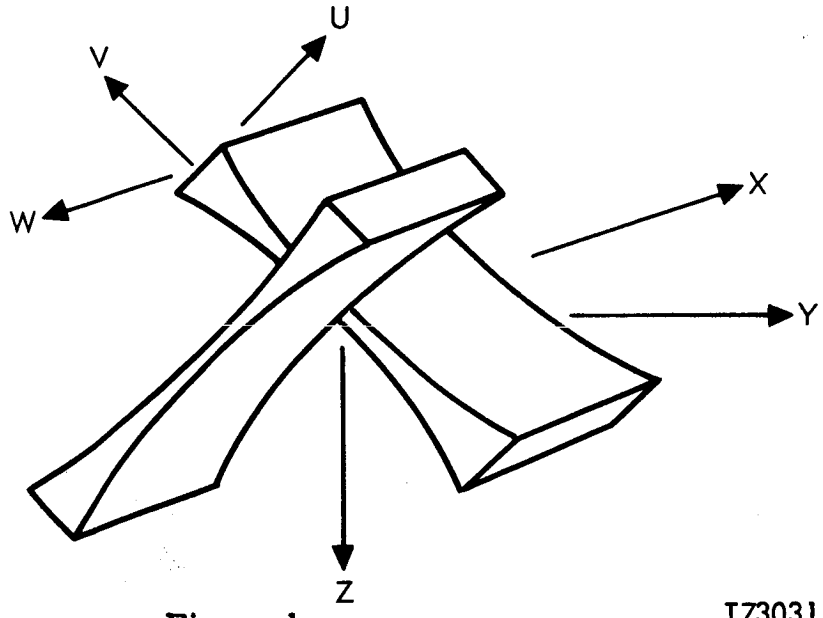

Figure 1 T73031

Each flexure is an integral part - that is, it is made from one piece of metal with no bond joints to connect the hinges to the body of the flexure. The metal used is high strength maraging steel - specifically, VasoMax 300 CVM. This material is solution annealed at 1500°F and aged at 900°F to obtain an ultimate tensile strength of 295 K psi, a yield of 285 K psi, and a proportional limit of 270 K psi.

Analysis indicates that the maximum load stress is induced in the flexure from radial g loads on the gyro; this stress is 570 psi/g. This would be a stress of 68 K psi for the 120 g landing shock (see reference 2). This is approximately 25% of the proprotional limit of 270 K psi.

Analysis also indicates that buckling from axial loading may be the weakest failure mode, and testing has proved this to be the case. The one flexure tested failed in buckling at 46 pounds. This is equivalent to 500 g's when assembled in the gyro. The sample of one is insufficient test data to establish a mean and one sigma value for the failure load. However, because of the consistency of metals and the tight dimensional control on the part, it is felt that a failure load of 40 lbs is a conservative estimate for the mean and 8 lbs as the one sigma value. Assuming a normal distribution, the probability of failure between 0 and 120 g's (or 0 and 11 lbs for a single flexure) is calculated by taking the integral of the normal distribution function between 0 and 11 lbs.

$$p\,(120\ g) = \frac{1}{F_\sigma \sqrt{2\pi}} \int_0^{11} e - \frac{(F - F_M)^2}{F_\sigma^2} \, dF$$

where F_M = mean failure load
= 40 lbs.
F_σ = one sigma value
= 8 lbs.

For convenience in evaluating this integral, make the following substitution:

$$u = \frac{F - F_M}{F_\sigma}$$

$$du = - \frac{dF}{F_\sigma}$$

The limits become:

$$u_{\text{lower}} = -\frac{F_M}{F_\sigma} = -5$$

$$u_{\text{upper}} = -\frac{11 - F_M}{F_\sigma} = -3.625$$

This integral is easily evaluated using Table 26.1 of reference 1 , and the probability of failure of a single flexure at g levels of 120 and less is

$$P\,(120\ g) = 1.45 \times 10^{-4}$$

and the failure rate is

$$F_R = \frac{P\,(120\ g)}{9968}$$

$$= .0146 \times 10^{-6}/\text{hr}$$

The total failure rate for the 12 flexures is

$$F_R\,(12) = .175 \times 10^{-6}/\text{hr}$$

2.0 DESCRIPTION AND PROBABILITY OF FAILURE OF THE GIMBAL PIN JOINT

The gimbals are each made in two halves that are connected by .046 inch diameter pins. The pin joint is shown schematically in Figure 2 below.

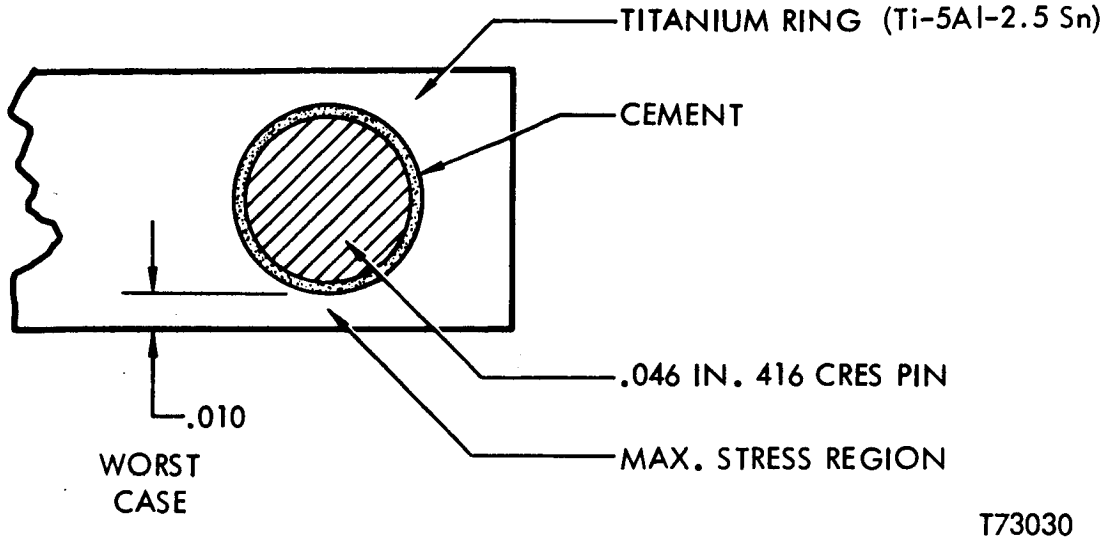

T73030

For a worst case approximation assume that one side of the ring adjacent to the hole carries the entire load from that pin (.092 lb.). The stress is then

$$S = \frac{.092}{.010 \times .190}$$

$$= 48 \text{ psi/g}$$

The maximum g load will be for the landing shock which will be 120 g's transmitted to the gyro. The corresponding maximum stress will be

$$S_{max} = 5.750\text{k psi @ 120 g}$$

The tensile strength of the Ti-5AL-2.5 SN gimbal alloy is 125 K psi; if 100 K psi is assumed as the mean value and 25 K psi as the one sigma

value with normal distribution, the the probability of failure at 5.75 K psi is

$$P(5.75) = \frac{1}{S_\sigma \sqrt{2\pi}} \int_0^{5.75} e^{-\frac{(S - S_M)^2}{S_\sigma^2}} \, dS$$

where S_M = mean failure stress
= 100 K psi
S_σ = 25 K psi

For the convenience of evaluating this integral make the following substitutions

$$u = \frac{S - S_M}{S_\sigma}$$

$$du = \frac{dS}{S_\sigma}$$

The limits become

$$u_{lower} = -\frac{S_M}{S_\sigma}$$
$$= -4.0$$

$$u_{upper} = 2 + \frac{5.75 - S_M}{S_\sigma}$$
$$-4.0 + .23$$

This is evaluated from Table 26.1 of reference 1 to be

$$P(5.75) = 4.8 \times 10^{-5}$$

This probability of failure gives a failure rate for each of the 12 gimbal pin joints of

$$F_R(1) = \frac{P(5.75)}{9968}$$

$$= .0048 \times 10^{-6}/\text{hr}$$

The failure rate for any one of the 12 pin joints is

$$F_R(12) = .058 \times 10^{-6}/\text{hr}$$

REFERENCES

M. Abramowitz and I. A. Stegun, Handbook of Mathematical Functions, National Bureau of Standards, 1964

A4.4 - PROBABILITY OF FAILURE OF THE EPOXY CEMENT JOINTS & BRAZED JOINTS IN TELEDYNE'S STRAPDOWN GYRO

INTRODUCTION

There are many papers on many aspects of the epoxy cements, which include papers on tensile strengths, shear strengths, stress distributions under various loads, joint configurations, high and low temperature characteristics, etc. However, a literature search did not produce any papers which considered applicable failure probabilities at low stress levels. It is necessary to have such probabilities to generate a failure rate for the strapdown gyro.

The purpose of this report, then is to establish probabilities of failure of the epoxy cement joints in Teledyne's strapdown gyro as a function of stress.

SUMMARY

The probability of failure of any one of the many cement joints in the IMU gyro is less than 2×10^{-5}. This produces a failure rate of less than 2×10^{-9}/hr when divided by a 10,000 hr mission time. This number is very conservative. This failure rate value takes into account maximum load stresses and temperature effects. The failure probability for the epoxy joints is obtained by assuming a normal distribution of the failure stress and taking failure test data and extrapolating to the lower stress levels that the gyro cement joints experience in the mission environment.

It is also concluded that any long term creep between parts joined by epoxy cement is less than one microinch provided the following conditions are met:

A. The cement used is Ablestk 185-3 or the equivalent.

B. The cure and post cure temperatures and times are correct.

C. The maximum service temperature is at least 20°F lower than the post cure temperature.

D. The maximum service stress is 1.0 K psi or less.

Tests were performed on each of the three types of epoxy joints in the gyro so that failure stress levels would be available.

Table 1 presents the calculated failure probabilities for each of the three types of test joint - aluminum to aluminum lap-shear, cres pin to titanium hole, and titanium to titanium lap-shear.

Table 2 summarizes the failure tests.

Figure 1 is a graph of failure probability versus stress for the titanium to titanium lap-shear at low stress levels.

Part 2 is a brief explanation of the normal distribution equations, so the tabulated values listed in Table 2 can be easily authenticated from a handbook.

Part 3 is a discussion justifying the normal distribution assumption.

Part 4 is a brief discussion of the temperature effects on the cement joints, which concludes that the temperature profile seen by the gyro during the mission will not significantly affect the failure probabilities.

1. TABLES AND FIGURES

Table 1. Probability of Failure From Stress of Epoxy Cement Joints

		Lap-Shear A_L to A_L	416 Pin In Hole of Ti	Lap-Shear Ti to Ti
Mean Failure Stress-PSI Tested Value		3150	3570	2760
Mean Deviation - PSI Tested Value		350	160	380
$\frac{S_m - S_o}{S_\sigma}$	$P(S_o)$	S_o	S_o	S_o
Mean Tested Value	.500	3150	3570	2760
1σ Calculated	.159	2800	3410	2380
2σ Calculated	$.23 \times 15^{-1}$	2450	3250	2000
3σ Calculated	$.135 \times 15^{-2}$	2100	3090	1620
4σ Calculated	$.317 \times 15^{-4}$	1750	2930	1240
5σ Calculated	$.287 \times 10^{-6}$	1400	2770	860
6σ Calculated	$.10 \times 10^{-8}$	1050	2610	480
7σ Calculated	$.128 \times 10^{-11}$	700	2450	100

$P(S_o)$, S_m, S_o and S are defined in Section 4.

Table 2. Summary of Epoxy Cement Joint Failure Tests

Description of Tests	Cement Type	Cure Temp	Post-Cure Temp	Mean Failure Stress	Mean Deviation
Lap-Shear Aluminum to Aluminum	Ablestik 185-3	165°F 2 Hrs	325°F 4 Hrs	3128 PSI	348 PSI
416 Cres Pin in Hole of Titanium		165°F 2 Hrs	325°F 4 Hrs	3570 PSI	160 PSI
Lap-Shear Titanium to Titanium		165°F 2 Hrs	325°F 4 Hrs	2765 PSI	382 PSI

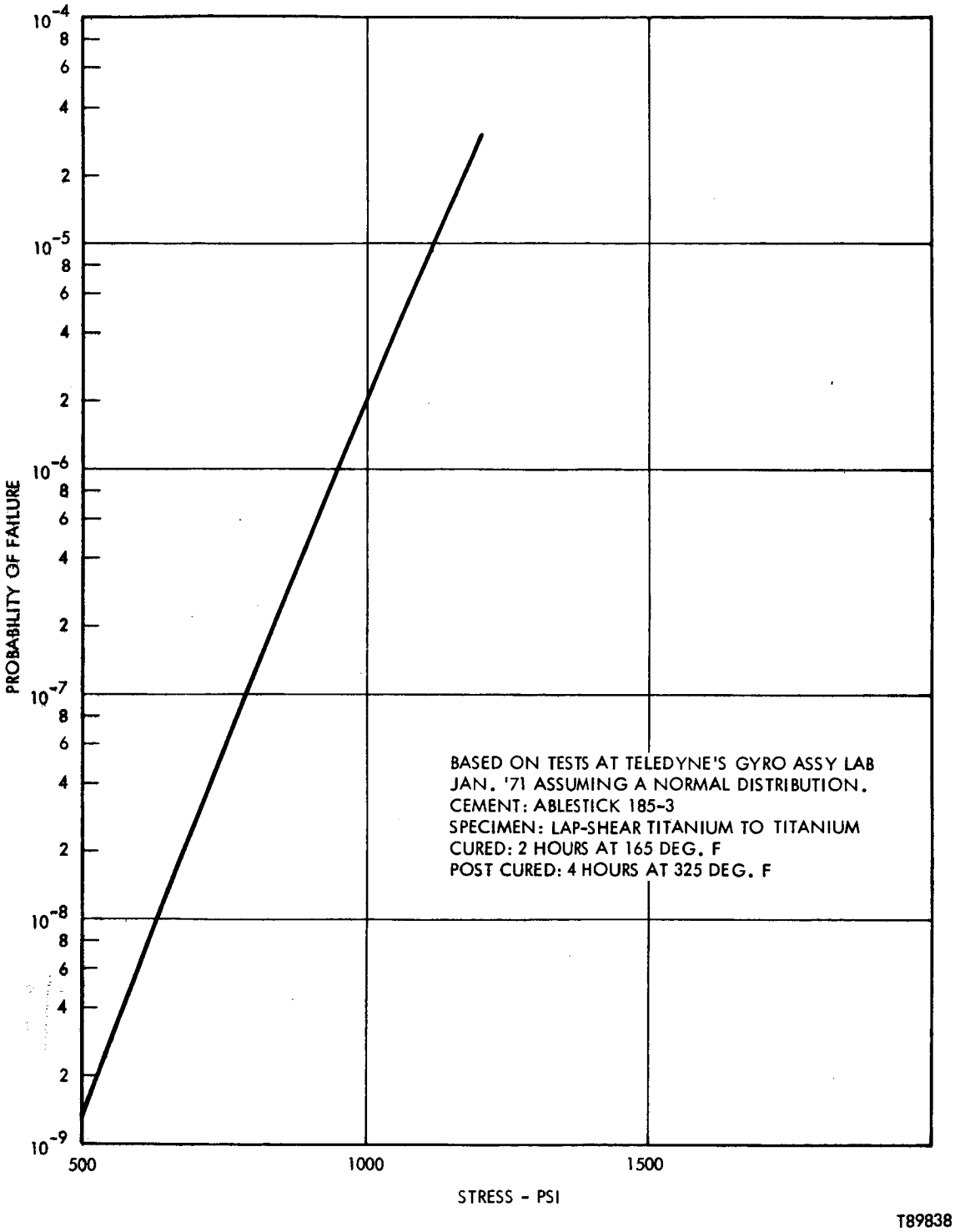

Probability of Failure vs. Stress Level for Epoxy Cement Joints

2. CALCULATING PROBABILITIES OF FAILURE ASSUMING A NORMAL DISTRIBUTION

If a Gaussian or normal distribution is assumed for the failure stress then a probability of failure can be calculated for low stress levels based on test data at high stress levels. This is a practical means of obtaining failure probabilities for low stress levels.

If the failure stress does have a normal distribution then the following applies:

The normal distribution or density function of S (stress) is:

$$P(S) = \frac{1}{S_\sigma \sqrt{2\pi}} \quad \epsilon - \frac{(S - S_m)^2}{2 S_\sigma^2}$$

Where S_m is the mean failure stress and is defined by

$$S_m = \int_{-\infty}^{\infty} S\, p(S)\, dS$$

and S_σ is the mean deviation stress and is defined by:

$$S_\sigma^2 = \int_{-\infty}^{\infty} (S - S_m)^2\, p(S)\, dS$$

and $$1 = \int_{-\infty}^{\infty} p(S)\, dS$$

$p(S)\,\Delta S$ is the probability of failure of a cement joint at a stress level throughout the range $S \pm 1/2\,\Delta S$.

The normal distribution function is

$$P(S_0) = \int_{-\infty}^{S_0} p(S)\, dS$$

$P(S_0)$ is the probability of failure of a cement joint with a stress level of S_0 or less.

For purposes of calculating $P(S_0)$ normalize S by letting

$$x = \frac{S_m - S_0}{S_\sigma}$$

Then the values of $P(S_0)$ are conveniently looked up in handbook tables.

Table 1 presents the probabilities of failure of three types of cement joints. The values of S_m and S_σ used for calculating these probabilities are the results of failure tests which are summarized in Table 2. The probabilities in Table 1 were taken from Tables 26.1 and 26.2 of Reference 1.

3. JUSTIFICATION OF THE NORMAL DISTRIBUTION ASSUMPTION

The stress level at which any given epoxy cement joint fails is determined by many factors. Some of these factors are only partially controllable, such as wetability of bonding surface, cement honogeneity, minor surface irregularities, local variations of cement thickness, etc.

If it is assumed that many of these factors which determine the cement failure stress vary in a random manner, then by applying the central limit theorem(see Reference 2) it can be proved that the failure stress level has a normal distribution for any given set of circumstances (such as joint configuration).

Each of the factors which determine the failure stress has its own distribution curve. Most of these curves tend to be a normal distribution but many of then are truncated to zero below some minimum level by the many systematic steps involved in producing a cement joint.

Some of these systematic steps are:

A. Processes used during the cementing operation to guarantee minimum levels of surface wetability.

B. Acceptance tests to guarantee minimum levels of cement homogeneity.

C. Inspection and tests of cement joints after curing.

The net effect of these systematic steps then is to cause the distribution curve of the cement joint failure stress to depart from a normal distribution curve by having a lower probability of failure at the lower stress levels and to be truncated to zero probability at some stress level.

Thus, the assumption of a normal distribution for the cement joint failure stress is a worst case or pessimistic approximation.

4. TEMPERATURE EFFECTS

There are three kinds of temperature effects to be considered as having some effect on the probability of failure of cement joints - (A) differential expansion from temperature gradients causing stresses in the cement joints; (B) differential expansion from a mismatch of α's (the coefficients of expansion) of the materials that are joined by cement, and (C) the nominal temperature changing the strength of the cement. These three points are discussed below.

A. In order to minimize temperature gradients a detailed heat transfer model of this gyro (shown in Section X of this report) was utilized so that various design choices could be evaluated for their effect on temperature gradients. The primary source of temperature gradients in the gyro is the torquer coil, and the torquer coil housing has been designed with a large heat capacity and low thermal resistance to the outside. The large heat capacity reduces temperature gradients from short term high rates, and the low resistance reduces temperature gradients from steady state rates.

The cement joints that experience high load stresses (flexure joints and gimbal pin joints) are in very low heat flow paths, and as a result the temperature gradients experienced by these joints are very low and will be of little consequence to the failure probability.

B. The stresses induced by the mismatch of α's (the coefficients of expansion) is reduced by matching α's as well as possible. The design for this gyro matches α's to below $0.2 \times 10^{-6}/°F$ in every joint.

The cement joints that experience high load stresses (flexure joints and gimbal pins) have their coefficients of expansion perfectly matched by handbook values. Thus, their actual mismatch will be within $0.1 \times 10^{-6}/°F$ and any resulting differential expansion will have little effect on the probability of failure of these joints.

C. It was originally intended to include the nominal temperature effect on cement strength in the failure model of the cement joint by making the failure probability a joint density function of stress and temperature. However, study shows that because of the slight effects at temperatures up to 300°F and the low operating temperature of the gyro (150°F), it is not necessary to include temperature in the failure model.

The AbleStick 185-3 cement that is used in this gyro is post cured at 325°F and has a lap-shear strength of 2800 psi or better at room temperature. Between 0°F and 200°F there is only a few percent change in this 2800 psi strength. At 300°F this strength drops to 2400 psi, but there is no measurable long term creep at this temperature and stress levels of 1,000 psi (see Reference 3).

Preliminary analysis indicates that the temperature extremes that will be seen by the gyro are 0°F to 180°F, and that the gyro temperature at the time of landing (the highest shock load) will be about 150°F.

The conclusion is that the temperatures to be experienced by the gyro mission should have no significant effect on the probability of failure of the cement joints.

5. REFERENCES

1. M. Abramowitz and I. A. Stegun, Handbook of Mathematical Functions, National Bureau of Standards, 1964

2. M. Cramer, The Elements of Probability Theory, John Wiley and Sons, New York, 1955

This page intentionally left blank

A5 - CIRCUIT CHARACTERISTICS OF THE A/D CONVERTER

An error model for the ADC is presented in Figure AD-12. Based on this model, equations for the total output error are derived as a general case. Each circuit is then analyzed in detail for its various contributions to the general error.

The output due to $E_1 = E_3$

$$\Sigma E_3 = \Sigma E_1 S_{y0} + b_0 + S_0 + b_1 + S_1 + E_1 S_{y1} + b_2 + S_2 + E_1 S_{y2}$$

$$+ b_3 + S_3 + E_1 Sy_3 + E_1$$

$$\Sigma E_3 = \Sigma[E_1 \underbrace{(S_{y0} S_{y1} S_{y2} S_{y3})}_{N_1} + \underbrace{(b_0 + b_1 + b_2 + b_3 + S_0 + S_1 + S_2 + S_3) + E_1}_{L}]$$

Output due to $E_2 = E_4$

$$\Sigma E_4 = \Sigma[E_2 \underbrace{(S_{y1} S_{y2} S_{y3})}_{N_2} + \underbrace{(b_0 + b_1 + b_2 + b_3 + S_0 + S_1 + S_2 + S_3) + E_2}_{L}]$$

The average output

$$\Sigma[E_3 + (-E_4)]/2 = \Sigma[E_1 (N_1) + L + E_1 - E_2 (N_2) + (L) - E_2]/2$$

For the gyro inputs; $E_1 = -E_2$

$$\Sigma[E_3 + E_4]/2 = \Sigma[E_1(N_1) + (L) + E_1 + E_1 (N_2) - (L) + E_1]/2$$

$$= \Sigma[E_1 (N_1) + E_1 (N_2) + 2E_1]/2$$

$$= \Sigma[E_1 (N_1 N_2) + 2E_1]/2$$

$$= \Sigma[E_1 (N_1 N_2)]/2 + \Sigma 2E_1/2$$

$$E_T = \Sigma E_1 (N_1 N_2)/2 + \Sigma E_1 \qquad (1)$$

Total Output Error

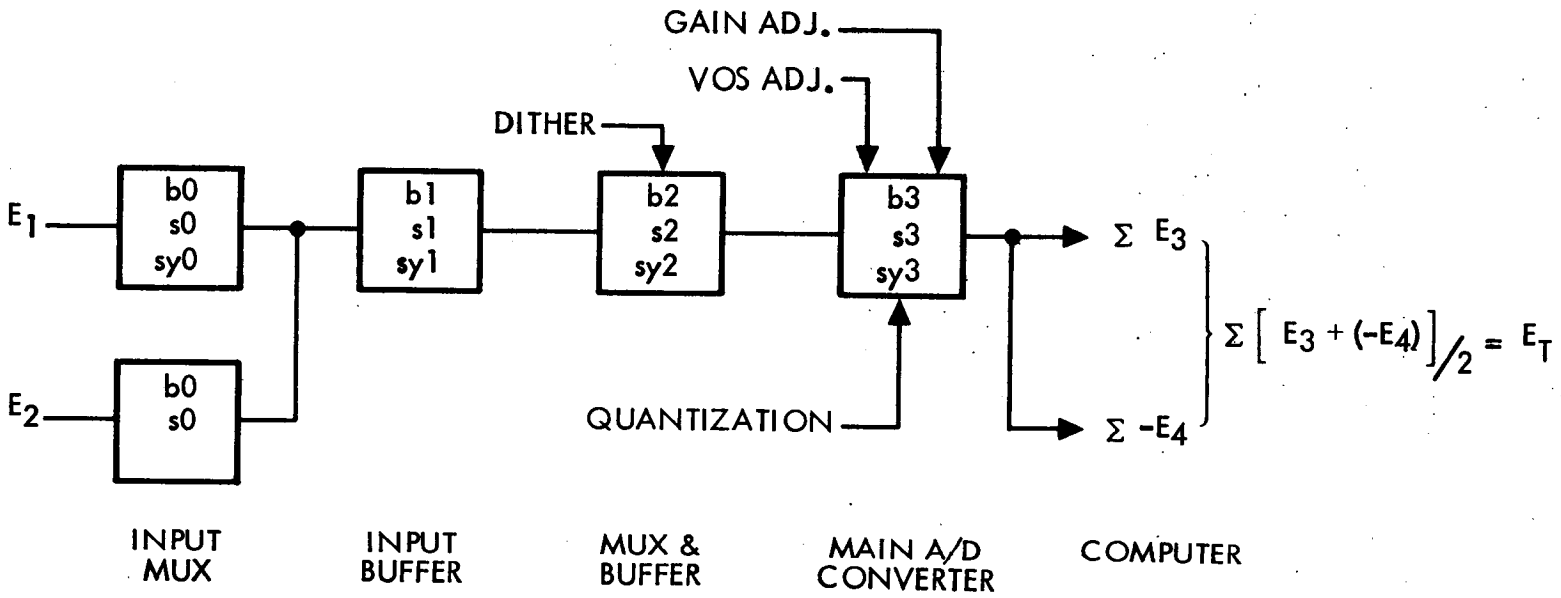

DEFINITIONS:

1. E_1 & E_2 ARE IDEAL INPUT VOLTAGES
2. b (x)'s ARE OFFSET VOLTAGE ERRORS INDEPENDENT OF INPUT SIGNAL
3. s (x)'s ARE LINEAR SCALE FACTOR ERRORS PROPORTIONAL TO INPUT VOLTAGE
4. sy (x)'s ARE NON-LINEAR ERRORS WHICH ARE DEPENDENT UPON INPUT VOLTAGE AND SCALE FACTOR CHANGE AFTER CALIBRATION
5. GAIN ADJUSTMENT REMOVES INITIAL SCALE FACTOR ERRORS
6. Vos ADJUSTMENT REMOVES INITIAL OFFSET VOLTAGE ERRORS
7. DITHER MINIMIZES QUANTIZATION ERROR BY COMPUTER AVERAGING
8. COMPUTER AVERAGING MINIMIZES LINEAR OFFSET VOLTAGE ERROR VARIATIONS

T89938

Figure AD-12. Gyro and Accelerometer ADC Error Diagram

The total output then consists of the desired output, E_1, and the error term $E_1 (N_1 N_2)/2$. The error term is made up of bias errors and scale factor errors which can not be removed by calibration. Also, variations of these errors due to temperature and aging after calibration. The errors will be derived for each section of the analog to digital converter system and then combined using the root-sum-square (RSS) method. This is an applicable method since the number of random error terms is large enough to be amenable to statical processes.

Input Multiplexer Error Analysis - The circuit consists of 8 multiplex switches, source resistors, and a buffer amplifier. Each switch is actually two switches paralleled to reduce the "on" resistance. The input signals come in through different switches of the same switch package. A common amplifier is used for signal buffering.

The multiplexer error is from three major sources and they are switch and input resistance difference between inputs, switch leakage current, and amplifier bias current.

An error model is shown below:

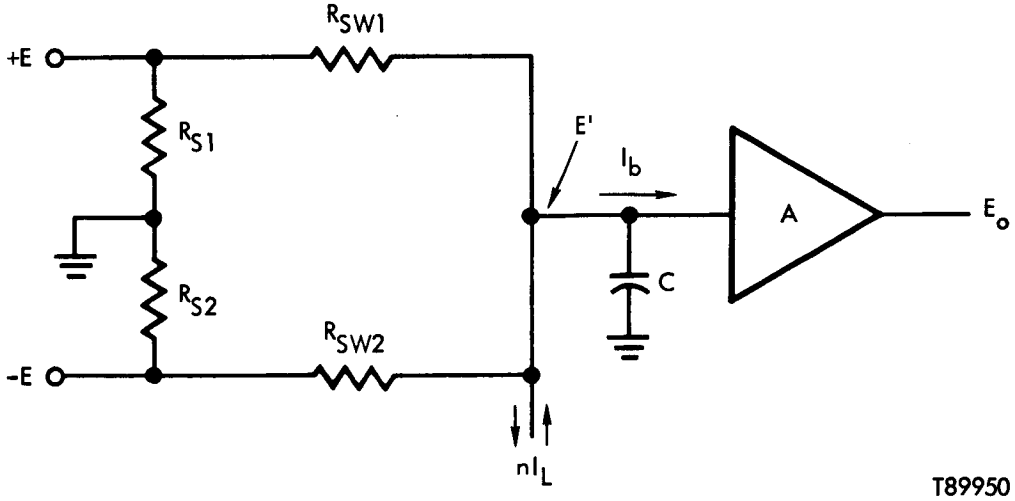

Where: R_{S1} = Source Resistance 1

R_{S2} = Source Resistance 2

R_{SW1} = Switch "on" Resistance 1

R_{SW2} = Switch "on" Resistance 2

nI_L = nx the individual switch leakage (n = 16)

I_b = Buffer Amplifier Bias Current

C = Total Loading Capacitance

E' = Actual Input Voltage to Buffer

A. Bias Errors

1. Initial Bias; $E' = (I_b + nI_L)(R + R_{SW})$

2. Differential Bias; $\Delta V_1 = +E - E_1'$

$$\Delta V_2 = -E - (-E_2')$$

$$\Delta V_B = \Delta V_1 + \Delta V_2 = +E - E_1' - E + E_2' = E_2' - E_1'$$

$$\Delta V_B = (R_{S2} + R_{SW2})(I_b + nI_L) - (R_{S1} + R_{SW1})(I_b + nI_L)$$

$$\Delta V_B = (I_b + nI_L)\,](R_{S2} - R_{S1}) + (R_{SW2} - R_{SW1})] \quad (2)$$

3. Temperature Variation and Channel Variation

$$\Delta V_{BT} = (\Delta I)(R) + (I)(\Delta R) + (I)(\Delta R_{SW})$$

$$\Delta V_{BT} = (\Delta I_b + \Delta nI_L)[(R_{S2} - R_{S1}) + (R_{SW2} - R_{SW1})] + (I_b + nI_L)[\Delta(R_{S2} - R_{S1}) + \Delta(R_{SW2} - R_{SW1})] + (I_b + nI_L)[\Delta R_{SW}] \quad (3)$$

B. Scale Factor Errors

1. Absolute; $V_S = (I_b + nI_L)[R_{SWA} - R_{SWB}]$ (4)

Where: R_{SWA} = Switch Resistance @ input voltage A

R_{SWB} = Switch Resistance @ input voltage B

2. Symmetry;

$$V_{SS} = (I_b + nI_L)\,[(R_{SW1A} - R_{SW2A}) - (R_{SW1B} - R_{SW2B})] \quad (5)$$

Where:

R_{SW1A} = Switch Resistance 1 @ input voltage A

R_{SW1B} = Switch Resistance 1 @ input voltage B

R_{SW2A} = Switch Resistance 2 @ input voltage A

R_{SW2B} = Switch Resistance 2 @ input voltage B

C. Settling Time Error

$$V_\tau = E\, e^{-T/\tau} = E\, e^{-T/(R_S + R_{SW})\,C} \quad (6)$$

D. Cross-Talk Error

$$V_c = \frac{E\,(R_{S1} - R_{S2})\,(R_{SW1} - R_{SW2})}{Z_c}$$

Where:

$$Z_c = \frac{1}{2\pi F_n C_{SD}}$$

nC_{SD} = n x MUX switch source to drain capacitance (n = 1)

f = Frequency of cross-talk voltage E.

$$V_c = E\,(2\pi f\, nC_{SD})\,(R_{S1} - R_{S2})\,(R_{SW1} - R_{SW2}) \quad (7)$$

Parameters for Input Multiplexer

1. Source Resistance (R_S) = 5K Ω nominal
2. Source Resistance Variation = ±0.2% end of life = 10 Ω
3. Switch Resistance (R_{SW}) = 400 Ω max/$2S_w$ = 200 Ω
4. Switch Resistance Variation = 40 Ω max/$2S_w$ = 20 Ω (within one 16 channel device)

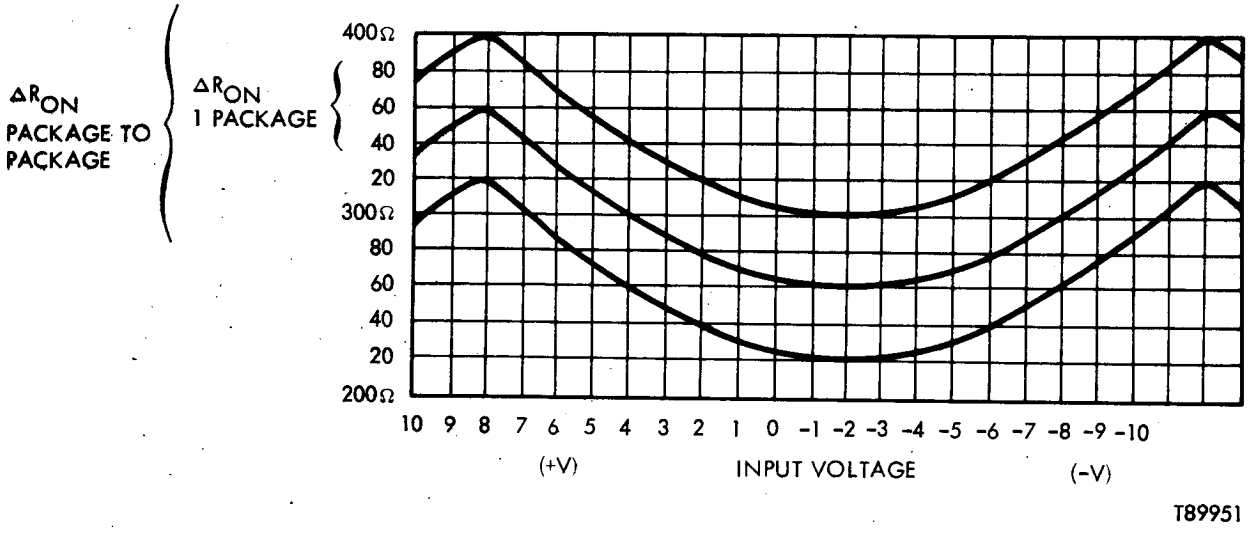

Figure AD-13. Switch Resistance Vs Input Voltage

5. Switch Resistance Symmetry = 60 Ω max/$2S_w$ = 30 Ω

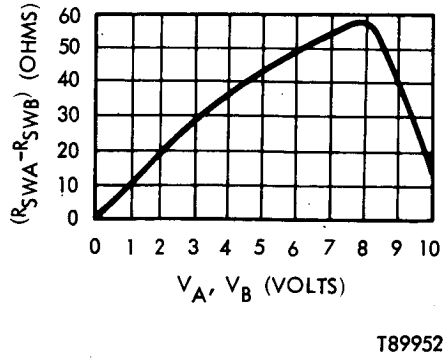

Figure AD-14. Switch Resistance Symmetry

6. Switch Linearity Variation = 1/2 Symmetry = 15 Ω

7. Switch Resistance Temp Variation ≈ 1 Ω/°C = 3 Ω for 3°C

8. Switch Leakage Current = nI_L = 60 na @ 60°C

9. Switch Leakage Temp Variation = 12 na for 3°C

Parameters for Input Buffer

1. Bias Current (I_b) = 150 na @ 60°C

2. Bias Current Variation (ΔI_b) ≈ 5 na (Temp, aging, and voltage)

3. Initial Offset Voltage = 6 mv max

4. Offset Voltage Drift = 20 μV/°C x 3°C = 0.06 mv

5. Common Mode Rejection Ratio (CMRR) = 80 DB

6. Differential CMRR = 100 DB

7. Open Loop Gain (OLG) = 80 DB

8. Differential Open Loop Gain (DOLG) = 100 DB

9. Power Supply Rejection Ratio (PSRR) = 80 DB

10. Settling Time = 0.01% in 2.5 μs for 20V step = 0 mv for 20 μs

Error Calculation - Input Multiplexer

A. Bias Errors

1. Initial: $E_B = (I_b + nI_L)[R_s + R_{SW}]$

E_B = (150 na + 60 na) [5K + .3K] @ V_{in} = 0V

E_B = (210 na) (5.3K) = 1.113 mv

This voltage is removed during calibration.

2. Differential Bias

$$\Delta V_B = (I_b + nI_L)\,[(R_{S2} - R_{S1}) + (R_{SW2} - R_{SW1})]$$

$$= (210\text{ na})\,[20\Omega + 30\Omega]$$

$$\Delta V_B = 0.0105\text{ mv}$$

3. Temperature Variation

$$\Delta V_B = (\Delta I_b + \Delta nI_L)[(R_{S2} - R_{S1}) + (R_{SW2} - R_{SW1})]$$

$$+(I_b + nI_L)[\Delta(R_{S2} - R_{S1}) + \Delta(R_{SW2} - R_{SW1}) + \Delta R_{SW}]$$

$$= (5\text{ na} + 12\text{ na})\,(20\Omega + 30\Omega)\quad (210\text{ na})[.3\Omega + 3\Omega + 20\,\Omega]$$

$$= (17\text{ na})\,(50\,\Omega) + (210\text{ na})\,(23.3\,\Omega)$$

$$\Delta V_{BT} = 0.85\,\mu v + 4.9\,\mu v \approx 6\,\mu v$$

B. Scale Factor Errors

1. Absolute;

$$V_S = (I_b + nI_L)[R_{SWA} - R_{SWB}]$$

$$= (210\text{ na})\,(100\,\Omega/2)$$

$$V_S = 0.0105\text{ mv}$$

2. Symmetry;

$$V_{SS} = (I_b + nI_L)[R_{SW1A} - R_{SW1B}) - (R_{SW1A} - R_{SW2B})]$$

$$V_{SS} = (210\text{ na})\,[\approx 1/2\text{ absolute} - 25\,\Omega]$$

$$V_{SS} = 0.005\text{ mv}$$

C. Settling Time Error

$$V_\tau = E\, e^{-T/(R_S + R_{SW})\, C}$$

$$(R_S + R_{SW})(C) = (5K + .2K)\ (100\ pf) = 0.52\ \mu s$$

$$T = 20\ \mu s$$

$$V_\tau = (20V)\ e^{-20/.52} = 20V\ e^{-38} = 0\ mv$$

D. Cross-Talk Error - Differential

$$V_c = E(2\ \pi\ f\ n\ C_{SD})\ (R_{S1} - R_{S2})(R_{SW1} - R_{SW2})$$

$$= 20V\ (2\pi)\ (5\ Hz)\ (15)\ (2pf)\ (20\Omega)\ (30\ \Omega)$$

$$V_c = 0.011\ mv$$

Input Buffer Error Analysis

A single buffer amplifier is used for both $\pm E$ and $-E$. Therefore, all offset type error will affect both voltages equally and will be removed either during calibration or by the logic as shown below:

$$\begin{array}{r} +E + \Delta \\ \underline{(-)\ -E + \Delta} \\ 2E \end{array}$$

} Offset Logically Removed by Subtraction

Offset removed by main A/D converter
Offset adjustment

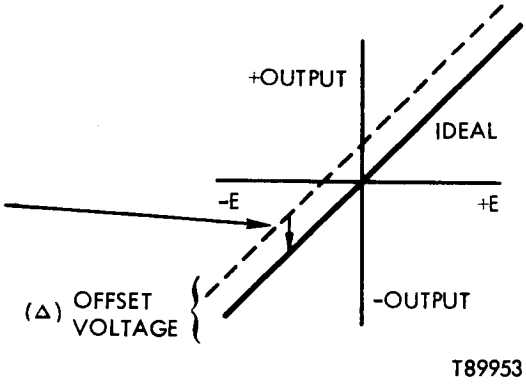

Figure AD-15. Buffer; V_{out} Vs V_{in}

The linear scalar type errors will be removed during the ADC offset voltage and gain calibration as shown below:

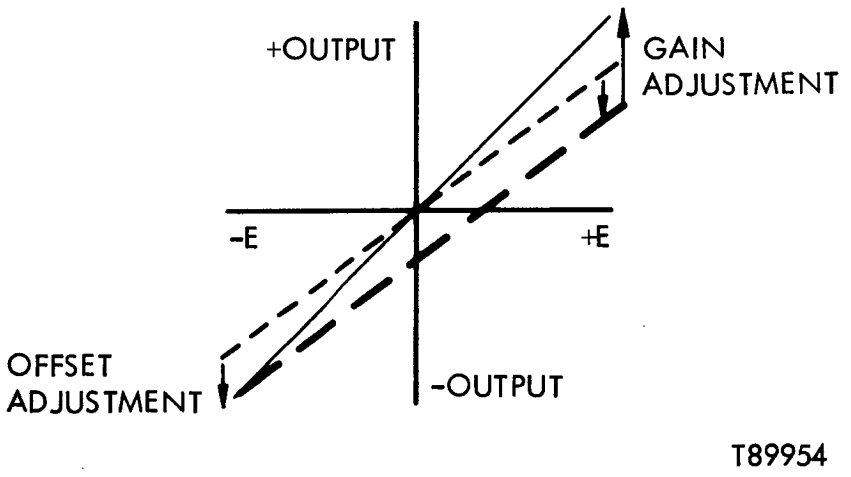

Figure AD-16. Error Adjustment

The non-linear and differential errors can not be removed.

Error Calculations - Input Buffer

A. Bias Current Errors - Included in MUX

B. Offset Voltage Errors

1. Initial; V_{0S} = 6 mv max

This error is removed during calibration.

2. Drift; ΔV_{0S} = 0.06 mv

This error is removed by the logic.

C. CMRR Errors

1. Linear; $V_{CMRR} = E/C_{MRR}$ = 10V/80 DB = 1 mv

This error is removed during calibration

2. Differential CMRR; $\Delta V_{CMRR} = E/D_{CMRR}$ = 10V/100 DB = 0.1 mv

D. Open Loop Gain Errors

1. Linear; V_{0L} = E/OLG = 10V/80 DB = 1 mv

This error is removed during calibration.

2. Differential OLG; ΔV_{OLG} = E/DOLG = 10V/100 DB = 0.1 mv

E. PSRR Error

$$V_{PSRR} = \Delta V_{PS}/PSRR = \frac{(30V)\ (.25\%)}{80\ DB} = 0.0075\ mv$$

F. Settling Time Error

$V_{\tau} \approx 0$ mv.

MUX and Buffer Error Analysis

The MUX and Buffer consists of a two channel multiplexer and a buffer amplifier. Only one channel is used for both +E and -E and the switch, being a JFET, has an "on" resistance independent of input voltage. This reduces all multiplexer errors to constant offset voltages which are removed by calibration and logic. The buffer errors are identical to those of the input buffer except for settling time.

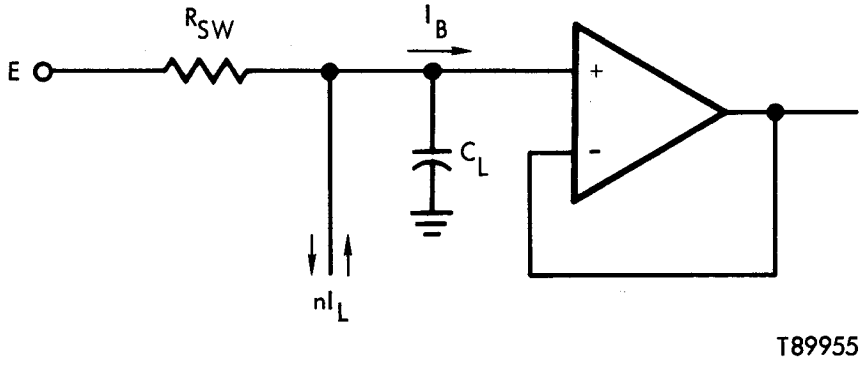

Figure AD-17. Error Model-Buffer

In Figure AD-17:

R_{SW} = Switch "on" Resistance
nI_L = nx Switch Leakage (n = 3)
I_b = Buffer Amp Bias Current
C_L = Total Loading Capacitance

Parameters for MUX

1. Switch Resistance (R_{SW}) = 100 Ω max

2. Switch Leakage Current (nI_L) = 3 x 25 na = 75 na @ 60°C

3. $C_L = [C_{D(ON)} + C_{S(ON)}] + 2\ C_{D(OFF)}$ + Stray ≈ 14 pf + 2 (6 pf) + 14 pf

   C_t = 40 pf

Parameters for Buffer

Same as input buffer except as noted below.

1. Differential Settling Time = 0.001% in 2.5 μs for 20 V step.

Error Calculations

1. MUX offset Error (Removed by calibration)

   $E_{OS} = (R_{SW})\ (nI_L + I_B)$ =(100 Ω)(75 na + 150 na) = 0.0225 mv

2. Settling Error ≈ $E\ e^{-T/\tau}$ = 0 mv

   $T = T' - T_{ON}$

   $T' = 2.5\ \mu s$; $T_{ON} = 0.25\ \mu s$

   $\tau = (R_{SW})\ (C_L) = 4$ ns

3. Buffer errors same as input buffer except;
   Differential Settling Error; V_τ = (20V)(.001%) = 0.2 mv

Main A/D Converter Error Analysis - The main A/D converter is a module consisting of many components. It is a high speed successive approximation converter which can be externally adjusted for offset and gain (scale factor). The specified parameters which affect accuracy are listed below:

Specified Parameters

Absolute Accuracy = 100 PPM (2mv)
Relatave Accuracy = 100 PPM (2mv)
Differential Linearity = 100 PPM (2mv)

PSRR = ±0.002%/%ΔV_S; E = (±0.002%)(15V)(1%) = ±3 μv

Diff Linearity TC = ±3 ppm/°C; E = (20V)(±3 ppm/°C)(3°C) = 0.18 mv

Gain TC = ±5 ppm/°C; E = (20V)(±5 ppm/°C)(3°C) = 0.3 mv

Offset TC = ±5 ppm/°C; E = (20V)(±5 ppm/°C)(3°C) = 0.3 mv

Monotonicity = implied in differential linearity spec.

Conversion Time = 18 μs max

Absolute Offset = ±10 mv externally adjustable (±40 mv Range)

Absolute Gain (Scale Factor) = externally adjustable = ±10 mv
(Range = ±40 mv)

The absolute accuracy of the Main A/D converter is used only to define the range over which the gain and offset need to be adjusted. Once calibrated the relative accuracy becomes the relevant specification. The relative accuracy includes initial linearity and initial differential linearity. Linearity, or actually nonlinearity, is defined as the variation from a straight line between the full scale end points of an analog input vs digital output transition point plot as shown in figure AD-18.

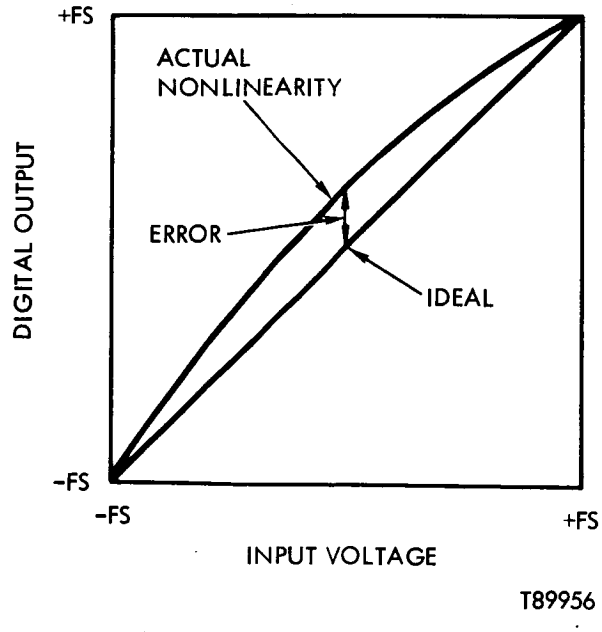

Figure AD-18. Nonlinearity of Main A/D Converter

The differential linearity, or nonlinearity is a measure of the variation in analog value change associated with a one-bit change in the associated digital number. Ideally, a one bit digital value change should have associated with it a constant incremental change in analog signal anywhere on the input/output transfer characteristic. Differential nonlinearity can be quantified in the following manner.

Assume an analog signal span Es, and an n-bit binary converter. A normalized 1-bit increment ΔEn can be defined as

$$\Delta E_n = E_S 2^{-n}$$

Differential linearity error, ϵ_{DL}, can be defined as $\epsilon_{DL} = (E - E_N)/ E_N$

where ΔE is the actual change in analog value associated with any 1-digit change in the binary number. This is illustrated in Figure AD-19.

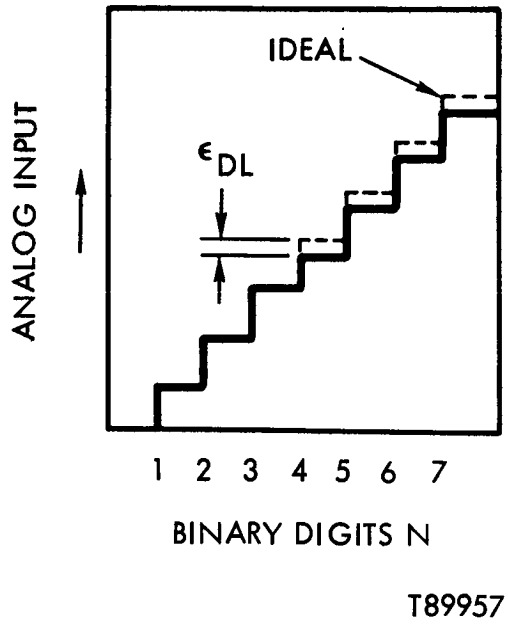

Figure AD-19. Differential Nonlinearity Error

This error is associated with specific bit positions in the ladder network and ladder switches. This error is then cyclic and symmetrical about the MSB which is zero volts.

The differential nonlinearity error will not add to the relative accuracy error and calibration of the Main A/D converter at the MSB will insure symmetry.

The changes in differential linearity and gain with temperature are independent functions and can be RSS'ed with the relative accuracy error.

The PSRR is sufficiently high as to allow its error to be insignificant.

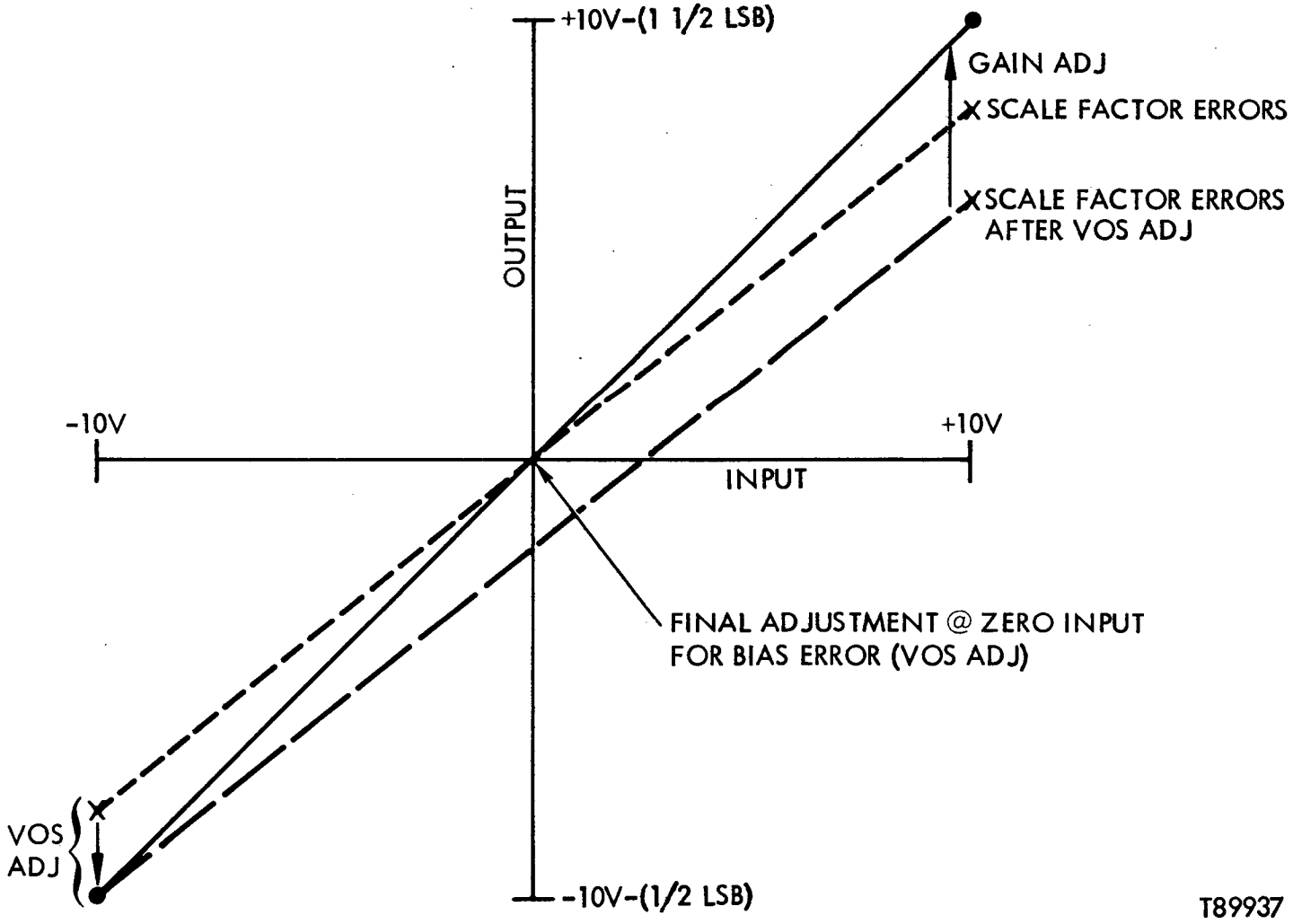

Figure AD-20. Main A/D Converter Error Adjustments

Table AD-1. Total Error Summary and Calculation

Error Parameter	Errors					
	Offset Voltage	Bias		Scale Factor		
				Absolute	Differential	
	E_1	E_1	E_1^2	E_2	E_2	E_2^2
	mv	mv	10-10V	mv	mv	10-10V
Input Multiplexer						
Bias: Initial	1.113					
Differential		0.0105	1.1			
Temperature		0.006	0.36			
Scale Factor:						
Absolute				0.0105		
Symmetry					0.005	0.25
Crosstalk-Differential:		0.011	1.21			
Input Buffer						
Input Current	Included In MUX					
Offset Voltage:						
Initial	6					
Drift	0.06					
CMRR:						
Linear				1.0		
Differential					0.1	100.
Open Loop Gain:						
Linear				1.0		
Differential					0.1	100.
PSRR:		0.0075	0.56			
Settling Time:		0			0	
MUX & Buffer						
MUX:						
Offset	0.0225					
Settling		0			0	
Buffer:						
Input Current	Included in MUX					
Offset Voltage:						
Initial	6					
Drift	0.06					

T89971

Table AD-1. Total Error Summary and Calculation (Continued)

Error Parameter	Errors: Offset Voltage E1	Bias: E1	Bias: $E1^2$	Scale Factor: Absolute E2	Scale Factor: Differential E2	Scale Factor: Differential $E2^2$
	mv	mv	$10^{-10}V$	mv	mv	$10^{-10}V$
MUX & Buffer (Continued)						
CMRR:						
Linear				1.0		
Differential					0.1	100.
Open Loop Gain:						
Linear				1.0		
Differential					0.1	100.
PSRR:		0.0075	0.56			
Differential Settling:					0.2	400.
Main A/D Converter						
Absolute Accuracy:				2		
Relative Accuracy:					2	40000
Differential Linearity:	Included in Rel.	Accuracy				
PSRR:		0.03	0.09			
Diff. Linearity Drift:					0.18	324.
Gain Drift:					0.3	900.
Offset Drift:	0.3					
Absolute Offset	10					
Absolute Gain:				10		
TOTAL	23.55 mv	0.045 mv	3.88 $x10^{-10}V$	16.01 mv	3.085 mv	42024 $x10^{-10}V$
RSS ERROR			0.02mv			2.1mv
RSS ERROR IN PPM OF FULL SCALE:			1 PPM			105PPM

From The Total Output Error Equation: $ET = \Sigma E1(N1N2)/2 + \Sigma E1$

The Total RSS Error Is: ET = 105 PPM + 1 PPM = 106 PPM

T89972

This page intentionally left blank